



**HAL**  
open science

# Localized Organic Electrografting on Conductive and Semiconductive Surfaces Induced by Local Probe Electrochemical Microscopy

Federico Grisotto

► **To cite this version:**

Federico Grisotto. Localized Organic Electrografting on Conductive and Semiconductive Surfaces Induced by Local Probe Electrochemical Microscopy. Material chemistry. Ecole Polytechnique X, 2010. English. NNT: . tel-00590964

**HAL Id: tel-00590964**

**<https://pastel.hal.science/tel-00590964>**

Submitted on 5 May 2011

**HAL** is a multi-disciplinary open access archive for the deposit and dissemination of scientific research documents, whether they are published or not. The documents may come from teaching and research institutions in France or abroad, or from public or private research centers.

L'archive ouverte pluridisciplinaire **HAL**, est destinée au dépôt et à la diffusion de documents scientifiques de niveau recherche, publiés ou non, émanant des établissements d'enseignement et de recherche français ou étrangers, des laboratoires publics ou privés.



# Thèse de doctorat de l'École Polytechnique

présentée par

**Federico GRISOTTO**

pour obtenir le titre de Docteur de l'École Polytechnique

## Localized Organic Electrografting on Conductive and Semiconductive Surfaces Induced by Local Probe Electrochemical Microscopy

Soutenue le 15 Décembre 2010 devant le jury composé de :

Dr. François OZANAM	Président
Prof. Jean PINSON	Rapporteur
Prof. Francesco PAOLUCCI	Rapporteur
Prof. Mehmet OTURAN	Examineur
Dr. Julienne CHARLIER	Directrice de thèse

Thèse préparée au Laboratoire de Chimie des Surfaces et des Interfaces (LCSI)

Service de Physique et de Chimie des Surfaces et Interfaces (SPCSI)

Institut Rayonnement Matière de Saclay (IRAMIS), CEA - Saclay



## REMERCIEMENTS

Ce travail a été réalisé à l'Institut Rayonnement Matière de Saclay (IRAMIS) du Commissariat à l'Energie Atomique (CEA) de Saclay, dans le service de Physique et de Chimie des Surfaces et des Interfaces (SPCSI) au sein du groupe de Chimie des Surfaces et des Interfaces dirigé par Monsieur Serge Palacin. Je le remercie de m'avoir accueilli au sein de son laboratoire, pour sa sympathie et pour les conseils qu'il m'a prodigués.

Je remercie vivement Madame Julienne Charlier d'avoir été ma directrice de thèse et de m'avoir initié à la recherche et conseillé durant ces trois années. Je tiens à lui témoigner toute mon amitié et ma reconnaissance pour avoir dirigé ces travaux avec tant d'intérêt, de disponibilité et de dynamisme.

J'adresse mes remerciements à Messieurs J. Pinson, Professeur Emérite de l'Université de Paris Diderot, et F. Paolluci, Professeur de l'Université de Bologne, qui ont accepté de juger ce travail. J'exprime ma reconnaissance à Messieurs M. Oturan, Professeur à l'Université Paris Est, et F. Ozanam, Directeur du Laboratoire de Physique de la Matière Condensée de l'Ecole Polytechnique d'avoir respectivement accepté de participer à ce jury et de le présider.

Mon passage au LCSl, riche en expériences tant au niveau scientifique que sur le plan culturel et humain, me marquera tout le long de ma vie professionnelle. Je tiens plus particulièrement à remercier Achraf Ghorbal, Cédric Goyer, Romain Metayé et Dimitry Aldakov pour notre fructueuse collaboration, nos discussions et leurs amitiés.

Que tous les membres du laboratoire permanents ou non trouvent ici ma reconnaissance pour leur aide, leur soutien et leur bonne humeur.

Enfin, je tiens également à remercier et à témoigner toute ma reconnaissance à mes parents qui m'ont permis de réaliser mes études et m'ont toujours encouragé et soutenu. Je les remercie vivement pour leur appui moral au cours de ces trois années.



## ABBREVIATIONS, NOTATIONS, SYMBOLS & ACRONYMS

AA	Acrylic acid
AD	Aryl diazonium
AFM	Atomic force microscopy
Ar°	Aryl radical
ArN <sub>2</sub> <sup>+</sup>	Aryl diazonium salt
ATRP	Atom transfer radical polymerization
BrB	Bromobenzene diazonium
BuMA	Buthylmethacrylate
CE	Counter-electrode
CEVP	Cathodic electrografting of vinylic polymers
CV	Cyclic voltammetry
DMF	Dimethylformamide
E <sub>CE</sub>	Counter-electrode potential
E <sub>UME</sub>	Ultramicroelectrode potential
HEMA	Hydroxylethylmethacrylate
HOR	Hydrogen oxidation reaction
IRAS	Infrared reflexion absorption spectroscopy
ITO	Indium Tin Oxide
LCSI	Laboratoire de chimie des surfaces et des interfaces
MAN	Methacrylonitrile
NBD or DNB	Nitrobenzene diazonium
OLED	Organic light emitting diode
ORR	Oxygen reduction reaction
PA or PAA	Polyacrylic acid
PET	Polyethyleneterephtalate
PNP	Polynitrophenylene
PP	Polyphenylene
RE	Refence electrode
SAM	Self-assembly monolayer
SC	Substrate collector
SECM	Scanning electrochemical microscopy
SEEP	Surface electroinitiated emulsion polymerization process
SEM	Scanning electron microscopy
SG	Substrate generator
SPM	Scanning probe microscopy
STM	Sacnning tunneling microscopy
TC	Tip collector
TEAP	Tetraéthylammonium perchlorate
TG	Tip generator
UME	Ultramicroelectrode
WD	Working distance
WE	Working electrode
XPS	X-Ray photoelectron spectroscopy

$A$	Electrode area
$\alpha$	Transfer coefficient
$a$	Radius of the conductive core of the ultramicroelectrode
$C_0$	Bulk concentration of $O$
$C_{O/R}(0, t)$	Surface concentration of $O$ or $R$ at time $t$
$d$	Working distance
$d/a$	Normalized working distance
$D_O$	Diffusion coefficient of $O$
$E$	Applied potential
$E^0$	Standard potential
$E_{CE}$	Potential of the counter-electrode
$E_S$	Potential of the substrate
$E_{we}$	Potential of the working electrode
$F$	Faraday constant
$i_T$	Tip current
$i_{T^{ss}}$	Steady-state diffusion-limited current
$I_N$	Normalized tip current, $i_T/i_{T^{ss}}$
$I_{sub}$ or $I_S$	Current applied or recorded on the substrate
$I_{UME}$	Current at the tip
$I_{sub}/I_{UME}$	Collection efficiency
$k_0$	Standard heterogeneous rate constant
$L$	Width of the grafted pattern
$L/2a$	Normalized width
$n$	Number of electrons transferred
$O$	Oxidized form of the redox species
$R$	Reduced form of the redox species
$R$	Gas constant
$r_0$	Radius of the hemisphere
$RG$	Dimensionless parameter: $r_g/a$
$r_g$	Total tip radius: $a$ plus the insulating sheath thickness
$T$	Absolute temperature
$v$	Scan rate ( $\mu\text{m s}^{-1}$ )

### XPS terminology

$d$	Layer thickness
$I$	Intensity signal of a coated substrate
$I_0$	Intensity signal of a bare substrate
$\lambda$	Electron attenuation length
FoV	Field of view

## Table of contents

<b>Introduction:</b> Why direct localized electro-grafting on conductive and semi-conductive surfaces through a mask-free process is important? .....	1
<b>Chapter 1: Electrochemistry background</b> .....	4
1.0 Electrochemical concept .....	4
1.1 Cyclic voltamperometry .....	4
1.2 Ultramicroelectrode .....	7
2.0 Scanning electrochemical microscopy .....	9
2.1 Instrumentation .....	10
2.2 Mode of operation .....	11
2.2.1 Feedback mode .....	12
2.2.2 Collection-generation modes .....	14
2.3 Main application of SECM .....	15
2.3.1 Imaging .....	16
2.3.2 Study of the reaction rate .....	17
2.3.3 Study of the corrosion .....	19
2.3.4 Electrocatalysis .....	19
2.3.5 Study of biological system .....	21
2.3.6 Localized modification of substrate: microstructuration .....	22
2.3.7 Hybrids techniques .....	23
Conclusion .....	24
References .....	25
<b>Chapter 2: Organic electrografting on conducting and semiconducting substrate</b> .....	30
1.0 Introduction .....	30
2.0 Electrografting of organic films on conducting and semiconducting substrate .....	33
2.1 Cathodic electrografting of vinylic polymers .....	33
2.2 Electrografting of polyphenylene coatings from diazonium salt .....	37
3.0 Indirect cathodic electrografting of vinylic polymer: the SEEP process .....	46
References .....	53
Annex 1: Experimental procedure for nano-friction experiments .....	56
Annex 2: Experimental procedure for the electrografted SEEP process .....	58

<b>Chapter 3: Localized electrografting: a strategy to tailoring the reaction and patterning polymer films on conductive surfaces</b> .....	59
1.0 Introduction .....	59
2.0 Localized electrografting with SECM .....	63
2.1 Localized electrografting with SECM: Proof of concept .....	65
2.2 Localized electrografting with SECM: Study of the influence of experimental parameters .....	69
2.2.1 Influence of the acrylic acid concentration .....	73
2.2.2 Influence of electrolysis duration .....	74
2.2.3 Influence of working distance and scan rate .....	76
2.2.3.1 Influence of the working distance in static mode .....	77
2.2.3.2 Influence of the scan rate .....	81
2.2.4 Influences of the RG parameters .....	87
3.0 Localized electrografting of the diazonium salts .....	90
4.0 Localized SEEP process: a “generic” process? .....	92
5.0 SECM as direct lithographic tool for conducting substrate .....	94
6.0 Extention of the process to sub-micronic resolution: AFM-SECM .....	95
6.1 Integrated AFM-SECM probe .....	96
6.2 Localized grafting at a sub-micronic scale .....	97
Conclusions .....	100
References .....	101
Annex 1: Preparation and characterisation of microdisk electrodes .....	104
Annex 2: SECM imaging process .....	104
Annex 3: Fabrication and characterisation of the AFM-SECM tip .....	106
Annex 4: Experimental setup for AFM-SECM experiments .....	107
<b>Chapter 4: Localized grafting in the four electrodes cell configuration, reasons investigation for a local effect</b> .....	109
1.0 Introduction .....	109
2.0 Influence of the applied potential to the microelectrode .....	114
3.0 Influence of the potential applied to the substrate .....	119
4.0 Influence of working distance on the localized reaction .....	122
5.0 Influence of electrolysis duration .....	124
5.1 Investigation of the kinetic of reaction .....	124
5.2 Potential/time optimization .....	127
6.0 XPS analysis of the localized grafted coating .....	130
7.0 Plausible steps mechanism responsible for the localized electrografting .....	133
8.0 Extention of the process to other conducting and semiconducting substrates (Pt, grapheme, n-type Si) .....	137

## INTRODUCTION

### **Why direct localized electro-grafting on conductive and semi-conductive surfaces through a mask-free process is important?**

Several years ago, a trend of interdisciplinary research started to connect the possibilities of conductive or semiconductive substrates with the versatility of organic molecules and biomolecules. Tailoring the interface between surfaces and organics is a prerequisite for numerous developments in different fields, such as medicine, genetics, electronics, sensing, and photovoltaics.

More particularly, the **localized** grafting, at a **micronic** or **submicronic** scale, of organic substances on surfaces is thus often a prerequisite in the design of bioelectronics devices, and a valuable component of some combinatorial screening strategies. Moreover, microelectronic devices including transistors, sensors, memories as well as micro-fluidic channels, and video-screen, are generally based on interfaces between conducting and quasi-insulating domains resulting from lithographic steps, ionic implantation and silicon oxide thermal growth. Most of the existing techniques require many steps of transformation and their implementation is often expensive.

The coating surface technology is a domain centered on the functional materials deposited on a substrate and giving special properties to the supporting structure. The **electro-grafting** is a technique able to introduce chemical functions covalently bonded on the surface. This is a guarantee of stability in the time and under aggressive environment. In this study we developed a one step technique that allows the **direct** localized electrografting of organic matter on homogeneous **conductive** and **semi-conductive** substrates at a micronic or sub-micronic scale. In order to limit the cost and the number of transformation steps, we researched a **mask-free** process allowing, in only one step, the localization of organic coating chemically bonded to initially homogeneous substrates thanks to the coating process itself. Therefore, we used a **Scanning Electrochemical Microscopy (SECM)** to promote the local electrografting of thin organic coatings. This study describes thus the steps undertaken to realize a robust one-step technique of localized surface modification by SECM. The work is centered on experimental evidences and characterizations that have driven the research and the subsequent improvement of the process.

To avoid any misunderstanding, it must be clearly noted that our work does not want to be a contribution to the theoretical and/or instrumental development of the SECM technique itself. Our followed objective is clearly to use SECM as an electrochemical tool allowing us to generate locally particular electrochemical conditions able to start the grafting process. For that reason, we have attempted to rationalize our observations in terms of basic electrochemical processes. Moreover, we do not have of

knowledge and the tools allowing to develop the modeling aspect inherent in the technique. Therefore, in the absence of some modeling, our analysis may remain rather qualitative. Nevertheless, we think that our experimental results are sufficiently rich to bring an interesting contribution to the SECM literature on patterning. We are also convinced that our experimental data set can constitute a solid base for forthcoming modeling challenges.

The manuscript is structured in five chapters.

In the first chapter, we introduce the SECM technique. Microelectrode (UME) properties, the core of this microscope, are briefly explained and the main applications are cited. Imaging of electrical surface properties and studies of surface reactions rates are also reported through some significant examples. To conclude this chapter, some interesting examples of local electrochemical modifications are listed.

The second chapter is devoted to several coating technologies and focuses more particularly on (i) the cathodic electro-grafting process, historically developed by the LCSi lab (*Laboratoire de Chimie des Surfaces et Interfaces*), (ii) the electro-grafting from diazonium salts and the formation of an adhesive primer layer, and (iii) the indirect cathodic electrografting of vinylic polymers initiated by the aryl radicals (also called the Surface Electroinitiated Emulsion Polymerisation process, SEEP).

Chapters 3 and 4 are devoted to the local electro-grafting process itself using the SECM tree- and four-electrodes configuration, respectively. Both chapters describe a series of systematic studies looking at the effect of key parameters and gather our main experimental results. Chapter 3 emphasizes more particularly the proof of concept, the lithographic capabilities of the developed process, and its extension to the sub-micronic scale. Chapter 4 tends to investigate more precisely the mechanism of the process. Thanks to an individual control of the potential applied to both electrodes, we are able to establish the necessary and sufficient conditions to induce the localized electro-grafting, making so possible the extension of the process to several conductive and semi-conductive substrates.

In opposition of the previous chapters which are devoted to the localized grafting of organic coatings on a substrate, the fifth chapter treats the local etching of a transparency semi conductive substrate (ITO). This chapter, in margin of the principal subject of the thesis, is nevertheless interesting for the prospects that it opens in the field of the patterning of microcircuits on flexible support such as those used for the organic light-emitting diodes (OLEDs) manufacture.

To conclude, the perspectives of this work are discussed through three examples of potential applications for which a preliminary concept of demonstration is presented: (i) the transposition of the localized process to a structured microelectrode, (ii) the

possibility to use the localized grafted surface as a mask for a subsequent global electrografting process, and (iii) the possibility to use the localized grafted surface for biological detection.



# CHAPTER 1

## ELECTROCHEMISTRY BACKGROUND

This chapter introduces the electrochemical concepts relevant to this work including cyclic voltammetry, ultramicroelectrodes, and scanning electrochemical microscopy. We also give examples of fields of applications for the SECM technique.

### 1. Electrochemical concepts

#### 1.1. Cyclic voltammetry (CV)

Cyclic voltammetry is a very versatile electroanalytical technique that has been applied to a variety of investigations including evaluation of electron transfer kinetics and elucidation of transfer mechanisms,<sup>[1]</sup> characterization of materials (e.g. catalyst surfaces,<sup>[2]</sup> conducting polymers<sup>[3]</sup>), and biomedical research (in-vivo monitoring of dopamine release in the brain, for example).<sup>[4]</sup>

Practically the surface undergo the CV, the working electrode (WE), is polarised respect a reference electrode (RE) and a current flow is installed between the WE and a counterelectrode (CE). During a CV experiment, the potential applied to the working electrode is varied with a linear potential sweep starting from an initial potential value ( $E_i$ ) to a switching potential ( $E_\lambda$ ), where the sweep direction is reversed and returned to the initial value (Figure 1A). The scan rate  $\nu$  of the potential sweep is an important parameter, since it determines the time scale of the experiment.<sup>[1]</sup> The resulting current is plotted against the applied potential. Figure 1B shows a CV for a one-electron transfer reaction defined by the following reaction



where O is the oxidized form of the involved redox species, and R is the reduced form.

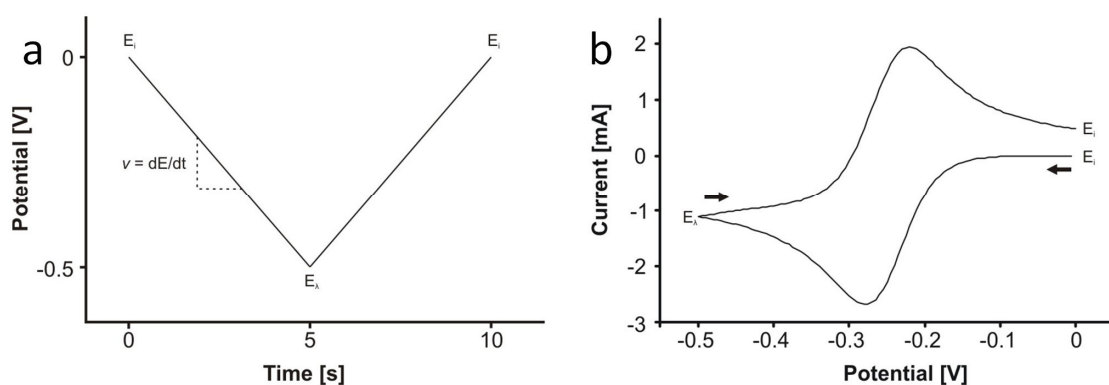


Figure 1: (a) Shape of the potential waveform applied during a CV scan. (b) CV for a reversible reaction at a macroscopic electrode.

The shape of the CV is determined by two processes, heterogeneous charge transfer at the interface, and diffusional mass transport. The heterogeneous charge transfer at the interface is described by Equation (1.1)<sup>[1]</sup>

$$i = n F A \left[ C_O(0, t) k^0 \exp\left(\frac{-\alpha n F (E - E^0)}{RT}\right) - C_R(0, t) k^0 \exp\left(\frac{(1 - \alpha) n F (E - E^0)}{RT}\right) \right] \quad (1.1)$$

where  $n$  is the number of electrons transferred in the electrode reaction,  $F$  is the Faraday constant,  $A$  is the electrode area,  $C_{O/R}(0, t)$  are the surface concentrations of  $O$  or  $R$  at time  $t$ ,  $k_0$  is the standard heterogeneous rate constant,  $\alpha$  is the transfer coefficient,  $E$  is the applied potential,  $E^0$  is the standard potential,  $R$  is the gas constant, and  $T$  is the absolute temperature.

Generally, mass transport may proceed as a result of three effects: convection, migration, and diffusion. However, only diffusional mass transport effects are considered in typical CV theory, since convection may be avoided in unstirred solutions, and migration may be suppressed by addition of an excess of supporting electrolyte. Electrode surface concentrations of the reactive species are dependent upon the applied potential and differ from the bulk concentrations during the electrochemical experiment.

Diffusion controlled mass transport occurs via the concentration gradient. Fick's second law of diffusion describes the time-dependent change of the diffusion field, and as a result, the time-dependent current observed at the electrode can be derived as follows<sup>[5]</sup>

$$i = n F A D_O \left[ \frac{\partial C_O(x, t)}{\partial x} \right]_{x=0} \quad (1.2)$$

where  $D_O$  is the diffusion coefficient of  $O$ ,  $\frac{\partial C_O(x, t)}{\partial x}$  is the concentration gradient in distance  $x$  at time  $t$ , and other parameters are as defined previously. Note that this relationship is only defined for planar diffusion. Solving Equation (1.2) leads to the Cottrell equation<sup>[6]</sup>

$$i = \frac{n F A \sqrt{D_O} C_O}{\sqrt{\pi t}} \quad (1.3)$$

where  $C_O$  is the bulk concentration of  $O$ , while other parameters are defined as before.

From Equations (1.2) and (1.3) it is evident that there are two components contributing to the current measured at the electrode, the heterogeneous charge transfer at the interface, and diffusion. However, depending on the rate of the heterogeneous charge transfer, one of the two components can prevail. In case the charge transfer proceeds fast ( $k_0 > 10^{-1} \text{ cm s}^{-1}$ , reversible case), the current measured is limited by mass transport (diffusion controlled process). For this case Equation (1.2) reduces to the Nernst equation, and the surface concentrations are dependent on the applied potential. The other boundary is represented by the irreversible case ( $k_0 < 10^{-5} \text{ cm s}^{-1}$ ), where the heterogeneous charge transfer is the rate limiting step determining the measured current. Quasi-reversible reactions are in between these two cases (approx.  $10^{-1} \text{ cm s}^{-1} > k_0 > 10^{-5} \text{ cm s}^{-1}$ ), and are consequently controlled by both the mass transport and the heterogeneous charge transfer.<sup>[1]</sup>

## 1.2. Ultramicroelectrodes

Ultramicroelectrodes (UMEs), commonly also called tips, are electrodes with characteristic dimensions on the micrometer or sub-micrometer scale. The properties of small electrodes have been investigated intensively since the 1980s.<sup>[7, 8]</sup> As already indicated earlier, the Cottrell equation is only defined for planar diffusion observed at macroscopic electrodes. During planar diffusion, mass transport occurs perpendicularly to the electrode surface, and may be mathematically described as one dimensional diffusion (scheme 1a). Despite diffusion at electrode edges deviating from planarity, edge effects are negligible at large electrode surfaces. At small electrode surfaces (i.e. UMEs), contributions from mass transport parallel to the electrode surface (i.e. electrode edges) are not negligible anymore, and have to be considered.



Scheme 1: Schematic representation of planar (a) and hemispherical (b) diffusion.

In this case, diffusion is referred to as hemispherical diffusion (for a disk electrode), and is mathematically described by two-dimensional diffusion processes (scheme 1b). Solving the diffusion equation leads to a modified Cottrell equation with a second term as follows<sup>[7]</sup>

$$i = \frac{nFA\sqrt{D_0}C_0}{\sqrt{\pi t}} + b \frac{nFAD_0C_0}{\sqrt{\pi a}} \quad (1.4)$$

where  $b$  is a prefactor that is influenced by the transition from the planar to the hemispherical diffusion field, and  $a$  is the radius of the electrode. Depending on the time scale of the experiment, either the first or the second term of the equation dominates. The first term is equivalent to the unmodified Cottrell equation dominating at short time scales. At longer time scales, the second term dominates and a steady-state current may be observed. Due to hemispherical diffusion towards the electrode surface, smaller electrodes need a shorter time to reach the steady-state. Zoski et al. calculated the time required to reach steady-state currents at disk electrodes with different electrode radii.<sup>[9]</sup> The authors concluded that at the assumed diffusion coefficient ( $10^{-5} \text{ cm}^2 \text{ s}^{-1}$ ) disks with radii of  $5 \mu\text{m}$  and  $0.5 \mu\text{m}$  required 1.3 s and 0.01 s, respectively, to reach steady-state. At macroelectrodes, this time is in the range of hours.<sup>[7]</sup> Given the small surface area, high current densities are observed during hemispherical diffusion.

As indicated earlier, the shape of a CV depends on the diffusional mass transport. Hemispherical diffusion leads to a sigmoidal shape of the CV. The time scale of the experiment can be directly influenced by the scan rate. Hence, at fast scan rates planar diffusion is observed, whereas at slow scan rates hemispherical diffusion dominates. Similarly, decreasing the electrode radius at a constant scan rate increases the contribution of hemispherical diffusion. This effect is visualized on figure 2.

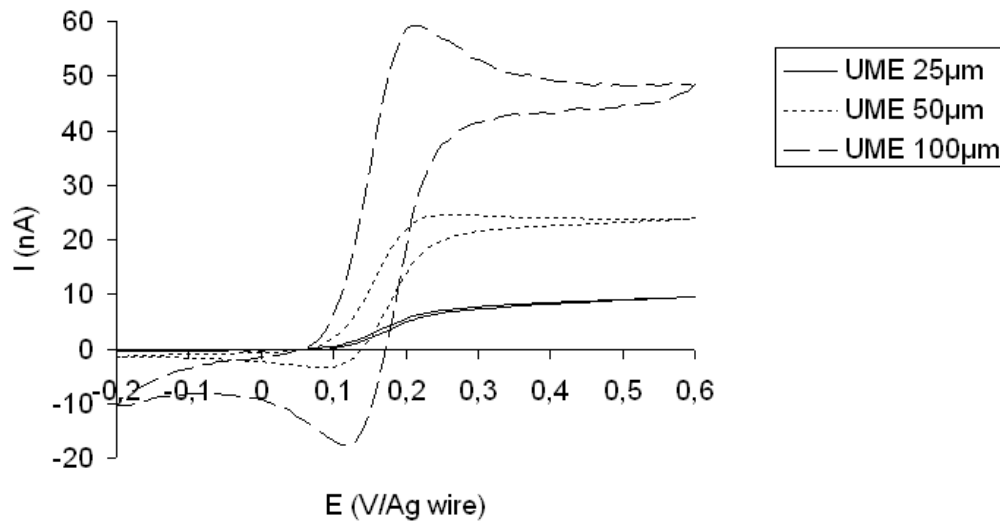


Figure 2: Cyclic voltammetry of the oxidation of ferrocene methanol ( $5 \cdot 10^{-3} \text{ mol.dm}^{-3}$ ) in  $\text{KCl } 10^{-2} \text{ mol.dm}^{-3}$  for three different ultramicroelectrodes sizes:  $100\mu\text{m-Pt UME}$  (dashed line),  $50\mu\text{m-Pt UME}$  (dotted line),  $25\mu\text{m-Pt UME}$  (solid line). Scan rate:  $50\text{mV s}^{-1}$ .

One of the advantages of the UMEs is thus the formation of a hemispherical diffusion field that allows more efficient mass transfer than that at macroscopic electrodes. For example, let's consider an ultramicroelectrode immersed in a solution containing an electrolyte and a redox species (e.g., a reducible species,  $O$ ), at the concentration  $C$  in solution. The tip initiates faradic reactions with electroactive species present in the solution. If the potential at the SECM tip is sufficient to reduce  $O$  to a species  $R$ , the special diffusion properties lead to a rapid establishment of a steady-state diffusion-limited current  $i_{T\infty}$ , which is proportional to the concentration of species  $O$ . When the tip is far (i.e., more than 4 tip electrode diameters), the steady-state current attained at the tip,  $i_{T\infty}$ , is given, for a disk-shaped electrode surrounded by an insulating sheath by equation (1.5)<sup>[7]</sup>:

$$i_{T\infty} = 4 n F D C a \quad (1.5)$$

All parameters were defined earlier.

Far from the substrate, the diffusion layer near the tip electrode is thus roughly hemispherical; however, this diffusion layer will be changed as the tip is brought closer

the substrate. In the next section, we will show how the nature (insulating, or conducting) of the substrate influences the current measured at the tip.

To conclude this paragraph, we can say that faster double-layer charging, reduced ohmic loss, and high-mass transport rates brought by UMEs have allowed them to revolutionize thermodynamic, kinetic, and electroanalytical measurements.<sup>[7, 10]</sup>

## 2. Scanning Electrochemical Microscope

Scanning Electrochemical Microscopy (SECM), one of the major developments in the field of electrochemistry in the past decade, has been shown to be a promising analytical tool for localized studies of surface reactions and their kinetics, for imaging at micro- or nano-scale and for local surface modifications. Since its introduction by Bard et al.<sup>[11, 12]</sup> and Engström et al.,<sup>[13, 14]</sup> in 1989, approximately 1000 papers<sup>[15]</sup> have been published on its methodology and applications, and numerous reviews and books have appeared.<sup>[15-20]</sup> It is not the aim of this manuscript to give an exhaustive review of the technique, and its more recent advances in theory and applications. Our goal is to give to the reader a brief and comprehensive overview of its fundamentals, and its general application in order to highlight the concepts that will be useful to discuss our experimental results.

Scanning electrochemical microscopy employs an ultramicroelectrode, also known as a tip, to induce chemical changes and collect electrochemical information while approaching or scanning the surface of interest (substrate). In other words, SECM involves the measurement of the current through the ultramicroelectrode when it is held or moved in a solution in the vicinity of a substrate. Substrates, which can be solid surfaces or liquids, perturb the electrochemical response of the tip, and this perturbation provides information about the nature and the properties of the substrate. The substrate may also be biased and serves as the second working electrode. Many different types of UMEs have been fabricated, e. g., microband electrodes, cylindrical electrodes, microrings, hemispherical, and disk-shaped electrodes.<sup>[21, 22]</sup> The last one is the most used for SECM experiments, though other shapes may be suitable for specific experiments.<sup>[23-31]</sup> In the following descriptions, we will focus only on the disk-shaped UMEs.

## 2.1. Instrumentation

The illustration of the SECM instrument used for this work is shown in figure 3. This instrument is composed by four main elements:

- the electrochemical cell including the UME probe, the substrate, the reference electrode and the counter-electrode.
- the positioning elements, translator stages, and motor controller allowing to control the relative positions of the substrate and the UME. Generally, the position normal to the substrate is taken as the z direction, while x and y are those in the plane of the substrate.
- a bipotentiostat allowing to control the potentials of the tip and/or the substrate versus the reference electrode and to measure the tip and substrate currents.
- Data acquisition system.

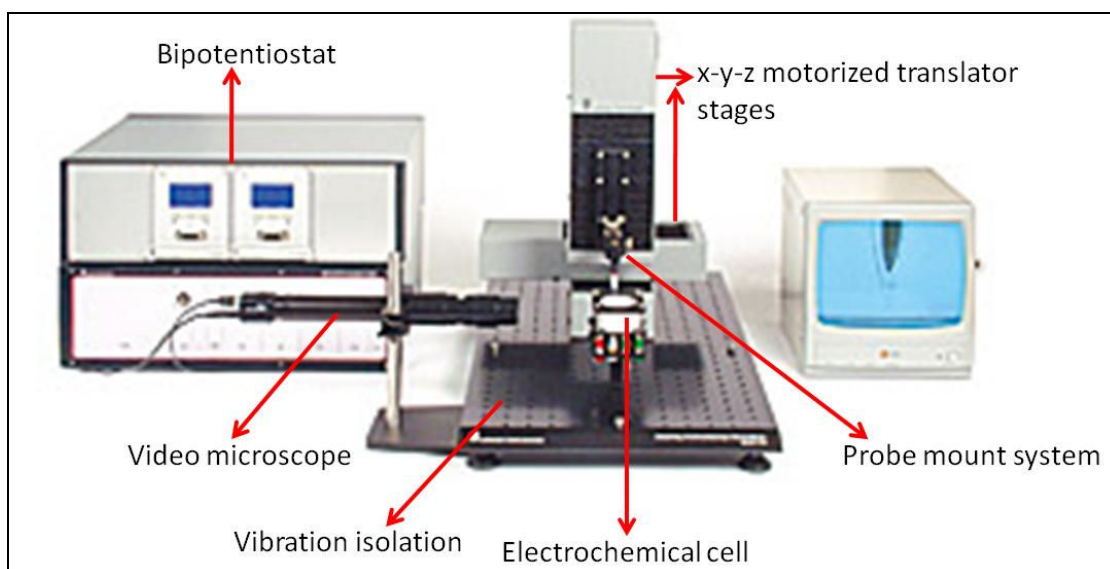


Figure 3: Illustration of the UNISCAN 370 SECM instrument showing translators, tip and cell mounts.

The relative positioning of the UME towards the substrate is a crucial point. More precisely, the substrate must be placed perpendicular to the z-axis (corresponding to the tip axis) and the tip must be placed in its support without showing inclination. The planarity of the substrate has to be checked before all experiments. This is done by setting the microelectrode potential on the reduction or oxidation plateau of the redox mediator ( $[\text{Fe}(\text{CN})_6]^{3-}$  or ferrocene methanol in our case, see chapter 3).

The precise positioning capabilities, which make high spatial resolution possible, give the SECM an important edge over other electrochemical techniques employing UMEs. For example, the SECM can pattern the substrate surface, visualize its topography, and probe chemical reactivity on the micrometer, or nanometer scale. At the same time, SECM differs from the other SPM techniques in its applicability to quantitative measurements (e. g., kinetic experiments) through well-developed and rigorous electrochemical theory.

The SECM tips can be prepared in different ways. An established procedure for the disk-shaped geometry (the most used configuration) involves heat sealing of a microwire or a carbon fiber in a glass capillary and connecting it with silver epoxy to a larger copper wire on the back side. The end of the capillary is then polished to expose a disk-shaped electrode. The sides of the glass insulating sheath are then ground down with abrasive to form a truncated cone and to allow closer approach to the substrate.<sup>[11]</sup> The important parameters of the tip geometry, reported on figure 4, are (i) the radius of the conductive core (i. e.,  $a$ ), and (ii) the total tip radius,  $r_g$  (i.e.,  $a$  plus the insulating sheath thickness). The dimensionless parameter  $RG = \frac{r_g}{a}$  is normally comprise between 5 and 10.

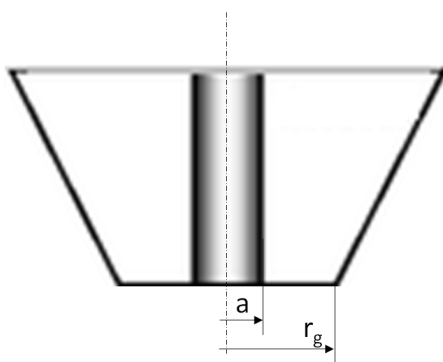


Figure 4: UME tip fundamental dimensions

## 2.2. Modes of operation

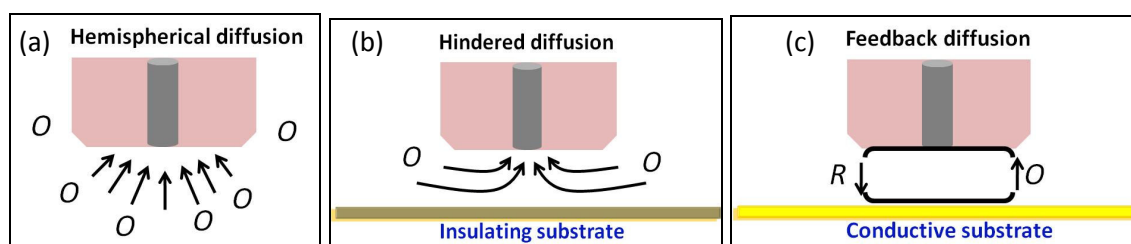
In this section, we briefly survey the fundamentals of various modes of the SECM operation. With essentially the same setup, several SECM modes of operation can indeed be realized including feedback mode, tip generation/substrate collection mode (TG/SC), substrate generation/tip collection mode (SG/TC), penetration mode, and ion transfer feedback mode.

### 2.2.1. Feedback mode

In a feedback mode, the tip serves as the working electrode in a three or four-electrode systems. The sample that is usually called the substrate may serve as a second working electrode. The electrodes are immersed in a solution containing one redox form of a quasi-reversible redox couple (e.g., a reducible species,  $O$ ) added to the supporting electrolyte as a mediator. The current at the tip of the electrode is a function of the solution composition, the distance between the tip and the substrate, and the nature of the substrate itself.

When the tip is moved close to an insulating substrate, diffusion of  $O$  to the tip is hindered (scheme 2b) and the tip current  $i_T$  is smaller than  $i_{T\infty}$ . This value of  $i_T$  depends upon the tip-substrate distance,  $d$ ;  $i_T$  decreases as  $d$  decreases. At the limit, when the distance  $d$  approaches zero,  $i_T$  also approaches zero. This decrease in current with distance is called *negative feedback*. It also depends upon the radius of the insulating sheath, which also blocks diffusion to the electrode.

When the tip is brought to within a few tip radii of a conductive substrate, the  $R$  species formed at the tip diffuse to the substrate where it can be oxidized back to  $O$ . While there is still blockage diffusion of  $O$  to the tip by the substrate, the current at the tip will increase due to the recycling of species  $O$  (scheme 2c) which produces an additional flux of  $O$  to the tip. In this case,  $i_T > i_{T\infty}$  and is essentially independent of the size of the insulating sheath. In the limit as  $d$  approaches zero, the tip will moved into a regime where electron tunnelling occurs and the tip current increases significantly. This increase of current with distance is called *positive feedback*.



Scheme 2: Basic principles of scanning electrochemical microscopy: (a) far from the substrate, diffusion leads to a steady-state current,  $i_{T\infty}$ ; (b) near an insulating substrate, hindered diffusion leads to  $i_T < i_{T\infty}$ ; (c) near a conductive substrate, feedback diffusion leads to  $i_T > i_{T\infty}$  [from reference<sup>[16]</sup>].

Note that while it is possible to drive the reaction  $R \rightarrow O + ne^-$  at the substrate by controlling its potential via a connection to an external potentiostat, this reaction occurs also often at an unbiased conductive substrate as well. Indeed, the potential of an unbiased conducting substrate is directly proportional to the concentrations of species.<sup>[32]</sup> Since the substrate is usually much larger than the tip electrode, most of it

will be bathed in solution containing only species  $O$ . In this case, following the Nernst equation (equation 2.1), the potential of the substrate will be established well positive of the  $E^0$  of the redox couple since  $C_R \approx 0$ .

$$E = E^0 + \frac{RT}{nF} \ln \left( \frac{C_O}{C_R} \right) \quad (2.1)$$

As  $E - E^0 \gg 0$ ,  $R$ , touching the substrate beneath the tip, is oxidised.

A plot of  $i_T$  versus  $d$ , as a tip is moved in the  $z$  direction, is called an *approach curve* (figure 5). These curves are given in dimensionless form by plotting the normalized current ( $I_N = \frac{i_T}{i_{T\infty}}$ ) versus the normalized working distance ( $L = d/a$ ). Since this plot involves only dimensionless variables, it does not depend upon the radius of the tip, the concentration or diffusion coefficient of  $O$ . From these curves one can readily find  $d$  from the measured  $i_T$  and the knowledge of  $a$ .

A quantitative description of approach curves can be obtained by solving the diffusion equations and can be found in the literature (see for example chapter 4 of reference<sup>[16]</sup>). Analytical relations of the dimensionless approach curves obtained for the situation of a disk electrode (for  $RG = 10$ ) and a planar substrate are reported below (equations 2.2 and 2.3) for a "ideal" conductive substrate (essentially infinite rate of regeneration of  $O$  from  $R$ ) and a "ideal" insulating substrate (zero rate of regeneration of  $O$ ).<sup>[23]</sup> Obviously, this situation represents the two limit cases. Two parameters are able to influence the experimental curves which will then be situated between these two limit cases: (i) the kinetic of the regeneration of the mediator on the surface; (ii) the UME geometry.

$$I_{N,conductor} = 0.68 + \frac{0.784}{L} + 0.331 \exp\left(\frac{-1.067}{L}\right) \quad (2.2)$$

$$I_{N,insulating} = \frac{1}{0.457 + \frac{1.460}{L} + 0.431 \exp\left(\frac{-2.350}{L}\right)} - \frac{0.145 L}{5.576 + L} \quad (2.3)$$

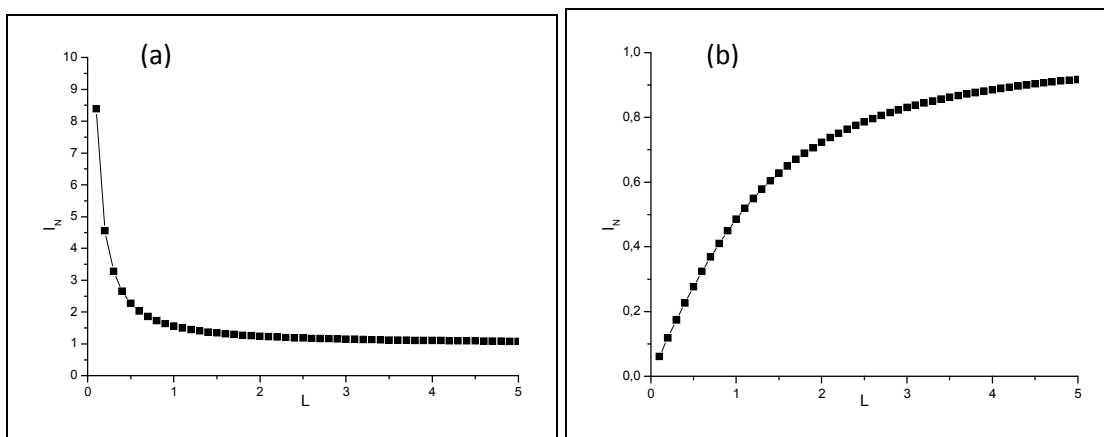


Figure 5: Theoretical approach curves for a tip electrode over a conductive (a) and insulating (b) substrate computed for  $RG = 10$  from equation (2.2) (curve a) and equation (2.3) (curve b).<sup>[23]</sup>

The feedback process is an important feature of the SECM method. The direction of the current feedback indicates the nature of the surface, while the magnitude of the signal gives an indication of the distance of the tip from the surface, or alternatively, an indication of the rate of species turnover at the substrate.

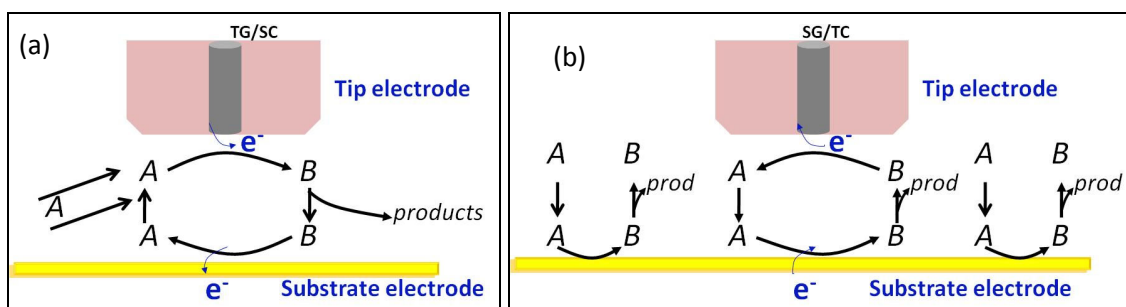
### 2.2.2 Collection-generation modes

In the generation/collection mode, both tip and substrate can be used as working electrodes, one working electrode generating species which are collected at the other electrode. We can distinguish two significantly different modes:

(i) the tip generation-substrate collection (TG/SC) mode (scheme 3a): the tip is used to generate a reactant (for example  $B$  in scheme 3a) that diffuses across the tip-substrate gap to react at the substrate surface. In the TG/SC mode, currents flowing through the tip ( $i_T$ ) and through the substrate ( $i_s$ ) have to be simultaneously recorded. In most cases, the substrate is considerably larger than the tip, so that the collection efficiency, given by  $i_s/i_T$  is essentially 1 for a stable tip-generated species when the working distance  $d$  is low ( $d \leq 2a$ ). Under these conditions, the tip-generated species,  $R$  predominantly diffuse to the large substrate, rather than escape from the tip-substrate gap. If generated species react on transit from tip to substrate,  $i_s/i_T$  becomes smaller, and its change with separation,  $d$ , allows determination of rate constant of homogeneous reaction.<sup>[33-37]</sup>

(ii) the substrate generation-tip collection (SG/TC) mode (scheme 3b): the tip probes the reactions that are occurring on a substrate. In this configuration, the tip acts only

as a collector of electroactive species. Historically, the first SECM-type experiments were carried out in this configuration to measure concentration profiles in the diffusion layer generated by a macroscopic substrate<sup>[13, 38]</sup>: a scan in the z direction can produce the concentration profile; the tip is moved through the diffusion layer occurring on the substrate and detects the current variations which are related to the local variation of the concentration of the electroactive species. On the other hand, a scan over the surface can identify hot spots, where reactions occur at higher rate.



*Scheme 3: principles of (a) the TG/SC mode and (b) the SG/TC mode for measuring follow-up chemical reactions of electrogenerated species. Species B, produced from a solution precursor species, A, at a generator electrode undergoes decomposition during transit to a collector electrode [from reference<sup>[16]</sup>].*

In addition, other modes such as ion-transfer feedback mode<sup>[39]</sup>, penetration mode<sup>[40]</sup>, equilibrium perturbation mode and potentiometric detection, were developed to investigate various specific electrochemical processes. Details on those modes can be found in the reviews listed in the references (16)

### **2.3. Main applications of SECM**

SECM is a powerful tool for studying structures and processes in micrometer- and submicrometer-sized systems. It can probe electron, ion, and molecule transfers, and other reactions at solid-liquid, liquid-liquid, and liquid-air interfaces.<sup>[41]</sup> This versatility allows for the investigation of a wide variety of processes, from metal corrosion to adsorption via metabolism in single living cells. SECM has also been shown to be a promising analytical tool for imaging at micro-/nano-scale and for local surface modifications. This section covers some applied research but does not give, in any way, an exhaustive list. We focus more particularly on some fields for which SECM give new opportunities.

### 2.3.1. Imaging

An important advantage of the SECM is the capability to image the surface topography or reactivity.<sup>[42]</sup> Two modes are used to map surfaces by SECM: the constant height mode and the constant distance mode.<sup>[32, 43]</sup> Constant height mode images are obtained by moving a probe laterally in the x-y plane above the substrate and monitoring the tip current,  $i_T$ , as a function of tip location. One can so obtain topographical images of conducting and insulating substrate if their surfaces are chemically homogeneous. On the other hand, since the SECM response is a function of the rate of heterogeneous reaction at the substrate, it can be used to image local chemical and electrochemical reactivity of surface features. The resolution attainable with the SECM largely depends upon the shape and the size of the tip, and the distance between tip and substrate.

Figure 6b shows an experimental SECM image of a portion of a hybrid Cu/polymer sample (fig. 6a) obtained in feedback mode at constant height image. The dark squares correspond to the conductive Cu pattern in front of which positive feedback is observed leading to an increase of the recorded current.

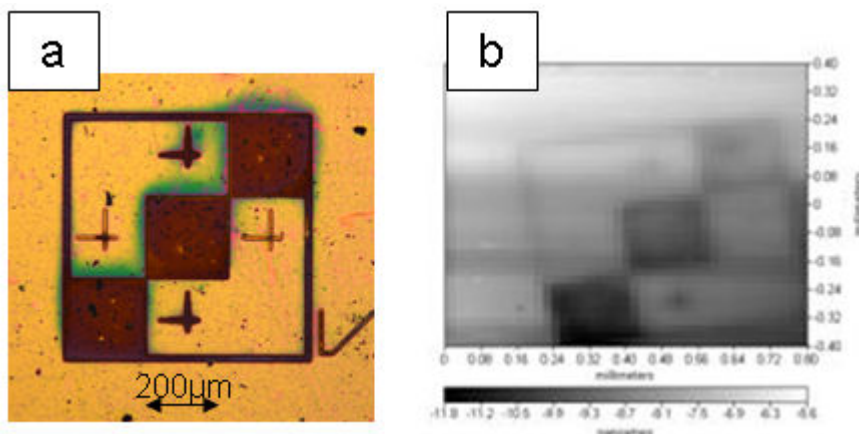


Figure 6: (a) Optical image of copper pattern on polymers film spin-coated on gold; (b) Constant height SECM image of a 800- $\mu\text{m}$  x 800- $\mu\text{m}$  portion of a hybrid Cu/polymer sample in a solution containing  $5 \cdot 10^{-3} \text{ mol} \cdot \text{dm}^{-3} \text{ K}_4\text{Fe}(\text{CN})_6$ , 25- $\mu\text{m}$  Pt. The imaging tip current was 8 nA on the insulating zone, and  $i_{T\infty} = 18.6 \text{ nA}$ ,  $d = 6 \pm 2 \mu\text{m}$ .

The height constant mode is efficient for relatively large tip electrodes. However, when smaller tips are used in the hope of attaining higher resolution, scanning in this mode becomes more difficult. Indeed, as shown above, positive and negative feedback effects are only measurable for  $L=d/a$  close to 1, which means smaller tips require shorter tip-substrate distances. In those conditions, irregularities in the sample surface, or tilt of the sample can cause a “tip crash”. The constant current mode is then more useful to provide independent information about the sample topography

and monitor local electrochemical activity/conductivity in proximity of solid/liquid interface.<sup>[44-46]</sup>

Therefore, for high resolution, SECM must be performed in the constant current mode. SECM has then to be coupled with other scanning probe microscopy techniques (SPM), such as AFM and STM, where the distance is adjusted by a feedback loop to the z-piezo to maintain the current constant. Several groups have undertaken the development of a combined AFM-SECM which represents a significant advance in SPM methodology.<sup>[15, 31, 41, 47-56]</sup> AFM gives high-resolution topographic information and is able to precisely control the distance between the sample and the probe, whereas SECM can provide detailed information of local chemical/electrochemical processes. Thus a raster in the AFM-SECM mode simultaneously produces a surface topographical map and a surface reactivity map. This makes the AFM-SECM combination very useful for imaging substrates of complex topography and variable reactivity. Works developed in that latter field are essentially devoted to cantilever tip probe development which have to act simultaneously as a force sensor for topographical AFM imaging, and an UME for electrochemical SECM imaging<sup>[48, 57-62]</sup> and to local electrochemical phenomena analysis, particularly for studying biological systems,<sup>[50, 63-65]</sup> and corrosion phenomena.<sup>[66, 67]</sup>

### 2.3.2. Study of the reactional rate

A greater understanding of interfacial kinetics and mechanisms in condensed-phase systems has been achieved, over the past decade, through the use of scanning electrochemical microscopy techniques.<sup>[11, 13, 14, 20, 41, 65, 68-75]</sup> The SECM response depends on the rate of mass transfer of a target species to the UME, positioned in a solution, close to the interface with a second phase, which may be a solid, liquid<sup>[76-81]</sup> or gas.<sup>[82]</sup>

The mass transfer rate, in turn, is governed by physicochemical processes at the part of the interface directly under the tip. The small characteristic dimension of the SECM probe enables high rates of diffusional mass transfer to be attained in the gap between the UME and the interface. This facilitates the measurement of fast interfacial processes, with high spatial resolution, under well-defined and calculable conditions.

SECM has thus proven a powerful approach for measuring the kinetics of homogeneous reactions coupled to the heterogeneous electron transfer. Various SECM methods are currently available for measuring homogeneous reactions within various electrochemical mechanisms such as irreversible first-order or second order

chemical reactions following electron transfer (i.e., the EC<sub>i</sub> and EC<sub>2i</sub> mechanisms respectively) (scheme 3).

To illustrate this paragraph, we will just take the EC<sub>i</sub> mechanism as example, as most of the SECM techniques have been applied practically to this class of reaction. For these investigations, both the tip and the substrate are electrodes, and the tip/substrate configuration essentially functions in the TG/SC mode.

In an EC<sub>i</sub> mechanism, the following processes occur:



For a generated stable species at the UME by a simple charge transfer process (relation (2.4)), the efficiency of the collection (relation (2.6)), defined by the  $i_s/i_T$  ratio, is close to 1 (100%) when the distance  $d$  is sufficiently small ( $d \leq 2a$ ). On the other hand, in the case of a chemical reaction coupled with the charge transfer, for which species produced at the probe reacts in the interelectrode space by generating an electro-inactive species (relation (2.5)), the  $i_s/i_T$  ratio decreases. This variation allows to reach the rate of the coupled chemical reaction;  $i_s/i_T$  ratio will tend towards 1 (slow chemical reaction), or towards 0 in the case of a very fast chemical reaction.

SECM has traditionally been applied to study processes at liquid/solid interfaces. For example, it has found particular use in: (i) measuring fast electron-transfer processes at electrodes<sup>[83-85]</sup> and immobilized redox enzymes<sup>[86-89]</sup>; (ii) characterizing dissolution and growth processes at a variety of materials including metals,<sup>[90-93]</sup> semiconductors,<sup>[94, 95]</sup> ionic crystals,<sup>[92]</sup> and polymers;<sup>[96]</sup> (iii) determining adsorption/desorption kinetics and surface diffusion rates.<sup>[97]</sup>

More recently, SECM has proved a powerful kinetic probe of reactions that occur at the interface between two immiscible liquids. SECM studies, hitherto, include the use of the equilibrium perturbation mode to probe molecular and ion transfer processes,<sup>[39, 98, 99]</sup> and the feedback mode to measure the rates of interfacial redox reactions.<sup>[77, 100]</sup> Part of the success of the SECM, over more conventional methodologies, stems from the ability to measure reaction rates under conditions where the contributions from transport and interfacial processes can readily be separated.

### 2.3.3. Study of corrosion

The SECM technique can be regarded as an ideal tool for the investigation of local corrosion phenomena. Indeed, localized corrosion such as pitting corrosion occurs in discrete location whose diameters are an ideal feature size for SECM analysis. Corrosion pits or defects generally initiate due to some chemical or physical heterogeneity at the surface, such as inclusions, second phase particles, flaws, mechanical damage, or dislocations. The corrosion mechanisms depend on the material composition, electrolyte and other environmental conditions.<sup>[101-103]</sup> Therefore, the small size of UMEs can be employed as probes to scan corrosive processes in closely defined spaces on the one hand, and serve as experimental models for local corrosive processes, on the other (fig. 7).<sup>[55, 102-111]</sup>

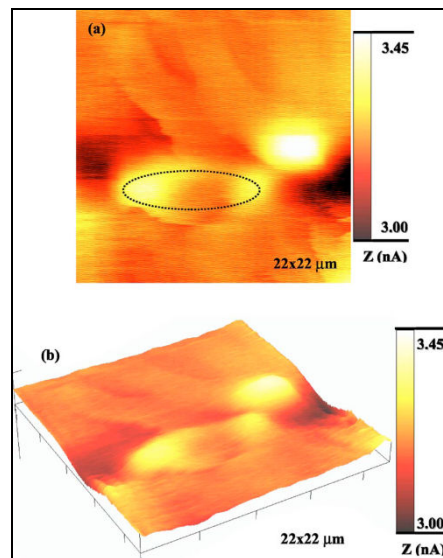
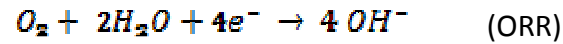


Figure 7: (a) 2D and (b) 3D SECM images of the surface of the EN W-3003 alloy in 20 mM NaCl and 5 mM KI electrolyte at anodic polarization of 200 mV. The dotted ellipse highlights enhanced current on the boundary around an elongated IMP (reprinted from reference [96]).

### 2.3.4. Electrocatalysis

Industry is looking for new catalytic materials, in particular to replace expensive platinum currently used to enhance the performance of fuel cells. Recent investigations carried out by several groups.<sup>[82, 111-117]</sup> have demonstrated the utility of SECM as a rapid and high throughput technique for screening electrocatalysts for various processes (fig. 8).

For example, the SECM has mostly been used to study two electrocatalytic reactions, the hydrogen oxidation (HOR) and the oxygen reduction reaction (ORR), because of their importance for fuel cells and other applications.



So far, Zhou et al.<sup>[115]</sup> studied proton reduction from a 0.001 M HClO<sub>4</sub> solution at different substrates (Pt, Au) by feedback mode of the SECM. The HOR rate was determined quantitatively at different substrate potentials from SECM approaches curves. They also studied the effect of the surface oxide and anion adsorption on hydrogen oxidation. Recently, Jayaraman and Hillier<sup>[113, 114]</sup> presented a screening method that quantitatively detects protons at a surface using the SECM.

On the other hand, Fernandez et al.<sup>[118-120]</sup> employed the TG/SC mode to study the ORR on the substrate in acidic solutions. The tip is placed close to the substrate and biased at a potential at which water is oxidized to oxygen. The substrate potential is fixed at a value corresponding to oxygen reduction to water. The reduction rate at the substrate surface reflects its electrocatalytic activity.

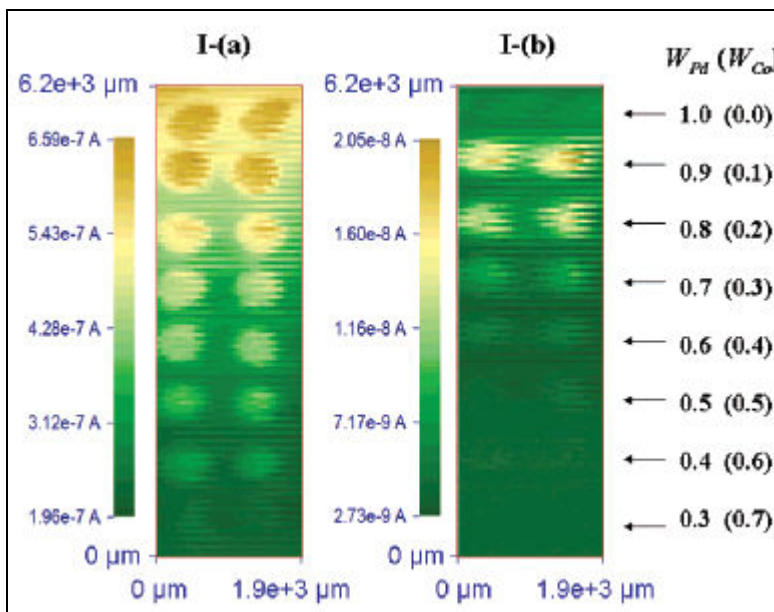


Figure 8: SECM TG-SC images of oxygen reduction activity measured on binary arrays in 0.5 M H<sub>2</sub>SO<sub>4</sub>. Tip-substrate distance = 30 μm, tip current = -160 nA. (I) Pd-Co, scan rate: 50 μm each 0.2 s, E<sub>s</sub> = 0.4 (I-a), 0.7 (I-b) V vs HRE; W<sub>M</sub> is the atomic ratio of metal M in the spot. (reprinted from reference [109])

### 2.3.5. Study of biological systems.<sup>[49, 54, 64, 67, 70, 121-131]</sup>

As already mentioned, UMEs have a cardinal advantage in electrochemical analysis because their size makes it possible to conduct electrochemical measurement in minute volumes and observe discrete spatial events in microscopically small areas. Hence, it is not surprising that microelectrodes were first used for measurements in living systems. SECM with electrochemical detection of metabolites can be used to map biochemical activity, thereby complementing techniques that image only the topography of biological specimens or biomolecules.

Two main types of SECM experiments on living cells are generation/collection measurements and feedback-mode amperometric experiments. The former approach involves tip positioning in the proximity of a field of immobilized cells, with a separation distance sufficiently long for the SECM feedback to be negligible. The tip in this case is used as a passive probe to monitor the concentration and/or fluxes of redox species generated (or consumed) by the cells. In contrast, the tip/cell separation distance in a feedback mode experiment is sufficiently small to observe either positive or negative feedback from a single immobilized cell. The tip is used to oxidize (or reduce) a redox mediator, and a cell acts as a substrate whose topography and redox reactivity can be probed.

SECM images of living cells were obtained in a constant-height mode, where the tip is rastered in a x-y plane above the substrate surface (an example is given fig. 9).<sup>[49, 54, 132]</sup> Using this approach, one can map the fluxes of oxygen and other redox species, image the cell topography under either positive or negative feedback conditions, and also map its redox reactivity.

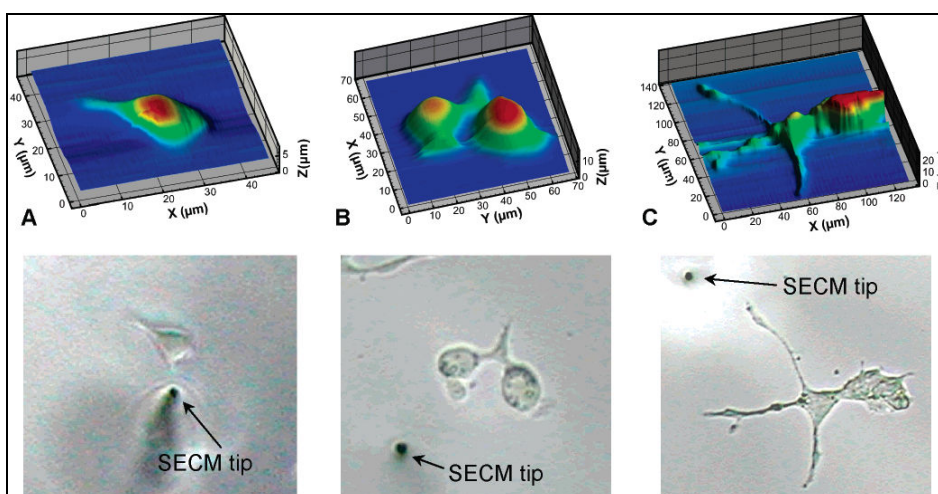


Figure 9 : Topographic images obtained using constant-current mode of SECM imaging as presented by Kurulugama et al. of (A) an undifferentiated PC12 cell, (B) early neurite

development and (C) a differentiated PC12 cell. In their work they also provide images using other feedback modes, namely constant-impedance and constant-distance. (Reprinted from reference [132]).

### 2.3.6. Localized modifications of substrate: microstructuring

The SECM was, since the beginning of its development in 1980's, used for the modification of the chemical structure of surfaces and for the realization of localized micro- and nano-pattern on conducting and semiconductor surfaces. Various systems and methods can be used in conjunction with SECM for fabricating small patterns on surfaces. Most of them can be divided in two main categories based on the mode of operation: the direct mode and the feedback mode.

In a typical direct mode experiment, the tip is held in a close proximity to the substrate, and the voltage is applied between them to cause the desired reaction at the substrate. In this mode, the substrate serves thus as the auxiliary electrode for the UME. A current at the UME causes an equally but oppositely directed current at the substrate electrode. The direct mode was used for semiconductor etching,<sup>[133]</sup> for metal deposition<sup>[134, 135]</sup> and etching,<sup>[134, 136, 137]</sup> for deposition of conducting polymer,<sup>[96, 138-140]</sup> for organic and biomolecule patterning,<sup>[121, 123, 141-143]</sup> and for local modulation of chemical properties.<sup>[144, 145]</sup>

In the feedback mode the substrate is unbiased (in most cases) and a mediator that shuttles between the UME and the surface is used. The tip-generated redox species must be able to induce the desired reaction (i.e., deposition or etching) at the substrate and be regenerated at its surface. Etching was performed in this manner on Cu,<sup>[93, 95, 146]</sup> GaAs,<sup>[93, 95]</sup> and Si.<sup>[147, 148]</sup>

In the same way, microelectrochemically generated organic radical anions can reduce the surface of fluoropolymers.<sup>[149-154]</sup> The resulting surfaces show locally varying wetting behaviour and can subsequently be metalized<sup>[155]</sup> or modified by another oligomer after oxidation step.<sup>[149]</sup>

Local material deposition could also be carried out by applying a precursor as a thin film to a substrate and converting it by means of an electrochemically generated oxidant or reductant into the desired microstructure.<sup>[156]</sup> For example, polyvinylpyridine films were loaded with PdCl<sub>4</sub><sup>-</sup> and AuCl<sub>4</sub><sup>-</sup> and converted by locally generated [Ru(NH<sub>3</sub>)<sub>6</sub>]<sup>2+</sup> into Pd and Au microstructures.<sup>[93]</sup> Conducting polymers can be locally formed by polymerization of the monomer.<sup>[140, 157]</sup> Polyaniline has been deposited onto different substrates by using a UME-induced pH shift in the interelectrode space, which initiated the electropolymerization in the vicinity of the

UME, whereas it did not occur outside this region.<sup>[158]</sup> The SECM probe can be used in various ways to locally inject metal ions into the solution that are reduced after diffusion to the substrate. Gold UMEs can be dissolved in the presence of complexing agents. Gold nanoparticles, arranged in micropatterns, can be deposited on conducting or semiconducting substrates by reduction of aureates generated at the UME.<sup>[159]</sup> At least, SECM in the feedback mode has also been exploited for microfabrication of organic and biological structures.<sup>[124, 160, 161]</sup>

### *2.3.7. Hybrid techniques*

Numerous hybrid techniques have evolved around SECM, including its combination with surface plasmon resonance (SPR-SECM),<sup>[141]</sup> electrochemical quartz crystal microbalance (EC-QCM SECM),<sup>[162-164]</sup> fluorescence spectroscopy (FS-SECM),<sup>[165]</sup> photoelectrochemical microscopy (PEM) or near-field scanning optical microscopy (NSOM-SECM),<sup>[166]</sup> electrogenerated chemiluminescence (ECL-SECM),<sup>[167]</sup> and atomic force microscopy (AFM-SECM),<sup>[19, 70, 168]</sup> the most widely used of these hybrid techniques.

### 3. CONCLUSIONS

Though the unconventional properties of ultramicroelectrodes were recognized only at the beginning of the 1980s, the exponential growth in literature on the subject testifies to their success. Faster double-layer charging, reduced ohmic loss, and high-mass transport rates have allowed them to revolutionize thermodynamic, kinetic, and electroanalytical measurements. <sup>[7, 10]</sup> As shown by this brief bibliography review, scanning electrochemical microscopy has proven to be a powerful instrument for the quantitative investigation and surface analysis of a wide range of processes that occur at interfaces: from classical electrochemical problems, such as the investigation of the localized corrosion and electrocatalytic reactions in fuel cells, sensor surfaces, biochips, and microstructured analysis systems, to mass transport through synthetic membranes, skin and tissue, as well as intercellular communication processes. It is possible to modify substrates locally by a multitude of defined chemical/electrochemical reactions and to test new approaches for prototyping of micro- and nanostructured functional surfaces, for example, in biosensors and biochips.

Numerous applications have stimulated the development of new methods and opened up previously inaccessible fields of research to electrochemistry. The development of UME and the combination of SECM and other techniques show much higher spatial resolution and precision. The greatest challenge of SECM will be to routinely do measurements with nanometer-sized electrodes, as these electrodes are much harder to produce and use than micron-sized ones. The persistent trend to smaller electrodes and simpler manufacturing techniques, assisted by efficient microsystems technologies, and the improvement of lateral resolution and sensitive detection will considerably expand the scope of applications in cell biology, surface sciences, and micro-/nanotechnology.

As we have recalled earlier, this thesis is not a contribution to the experimental and/or theoretical development of the SECM itself. Our objective is to demonstrate that SECM can be used as an actual lithographic tool for local electrografting of non conducting polymer, allowing a “free” patterning of homogeneous conducting or semiconducting substrates which can serve as template in devices realization. However, we will track the experimental parameters able to affect the resolution of the process on the basis of the theoretical principles recalled herein. SECM will also be combined with AFM technique in order to improve the resolution of the process. But, first of all, we have to describe the electrografting process itself before exploring it in a local way. It is the subject of the next chapter.

## REFERENCES

- [1] J. Heinze, *Angew. Chem., Int. Ed. Engl.* **1984**, *23*, 831.
- [2] D. R. Lowde, J. O. Williams and B. D. McNicol, *Appl. Surf. Sc.* **1978**, *1*, 215.
- [3] J. Heinze and M. Dietrich, *Mater. Sci. For.* **1989**, *42*, 63.
- [4] D. L. Robinson, B. J. Venton, M. L. A. V. Heien and R. M. Wightman, *Clin. Chem.* **2003**, *49*, 1763.
- [5] A. Bard, in *"Electrochemical Methods: Fundamentals and Applications"*, 2nd ed.; John Wiley & Sons, Inc.: New York, **2001**.
- [6] F. G. Cottrell, *Zeit. Physikal. Chem.* **1903**, *42*, 385.
- [7] J. Heinze, *Angew. Chem., Int. Ed. Engl.* **1993**, *32*, 1268.
- [8] M. Fleischmann, S. Pons, D. R. Rolison and P. P. Schmidt, *Ultramicroelectrodes* **1987**, *Datatech Systems, Morganton*.
- [9] C. G. Zoski, A. M. Bond, E. T. Allinson and K. B. Oldham, *Anal. Chem.* **1990**, *62*, 37.
- [10] R. J. Forster, *Chem. Soc. Rev.* **1994**, *23*, 289.
- [11] A. J. Bard, F.-R. F. Fan, J. Kwak and O. Lev, *Anal. Chem.* **1989**, *61*, 132.
- [12] H. Y. Liu, F.-R. F. Fan, C. W. Lin and A. J. Bard, *J. Am. Chem. Soc.* **1986**, *108*, 3838.
- [13] R. C. Engstrom, M. Weber, D. J. Wunder, R. Burgess and S. Winkquist, *Anal. Chem.* **1986**, *58*, 844.
- [14] R. C. Engstrom, T. Meaney, R. Tople and R. M. Wightman, *Anal. Chem.* **1987**, *59*, 2005.
- [15] S. Amemiya, A. J. Bard, F.-R. F. Fan, M. V. Mirkin and P. R. Unwin, *Annu. Rev. Anal. Chem.* **2008**, *1:4*, 1.
- [16] A. J. Bard and M. V. Mirkin, *Scanning Electrochemical Microscopy*; Marcel Dekker, Inc., New York, Basel **2001**.
- [17] F. Bedioui, S. Griveau and A. Pailleret, *Technique de l'ingénieur* **2009**, *P2 132*, 1.
- [18] F. Kanoufi, *L'actualité chimique* **2007**, *311*, 36.
- [19] P. Sun, F. O. Laforge and M. V. Mirkin, *Phys. Chem. Chem. Phys.* **2007**, *9*, 802.
- [20] G. Wittstock, M. Burchardt, S. E. Pust, Y. Shen and C. Zhao, *Angew. Chem. Int. Ed.* **2007**, *46*, 1584.
- [21] R. M. Wightman and D. O. Wipf, *Electroanal. Chem.* **1988**, *15*, 267.
- [22] C. Amatore, *Physical Electrochemistry: Principles, Methods and Applications* **1995**, I. Rubinstein, Ed. Marcel Dekker, Inc.: New York, p.131.
- [23] C. A. Mirkin, F.-R. F. Fan and A. Bard, *J. Electroanal. Chem.* **1992**, *328*, 47.
- [24] C. G. Zoski, B. Liu and A. Bard, *Anal. Chem.* **2004**, *76*, 3646.
- [25] Y. Selzer and D. Mandler, *Anal. Chem.* **2000**, *72*, 2383.
- [26] J. Mauzeroll, E. A. Hueske and A. J. Bard, *Anal. Chem.* **2003**, *75*, 3880.
- [27] S. Daniele, C. Bragato, I. Ciani and M. A. Baldo, *Electroanalysis* **2003**, *15*, 621.
- [28] C. Demaille, M. B. Brust, Tsionsky and J. Bar, *Anal. Chem.* **1997**, *69*, 2323.
- [29] Y. Lee, S. Amemiya and A. J. Bard, *Anal. Chem.* **2001**, *73*, 2261.
- [30] P. Liljeroth, C. Johans, C. J. Slevin, B. M. Quinn and K. Kontturi, *Anal. Chem.* **2002**, *74*, 1972.
- [31] J. V. Macpherson and P. R. Unwin, *Anal. Chem.* **2000**, *72*, 276.
- [32] M. V. Mirkin and R. B. Horrocks, *Anal. Chim. Acta* **2000**, *406*, 119.
- [33] P. R. Unwin and A. Bard, *J. Phys. Chem.* **1991**, *95*, 7814.
- [34] F. Zhou, P. R. Unwin and A. Bard, *J. Phys. Chem.* **1992**, *96*, 4917.
- [35] F. Zhou and A. Bard, *J. Am. Chem. Soc.* **1994**, *116*, 393.
- [36] D. A. Treichel, C. A. Mirkin and A. Bard, *J. Phys. Chem.* **1994**, *98*, 5751.
- [37] P. R. Unwin, J. Bar and C. Demaille, *J. Phys. Chem.* **1996**, *100*, 14137.
- [38] R. C. Engstrom, T. Meaney, R. Tople and R. M. Wightman, *Anal. Chem.* **1987**, *59*, 2005.
- [39] Y. H. Shao and C. A. Mirkin, *J. phys. Chem. B* **1998**, *102*, 9915.
- [40] C. Cannes, F. Kanoufi and A. J. Bard, *Langmuir* **2002**, *18*, 8134.

- [41] A. L. Barker, M. Gonsalves, J. V. Macpherson, C. Slevin and P. R. Unwin, *Anal. Chim. Acta* **1999**, *385*, 223.
- [42] P. S. Dobson, J. M. R. Weaver, M. N. Holder, P. R. Unwin and J. V. Macpherson, *Anal. Chem.* **2005**, *77*, 424.
- [43] S. Amemiya, J. Guo, H. Xiong and D. A. Gross, *Anal. Bioanal. Chem.* **2006**, *386*, 458.
- [44] M. Etienne, A. Schulte, S. Mann, G. Jordan, I. D. Dietzel and W. Schuhmann, *Anal. Chem.* **2004**, *76*, 3682.
- [45] B. B. Katemann, A. Schulte and W. Schuhmann, *Chem. Eur. J.* **2003**, *9*, 2025.
- [46] B. B. Katemann, A. Schulte and W. Schuhmann, *Electroanalysis* **2004**, *16*, 60.
- [47] M. N. Holder, C. E. Gardner, J. V. Macpherson and P. R. Unwin, *J. Electroanal. Chem.* **2005**, *585*, 8.
- [48] R. J. Fasching, Y. Tao and F. B. Prinz, *Sens. Act. B* **2005**, *108*.
- [49] Y. Hirata, S. Yabuki and F. Mizutani, *Bioelectrochemistry* **2004**, *63*, 217.
- [50] J. Abbou, A. Anne and C. Demaille, *J. Am. Chem. Soc.* **2004**, *126*, 10095.
- [51] C. E. Jones, J. V. Macpherson, Z. H. Barber, R. E. Somekh and P. R. Unwin, *Electrochem. Comm.* **1999**, *1*, 55.
- [52] A. Kueng, C. Kranz, B. Mizaikoff, A. Lugstein and E. Bertagnolli, *Appl. Phys. Lett.* **2003**, *82*, 1592.
- [53] A. Davoodi, A. Farzadi, J. Pan, C. Leygraf and Y. Zhu, *J. Electrochem. Soc.* **2008**, *155*, C474.
- [54] P. L. T. M. Frederix, P. D. Bosshart, T. Akiyama, M. Chami, M. R. Gullo, J. J. Blackstock, K. Dooleweerd, N. F. de Rooij, U. Staufer and A. Engel, *Nanotechnology* **2008**, *19*, 384004.
- [55] A. Davoodi, J. Pan, C. Leygraf and S. Norgren, *Electrochim. Acta* **2007**, *52*, 7697.
- [56] M. R. Gullo, P. L. T. M. Frederix, T. Akiyama, A. Engel, N. F. deRooij and U. Staufer, *Anal. Chem.* **2006**, *78*, 5436.
- [57] F.-R. F. Fan and C. Demaille, in *Scanning Electrochemical Microscopy 2001*, A. J. Bard and M. V. Mirkin Ed., Marcel Dekker: New York.
- [58] D. P. Burt, P. S. Dobson, J. H. Weaver, N. R. Wilson, P. R. Unwin and J. V. Macpherson, *IEEE Sens. Conf.* **2007**, 712.
- [59] A. Lugstein, E. Bertagnolli, C. Kranz and B. Mizaikoff, *Surf. Interf. Anal.* **2002**, *33*, 146.
- [60] H. Shin, P. J. Hesketh, B. Mizaikoff and C. Kranz, *Sens. Act. B* **2008**, *134*, 488.
- [61] M. Salomo, S. E. Pust, G. Wittstock and E. Oesterschulze, *Microelectr. Eng.* **2010**, *87*, 1537.
- [62] O. Sklyar, A. Kueng, C. Kranz, B. Mizaikoff, A. Lugstein, E. Bertagnolli and G. Wittstock, *Anal. Chem.* **2005**, *77*, 764.
- [63] C. Kranz, A. Kueng, A. Lugstein, E. Bertagnolli and B. Mizaikoff, *Ultramicroscopy* **2004**, *100*, 127.
- [64] D. Grieshaber, R. MacKenzie, J. Vörös and E. Reimhult, *Sensors* **2008**, *8*, 1400.
- [65] K. Wang, C. Goyer, A. Anne and C. Demaille, *J. Phys. Chem. B* **2007**, *111*, 6051.
- [66] A. Davoodi, J. Pan, C. Leygraf and S. Norgren, *Electrochem. Sol. St. Lett.* **2005**, *8*, B21.
- [67] S. Szunerits, S. Pust and G. Wittstock, *Anal. Bioanal. Chem.* **2007**, *389*, 1103.
- [68] A. J. Bard, G. Denuault, C. Lee, D. Mandler and D. O. Wipf, *Acc. Chem. Res.* **1990**, *23*, 357.
- [69] A. L. Barker, J. V. Macpherson, C. J. Slevin and P. R. Unwin, *J. Phys. Chem. B* **1998**, *102*, 1586.
- [70] M. A. Edwards, S. Martin, A. L. Whitworth, J. V. Macpherson and P. R. Unwin, *Physiol. Meas.* **2006**, *27*, R63.
- [71] R. C. Engstrom, B. Small and L. Kattan, *Anal. Chem.* **1992**, *64*, 241.
- [72] D. G. Georganopoulou, M. V. Mirkin and R. W. Murray, *Nano Lett.* **2004**, *4*, 1763.
- [73] F. O. Laforge, T. Kakiuchi, F. Shigematsu and M. V. Mirkin, *Langmuir* **2006**, *22*, 10705.
- [74] J. V. Macpherson, N. Simjee and P. R. Unwin, *Electrochim. Acta* **2001**, *47*, 29.
- [75] M. V. Mirkin, M. Arca and A. J. Bard, *J. Phys. Chem.* **1993**, *97*, 10790.

- [76] X. Q. Lu, J. Y. Ma, X. H. Liu, C. W. Dong and W. T. Wang, *Chin. Chem. Lett.* **2010**, *21*, 89.
- [77] C. Wei, A. J. Bard and M. V. Mirkin, *J. Phys. Chem.* **1995**, *99*, 16033.
- [78] X. Q. Lu, D. F. Dong, X. H. Liu, D. N. Yao, W. T. Wang and Y. M. Xu, *Chin. Chem. Lett.* **2010**, *21*, 225.
- [79] F. Li, B. Su, F. C. Salazar, R. P. Nia and H. H. Girault, *Electrochem. Comm.* **2009**, *11*, 473.
- [80] F. Li, A. L. Whitworth and P. R. Unwin, *J. Electroanal. Chem.* **2007**, *602*, 70..
- [81] F. o. O. Laforge, T. Kakiuchi, F. Shigematsu and M. V. Mirkin, *Langmuir* **2006**, *22*, 10705.
- [82] H. Liu, *Electrochem. Comm.* **2009**, *11*, 885..
- [83] S. Bollo, S. Finger, J. C. Sturm, L. J. Núñez-Vergara and J. A. Squella, *Electrochim. Acta* **2007**, *52*, 4892..
- [84] L. McKay and R. J. LeSuer, *Electrochim. Acta* **2008**, *53*, 8305.
- [85] X. Lu, Q. Wang and X. Liu, *Anal. Chim. Acta* **2007**, *601*, 10.
- [86] C. Zhao and G. Wittstock, *Biosens. Bioelectron.* **2005**, *20*, 1227.
- [87] F. Boussicault and M. Robert, *Chem. Rev.* **2008**, *108*, 2622..
- [88] J. Strutwolf, J. Zhang and P. R. Unwin, *Progr. React. Kin. Mech.* **2007**, *32*, 195.
- [89] C. Zhao and G. Wittstock, *Anal. Chem.* **2004**, *76*, 3145.
- [90] J. V. Macpherson and P. R. Unwin, *J. Phys. Chem.* **1996**, *100*, 19475..
- [91] J. V. Macpherson, P. R. Unwin, A. C. Hillier and A. J. Bard, *J. Am. Chem. Soc.* **1996**, *118*, 6445.
- [92] J. V. Macpherson and P. R. Unwin, *J. Phys. Chem.* **1994**, *98*, 1704..
- [93] D. Mandler and A. J. Bard, *J. Electrochem. Soc.* **1990**, *137*, 1079.
- [94] D. Mandler and A. J. Bard, *J. Electrochem. Soc.* **1990**, *137*, 2468.
- [95] D. Mandler and A. Bard, *Langmuir* **1990**, *6*, 1489.
- [96] C. Kranz, H. E. Gaub and W. Schuhmann, *Adv. Mater.* **1996**, *8*, 634.
- [97] P. R. Unwin and A. Bard, *J. Phys. Chem.* **1992**, *96*, 5035.
- [98] Z. Ding, B. M. Quinn and A. J. Bard, *J. Phys. Chem. B* **2001**, *105*, 6367..
- [99] A. L. Barker, P. R. Unwin and J. Zhang, *Electrochem. Comm.* **2001**, *3*, 372..
- [100] T. Solomon and A. Bard, *J. Phys. Chem.* **1995**, *99*, 17487.
- [101] G. T. Burstein, C. Liu, R. M. Souto and S. P. Vines, *Corr. Eng. Sci. Technol.* **2004**, *39*, 25.
- [102] L. Niu, Y. Yin, W. Guo, M. Lu, R. Qin and S. Chen, *J. Mater. Sci.* **2009**, *44*, 4511.
- [103] A. Davoodi, J. Pan, C. Leygraf and S. Norgren, *J. Electrochem. Soc.* **2008**, *155*, C211.
- [104] A. Davoodi, J. Pana, C. Leygraf and S. Norgren, *Appl. Surf. Sci.* **2006**, *252*, 5499.
- [105] K. Eckhard, W. Schuhmann and M. Maciejewska, *Electrochim. Acta* **2009**, *54*, 2125.
- [106] C. Gabrielli, S. Joiret, M. Keddou, N. Portail, P. Rousseau and V. Vivier, *Electrochim. Acta* **2008**, *53*, 7539.
- [107] D. Jope, J. Sell, H. W. Pickering and K. G. Weil, *J. Electrochem. Soc.* **1995**, *142*, 2170.
- [108] W. Zahn, A. Zösch and H. D. Schnabel, *Anal. Bioanal. Chem.* **2003**, *375*, 871.
- [109] R. Zhu, Z. Qin, J. J. Noël, D. W. Shoesmith and Z. Ding, *Anal. Chem.* **2008**, *80*, 1437.
- [110] R. Zhu, S. M. Macfie and Z. Ding, *J. Exp. Bot.* **2005**, *56*, 2831.
- [111] C. Jung, C. M. Sanchez-Sanchez, C.-L. Lin, J. Rodriguez-Lopez and A. J. Bard, *Anal. Chem.* **2009**, *81*, 7003.
- [112] C. A. Martinez-Huitle, S. Ferro and A. De Battisti, *Electrochim. Acta* **2004**, *49*, 4027.
- [113] S. Jayaraman and A. C. Hillier, *J. Phys. Chem. B* **2003**, *107*, 5221.
- [114] S. Jayaraman and A. C. Hillier, *Langmuir* **2001**, *17*, 6401.
- [115] J. Zhou, Y. Zu and A. J. Bard, *J. Electroanal. Chem.* **2000**, *491*, 22.
- [116] M. Black, J. Cooper and P. McGinn, *Meas. Sci. Technol.* **2005**, *16*, 174.
- [117] A. R. Kucernak, P. B. Chowdhury, C. P. Wilde, G. H. Kelsall, Y. Y. Zhu and D. E. Williams, *Electrochim Acta* **2000**, *45*, 4483.
- [118] J. L. Fernandez, D. A. Walsh and A. J. Bard, *J. Am. Chem. Soc.* **2004**, *127*, 357.
- [119] C.-L. Lin, C. M. Sanchez-Sanchez and A. J. Bard, *Electrochem. Sol. St. Lett.* **2008**, *11*, B136.

- [120] J. L. Fernandez and A. J. Bard, *Anal. Chem.* **2003**, *75*, 2967.
- [121] E. Fortin, P. Mailley, L. Lacroix and S. Szunerits, *Analyst* **2006**, *131*, 186.
- [122] M. Maciejewska, D. Schäfer and W. Schuhmann, *Electrochem. Comm.* **2006**, *8*, 1119.
- [123] S. A. G. Evans, K. Brakha, M. Billon, P. Mailley and G. Denuault, *Electrochem. Comm.* **2005**, *7*, 135.
- [124] W. B. Nowall, D. O. Wipf and W. G. Khur, *Anal. Chem.* **1998**, *70*, 2601.
- [125] W. Nogala, M. Burchardt, M. Opallo, J. Rogalski and G. Wittstock, *Bioelectrochem.* **2008**, *72*, 174.
- [126] M. J. K. Ludden, J. K. Sinha, G. Wittstock, D. N. Reinhoudt and J. Huskens, *Org. Biomol. Chem.* **2008**, *6*, 1553.
- [127] P. L. T. M. Frederix, M. R. Gullo, T. Akiyama, A. Tonin, N. F. De Rooij, U. Staufer and A. Engel, *Nanotechnology* **2005**, *16*, 997.
- [128] C. Zhao, I. Zawisza, M. Nullmeier, M. Burchardt, M. Trauble, I. Witte and G. Wittstock, *Langmuir* **2008**, *24*, 7605.
- [129] P. M. Diakowski and Z. Ding, *Phys. Chem. Chem. Phys.*, **2007**, *9*, 5945.
- [130] R. Zhu, S. Xu, G. Podoprygorina, V. Bol`hmer, S. Mittler and Z. Ding, *J. Phys. Chem. C* **2008**, *112*, 15562.
- [131] M. Burchardt and G. Wittstock, *Bioelectrochemistry* **2008**, *72*, 66.
- [132] R. T. Kurulugama, D. O. Wipf, S. A. Takacs, S. Pongmayteegul, P. A. Garris and J. E. Baur, *Anal. Chem.* **2005**, *77*, 1111.
- [133] C. W. Lin, F.-R. F. Fan and A. Bard, *J. Electrochem. Soc.* **1987**, *134*, 1038.
- [134] D. H. Craston, C. W. Lin and A. Bard, *J. Electrochem. Soc.* **1988**, *135*, 785.
- [135] F. Forouzan and A. Bard, *J. Phys. Chem. B* **1997**, *101*, 10876.
- [136] O. E. Hüsser, D. H. Craston and A. Bard, *J. Vac. Sc. Technol. B* **1988**, *6*, 1873.
- [137] O. E. Hüsser, D. H. Craston and A. Bard, *J. Electrochem. Soc.* **1989**, *136*, 3222.
- [138] Y.-M. Wu, F.-R. F. Fan and A. Bard, *J. Electrochem. Soc.* **1989**, *136*, 885.
- [139] C. Kranz, M. Ludwig, H. E. Gaub and W. Schumann, *Adv. Mater.* **1995**, *7*, 568.
- [140] C. Kranz, M. Ludwig, H. E. Gaub and W. Schumann, *Adv. Mater.* **1995**, *7*, 38.
- [141] E. Fortin, Y. Defontaine, P. Mailley, T. Livache and S. Szunerits, *Electroanalysis* **2005**, *17*, 495.
- [142] H. Sugimura, T. Uchida, N. Shimo, N. Kitumara and H. Mashuhara, *Ultramicroelectrodes* **1992**, *42-44*, 468.
- [143] T. Matrab, C. Combellas and F. Kanoufi, *Electrochem. Comm.* **2008**, *10*.
- [144] S. Schwamborn, L. Stoica, S. Neugebauer, T. Reda, H.-L. Schmidt and W. Schumann, *ChemPhysChem* **2009**, *10*, 1066.
- [145] T. H. Treutler and G. Wittstock, *Electrochim. Acta* **2003**, *48*, 2923.
- [146] D. Mandler and A. J. Bard, *J. Electrochem. Soc.* **1989**, *136*, 3143.
- [147] S. Meltzer and D. Mandler, *J. Chem. Soc., Faraday Trans.* **1995**, *91*, 1019.
- [148] Y. Zu, L. Xie, B. Mao and Z. Tian, *Electrochim. Acta* **1998**, *43*, 1683.
- [149] C. Combellas, A. Fuchs, F. Kanoufi, D. Mazouzi and S. Nunige, *Polymer* **2004**, *45*, 4669.
- [150] C. Combellas, J. Ghilane, F. Kanoufi and D. Mazouzi, *J. Phys. Chem. B* **2004**, *108*, 6391.
- [151] C. Combellas, F. Kanoufi and S. Nunige, *Chem. Mater.* **2007**, *19*, 3830.
- [152] C. Combellas, F. Kanoufi, D. Mazouzi, A. Thiebault, P. Bertrand and N. Medard, *Polymer* **2003**, *44*.
- [153] C. Combellas, F. Kanoufi and D. Mazouzi, *J. Electroanal. chem.* **2006**, *589*, 243.
- [154] C. Combellas, F. Kanoufi and D. Mazouzi, *J. Phys. Chem. B* **2004**, *108*, 19260.
- [155] C. Combellas, F. Kanoufi, D. Mazouzi and A. Thiébault, *J. Electroanal. Chem.* **2003**, *556*, 43.
- [156] S.-Y. Jang, M. Marquez and G. A. Sotzing, *Synth. Met.* **2005**, *152*, 345.

- [157] K. Borgwarth, N. Rohde, C. Ricken, M. L. Hallensleben, D. Mandler and J. Heinze, *Adv. Mater.* **1999**, *11*, 1221.
- [158] J. Zhou and D. O. Wipf, *J. Electrochem. Soc.* **1997**, *144*, 1202.
- [159] S. Meltzer and D. Mandler, *J. Electrochem. Soc.* **1995**, *142*, L82.
- [160] H. Shiku, T. Uchida and T. Matsue, *Langmuir* **1997**, *13*, 7239.
- [161] H. Shiku, T. Takeda, M. Yamada, T. Matsue and T. Uchida, *Anal. Chem.* **1995**, *67*, 312.
- [162] D. E. Cliffel and A. Bard, *Anal. Chem.* **1998**, *70*, 1993.
- [163] B. Gollas, P. N. Bartlett and G. Denuault, *Anal. Chem.* **2000**, *72*, 349.
- [164] C. H. Xiang, Q. J. Xie, J. M. Hu and S. Yao, *J. Electroanal. Chem.* **2005**, *584*, 201.
- [165] F. M. Boldt, J. Heinze, M. Diez, J. Petersen and M. Borsch, *Anal. Chem.* **2004**, *76*, 3473.
- [166] G. D. Shi, L. F. Garfias-Mesias and W. H. Smyrl, *J. Electrochem. Soc.* **1998**, *145*, 2011.
- [167] F. R. F. Fan, D. E. Cliffel and A. Bard, *Anal. Chem.* **1998**, *70*, 2941.
- [168] C. E. Gardner and J. V. Macpherson, *Anal. Chem.* **2002**, *74*, 576A.

## CHAPTER 2

### ORGANIC ELECTROGRAFTING ON CONDUCTING AND SEMICONDUCTING SUBSTRATES

#### 1. Introduction

The modification of the surface of materials is a very important issue since a great part of their properties is expressed via their surfaces. In particular, organic coatings on metals are ubiquitous today, and find applications in various fields including biocompatibility, protection against corrosion, lubrication, soldering, wettability, adhesion. As we will see below, many routes that we can roughly divided in “physisorption techniques” (such as painting, spin coating, vacuum evaporation) and “chemisorption techniques” (such as plasma polymerization, self-assembled mono- and multilayers largely used in template chemistry, cathodic or anodic electropolymerization) have been developed by research teams in order to synthesize and/or functionalize organic or composite layers and also induce new properties for materials. One major problem to be tackled is however the usually weak and short-term adhesion between organic matter and inorganic materials.

Therefore, among the numerous methods commonly used for the formation of organic coatings on surfaces, six can be emphasized for their industrial importance, the efforts made by research institutions to develop them, and their ability to provide submicrometer deposition, which is a common goal in numerous high-tech industries:

- **Plasma deposition of polymers** for producing highly robust polymeric coatings has been known for 50 years.<sup>[1-5]</sup> Strong chemical linkages that are assumed to be formed between the reactive species produced within the plasma and the surface of the substrate lead to highly adherent films. Since the glow discharge is a very energetic process, organic gases or vapors that are not regarded as monomers for conventional polymerization can be used. Indeed, free radicals are generated whatever the starting organic species, and the final deposit is very different from a conventional polymer film prepared by a casting technique: the plasma polymer does not contain regular repeat units, but branched and randomly terminated chains with a high degree of cross-linking. In some cases, free radicals remain trapped within the highly cross-linked structure, and their subsequent recombination results in ageing of the coatings. Plasma polymerization has been widely used for corrosion protection, scratch-resistant coatings, and anti-adhesive applications, although deposition rates are generally low. Moreover the implementation of this technique requires specific chambers, which weighs down its cost.

- **Spin coating** is the most widely used technique for organic coatings based on polymer solutions, for example, photosensitive resins used in lithography in the microelectronics industry, antireflection coatings for flat-screen displays and television tubes, and compact discs. The range of obtained thicknesses is generally 1-200  $\mu\text{m}$ , but thinner films can be produced with dilute solutions and high spinning rates. The homogeneity of the spin-coated film strongly depends on the quality of the pristine solution and the chosen combination of solvent, spinning rate, and atmosphere. Spin coating is ideal for temporary organic coatings (as is the case with lithographic resins), since the organic film is only physisorbed on the substrate. Spin coating is also widely used to prepare inorganic coatings from sol-gel solutions.
- **Vapor deposition** is generally used for inorganic coatings (ceramics, silicon carbide, nitrides, metals), but can also be applied to small organic molecules, for example, in the fabrication of organic thin-film transistors, organic light-emitting diodes, and organic photovoltaic cells. Soft conditions (low pressure, flash heating) are generally chosen to prevent thermal degradation of the organics during vaporization and retain the molecular properties in the final film. Hence, only weak interactions can be created between the molecular film and the substrate. This technique is thus limited to organic coatings that are not subject to mechanical or thermal constraints. Vapor-deposited films can be locally highly crystalline, but are often prone to defects such as grain boundaries, cracks, and disclinations.<sup>[6, 7]</sup>
- **Electrodeposition** has been known for years for coating conducting surfaces with metals. Electroplating is currently the most widely used method for coating surfaces in the automotive, petrochemical, and aerospace industries; propulsion, combustion, and microwave applications; printed circuit boards, vias, and copper interconnections for electronics; and many decorative applications. For a long time organic electrodeposition was limited to conducting polymer coatings that were developed in the 80s together with the fundamentals of polymer conductivity. After more than 30 years of basic research, both on mechanisms and processability, conducting polymers are now starting to be used industrially in light-emitting displays.
- **Self-assembly (SAM)** is a very attractive technique for forming organic coatings.<sup>[8, 9]</sup> Indeed, it combines low-cost processes that are music to industrial ears, soft conditions that prevent degradation of the coating molecules, and spontaneous formation of true chemical linkages between the molecules and the substrates. The substrate is put in contact with a solution containing the molecular precursors bearing a reactive group capable of specific interactions with the surface. So as, the surfaces of oxides, noble metals, and silicon can be successfully functionalized provided suitable reactive molecules are used (halogenosilanes, alkoxysilanes, organophosphonates, carboxylic acids, thiols,

disulfides, selenols, alkenes, alkynes, etc.). Van der Waals interactions between neighboring chemisorbed molecules generally lead to long-distance ordering in the first monolayer. Self-assembly from solution or the gaseous state (for smaller molecules) provides very good coverage in short times. SAM of thiols on noble metals constitutes doubtless the prototype of self-assembled layers because they are easy to realize. Their structure and the interfacial linkage are perfectly characterized on a molecular scale by depositing them on single-crystal substrates which make them clearly the method of choice for fundamental studies on the molecule-metal bonds.<sup>[9-11]</sup> However, from a technological point of view, these SAM are poorly stable because they give weak interfacial bonds (190 kJ/mol for the Au-S bond) that can be easily broken under harsh conditions (high temperature, oxidative or reductive potentials, solvents, etc.). Multilayers can be obtained by sequential steps, but self-assembly is the method of choice for molecular-thick films used under moderate conditions and were up to now confined to prospective applications such as molecular electronics.<sup>[12-16]</sup> SAM on oxides, which include metals and semiconductors covered with an oxide layer, are carried out with fatty acids, phosphonic acids and organic derivatives of silicon.<sup>[8, 9]</sup> In the former cases, the initial reaction is an acid-base like reaction with the formation of a complex between the surface metallic cation and the carboxylate (or phosphonate) groups. In the latter case (chlorosilanes, alkoxy silanes etc), the reaction leads to the formation of polysiloxanes, which are linked to the surface via M-O-Si bridges, where M indicates an atom of the surface.<sup>[17]</sup> Lastly, among the chemical methods of functionalization, let us quote the hydrosilylation reaction of hydrogenated-silicon substrates by alkenes which makes it possible to carry out functionalized alkyls layers directly on silicon.<sup>[18, 19]</sup> These alkyl layers are covalently bonded to the silicon surface via the high energetic Si-C bond (360 kJ/mol) and can be easily obtained by thermal (with or without catalyst) or photochemical (UV) ways.<sup>[20]</sup>

- **Electrografting** is a relatively new technique that allows the deposition of very thin organic films (typically between one monolayer and 50 nm) via very strong substrate-molecule links (fig. 1).<sup>[21]</sup> Often compared (or confused) with the anodic electrodeposition of conducting polymers from conjugated monomers, this grafting method is an electro-initiated process, which requires a charged electrode only for the grafting step, but not for thickening. A typical example is given by the electro-grafting of vinylic polymer films. The reaction mechanism of the electrografting was in particular described by C. Bureau et al.<sup>[22-24]</sup> The growth of the grafted chains proceeds by purely chemical polymerization, i.e. independently of the polarization of the conducting surface, which gave place to the initial grafting. Thus, the layer thickness is not controlled by the amount of charge injected in the system, as for the electrodeposition of metals or

conducting polymers, but fully tuned by the characteristics of the monomer solution (type of monomer, concentration, solvent, salt, temperature and possible side reaction).



*Figure 1: Electrografted film of polymethacrylonitrile on half part of a French coin.*

Reactive species like radicals can also give rise to the formation of grafted films. They can be easily generated in ambient conditions, both in solution and in gaseous phases. In particular, diazonium compounds, whose chemistry has been known for long thanks to their applications in dye chemistry and photochemistry, are prone to easily generate radicals. Their electrochemical reduction on various conductive surfaces is a very effective means for generating thin films containing a wide range of chemical functionalities.<sup>[25]</sup>

After this brief introduction, we will focus now on the mechanisms of the electrografting process.

## **2. Electrografting of organic films on conducting and semiconducting substrates**

### ***2.1. Cathodic electrografting of vinylic polymers***

LCSI has historically been developing the cathodic electrografting of vinylic polymers (CEVP) via an electro-induced anionic polymerization that starts from a precursor chemically bound to the electrode.<sup>[26]</sup> Strong efforts were devoted in past years both to the theoretical interpretation of the mechanism and towards practical applications of the process.<sup>[22-24, 27-43]</sup> If the mechanism was highly debated<sup>[22, 44]</sup>, it is now well established.<sup>[23, 39, 43]</sup> Reader may report to Palacin's review for a detailed overview of the experimental facts from which the mechanism was established.<sup>[21]</sup> This method found applications in many fields such as lubrication<sup>[45, 46]</sup>, surface chemistry for biological purposes<sup>[27]</sup>, heavy metal depollution<sup>[42]</sup>, detection of toxic agents with grafted molecularly imprinted polymers, selective capture and electro-induced release

of metallic ions<sup>[42]</sup>, composites nanotubes fabrications.<sup>[47]</sup> This technical approach was rewarded in 2001 by the creation of Alchimer spin-off company, which applies the process in the microelectronics fields.

In this CEVP process, electro-active organic species, such as vinylic monomers containing an electro-attractive group, can be reduced (fig. 2a, example of the electrografting of methacrylonitrile (MAN)). Their electro-reduction results in the formation of radical ions that may undergo chemical reactions either with species in solution or with the electrode surface (fig. 2a). The latter route is the key step explaining the formation of grafted films. The resulting organic films are generally insulating, highly adherent, and optically transparent. The formation of this strong interfacial bond is a key point for the properties of the final interfaces, which can then be further processed by classical methods of organic chemistry. For example, the electrografted polymethacrylonitrile films can be used for direct immobilization of proteins through spontaneous reactions between the nitrile groups from the film and the amino groups from the amino-acids of the protein.<sup>[27]</sup> The final protein film is stable towards aqueous rinsing and can be used for protein-substrate recognition.

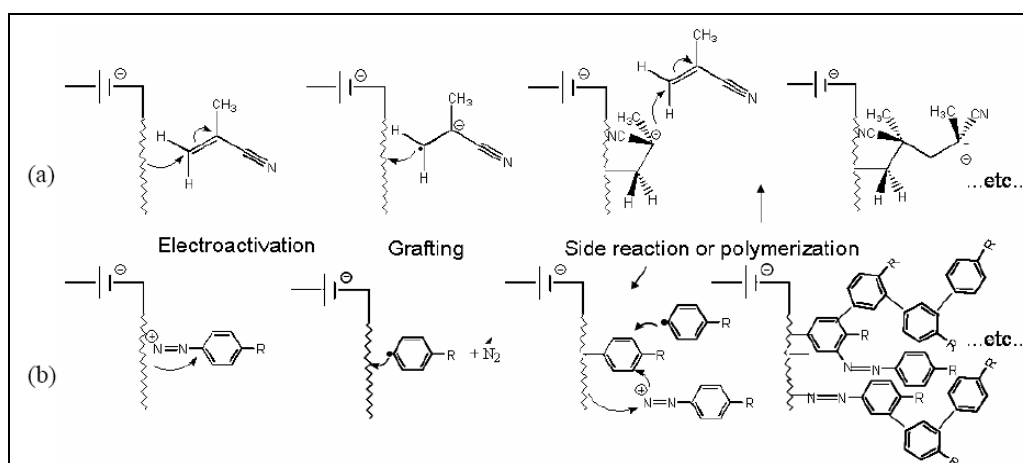


Figure 2: Principle of the electrografting of (a) vinylic monomers (MAN) and (b) aryl diazonium derivatives.

It is not the purpose of the present work to give detailed description of that process, however, some main characteristics of CEVP should be reminded here, before switching to more recent processes:

- i. CEVP only applies in dry organic solvents on a few vinylic monomers, able to be electroreduced: acrylates, acrylonitrile, vinylpyridine exhibit a reduction peak around -2.5 V vs Ag/AgCl.

- ii. CEVP produces truly grafted polymer films. Indeed, the carbon-to-metal bond was evidenced by XPS.<sup>[41]</sup> (fig. 3)

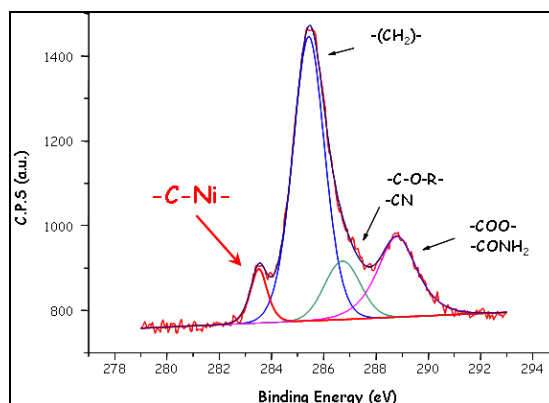


Figure 3: X-ray photoelectron spectra of C 1s levels of a nickel surface obtained by electrochemical polarization of 2-butenitrile in acetonitrile. (from reference 41).

- iii. CEVP also produces large amounts of non-grafted polymer chains, mainly arising from radical-anions that did not graft on the electrode, or grafted and were released before reaction with another monomer. As the grafted anion can reasonably be considered as a metastable moiety, the polymerization from the substrate can be seen as a stabilization process for the grafted species, since the negative charge is driven away for the charged cathode during propagation. The non-grafted chains can be easily washed away from the substrate with a suitable solvent.
- iv. The propagation step is independent from the applied tension; hence the final thickness of the grafted film only depends on the experimental conditions: concentration, solvent, temperature... CEVP is then an electro-induced process, not an electro-driven one as the anodic polymerization of conducting polymers
- v. Thanks to the local generation of active and short-living species, CEVP can be localized provided the cathode-substrate exhibits areas of different work functions, as for composite surfaces (fig. 4a)<sup>[33]</sup> or locally doped semiconductors (fig. 4b).<sup>[34]</sup>

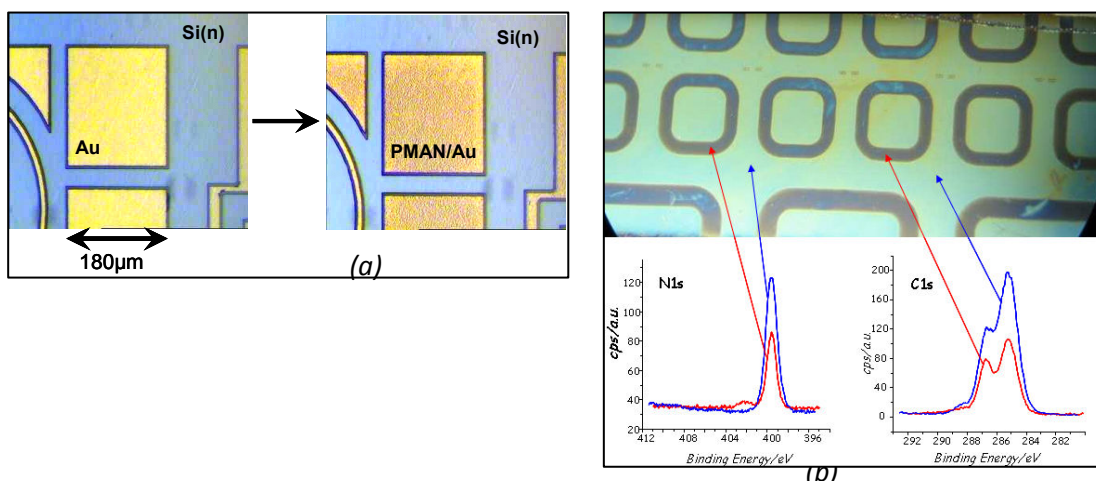


Figure 4: (a) optical microscopy pictures of bare gold pattern on silicon (left) and grafted gold pattern (right) after electro-grafting of pMAN at  $-3.0\text{ V vs. Ag}^+/\text{Ag}$  (from reference 33); (b) localized electrografting obtained on locally doped silicon: coating on poorly doped areas is thicker than on highly doped areas, as evidenced by local XPS analysis. (from reference 34).

- vi. CEVP is a quite fast process when compared to other grafting-from processes such as surface-induced ATRP, for example.<sup>[48]</sup>

The above list clearly emphasizes the ability of CEVP to produce truly grafted polymer films onto any conducting substrate. However, CEVP suffers from several drawbacks which obviously limit its practical use, particularly in industrial conditions:

- i. Due to its anionic mechanism, CEVP requires strictly anhydrous conditions.
- ii. The applied potential is highly cathodic, which might be detrimental for substituted monomers bearing fragile groups.
- iii. The thickness and the coverage ratio of the final polymer film cannot be tuned separately.

For those reasons, CEVP cannot be considered for real applications, unless very specific. There is thus a clear need for an alternative method which could provide similar grafted polymer films in less demanding conditions. As shown below, this was made possible by changing from a direct and purely anionic mechanism to an indirect and radical one.

## 2.2. Electrografting of polyphenylene coatings from diazonium salts

The CEVP mechanism, detailed above, relies on radical ions as reactive species that start both the grafting (radical) and the polymerization (anion) processes. However, many polymerization processes currently used in practical applications are based on purely radical mechanisms. Indeed, radicals are often used because they can be easily generated in ambient conditions, both in solution and in gaseous phases. Aryl diazonium derivatives (AD), well known thanks to their applications in dye and photochemistry, are prone to easily generate radicals. The functionalization of surfaces by electrochemical reduction of aryl diazoniums was discovered by Pinson and al. in 1992. The success of the method, now widely used, is due to the fact that the reaction makes it possible to covalently attach aryl groups on carbon, most of the metals, semiconductors, as well as on conducting oxides and stainless steel.<sup>[25]</sup> The mechanism of electrografting from AD derivatives is highly similar to the cathodic electrografting of vinylic polymers, although the reduced species is neutral. Both aqueous and nonaqueous solutions of diazonium salts undergo a one electron irreversible reduction that generates aryl radical species near the interface. A monolayer may be obtained through a precise control of the charge flow,<sup>[49]</sup> but the process generally gives polyphenylene-like coatings via direct reactions between the grafted species and radicals generated in excess at the electrode (fig. 2b). It must be noted that the formation of the polyphenylene-like moiety may also be prevented by using sterically hindered<sup>[50]</sup> or cleavable precursors.<sup>[51]</sup>

Mechanisms of the diazonium salts electrografting has been widely described in the literature specially by Bélanger et al.<sup>[52, 53]</sup> and Pinson et al.<sup>[54-58]</sup> As depicted in figure 2b, the binding of aryl groups to the substrate occurs in two steps: (1) the formation of a phenyl radical by the electrochemical reduction of the diazonium function then (2) the formation of a covalent bond between the surface atoms and the aryl radical. Under usual conditions (high concentrations, i.e. >1 mM,<sup>[59-62]</sup> and long deposition times at excessive negative potentials<sup>[59, 63]</sup>), the generation of aryl radicals may continue and lead to the formation of multilayer films by reaction of those extra radicals with molecules already bonded to the surface.<sup>[61]</sup> But, as described by Pinson et al.,<sup>[55, 58]</sup> those extra radicals could also react in solution to give diazenes (Ar-N=N-Ar) which eventually precipitate to form a physisorbed layer.

In most of the published data, the characterization of the resulting films is exclusively based on ex-situ observations.<sup>[60, 63-65]</sup> Accordingly, those studies may suffer from a lack of accuracy, regarding the film adhesion properties or film thickness, two properties which definitely govern technical applications of these organic layers. Therefore, experiments were undertaken in order to investigate the multilayer formation of polyphenylene films by coupling, *in situ*, electrochemistry and AFM analysis. We will report to the annex of this chapter to find the detailed experimental procedure. By

combining AFM and XPS characterizations, we were able to investigate not only the threshold conditions necessary for the polyphenylene grafting on the substrate but also, to define the chemical changes in the organic films under the AFM tip shear.<sup>[66]</sup> Nano-friction experiments appear thus as a very interesting tool for the comprehension of the adhesion in the interface (substrate/first grafted layer). It must be mentioned that, in SPM-based nanolithography,<sup>[67-69]</sup> “nano-friction process”, or “nanoshaving” was already mainly used to pattern self-assembled monolayers, as originally demonstrated by Liu et al.<sup>[70]</sup> The process was more recently applied to thin polymer films<sup>[71]</sup> or biofilms.<sup>[72]</sup> Nanoshaving is actually part of many scanning-probe lithography methods that were recently reviewed.<sup>[73]</sup>

Since low-roughness substrates are required for AFM analyses, we choose to thoroughly study the electroreduction of the 4-nitrobenzenediazonium tetrafluoroborate (NBD) on n-type silicon with its native oxide. To our knowledge, most of the works undertaken on the grafting of diazonium salts on silicon substrates were carried out on Si-H terminated substrates.<sup>[49, 74-81]</sup> But we have already shown that the native silicon dioxide layer does not prevent electrografting process. For example, successful electrografting of vinylic polymers on native silicon dioxide has been already reported.<sup>[34]</sup> In fact, the native oxide layer is thin enough (less than 2 nm thick as measured by XPS) to allow electron tunneling from the underlying silicon to the electrolytic solution. Since the native silicon dioxide layer does not prevent electrografting process and the substrates are much more easily produced and manipulated than Si-H ones, we concentrate our study on silicon with its native oxide layer.

Figure 5a gives the voltamperogram recorded when reducing NBD on n-type silicon together with the evolution of the measured thickness of the resulting poly-nitrophenylene films grafted after one voltamperometric scan as a function of the applied potential. This result is consistent with our expectation that the film thickness increases with the absolute value of the applied potential. Indeed, the more negative the applied potential, the higher the amount of electro-generated radicals, and the thicker the final grafted film. Actually, when the applied potential becomes more cathodic, the amount of aryl radicals resulting from the electroreduction of the diazonium salts increases, which promotes the growth of a thick multilayer film by coupling between the generated radicals and the already grafted phenyl rings. We should highlight that, as shown in figure 5b, the thickness of the film increases ca. exponentially with respect to the applied potential.

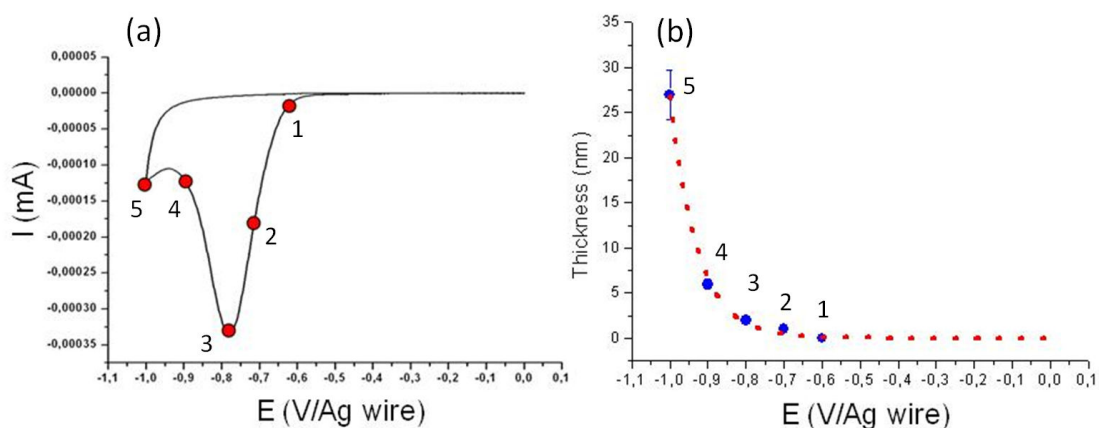


Figure 5: (a) Cyclic voltamperogram in the cathodic range recorded with a sweep rate of  $10 \text{ mV s}^{-1}$  for the electrolytic solution (nitrophenyl diazonium tetrafluoroborate  $5 \cdot 10^{-3} \text{ mol.dm}^{-3}$ /DMF/TEAP  $8 \cdot 10^{-2} \text{ mol.dm}^{-3}$ ) on n-type silicon substrate with its native oxide; (b) Applied potential dependence of the polyphenylene thickness growth on silicon substrates: red scatter: experimental data, black dotted line: exponential fit data. (from reference 64).

As shown on figure 5, the thickness of the polyphenylene-like grafted layer becomes detectable once the applied potential reaches ca.  $-0.7 \text{ V/Ag}$ . That threshold value of the applied potential for which an electrografted film on silicon surfaces can be detected was confirmed by XPS analysis. To remove most of the physisorbed species, samples were successively washed with water and ethanol and then dried under nitrogen before XPS analyses. A survey spectrum and high-resolution spectra regions were recorded for each electrografted sample. Figure 6 gives the N 1s core-level XPS spectrum for polynitrophenylene films electrografted on Si/SiO<sub>2</sub> at  $-0,7 \text{ V/Ag}$  (fig. 6a) and  $-0.6 \text{ V/Ag}$  (fig. 6b). Two peaks located at about 400,6 eV and 406.4 eV are clearly observed on figure 6a and assigned according to literature.<sup>[82, 83]</sup> The 400 eV peak is attributed to the presence of the mixture of azo ( $-\text{N}=\text{N}-$ )<sup>[84]</sup> and amino ( $\text{NH}_2$ ) groups, whereas the 406 eV peak is due to the presence of the nitro ( $\text{NO}_2$ ) group. Almost no signal is detected on figure 6b, meaning that the potential required for electrografting polynitrophenylene films on Si/SiO<sub>2</sub> in our experimental conditions has to be more negative than  $-0.6 \text{ V/Ag}$ .

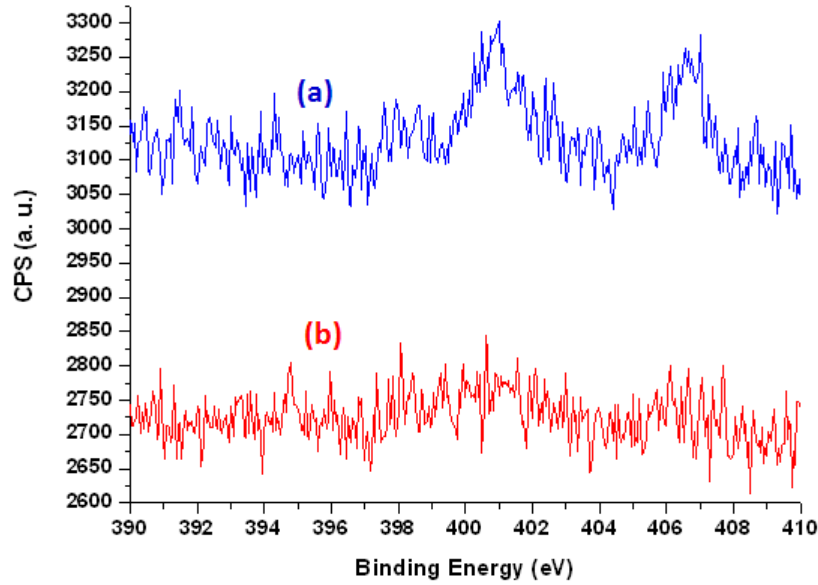


Figure 6: N 1s core level spectra of polyphenylene films grafted on n-type silicon substrates at a potential of (a) -0.7 V/Ag and (b) -0.6 V/Ag. Acquisition conditions: X-ray source= 150 W, and pass energy= 20 eV.

Another key parameter of the mechanism of the electrografting from diazonium salts was derived from the mechanical analysis of the grafted polyphenylene-like film.<sup>[66]</sup> After electrografting, the homogeneous polyphenylene films can be patterned, *in situ*, using AFM friction mode. We observed that applied normal forces in the  $1.2 \pm 0.2$  nN range were not sufficient to remove any matter in a homogeneous way. Thereby, normal forces were progressively increased with approximately 1 nN step until the rubbed area of  $5 \times 5 \mu\text{m}^2$  was smooth and homogeneous. For all the studied applied potential, the depth, homogeneity and smoothness of the rubbed area were found constant for normal forces ranging from  $11.2 \pm 0.2$  nN to  $15.2 \pm 0.2$  nN. Therefore, a 13.2 nN normal force was selected and applied in all our nano-friction experiments, which were performed at 0.5 Hz scan rate with a scanning density of 512 lines/frame. The topography of the rubbed zones is shown in figure 7. According to previous XPS analysis, AFM images show that nano-friction under a 13.2 nN normal force is efficient only when the applied potential during electrografting was more cathodic than -0.6 V/Ag. In that case a square structure can be observed by contact mode AFM. Moreover, the amount of rubbed matter increases regularly with the value of the applied final potential.

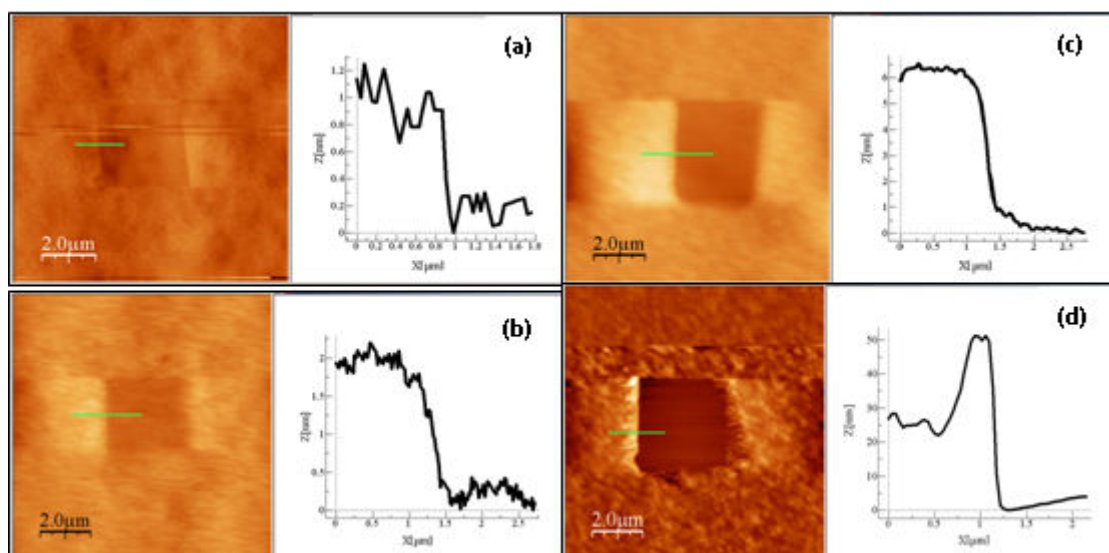


Figure 7: AFM topography images of structured polyphenylene films with a 13.2 nN normal force. Films grafted under (a)  $-0.7$  V/Ag (b)  $-0.8$  V/Ag (c)  $-0.9$  V/Ag and (d)  $-1$  V/Ag. Contact mode, image area =  $5 \times 5 \mu\text{m}^2$ .

The results described above rise the crucial question: under the friction effect of the AFM tip, is the polyphenylene film completely or partially removed?

As no qualitative or quantitative information about friction effects on polyphenylene films can be found in the literature, we used XPS mapping analysis on damaged areas to investigate the efficiency of mechanical rubbing. As the  $5 \times 5 \mu\text{m}^2$  rubbed areas used for the AFM analysis are in the lower limit of detection of our XPS mapping technique, we specifically used  $50 \times 50 \mu\text{m}^2$  zones for the XPS mapping analysis (fig. 8a), and the polyphenylene films were electrografted with an applied potential of  $-1$  V/Ag in order to get the maximum contrast between rubbed and non-rubbed zones. Samples were analyzed before and after sonication in ethanol so as to observe a possible presence of debris.

As depicted in figure 8b, one can easily distinguish the rubbed zone on combined elemental maps of carbon, nitrogen and silicon. Scratched squares corresponds to decrease in concentration of C and N atoms, whereas the signal of the Si substrate appears. The results shown in figure 8 undoubtedly prove that the AFM tip acted as a “shaver” on electrografted polyphenylene films, partially or completely removing polyphenylene chains from the Si/SiO<sub>2</sub> surface. Once again, XPS observations are in good agreement with AFM topographical analysis which shows a thinner film in the rubbed zones due to the mechanical damage. Complementary XPS analysis with a smaller spot size ( $27 \mu\text{m}$ ) have been carried out “in” and “out” of the damaged zones shown on figure 8, in order to locally analyse the chemical composition of the sample. Figure 8c shows XPS spectra recorded “in” and “out” of the rubbed polyphenylene film. Figure 8c brings two conclusions: (i) the intensity of the nitro and the azo peaks in

the N1s region undoubtedly decreases from the "out" to the "in" zone, which confirms the AFM analysis and the efficiency of the friction-induced rubbing: polyphenylene chains are actually "shaved" and removed from the interface upon the tip action. (ii) The "in" zone exhibits non-zero intensity for the nitro and azo peaks in the N1s region, which clearly indicates that the rubbing did not remove all the polyphenylene matter from the Si/SiO<sub>2</sub> surface. Besides, it should be noted that no changes in the "in" and "out" zones were observed by XPS upon sonication in ethanol during 10 minutes. Consequently, we deduce that (i) the initial washing with water and ethanol was sufficient to remove all physisorbed moieties (ii) the XPS signal observed in the "in" zone does not arise from ungrafted fragments generated during friction, but more likely from segments of polynitrophenylene chains which remains bonded to the Si/SiO<sub>2</sub> surface.

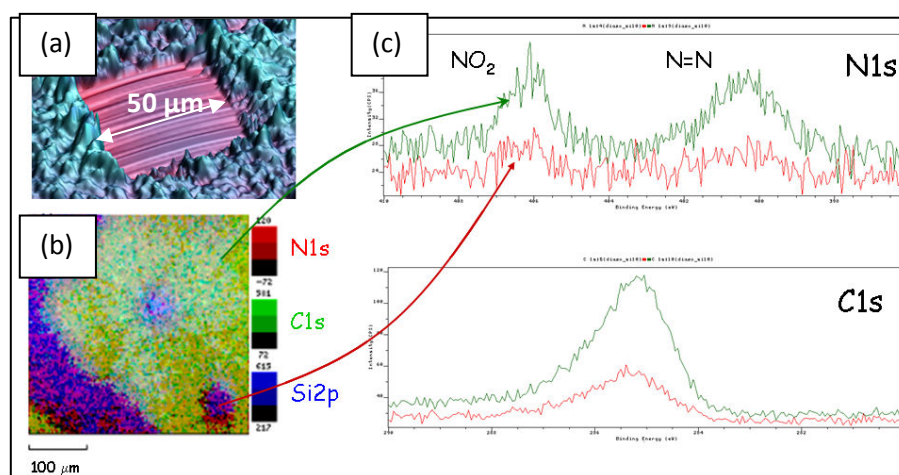


*Figure 8: (a): AFM image of the area rubbed with the AFM tip in the PNP grafted multilayer; (b): Elemental map of N, C, and Si (respectively red, green and blue) obtained by XPS mapping analysis on rubbed polyphenylene films; (c) N 1s and C 1s core level spectra of rubbed (red) and non-rubbed (green) areas on the PNP grafted multilayer. (from reference 64).*

The latter assumption may be supported by a detailed analysis of the different bonds that can be observed in our electrografted polyphenylene multilayers (table 1). Indeed, the first layer issued from the electroreduction of diazonium salts is supposed to be covalently grafted to the surface, which is here native silicon dioxide. Thus, it is likely the covalent grafting relies on Si-C and/or Si-O-C bonds, while the bonds involved in the multilayer formation are either C-N or C-C bonds.<sup>[85, 86]</sup> Our study indicates that the overall energy of the interfacial bonds (mainly Si-C and/or Si-O-C bonds at the Si/SiO<sub>2</sub> – polyphenylene interface) is stronger than the energy responsible for the cohesion of the multilayer structure (scheme 1). Indeed, our AFM and XPS analysis show that bonds at the interface (first layer/surface) resist to the mechanical stresses imposed by the tip, whereas under the same conditions bonds in the multi-layer do not. We assume that result arises both from slight differences in energy between the

corresponding bonds, but also from a higher number of bonds at the interface than within the multilayer structure.

Chemical bond	Energy (KJ/mol)
C-N	305
C-C	347
C-O	358
C-Si	360
N=N	418
Si-O	452

Increase of the bond energy

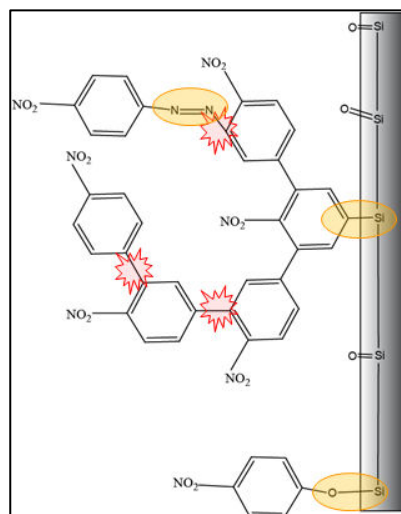


Table 1: Energies of the different bonds that can be observed in the electrografted film on Si/SiO<sub>2</sub> substrate. (from references 83 and 84).

Scheme 1: sketch of the plausible shaving process in the multi-layer.

Moreover, the thickness of the residual film can then be estimated using the standard overlayer model, which, for a take off angle of 90°, is given by:

$$\frac{I}{I_0} = \exp\left(\frac{-d}{\lambda}\right)$$

Where “I<sub>0</sub>” is the intensity of Si 2p peaks from a non grafted silicon substrate, “I” is the Si 2p peaks intensity from the polynitrophenylene rubbed zone, “λ” is the electron attenuation length for Si peaks and “d” the layer thickness.

To obtain the film thickness from this formula, Si 2p peaks intensity was deduced from figure 9 depicting the core level spectra of rubbed “in” area of electrografted substrate at -1 V/Ag and non grafted Si/SiO<sub>2</sub> surface.

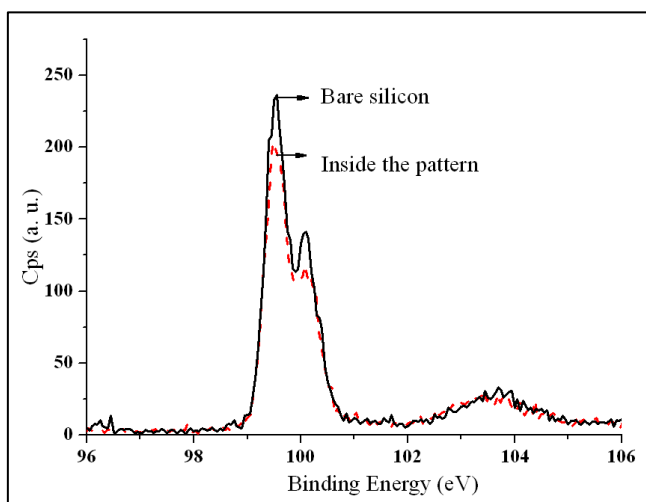


Figure 9: Si 2p core level spectra of the rubbed area on a Si/SiO<sub>2</sub>/polyphenylene substrate electrografted at a potential of -1 V/Ag (dashed line) and a bare Si/SiO<sub>2</sub> substrate (solid line). Acquisition conditions: X-ray source= 225 W, high resolution FoV2 (27 x 27 μm<sup>2</sup>), and pass energy= 40 eV.

The electron attenuation length for Si was obtained from Henry de Villeneuve et al.<sup>[78]</sup>, where the “ $\lambda$ ” value was equal to 4±0.5 nm. Thus the residual film in our rubbed zone was estimated at 0.6±0.07 nm, which is pretty close to the 0.7±0.08 nm thickness given by Allongue for an electrografted phenyl monolayer.<sup>[74]</sup>

This study is thus the first attempt at deciphering the mechanical properties of grafted polyphenylene films arising from the electroreduction of aryldiazonium salts. AFM allowed us to selectively shave the grafted film and local XPS analysis confirmed that few-monolayer-thick polyphenylene-like film remains grafted even after strong mechanical stress within the rubbed areas. The grafted film thus behaves as a bilayer, with a strongly adherent first layer, covalently linked to the substrate and closely packed, and a multilayer-like overlayer weakly adherent to the former one which behaves as a poorly reticulated polymer. The latter layer is expected to arise from "extra" radicals generated in large excess at strongly cathodic potentials while the substrate is already coated with the former layer, which is probably formed very quickly from the first generated radicals at the reduction peak (as indicated by the fast decrease of the recorded intensity after the first cycle in cyclic voltamperometry). The mechanical analysis of the grafted film thus confirms the polyphenylene-like structure of the grafted film and emphasizes that its cross-linking probably decreases from the substrate-film interface to the outer surface.

That assumption was recently confirmed by comparison between electrografted polyphenylene-like films and thiol-based self-assembled monolayers (SAM) both derived from nitrobenzene moieties.<sup>[87]</sup> Indeed, sonication and refluxing in acetonitrile or ethanol both remove more material from the electrografted poly-nitrophenylene (PNP) film relative to the 4-nitrobenzenethiol SAM. But the SAM was totally displaced by exchange reaction with octadecanethiol, while more than 25% of the pristine grafted PNP film remained on the substrate after the same treatment. That study

confirms that electrografted polyphenylene-like films are mainly a dense, yet disordered multilayer film that likely contains some strongly physisorbed material.

Let us now emphasize one peculiar characteristic of the electroreduction of diazonium salts. Unlike the cathodic electroreduction of vinylic monomers, or the electro-oxidation of conjugated moieties such as aniline, thiophene or pyrrole derivatives, the active species generated at the electrode are not charged ones. They are thus able to evolve depending only on their own stability and the local conditions (concentration, solvent, temperature...) that may influence their fate, whatever the applied electric field at the electrode-electrolyte interface. That can be evidenced by our attempts to localize the electrografting of polyphenylene-like films from the reduction of diazonium salts in a SECM environment. We could expect the aryl radicals formed at the cathode under the SECM micro-electrode to eventually graft locally before any diffusion in the surrounding areas. That hypothesis proved wrong as shown on figure 10: at moderate cathodic potential, it is not possible to observe any localized grafting, since the aryl radicals appear to be sufficiently long-lived to reach areas out of the zone facing the SECM micro-electrode.

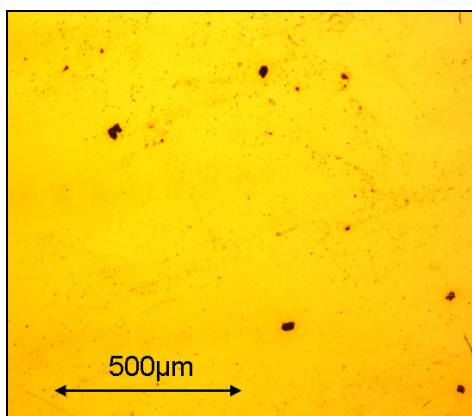


*Figure 10: Optical microscopy image of the localization attempt: no localized effect is observed. 100 μm-Pt UME at a fixed tip-substrate distance of 20 μm; NBD 5 10<sup>-3</sup> mol.dm<sup>-3</sup>, TEAP 0,25 mol.dm<sup>-3</sup>, in dimethylformamide; cyclic voltammetry 0 V→-0,4 V/Ag wire, scan rate 20 mV s<sup>-1</sup>.*

However, as we will see in the chapter 3, localized electrografting of diazonium salts under the SECM tool could actually be observed when specific potential conditions for both substrate and microelectrode are reached. So as, the electroreduction of diazonium salts can nevertheless be considered as a "radical-generator" for processes occurring in solution.

### 3. Indirect cathodic electrografting of vinylic polymers: the SEEP process

As recently reviewed, diazonium salts are very good radical sources for many radical processes including radical polymerization.<sup>[88, 89]</sup> It was thus interesting to investigate using electroreduced diazonium salts as precursors for radical polymerization, and the behaviour of the resulting oligomers towards the electrode surface. Our lab demonstrated recently the successful cathodic polymerization of vinylic monomers on metal substrates by using electro-induced initiators, such as aryldiazonium salts.<sup>[90, 91]</sup> The process, that was called Surface Electroinitiated Emulsion Polymerisation (SEEP), proved efficient in aqueous conditions both for water-soluble vinylic monomers and for lipophilic monomers in emulsion conditions. The grafting process can be split in three steps:

(i) the first one is purely electrochemical and leads both to a first grafted layer of almost pure polyphenylene (PP) film and the formation of radicals initiating the vinylic radical polymerization. The cathodic current flow produces aryl radicals from the aryl diazonium salt in the vicinity of the cathode (fig. 11, reaction 1), which immediately graft onto the electrode surface (fig. 11, reaction 2). The excess of phenyl radicals can either contribute to the thickening of the grafted layer (fig. 11, reaction 3) or initiate the vinylic radical polymerization (fig.11, reactions 4).

(ii) the second one is purely chemical: it is the vinylic radical polymerization (fig. 11, reactions 5) which occurs either in solution for soluble monomers, or within droplets stabilized by the surfactant for non-soluble ones.

(iii) at the end of the propagation reaction, macroradicals react with the previously grafted polyphenylene layer to form the final grafted copolymer-like film (fig. 11, reaction 6).

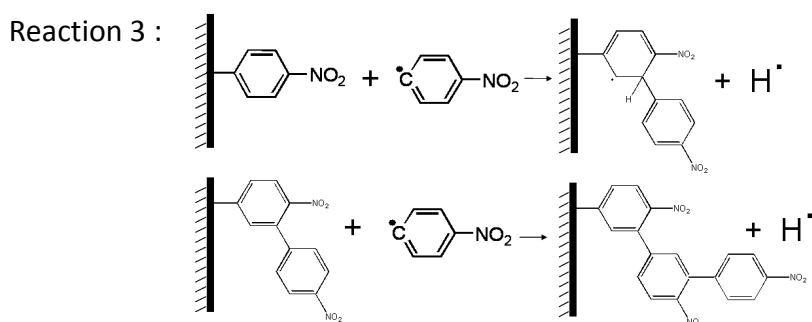
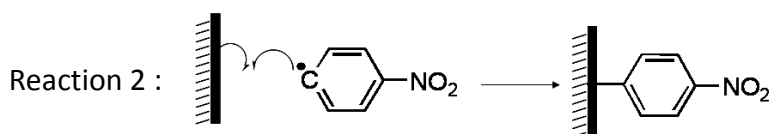
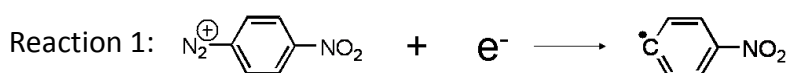
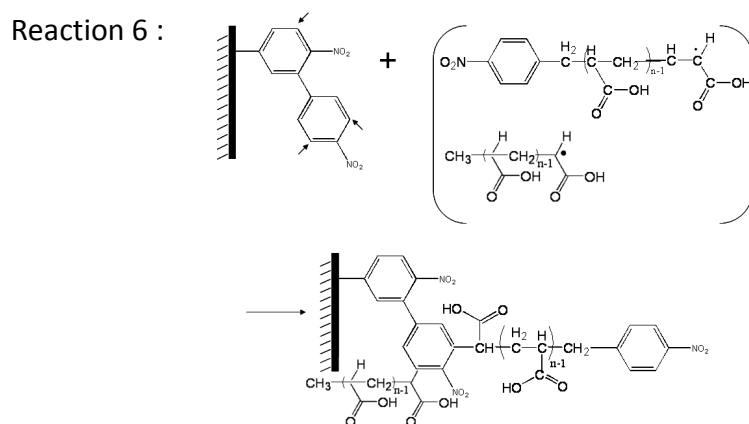
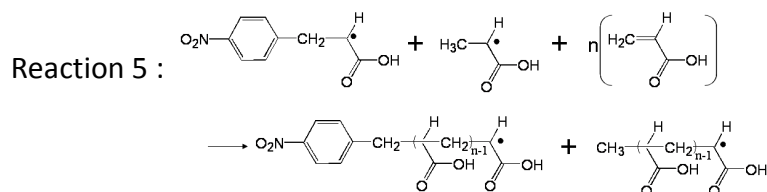
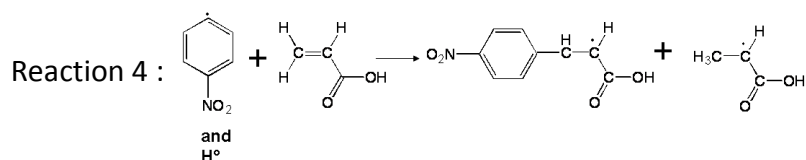


*Figure 11: Proposed mechanism for the electrografting process on conducting surfaces from a mixture of aryldiazonium salts (for example, nitrobenzene diazonium salt) and vinylic monomers (for example, acrylic acid).*



In the context of this work, we applied the SEEP process to both water-soluble vinylic monomer (acrylic acid - AA, hydroxyethylmethacrylate - HEMA) and non soluble monomers (butylmethacrylate – BuMA) with different diazonium salts (nitrobenzene diazoniumtetrafluoroborate – NBD, bromobenzene diazonium - BrB). We used aqueous solution for soluble monomers, or organic solvent (dimethylformamide – DMF) for non soluble ones. In this last case, we prefer indeed to use organic solvent instead of droplets stabilized by the surfactant because it is experimentally too difficult to ensure a sufficiently efficient emulsion in the very small volume of the electrochemical cell (500  $\mu$ l).

The capabilities of the SEEP process is reported below for an acrylic acid - nitrobenzene diazoniumtetrafluoroborate (NBD) mixture. By applying cyclic voltamperometry to a gold substrate in a classical three-electrode electrochemical cell configuration (with Ag and Pt wires as the reference and counter electrodes, respectively), a grafted copolymer-like film (polynitrophenylene-polyacrylic acid or PNP-PA) is obtained (see annex 2 for a detailed experimental procedure). The voltamperometric curves (fig. 12) are characteristic of an electrode passivation resulting from its progressive coating by a polymer film.

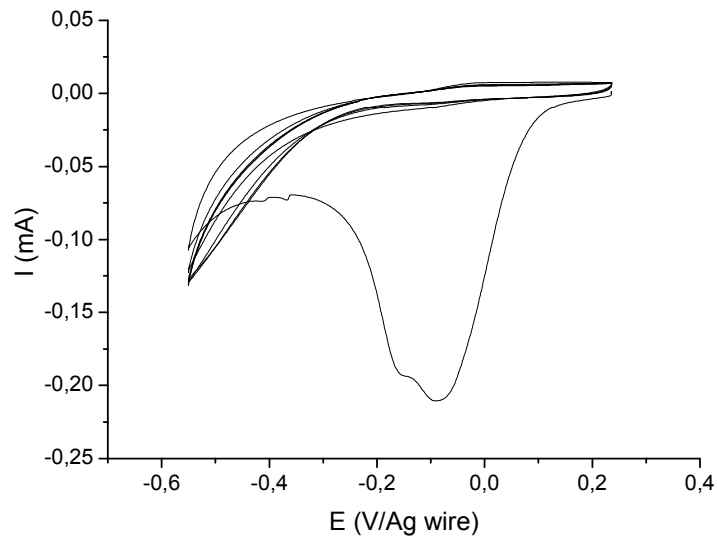


Figure 12: cyclic voltammetry of gold sheet electrografted by PNP-PA; grafting solution  $\text{NBD } 2 \cdot 10^{-3} \text{ mol.dm}^{-3}$ ,  $\text{AA } 2 \text{ mol.dm}^{-3}$ ,  $\text{H}_2\text{SO}_4 \text{ } 0.25 \text{ mol.dm}^{-3}$ , scan rate  $20 \text{ mV s}^{-1}$ .

The IRRAS spectrum recorded on the grafted film (fig. 13) shows the characteristic acid group of polyacrylic acid (PAA) at  $1727 \text{ cm}^{-1}$  (stretching vibration of  $\text{C}=\text{O}$  group) and the  $\text{NO}_2$  bands of the expected polynitrophenylene-like film (PNP) at  $1524$  and  $1350 \text{ cm}^{-1}$  attributed to the stretching vibration of this group.

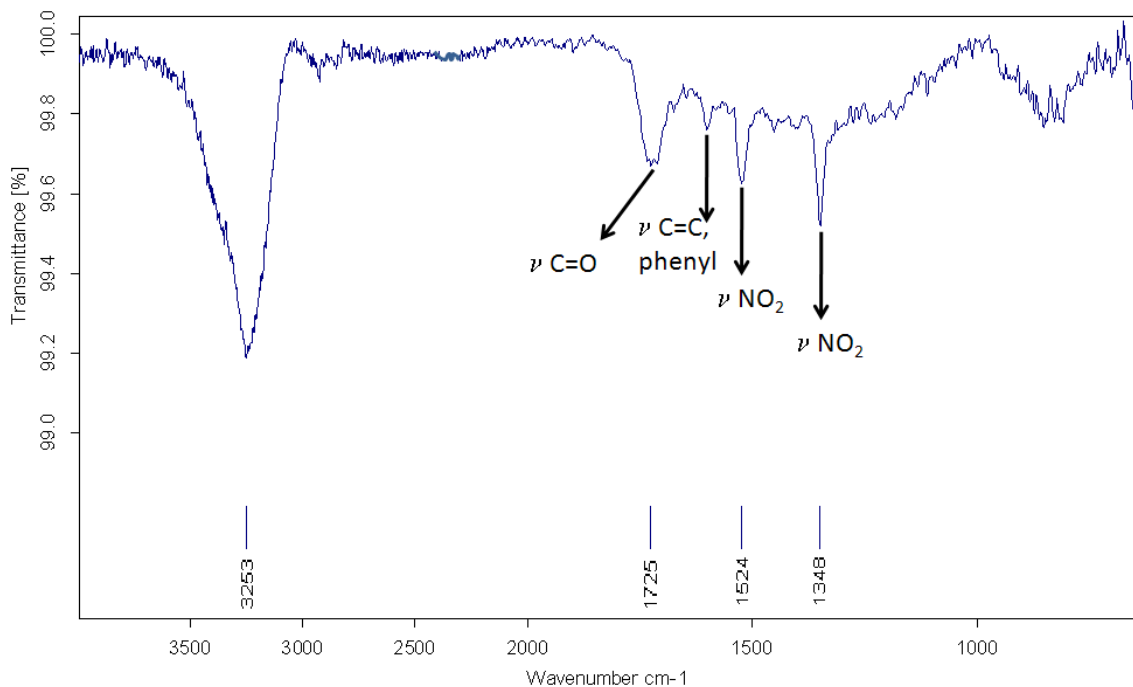
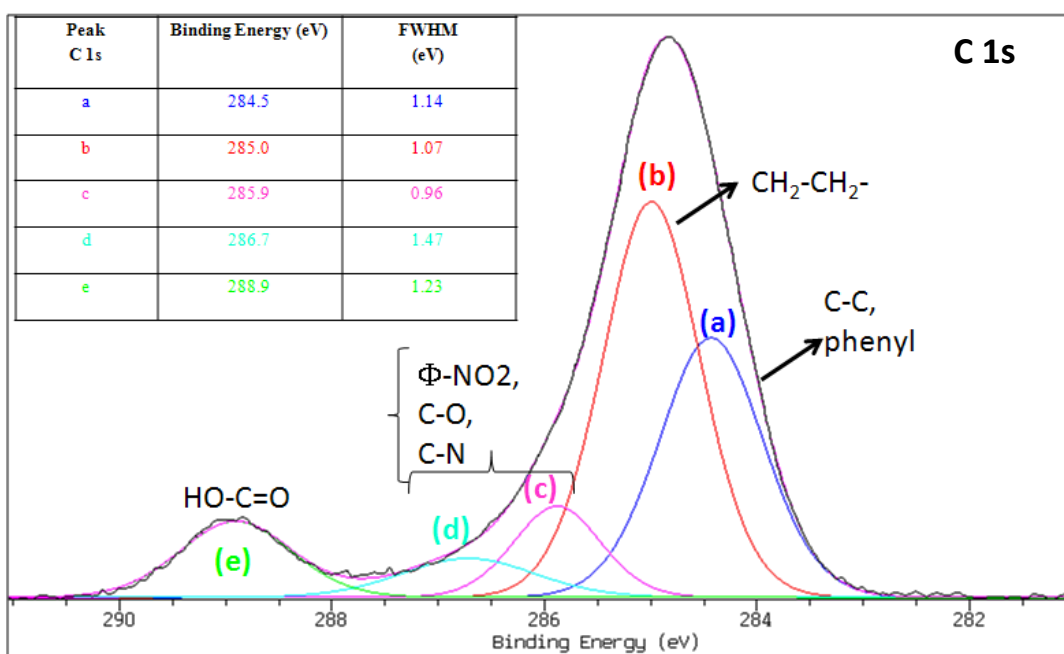


Figure 13: IRAS spectrum of PNP-PA film obtained by cyclic voltamperometry, final potential:  $-0.7 \text{ V/Ag wire}$ ;  $\text{NBD } 2 \cdot 10^{-3} \text{ mol.dm}^{-3}$ ,  $\text{AA } 2 \text{ mol.dm}^{-3}$ ,  $\text{H}_2\text{SO}_4 \text{ } 0.25 \text{ mol.dm}^{-3}$ .

The XPS analysis confirms also the presence of both polymers (fig. 14). Indeed, the C 1s peak shows the PNP with the peak around 284.5 eV attributed to the carbon double bond of phenyl groups and the PAA with the peak centred near 289 eV, assigned to acid groups (-COOH). In the N 1s region, one distinguishes a peak centred at 406 eV characteristic of the NO<sub>2</sub> groups. The second peak around 399 eV can be assigned to reduced nitrogen (NH<sub>2</sub>) with its corresponding protonated form NH<sub>3</sub><sup>+</sup> (shoulder near 402 eV). The contribution around 400.2 eV is attributed to azo groups (-N=N-) coming either from incomplete electroreduction of the diazonium group<sup>[84]</sup> or from a direct copulation reaction between the diazonium salt and any grafted aromatic ring in PNP. On the O 1s region, we detect two peaks corresponding to the contribution of the carboxylic group of PAA and one peak related to the nitro group of PNP. It must be noted that more than 95% of the O 1s signal comes from the sum of the contributions of the carboxylic and nitro groups.



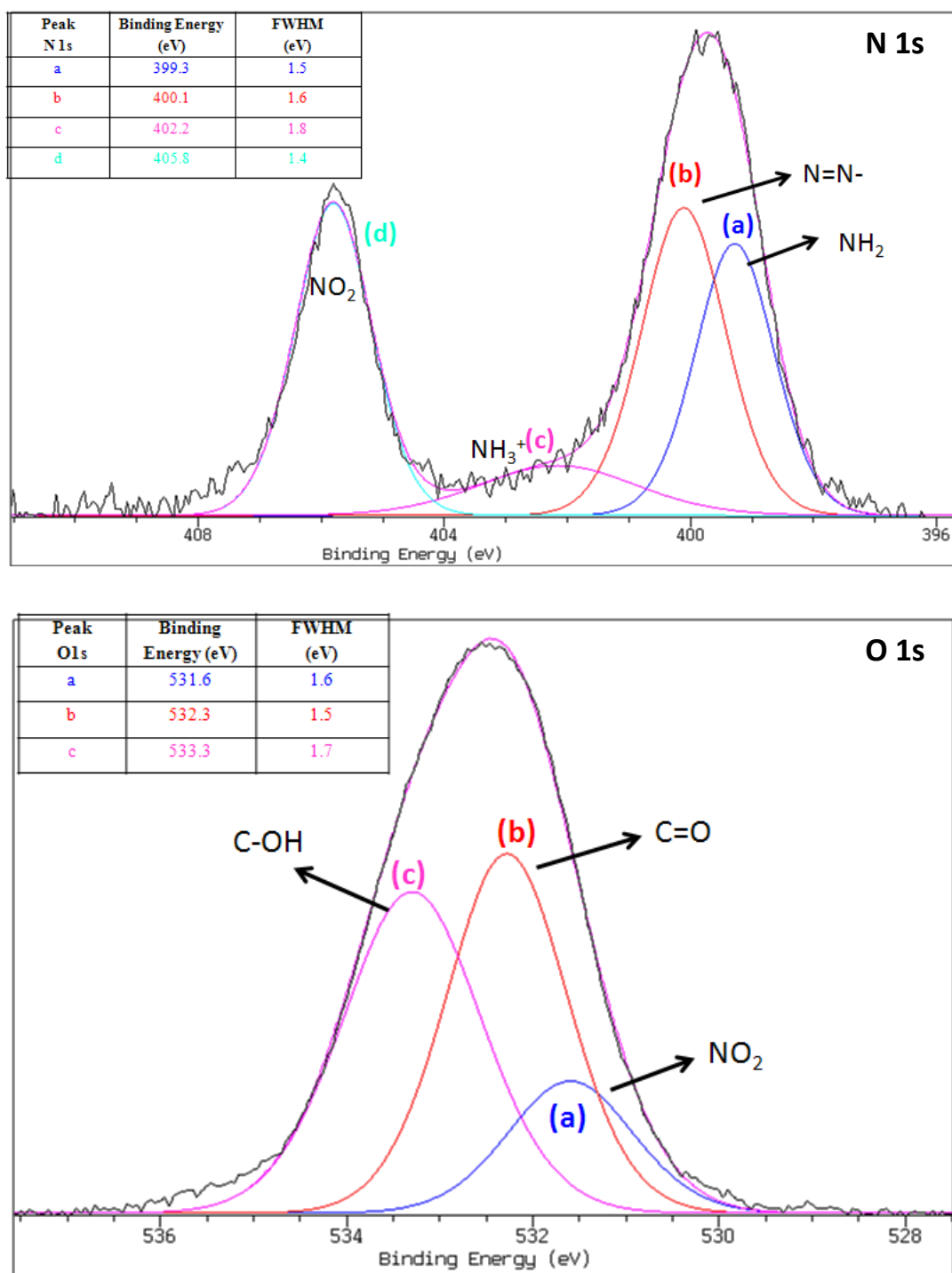


Figure 14: XPS spectra of the core levels C 1s, N 1s, and O 1s of the electrografted PNP-PAA film on gold substrate obtained by cyclic voltamperometry; insert: results of peak decomposition. Final potential:  $-0.7$  V/Ag wire; NBD  $2 \cdot 10^{-3}$  mol.dm<sup>-3</sup>, AA 2 mol.dm<sup>-3</sup>, H<sub>2</sub>SO<sub>4</sub> 0.25 mol.dm<sup>-3</sup>.

In order to optimize the quality of the grafted coating (i.e., conformity, homogeneity, thickness), several electrochemical protocols were tested: cyclic voltamperometry, chronoamperometry, chronopotentiometry. In all cases, the final grafted coating should be considered as a bilayered "PNP-PA" copolymer, with a primer layer almost

entirely formed by the PNP and a top-layer, which thickness depends on the experimental protocol, based on vinylic polymer chains connected to PNP and likely reticulated by aryl groups. Moreover, Teissier et al.<sup>[91]</sup> established that, for the SEEP process under emulsion, the thickness of the coating increases when the proton reduction regime is reached on the substrate. In our experimental conditions, we also observed this behavior. As checked by XPS (fig. 15) and infrared analysis (fig. 16), the thickness of the grafted coating increases with the final potential.

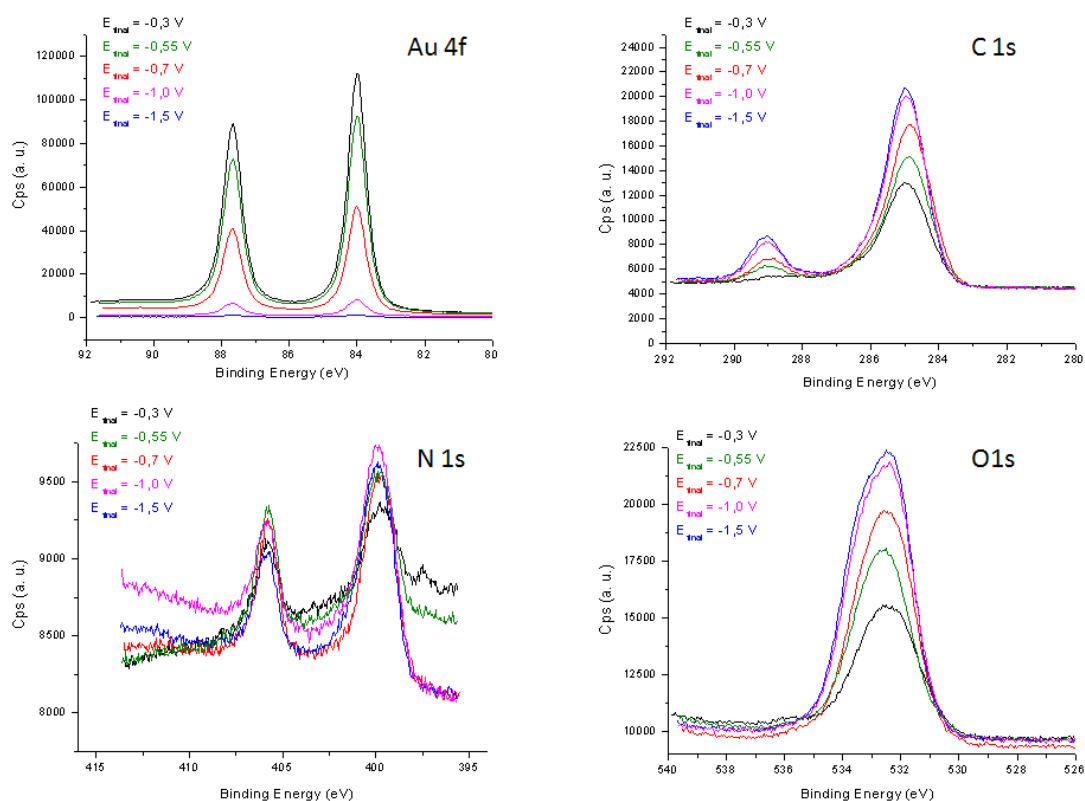


Figure 15: XPS spectra of the core levels Au 4f, C 1s, N 1s, and O 1s of the electrografted PNP-PAA film on gold substrate obtained by cyclic voltamperometry as a function of the final potential.  $NBD\ 2\ 10^{-3}\ mol.dm^{-3}$ ,  $AA\ 2\ mol.dm^{-3}$ ,  $H_2SO_4\ 0.25\ mol.dm^{-3}$ .

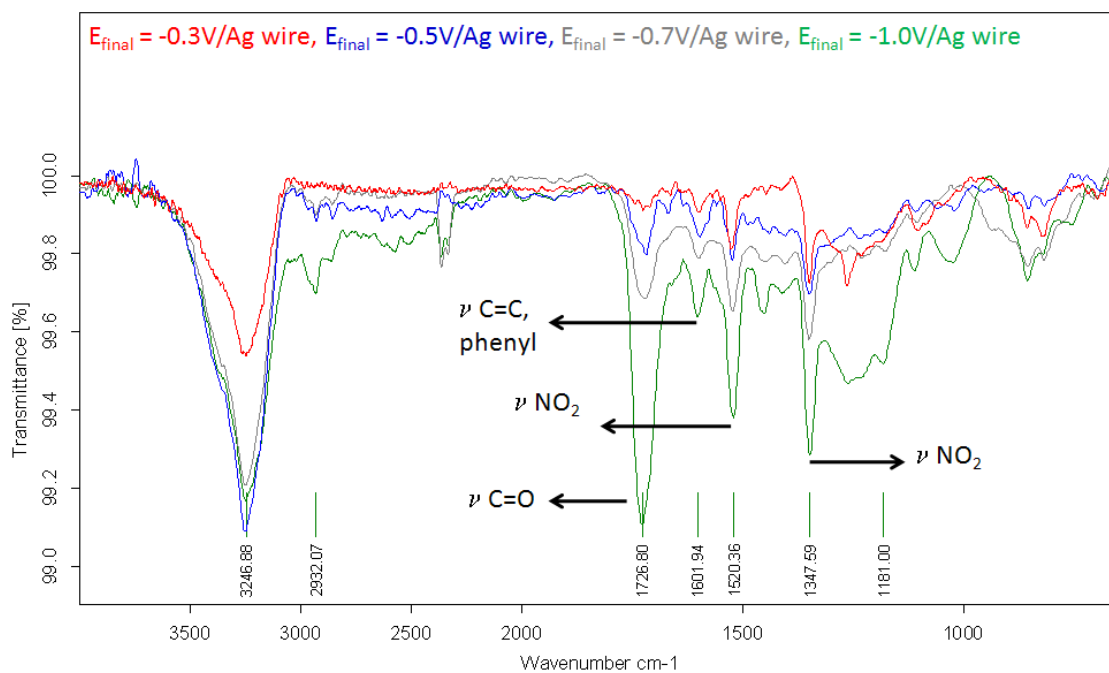


Figure 16: IRAS spectra of the electrografted PNP-PAA film on gold substrate obtained by cyclic voltamperometry as a function of the final potential.  $NBD 2 \cdot 10^{-3} \text{ mol.dm}^{-3}$ ,  $AA 2 \text{ mol.dm}^{-3}$ ,  $H_2SO_4 0.25 \text{ mol.dm}^{-3}$ .

Hence, our results clearly evidence that, in the conditions of our reactions, enough radicals are produced to allow that indirect initiation and the eventual termination of the vinylic macro-radicals. SEEP may then be considered as an improvement of CEVP since similar grafted coatings are obtained with no need for anhydrous conditions and highly cathodic potentials. The key point of that improvement was to shift from a direct anionic induction to an indirect radical one. In other words, the key player here is the diazonium salt, which outstanding properties make that shift possible.

As depicted by the mechanism, grafting of the primer layer is electro-initiated and thus should be sensitive to the current lines which are orthogonal to the ohmic isopotentials. On the contrary, growing of the polymer film is radical-type and is therefore poorly influenced by the electric field. However, we can expect that the radical species involved in the growth of the polymer film are actually sensitive to the diffusional field resulting in changes of concentration in the vicinity of the electrodes. Moreover, as checked in our experimental conditions, the reduction of protons plays a crucial role for the growth of the polymer. Therefore, as all ionic species present in the electrolytic solution, the protons should also be sensitive to the current lines and then participate to the localized effect. In other words, all these phenomena would contribute to localize the grafting. It is the aim of the next chapter.

## REFERENCES

- [1] M. Konuma, *Film Deposition by Plasma Techniques*, Springer Verlag, Berlin **1992**.
- [2] H. Biederman and Y. Osada, *Plasma Polymerization Processes*, Elsevier, Amsterdam **1992**.
- [3] M. J. Danilich and R. E. Marchant, *J. Appl. Polym. Sci. Appl. Polym. Symp.* **1994**, 54.
- [4] S. D. Bodas, S. M. Desai and S. A. Gangal, *Appl. Surf. Sci.* **2005**, 245, 186.
- [5] C. Wang and J. R. Chen, *Appl. Surf. Sci.* **2007**, 253.
- [6] C. F. Powell, J. H. Oxley and J. M. J. Blocher, *Vapor Deposition*, Wiley, New York **1996**.
- [7] J. E. Mahan, *Physical Vapor Deposition of Thin Films*, Wiley, New York **2000**.
- [8] A. Ulman, *Chem. Rev.* **1995**, 96, 1533.
- [9] J. C. Love, L. A. Estroff, J. K. Kriebel, R. G. Nuzzo and G. M. Whitesides, *Chem. Rev.* **2005**, 105, 1103.
- [10] D. P. Woodruff, *Surf. Sci. Rep.* **2007**, 62, 1.
- [11] G. Poirier, *Chem. Rev.* **1997**, 97, 1117
- [12] D. Fischer, A. Curioni and W. Andreoni, *Langmuir* **2003**, 19, 3567.
- [13] L. Patrone, S. Palacin, J. Charlier, F. Armand, J. P. Bourgoin, H. Tang and S. Gauthier, *Phys. Rev. Lett.* **2003**, 91, 96802.
- [14] A. Nitzan and M. A. Ratner, *Science* **2003**, 300, 1384.
- [15] W. Wang, T. Lee and M. A. Reed, *Phys. Rev. B* **2003**, 68, 035416.
- [16] C. K. Yee, A. Ulman, J. D. Ruiz, A. Parikh, H. White and M. Rafailovich, *Langmuir* **2003**, 19, 9450.
- [17] S. Onclin, B. J. Ravoo and D. N. Reinhoudt, *Angew. Chem. Int. Ed.* **2004**, 44, 6282.
- [18] J. M. Buriak, *Chem. Rev.* **2002**, 102, 1271.
- [19] D. D. M. Wayner and R. A. Wolkow, *J. Chem. Soc., Perkin Trans.* **2002**, 2, 23.
- [20] P. Gorostiza, C. Henry de Villeneuve, C. Q. Y. Sun, F. Sanz, X. Wallart, R. Boukherroub and P. Allongue, *J. Phys. Chem. B* **2006**, 110, 5576.
- [21] S. Palacin, C. Bureau, J. Charlier, G. Deniau, B. Mouanda and P. Viel, *ChemPhysChem* **2004**, 5, 1468.
- [22] C. Bureau, G. Deniau, P. Viel and G. Lecayon, *Macromolecules* **1997**, 30, 333.
- [23] J. Charlier, C. Bureau and G. Lecayon, *J. Electroanal. Chem.* **1999**, 465, 200.
- [24] C. Bureau, *J. Electroanal. Chem.* **1999**, 479, 43.
- [25] J. Pinson and F. Podvorica, *Chem. Soc. Rev.* **2005**, 34, 429.
- [26] G. Lécayon, A. Le Moel and C. Le Gressus, *Le Vide, Les Couches Minces* **1980**, 201, 638.
- [27] S. Ameer, C. Bureau, J. Charlier and S. Palacin, *J. Phys. Chem. B* **2004**, 108, 13042.
- [28] C. Bureau, M. Defranceschi, J. Delhalle, G. Deniau, J. Tanguy and G. Lécayon, *Surf. Sci.* **1994**, 311, 349.
- [29] C. Bureau, M. Defranceschi, J. Delhalle, G. Lécayon and D. R. Salahub, *J. Mol. Struct. (Theochem)* **1995**, 330, 279.
- [30] C. Bureau and J. Delhalle, *J. Surf. Anal.* **1999**, 6, 159.
- [31] C. Bureau, G. Deniau, F. Valin, M.-J. Guittet, G. Lecayon and J. Delhalle, *Surf. Sci.* **1996**, 355, 177.
- [32] C. Bureau, J.-M. Soudan and G. Lecayon, *Electrochim. Acta* **1999**, 44, 3303.
- [33] J. Charlier, S. Ameer, J. P. Bourgoin, C. Bureau and S. Palacin, *Adv. Funct. Mater.* **2004**, 14, 125.
- [34] J. Charlier, L. Baraton, C. Bureau and S. Palacin, *ChemPhysChem* **2005**, 6, 70.
- [35] C. Doneux, R. Caudano, J. Delhalle, E. Léonard-Stibbe, J. Charlier, C. Bureau, T. Tanguy and G. Lécayon, *Langmuir* **1997**, 13, 4898.
- [36] C. Doneux, J. Riga, J. J. Verbist, J. Delhalle, J. Charlier, E. Leonard-Stibbe, G. Deniau and G. Lecayon, *AIP Conf. Proceed.* **1996**, 59.
- [37] G. Deniau, T. Thome, D. Gaudin, C. Bureau and G. Lécayon, *J. Electroanal. Chem.* **1998**, 451, 145.

- [38] G. Deniau, J. Charlier, B. Alvado, S. Palacin, P. Aplincourt and C. Bauvais, *J. Electroanal. Chem.* **2006**, 586, 62.
- [39] G. Deniau, P. Viel, C. Bureau, G. Zalczer, P. Lixon and S. Palacin, *J. Electroanal. Chem.* **2001**, 505, 33.
- [40] G. Deniau, G. Zalczer, J. Tanguy and G. Lecayon, *AIP Conf. Proceed.* **1996**, 334.
- [41] G. Deniau, L. Azoulay, P. Jégou, G. Le Chevallier and S. Palacin, *Surf. Sci.* **2006**, 600, 675.
- [42] P. Viel, D. L., L. J., M. Sallé and S. Palacin, *Appl. Surf. Sci.* **2007**, 253, 3263.
- [43] P. Viel, C. Bureau, G. Deniau, G. Zalczer and G. Lecayon, *J. Electroanal. Chem.* **1999**, 470, 14.
- [44] M. Mertens, C. Calberg, L. Martinot and R. Jérôme, *Macromolecules* **1996**, 29, 4910.
- [45] A. Benedetto, P. Viel, S. Noël, N. Izard, P. Chenevier and S. Palacin, *Surf. Sci.* **2007**, 601, 3687.
- [46] A. Benedetto, M. Balog, H. Rayah, F. Le Derf, P. Viel, S. Palacin and M. Sallé, *Electrochim. Acta* **2008**, 53, 3779.
- [47] T. Defever, G. Deniau, S. Palacin, L. Goux-capes, S. Barrau, M. Mayne L'Hermite and J. P. Bourgoin, *J. Electroanal. Chem.* **2006**, 589, 46.
- [48] B. Mouanda, E. Bassa, G. Deniau, P. Jegou, P. Viel and S. Palacin, *J. Electroanal. Chem.* **2009**, 629, 102.
- [49] P. Allongue, C. Henry de Villeneuve and J. Pinson, *Electrochim. Acta* **2000**, 45, 3241.
- [50] C. Combellas, F. Kanoufi, J. Pinson and F. I. Podvorica, *J. Am. Chem. Soc.* **2008**, 130, 8577.
- [51] L. T. Nielsen, K. H. Vase, M. Dong, F. Besenbacher, S. U. Pedersen and K. Daasbjerg, *J. A.m. Chem. Soc.* **2007**, 129, 1888.
- [52] A. Laforgue, T. Addou and D. Bélanger, *Langmuir* **2005**, 21, 6855.
- [53] C. Saby, B. Ortiz, G. Y. Champagne and D. Belanger, *Langmuir* **1997**, 13, 6805.
- [54] A. Adenier, E. Cabet-Deliry, T. Lalot, J. Pinson and F. Podvorica, *Chem. Mater.* **2002**, 14, 4576.
- [55] K. Boukerma, M. M. Chehimi, J. Pinson and C. Blomfield, *Langmuir* **2003**, 19, 6333.
- [56] P. Allongue, M. Delamar, B. Desbat, O. Fagebaume, R. Hitmi, J. Pinson and J.-M. Saveant, *J. Am. Chem. Soc.* **1997**, 119, 201.
- [57] P. Doppelt, G. Hallais, J. Pinson, F. Podvorica and S. Verneyre, *Chem. Mater.* **2007**.
- [58] C. P. Andrieux and J. Pinson, *J. Am. Chem. Soc.* **2003**, 125, 14801.
- [59] P. A. Brooksby and A. J. Downard, *J. Phys. Chem. B* **2005**, 109, 8791.
- [60] F. Anariba, S. H. DuVall and R. L. McCreery, *Anal. Chem.* **2003**, 75, 3837.
- [61] J. K. Kariuki and M. T. McDermott, *Langmuir* **2001**, 17, 5947.
- [62] J. K. Kariuki and M. T. McDermott, *Langmuir* **1999**, 15, 6534.
- [63] P. A. Brooksby and A. J. Downard, *Langmuir* **2004**, 20, 5038.
- [64] M.-C. Bernard, A. Chaussé, E. Cabet-Deliry, M. M. Chehimi, J. Pinson, F. Podvorica and C. Vautrin-UI, *Chem. Mater. B* **2003**, 15, 3450.
- [65] T. Matrab, M. Save, B. Charleux, J. Pinson, E. Cabet-deliry, A. Adenier, M. M. Chehimi and M. Delamar, *Surf. Sci.* **2007**, 601, 2357.
- [66] A. Ghorbal, F. Grisotto, M. Laudé, J. Charlier and S. Palacin, *J. Coll. Interf. Sci.* **2008**, 328, 308.
- [67] R. Garcia, R. V. Martinez and J. Martinez, *Chem. Soc. Rev.* **2006**, 35, 29.
- [68] S. Kramer, R. R. Fuierer and C. B. Gorman, *Chem. Rev.* **2003**, 103, 4367.
- [69] J. Zhao and K. Uosaki, *Nano Lett.* **2002**, 2, 137.
- [70] G. Y. Liu, S. Xu and Y. L. Qian, *Acc. Chem. Res.* **2000**, 33, 457.
- [71] M. Kaholek, W. K. Lee and B. LaMattina, *Nano Lett.* **2004**, 4, 373.
- [72] R. E. Ionescu, R. S. Marks and L. A. Gheber, *Nano Lett.* **2003**, 3, 1639.
- [73] X. N. Xie, H. J. Chung and C. H. Sow, *Mater. Sc. Eng. R-Reports* **2006**, 54, 1.
- [74] P. Allongue, C. Henry de Villeneuve, G. Cherouvrier, R. Cortes and M. C. Bernard, *J. Electroanal. Chem.* **2003**, 550-551, 161.

- [75] P. Allongue, C. Henry de Villeneuve, J. Pinson, F. Ozanam, J.-N. Chazaviel and X. Wallart, *Electrochim. Acta* **1998**, *43*, 2791-2798.
- [76] P. Hartig, J. Rappich and T. Dittrich, *Appl. Phys. Lett.* **2002**, *80*, 67.
- [77] M. P. Stewart, F. Maya, D. V. Kosynkin, S. M. Dirk, J. J. Stapleton, C. L. McGuinness, D. L. Allara and J. M. Tour, *J. Am. Chem. Soc.* **2004**, *126*, 370.
- [78] C. Henry de Villeneuve, J. Pinson, M. C. Bernard and P. Allongue, *J. Phys. Chem. B* **1997**, *101*, 2415.
- [79] C. Henry de Villeneuve, J. Pinson, F. Ozanam, J. N. Chazalviel and P. Allongue, *Mater. Res. Soc. Symp. Proceedi.* **1997**, *451*, 185.
- [80] J. Rappich, A. Merson, K. Roodenko, T. Dittrich, M. Gensch, K. Hinrichs and Y. Shapira, *J. Phys. Chem. B* **2006**, *110*, 1332.
- [81] M. P. Stewart, F. Maya, D. V. Kosynkin, S. M. Dirk, J. Stapleton, C. L. McGuinness, D. L. Allara and J. M. Tour, *J. Am. Chem. Soc.* **2001**, *126*, 370.
- [82] B. Ortiz, C. Saby, G. Y. Champagne and D. Bélanger, *J. Electroanal. Chem.* **1998**, *455*, 75.
- [83] A. Merson, T. Dittrich, Y. Zidon, J. Rappich and Y. Shapira, *Appl. Phys. Lettr.* **2004**, *85*, 1075.
- [84] M. D'Amours and D. Bélanger, *J. Phys. Chem. B* **2003**, *107*, 4811.
- [85] T. L. Cottrell, in: *The Strengths of Chemical Bonds, 2nd Ed., Butterworths London* **1958**.
- [86] Y.-Y. Xu, T. Muramatsu, M. Taniyama, T. Aoki and Y. Hatanaka, *Thin Solid Films* **2000**, *368*, 181.
- [87] D. M. Shewchuk and M. T. McDermott, *Langmuir* **2009**, *25*, 4556.
- [88] X. Zhang and J. P. Bell, *J. Appl. Pol. Sci.* **1999**, *73*, 2265.
- [89] R. H. Markus, *Chemistry* **2009**, *15*, 820.
- [90] G. Deniau, L. Azoulay, L. Bougerolles and S. Palacin, *Chem. Mater.* **2006**, *18*, 5421.
- [91] L. Tessier, G. Deniau, B. Charleux and S. Palacin, *Chem. Mater.* **2009**, *21*, 4261.
- [92] I. Horcas, *Rev. Sci. Instrum.* **2007**, *78*, 013705.

## Annex 1: Experimental procedure for nano-friction experiments

4-nitrobenzenediazonium tetrafluoroborate 97% (molecular formula:  $C_6H_4N_3O_2 BF_4$ ) and tetraethylammonium perchlorate (TEAP - purity  $\geq 99.0\%$  - molecular formula:  $(C_2H_5)_4N(ClO_4)$ ) were purchased from Sigma-Aldrich and used as received. The electrolytic medium was made of a freshly solution of the diazonium salt ( $5 \cdot 10^{-3} \text{ mol.l}^{-1}$ ) dissolved in N,N-dimethylformamide (DMF - Fluka, purity  $\geq 99.8\%$ ). The supporting electrolyte was the tetraethylammonium perchlorate ( $8 \cdot 10^{-2} \text{ mol.l}^{-1}$ ). Substrates were ( $2 \times 2$ )  $\text{cm}^2$  slices of n-type Si(100) one-side-polished silicon wafers (supplied by ACM - France) with native silicon oxide on top. A continuous gold layer (180 nm thick) on a chromium underlayer (15 nm thick) was evaporated on the back of the Si/SiO<sub>2</sub> substrate to ensure an ohmic contact. Before use, the silicon wafers were systematically washed and sonicated for 15 minutes successively in water, acetone and ethanol, and then dried under a stream of nitrogen before their use as working electrodes during electrografting. For the results relevance we used silicon slices cut from the same wafer for all the electrochemical graftings. Besides, the concentration of the electrolytic solution was maintained constant to preserve a constant open circuit potential. The fluid cell defined the active area in the electrochemical reaction ( $33.9 \text{ mm}^2$ ) of the Si/SiO<sub>2</sub> working electrode.

Electrochemical experiments and the in situ analysis were performed with a Molecular Imaging PicoSPMLe commercial AFM microscope (PicoScan 2100 controller - Scientec, France) equipped with a home-modified fluid cell containing the electrolytic solution. The AFM is mounted on a floating table to achieve vibration isolation during investigations and characterizations. Electrografting was carried out using cyclic voltamperometry (Bipotentiostat-BioLogic Science Instruments controlled by a computer with the software EC-LAB v9.30) with a standard three electrodes arrangement. Silver and platinum wires were used as the reference and the counter electrode, respectively. All potentials reported herein are with respect to the reference electrode. Solutions for electrochemistry were not degassed prior to use, and all measurements were made at room temperature. All cyclic voltamperograms were recorded with a scan rate of  $10 \text{ mVs}^{-1}$ .

Patterning (friction mode) and topographical characterization (contact mode) of polynitrophenylene films were consecutively performed directly in the electrolytic solution using the same silicon tip. The thickness of structured polynitrophenylene films was determined using the AFM contact mode. AFM images were recorded using the retrace signal. The scan rate was in the range 0.1–0.25 Hz with a scanning density of 512 lines/frame and 0 V deflection set point. Each scan was duplicated to ensure that any features observed were reproducible.

X-Ray photoelectron spectroscopy (Kratos Axis Ultra DLD) analysis and mapping were performed with a high-resolution monochromatic Al(K $\alpha$ ) X-ray source (1486.6 eV). The photoemission angle was always normal to the surface. During XPS investigations, a survey spectrum (0-1200 eV) and core-level spectra of O 1s (526 – 538 eV), N 1s (396 – 410 eV), C 1s (280 – 290 eV), Si 2p (94 -106 eV) regions were systematically recorded. XPS images were recorded with a high resolution field of view (FoV 2, 400x400  $\mu\text{m}^2$ ) and local analyses were performed with a small spot size (27x27  $\mu\text{m}^2$ ). Moreover, quantitative XPS analyses have been performed so as to determine the thickness of a possible residual film in the rubbed zone.

## Annex 2: Experimental procedure for the electrografted SEEP process

The electrografting experiments were carried out in a one-compartment teflon cell with a standard three-electrode arrangement with the substrate as the working electrode, a counter-electrode (Pt foil or Pt wire) and a reference electrode (Ag wire, its potential is 0,22 V/NHE). The working electrodes were Pyrex glass plates coated with 2 nm of chromium and 100 nm of gold (99.99 %) by vacuum evaporation. All electrografting experiments were performed by controlling the applied potential with a potentiostat (BioLogic Science Instruments) controlled by a computer with the software EC-LAB v9.30. The electrolytic medium was made of commercial acrylic acid (Aldrich) in acidic aqueous solution ( $\text{H}_2\text{SO}_4$  0.25 mol.  $\text{l}^{-1}$ , analytical grade) in presence of 4-nitrobenzenediazonium tetrafluoroborate (Aldrich,  $2 \times 10^{-3}$  mol.  $\text{l}^{-1}$ ). The electro-initiated polymerization technique consists in applying cyclic voltamperometric or chronoamperometric or chronopotentiometric modes to the solution.

The grafting of diazonium salts on metallic or semiconducting substrates takes place only beyond a threshold polarization potential. The reduction of diazonium salt in acidic aqueous solution takes place beyond -0.1 V vs. the  $\text{Ag}^+/\text{Ag}$  reference electrode, for metallic substrates and 0.2 V vs. the  $\text{Ag}^+/\text{Ag}$  reference for semiconductive substrate. For solution in DMF the threshold potential is beyond -0.8 V vs. the  $\text{Ag}^+/\text{Ag}$  reference, for semiconductive n-type substrates. The grafted molecule has a characteristic spectroscopic feature which can be used as a probe to trace the growth of the grafted layer on the surface. The organic grafted coating was then studied with different analytical techniques:

- Optical microscopy (Leica DMLM with CDD camera Leica DFC 320)
- Atomic Force Microscopy (Molecular Imaging PicoLe AFM microscope, Scientec, France) in contact or tapping. AFM Images were analyzed with the WSxM software.<sup>[92]</sup>
- X-Ray photoelectron spectroscopy (Kratos Axis Ultra DLD, Al  $\text{K}\alpha$  monochromatic source)
- Infrared spectroscopy in the reflection-absorption mode (Bruker IFS66 coupled with a HYPERION™ 3000 microscope and Bruker VERTEX 70 spectrometer with a mono reflection ATR Pike-Miracle™ device)



## CHAPTER 3

### LOCALIZED ELECTROGRAFTING: A STRATEGY TO TAILORING THE REACTION AND PATTERNING POLYMER FILMS ON CONDUCTIVE SURFACES

#### 1. Introduction

Modified surfaces containing spatially defined functionalities are a desirable goal for numerous applications. Recent years have seen considerable progress in the development of microfabricated systems for use in the chemical and biological sciences. Existing approaches typically expose macroscopic areas of a substrate to milliliter quantities of solution to attach one type of molecule, sometimes using light and specialized chemistry to carry out localized reactions.<sup>[1-7]</sup> Thus, localized addressing can be obtained under electronic or photochemical radiation,<sup>[8]</sup> by using micro-robotic pipetting of microdroplets,<sup>[9]</sup> by two-dimensional electrophoretic technique,<sup>[10]</sup> with printing technique by microcontact.<sup>[11-15]</sup> Most of these techniques summarized in table 1 require multiple step processes and their implementation is usually tedious and expensive. Due to the requirement of a continuous scaling down, technologies and systems should be miniaturised to close the recent gap between micro- and nanotechnology. Therefore, microsystems have to be continuously developed.

	<b>Description</b>	<b>limiting resolution</b>	<b>drawback</b>
<b>Lighting lithography</b>	The surface modification is realized in a patterned fashion across a surface covered with a film selectively removed or directly troughs beam focalization	linewidths on the order of 10 nm	
<b>Photolithography</b>	Optical lithography, is a process used in microfabrication to selectively remove parts of a thin film or the bulk of a substrate. It uses light to transfer a geometric pattern from a photo mask to a light-sensitive chemical photo resist, or simply "resist," on the substrate. <sup>[16]</sup>	1 $\mu$ m	Defocus, aberration of the lens

<b>Immersion lithography</b>	It is a photolithography resolution enhancement technique that replaces the usual air gap between the final lens and the wafer surface with a liquid medium that has a refractive index greater than one. <sup>[17]</sup>	45nm	Bubbles, temperature and pressure variations in the immersion fluid
<b>Laser beam lithography</b>	It is a technique using a focused laser beam to locally induce surface modification, by thermal effect or by matter evaporation. <sup>[18]</sup>	100nm	Redeposition, substrate attack
<b>X-ray lithography</b>	Photolithographic process using X-rays and special conceived mask, to irradiated with a wave length under-micrometric. <sup>[19]</sup>	30nm	X-ray mask distortion
<b>Electrons beam (E-beam) lithography</b>	E-beam lithography consists of shooting a narrow, concentrated beam of electrons onto a resist coated substrate. Electrons can induce the deposition of substances onto a surface (additive), or etch away at the surface (subtractive). <sup>[20]</sup>	10nm	Proximity effect: electrons backscattering, vacuum
<b>Focused ion beam (FIB) lithography</b>	Processes for removing material include direct ion milling, chemical etching with a reactive gas, reactive ion etching, ion implantation with post chemical etch, deposition (simultaneous FIB and gas jet), FIB induced nucleation, and ion resist lithography. <sup>[21]</sup>	10nm	Vacuum
<b>Soft lithography</b>	It is a technique able to replicating structures without any kind of beam	<50nm	
<b>Microcontact printing</b>	.An elastomeric stamp is used to directly print molecules charged ink on a variety of different substrates. The layer can be used as a mask to pattern the underlying films. <sup>[22]</sup>	10nm	Mask positioning and deformation

<b>Magnetolithography</b>	It is based on applying a magnetic field on the substrate using paramagnetic metal masks named "magnetic mask". <sup>[23]</sup>	30nm	Multistep process
<b>Nanoimprint lithography</b>	The technique uses compression molding to create a thickness contrast pattern in a thin resist film carried on a substrate, followed by anisotropic etching to transfer the pattern through the entire resist thickness. <sup>[24]</sup>	Metal patterns with a feature size of 25nm and a period of 70 nm	effective template cleaning, bubble defects
<b>Dip Pen Nanolithography</b>	It is a scanning probe technique where an atomic force microscopy tip is used to transfer molecules to a surface via a solvent meniscus. <sup>[25]</sup>	<100 nm	Planarity

In this context, the objective of our work is to develop a cheap and mask-free technique by combining local probes techniques (Scanning ElectroChemical Microscopy, SECM and Electrochemical Atomic Force Microscopy, AFM-SECM and electrografting processes in view of tuning locally chemical and physical surface properties on initially homogeneous substrates. The general idea is to spatially confine, under the micro-electrode, the grafting of a primer adhesive layer to micrometer or sub-micrometer-scale domains.

Following earlier works devoted to localized electrografting under CEVP conditions,<sup>[26, 27]</sup> we demonstrated that the electrografting of polyphenylene-like films may be localized on semiconducting substrates either using light to promote the grafting onto enlightened areas (fig. 1),<sup>[28]</sup> or taking advantage of existing differences in effective work functions when using composite substrates as often found in real microelectronics devices (fig. 2).<sup>[29, 30]</sup>

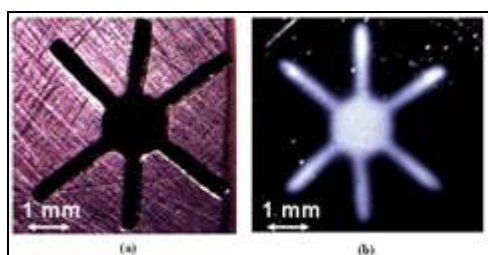


Figure 1: (a) optical image of the cross stainless-steel mask used for the photo-electrografting process; (b) optical image of the photo-electrografted coating on Si-p substrate after electrochemical process: chronoamperometry: 15s at -0.85 V/MSE (from ref. 28).

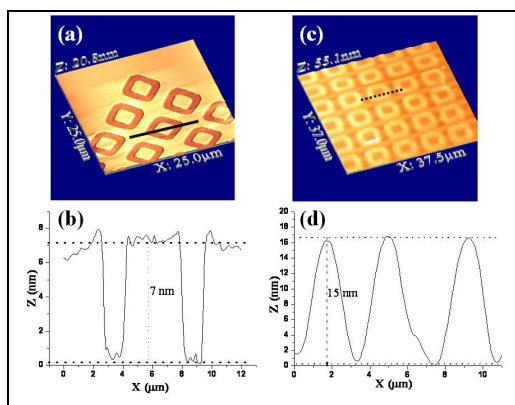


Figure 2: AFM picture in contact mode of the pattern (a, c) and AFM topographical profile (b, d) of (left) the pristine topographical profile of the implanted pattern (where the level of doped areas is 7 nm lower than for undoped areas, because of the chemical treatments after implantation); (right) the same pattern after the electrografting of NBD: Doped areas are now 15 nm in relief with respect to undoped areas (from ref. 29-30 ).

These results emphasize the ability of electro-induced processes to be strongly dependent on local conditions since the generation of the active species, either charged as in CEVP or neutral as for the reduction of diazonium salts, actually occurs at the electrode surface. **We thus decided to study the potentialities of a local conducting probe to induce, electrochemically, a non conducting organic grafting by applying the SEEP process.** As depicted by the SEEP mechanism (see chapter 2, section 3), grafting of the primer layer is electro-initiated and thus should be sensitive to the current lines which are orthogonal to the ohmic isopotentials. On the contrary, growing of the polymer film is radical-type and is therefore likely to be poorly influenced by the electric field. However, we can expect that the radical species involved in the growth of the polymer film are actually sensitive to the diffusional field resulting in changes of concentration in the vicinity of the electrodes. Moreover, it is established that the reduction of protons plays a crucial role for the growth of the polymer.<sup>[31]</sup> The combination of these phenomena would contribute to localize the grafting. Therefore, by using a micro-electrode (UME), we can expect to localize all the electrochemical phenomena involved in the whole process.

The major aims of the present work will thus be: (i) to validate the localized electrografting concept; (ii) to elaborate electrochemical protocols able to improve the localization process; (iii) to assess the ultimate resolution that can be achieved by the method; (iv) to evaluate the possibility to scale up this process by using multi-microelectrodes. The process could thus be considered as a "third way" between micro-/nano-electronics (print, primary coating...) on one hand, and self-assembly on the other hand.

## 2. Localized electrografting with SECM

As mentioned above, our objective is to use SECM as a lithographic tool which could offer an alternative manufacturing process to the currently used lithographic methods primarily based on self-assembly monolayer technology.

Most of the methods used in conjunction with SECM for fabricating small patterns on surfaces can be divided into two main categories based on the mode of operation: the direct mode and the feedback mode. In the direct mode, the substrate serves usually as the auxiliary electrode, while in the feedback mode the substrate is unbiased and a mediator that shuttles between the UME and the substrate is used. More versatile, the feedback mode was widely used to fabricate microstructures. Surface modifications by the direct mode have been more rarely evoked and except for the electrodeposition of ten-micron large domains of conducting polymers such as polypyrrole,<sup>[32]</sup> and the deposition of metal starting from the corresponding salt by local reduction,<sup>[33]</sup> it generally consists in the electrochemical transformation of SAMs.<sup>[34]</sup>

The SECM experiments were performed on a SECM370 unit (Uniscan Instruments) in a one-compartment Teflon cell. The electrografting process was carried out with a standard three-electrode arrangement. The working electrodes were Pyrex glass plates coated with 2 nm of chromium and 100 nm of gold (99.99 %) by vacuum evaporation. The reference electrode was a pseudo-reference Ag wire ( $\Phi = 1$  mm) and the UMEs acted as counter-electrode in the electrical circuit. The Pt microdisk electrodes were prepared according to the literature (see annex 1 for a brief description of the UMEs' fabrication). The tip was moved by a horizontal and vertical translation stage driven by an electric micro-step engine. Potential and current were imposed or measured by a potentiostat/galvanostat system integrated to the SECM370 workstation. The z-approach curves (fig.3) and the X-Y planarity of the sample were realized by setting the microelectrode potential on the reduction plateau of  $[\text{Fe}(\text{CN})_6]^{3-}$  ( $5 \times 10^{-3}$  mol.  $\text{dm}^{-3}$ , KCl 0.1 mol.  $\text{dm}^{-3}$ ). The current as a function of time is recorded upon approaching the surface and translated later into a current-distance curve using the SECM calibration curves for insulating and conducting substrates and the approach speed.<sup>[35, 36]</sup> In the negative feedback as in the positive feedback, the magnitude of the variation of the current fits the theoretical treatment.

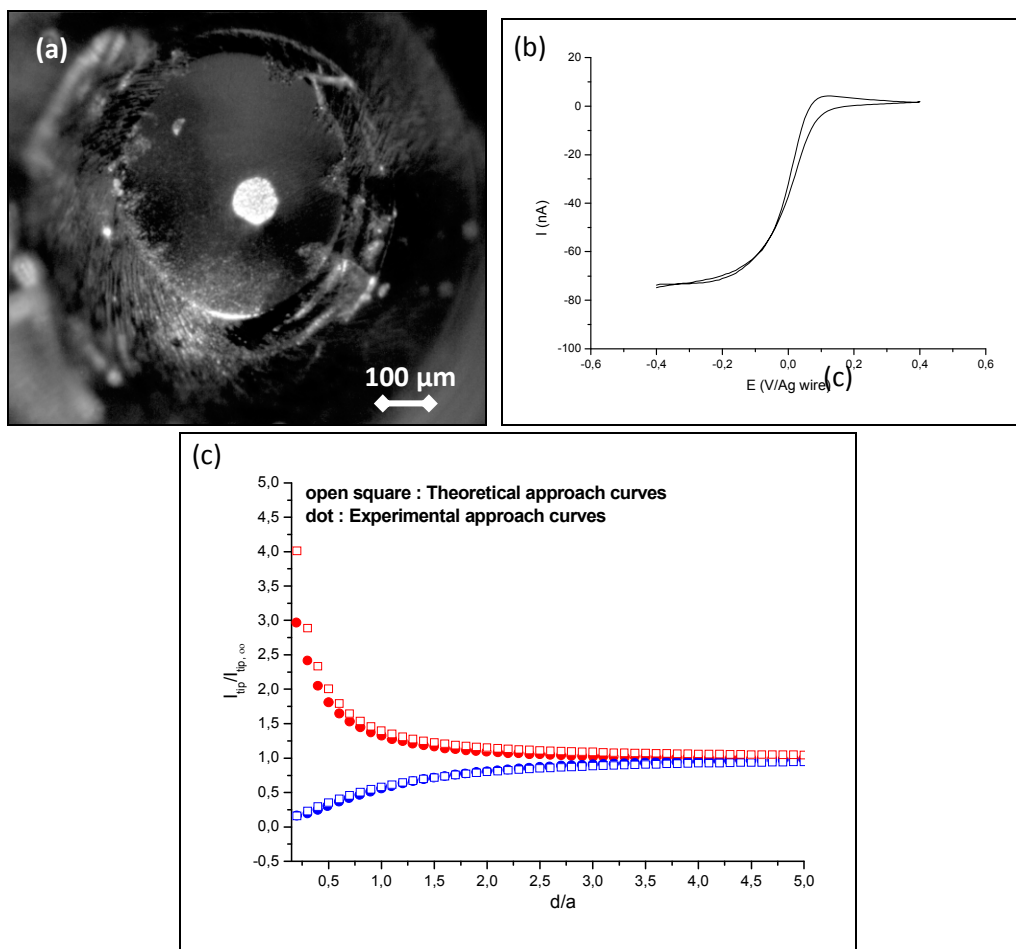
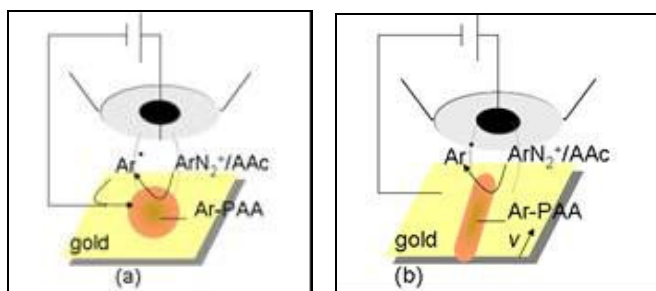


Figure 3: (a) optical microscopy image of the 100µm-Pt UME (RG = 4.9), (b) steady-state current at the 100 µm-Pt UME, (c) experimental vs. theoretical approach curves for a conducting substrate (red), and an insulating substrate (blue).

After the alignment process, the ferrocyanide solution was pumped off and, after rinsing the cell with ultra-pure water, replaced with the electrolytic solution. The electrolytic medium was made of commercial acrylic acid (Aldrich) in acidic aqueous solution ( $H_2SO_4$  0.25 mol.  $dm^{-3}$ , analytical grade) in presence of 4-nitrobenzenediazonium tetrafluoroborate (Aldrich,  $2 \times 10^{-3}$  mol.  $dm^{-3}$ ). Acrylic acid was chosen for its hydro-solubility. All reagents were used as received.

The electro-initiated polymerization technique consists in applying chronoamperometric or chronopotentiometric techniques. The SECM tool was used either in static mode to make dots (scheme 1a) or in dynamic mode to draw lines (scheme 1b). All the samples were sonicated in ethanol and water before analyses to remove any un-grafted matter.



Scheme 1: schematic principle of the localized electrografting in the static mode (a) and dynamic mode (b).

## 2.1 Localized electrografting with SECM: Proof of concept

As seen in the chapter 2, the first attempts to localize the electrografting of the diazonium salts were unsuccessful. If the potential applied to the substrate was limited to the range of the diazonium reduction peak ( $0 < E_{we} < -0.4V/Ag$  wire), only a homogeneous grafting was observed. However, the localization appears for more cathodic applied potentials, i.e. reaching the reduction regime of protons. Below are shown the very first localized grafting obtained by applying chronoamperometric technique (continuous or pulse technique) and by setting the potential to  $-0.7V$  vs. Ag wire (fig. 4).

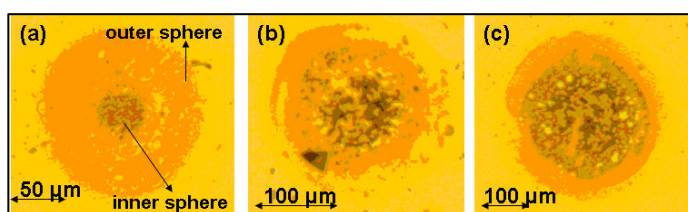


Figure 4: Optical microscopy images of the localized electrografted polymer pattern obtained with (a)  $25\ \mu\text{m}$ -Pt UME, (b)  $50\ \mu\text{m}$ -Pt UME, (c)  $100\ \mu\text{m}$ -Pt UME, at a tip-substrate distance closed to  $20\ \mu\text{m}$ .  $\text{NBD}\ 2\ 10^{-3}\ \text{mol}\cdot\text{dm}^{-3}$ ,  $\text{AA}\ 0.7\ \text{mol}\cdot\text{dm}^{-3}$ ,  $\text{H}_2\text{SO}_4\ 0.25\ \text{mol}\cdot\text{dm}^{-3}$ ; coating obtained by pulse chronoamperometry ( $E_{we}=-0.7V/Ag$  wire,  $t$  polarization =  $0.1s$ ,  $t$  relaxation =  $0.01s$ , 4 pulses).

On the optical pictures, we observe clearly a disc pattern which mimics the UME tip. We distinguish an inner and an outer disc whose diameters are approximately two times and three times, respectively, the size of the UME tip. However, for the smallest UME tip, the outer disc diameter increases drastically compared to the tip diameter.

Infrared measurement performed on the disc pattern reveals unambiguously the presence of a localized electrografted organic coating film on the surface, with the usual IR features of polynitrophenylene ( $1530$  and  $1350\ \text{cm}^{-1}$  corresponding to the  $\text{NO}_2$  and  $1600\ \text{cm}^{-1}$  related to the phenyl group) and polyacrylic acid ( $1730\ \text{cm}^{-1}$  characteristic of the carbonyl group).

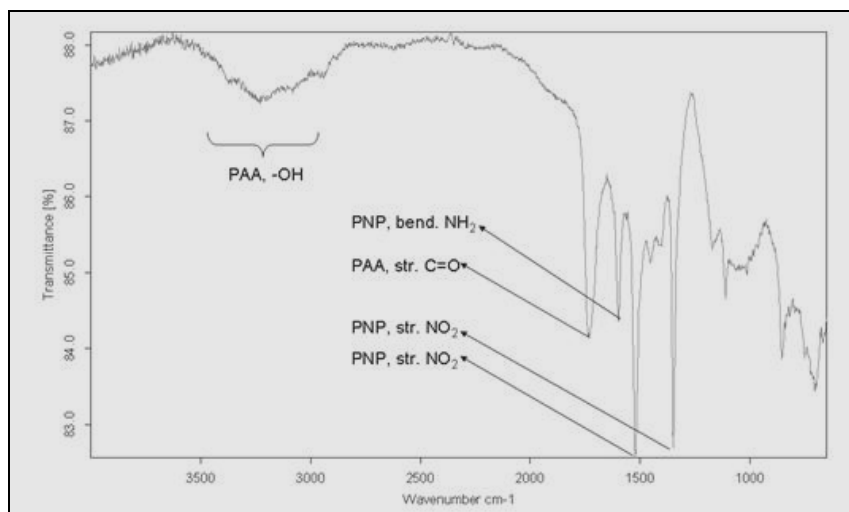


Figure 5: Infrared spectrum in IRRAS mode recorded on the grafted pattern after sonicated rinse.

In the same way, XPS mapping ( $400\ \mu\text{m} \times 400\ \mu\text{m}$ ) as a function of the core level (Au 4f, N 1s, O 1s, C 1s) performed on the pattern obtained with the  $100\ \mu\text{m}$  UME tip, exhibits the localization of the organic layer. More precisely, on figure 6a, we observe that the polynitrophenylene coating is the major component of the trace and that the polyacrylic acid film is preferentially concentrated around the external perimeter of the inner sphere. The Au 4f core level attenuation signal (fig. 6b) confirms also unambiguously the formation of a thicker organic coating in front of the microelectrode surrounded by the glass coating. It is also interesting to observe that outside the pattern, the  $\text{NO}_2$  contribution (406 eV) disappears completely (fig. 6c). This result indicates most probably that outside the pattern, the nitro group is reduced into amine group under our electrochemical conditions. Inside the the pattern, the  $\text{NO}_2$  groups seem partially protected by the polymer film.

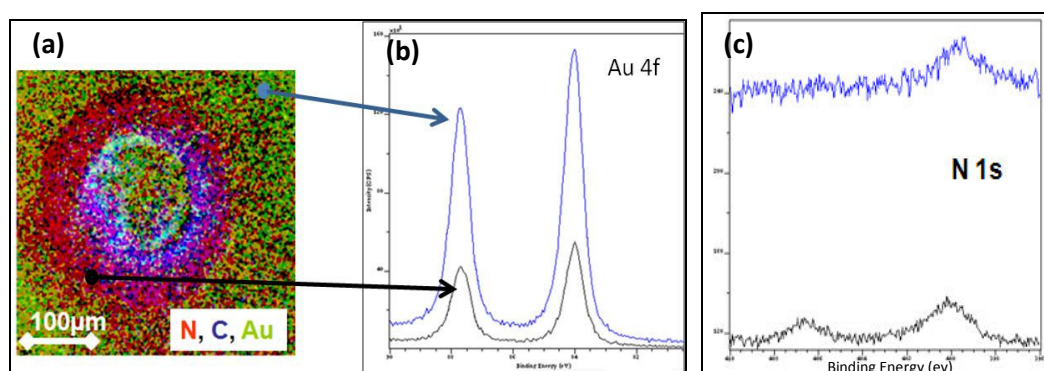


Figure 6: (a) XPS mapping (FoV 2,  $400\ \mu\text{m} \times 400\ \mu\text{m}$ , high resolution) of C 1s, N 1s, Au4f core levels; (b) comparison of the intensities of the Au 4f and N 1s core levels spectra recorded on the pattern (black) and outside the pattern (blue).

The SECM tool was also used in a dynamic mode where the 50  $\mu\text{m}$ -Pt UME tip was moved over 2.2 mm at a fixed distance above the substrate ( $d = 20\mu\text{m}$ ) at a scan rate of  $50 \mu\text{m s}^{-1}$ . The sample was continuously polarized at  $-0.7\text{V}$  vs. Ag wire during the scan. The line trace (fig. 7) exhibits a  $80 \mu\text{m}$  large inner trace and a  $110\mu\text{m}$  large outer trace.

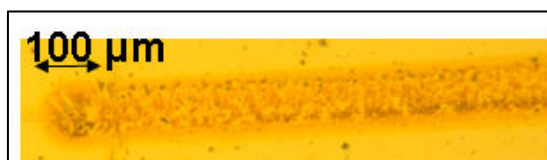


Figure 7: Optical microscopy image of the localized electrografted polymer line pattern drawn with the  $50\mu\text{m}$ -Pt UME at a fixed tip-substrate distance ( $20 \mu\text{m}$ ) and at a scan rate of  $50 \mu\text{m s}^{-1}$ .  $\text{NBD } 2 \cdot 10^{-3} \text{ mol.dm}^{-3}$ ,  $\text{AA } 0.7 \text{ mol. dm}^{-3}$ ,  $\text{H}_2\text{SO}_4 \text{ } 0.25 \text{ mol.dm}^{-3}$ ; coating obtained by continuous chronoamperometry at  $-0.7\text{V}$  vs. Ag wire.

When compared to the static mode, it seems that the dynamic one makes it possible to appreciably reduce the dimensions of the grafted pattern (for a given UME diameter), in particular for the outer trace. This phenomenon is probably related to the flux profile of the solution in connection with the rate at which the probe is moved. It is also very interesting to note that whatever the working distance from the substrate surface, the shape of the trace does not vary significantly (fig. 8). This means that this parameter is not so critical, which is very encouraging in view to transfer the technique to the AFM-SECM for which the working distance is a more difficult parameter to control.

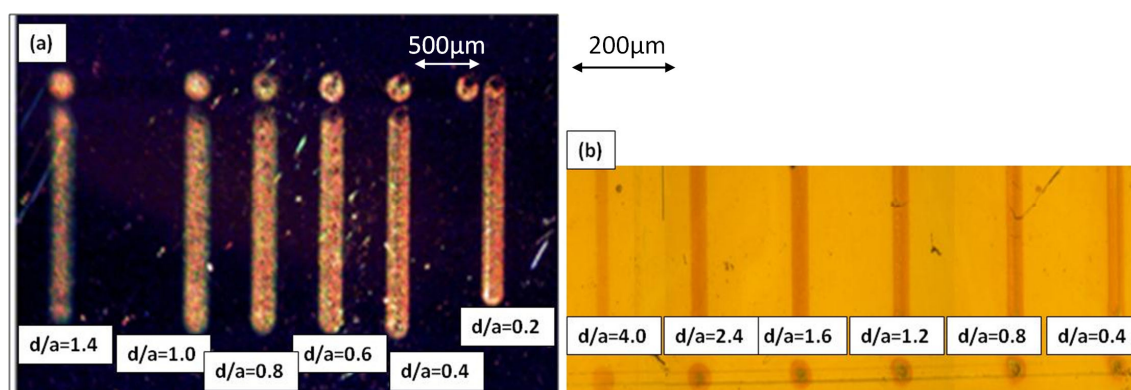


Figure 8: optical microscopy images of localized graftings obtained at different working distance ( $d$ , working distance;  $a$  tip's radius) with (a) the  $100 \mu\text{m}$ -Pt UME, (b) the  $25\mu\text{m}$ -Pt UME. Chronoamperometry ( $E_{we} = -0.7\text{V}/\text{Ag wire}$ ,  $2\text{s}$ , tip's rate:  $50\mu\text{ms}^{-1}$ ).

More precisely, on figure 9, we observe that the normalized width of the grafted dots (diameter of the dot divided by the diameter of the tip–  $L/2a$ ) varies very slowly with the normalized working distance ( $d/a$ ). It is well known that at small distances, the

area of the sample that provides the electrochemical activity corresponds to that of the tip, and, therefore, the microelectrodes characteristics of the tip are transferred to the fraction of the sample situated in front of microdisk. [37] When  $d$  increases, the area is slightly enlarged because of the diffusion occurring parallel to the surface.

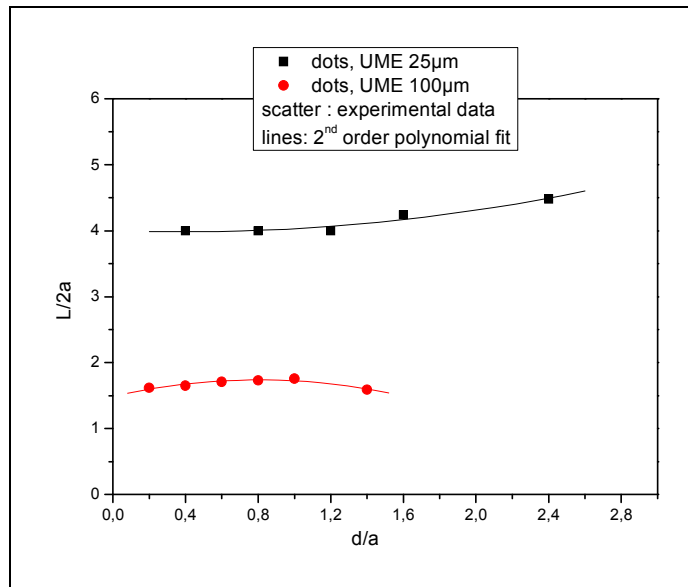


Figure 9: Evolution of the normalized width  $L/2a$  of the localized dots as a function of the normalized working distance  $d/a$  obtained for both  $25\mu\text{m}$ -Pt UME (black) and  $100\mu\text{m}$ -Pt UME (red) respectively.

## 2.2 Localized electrografting with SECM: Study of the influence of the experimental parameters

Previous studies in our lab undertaken on the SEEP process have demonstrated that the optimized concentration of aryl diazonium salt in the electrolytic medium for starting the process is close to  $2 \cdot 10^{-3} \text{ mol}\cdot\text{dm}^{-3}$ . We thus took this data as a constant and we made the choice to study the influence of other parameters such as acrylic acid concentration, nature of the solvent (aqueous or organic), electrochemical conditions (chronoamperometry, chronopotentiometry, rate of scanning) on the performances (lateral resolution and thickness of the coating) of the localized grafting. We have also seen previously that localized grafting occurs only when the applied potential to the substrate is cathodic enough. But what means “cathodic enough”? Figure 10 shows the evolution of the potential experienced by the working electrode when an increasing current intensity is imposed to the substrate for the 25  $\mu\text{m}$ -Pt UME and the 100  $\mu\text{m}$ -Pt UME respectively at a normalized working distance equal to 0.6.

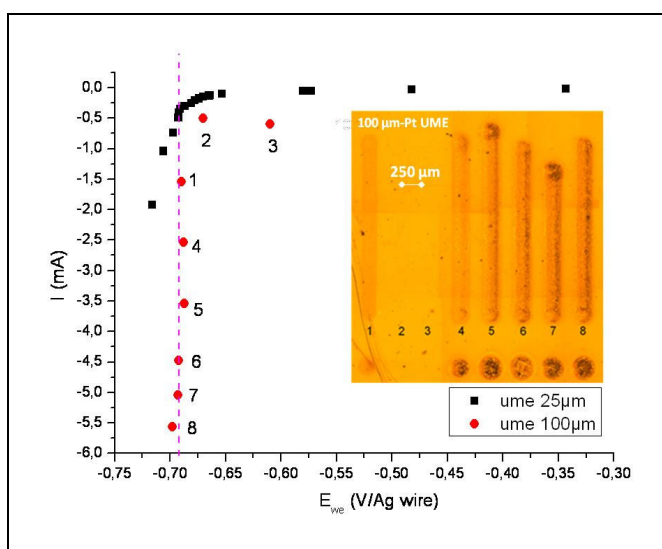


Figure 10: curves reconstructed from the recorded  $E_{we}$  during chronopotentiometry experiments with different imposed current values: 25 $\mu\text{m}$ -Pt UME (black), 100 $\mu\text{m}$ -Pt UME (red);  $d/a=0.6$ ,  $t=5s$ . Dashed line: start of the proton reduction regime  
Insert: optical microscopy images of the localized grafting as a function of the imposed current for the 100  $\mu\text{m}$ -Pt UME.

As shown by the insert of the figure 10, the localized grafting is detected only when the applied current is high enough in absolute value ( $> -0.5 \text{ mA}$ ). In these conditions, the potential experienced by the substrate corresponds to a cathodic potential able to induce the reduction of protons (dashed line on fig. 10). We observe that the size of the grafted pattern does not change with the intensity of the current. However, its thickness increases with the applied current and, for the highest current range, the homogeneity of the localized coating seems affected (fig. 11a). For  $d/a < 1$ , the thickness of the coating increases linearly with the current range (fig. 11b). The graphs in figure 11 show also that the thickness of the coating increases when the working distance decreases. We will come back to this point in the next paragraph.

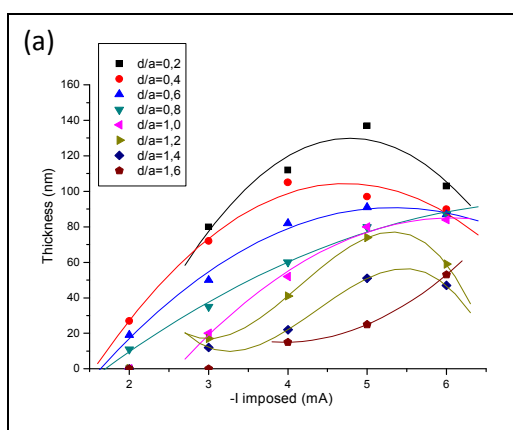


Figure 11a: Thickness of the dots as a function of the current range for different working distances ( $d/a$ ). 100  $\mu\text{m}$ -Pt UME, NBD  $2 \cdot 10^{-3} \text{ mol} \cdot \text{dm}^{-3}$ , AA  $0.7 \text{ mol} \cdot \text{dm}^{-3}$ ,  $\text{H}_2\text{SO}_4$   $0.25 \text{ mol} \cdot \text{dm}^{-3}$ , chronopotentiometry,  $t=5 \text{ s}$   
Scatter: experimental data, line: 2<sup>nd</sup> polynomial fit.

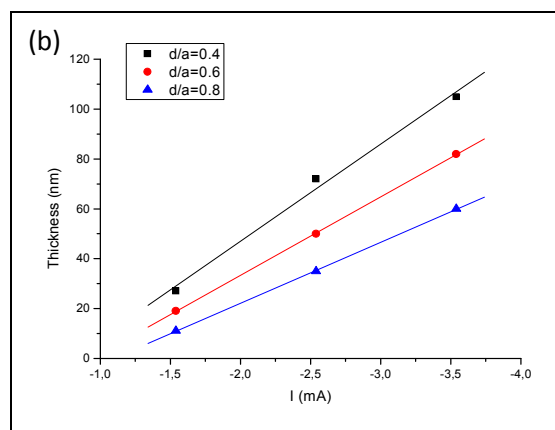


Figure 11b: Linear relationship between the thickness of the coating and the current range for  $d/a < 1$ ; 100  $\mu\text{m}$ -Pt UME, NBD  $2 \cdot 10^{-3} \text{ mol} \cdot \text{dm}^{-3}$ , AA  $0.7 \text{ mol} \cdot \text{dm}^{-3}$ ,  $\text{H}_2\text{SO}_4$   $0.25 \text{ mol} \cdot \text{dm}^{-3}$ , chronopotentiometry,  $t=5 \text{ s}$   
Scatter: experimental data, line: linear fit.

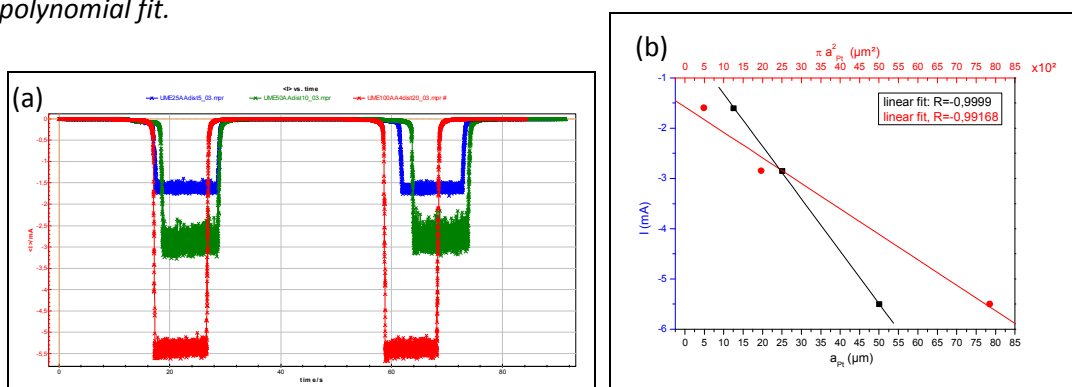


Figure 12: (a) comparison between the current intensities recorded during chronopotentiometry experiments ( $E_{we}=-0.7\text{V}/\text{Ag}$  wire) for 25  $\mu\text{m}$ -Pt (blue), 50  $\mu\text{m}$ -Pt (green) and 100  $\mu\text{m}$ -Pt (red) UMEs ; (b) Linear relationship between the recorded current and the radius of the microelectrode (black) or the area of the microelectrode (red).

Therefore, for the chronopotentiometry experiments, we choose a current in the range of -2 mA for which (i) the protons reduction regime is actually reached for all the considered UME, (ii) the grafted coating is homogeneous, and (iii) thick enough to be easily detected. We also point out that the average current flowing through the cell is directly proportional to the radius of the microelectrode and not to its area (fig. 12b). It is also interesting to note that when the reduction of the protons occurs on the substrate, the potential of the UME counter-electrode increases exponentially to very high values where electrolysis of water occurs (fig. 13) when the UME is placed close to the surface.

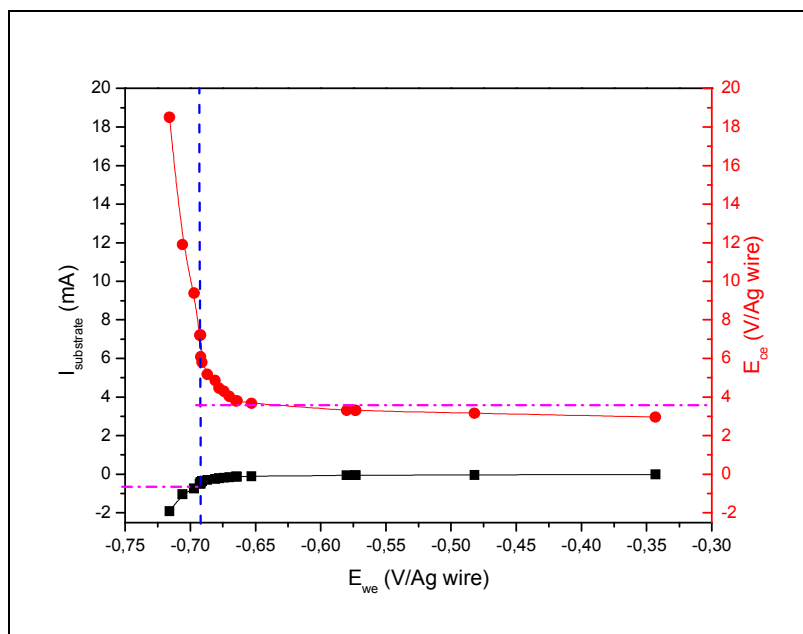


Figure 13: curves reconstructed from the recorded  $E_{we}$  and  $E_{ce}$  during chronopotentiometry experiments with different applied current values:  $25 \mu\text{m-Pt UME}$ ,  $d/a=0.6$ ,  $t=5 \text{ s}$ .  $\text{NBD } 2 \cdot 10^{-3} \text{ mol.dm}^{-3}$ ,  $\text{AA } 0.7 \text{ mol. dm}^{-3}$ ,  $\text{H}_2\text{SO}_4 \text{ } 0.25 \text{ mol.dm}^{-3}$ .

The crucial role played by the reduction of protons on the localization of the electrografting SEEP process can be evidenced by reproducing the same kind of experiments in aprotic organic solvent (dimethylformamide, DMF) with a non protic monomer (Butylmethacrylate, BuMA). Figure 14 shows an optical microscopy image of a typical spot pattern. Each spot shows inner circular centers and outer rings.

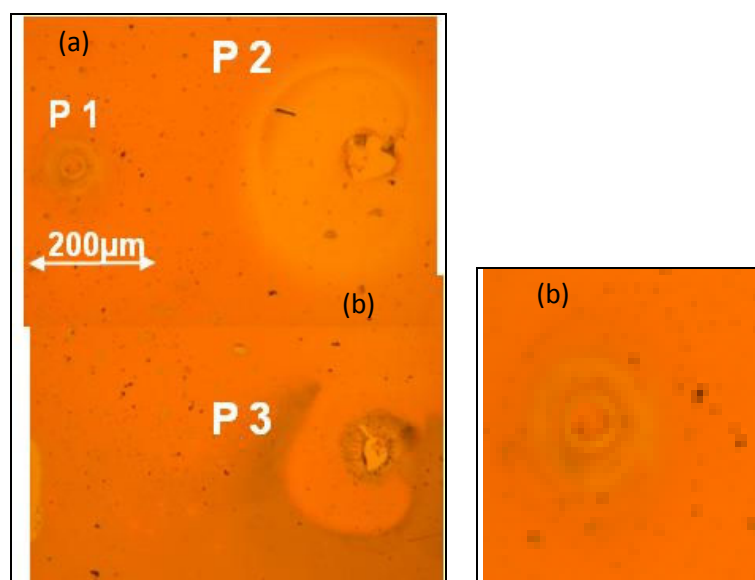


Figure 14: (a) optical microscopy image of dot pattern imprinted on gold substrate with a  $50\mu\text{m-Pt UME}$ , (b) zoom of the "Liesegang ring" like pattern.  $[\text{BuMA}]:0.7 \text{ mol. dm}^{-3}$ ,  $\text{DNB}:2 \cdot 10^{-3} \text{ mol.dm}^{-3}$ ,  $\text{Et}_4\text{NBF}_4: 0.2 \text{ mol.dm}^{-3}$ ,  $\text{DMF}$ ,  $d/a=0.8$ ,  $t=5\text{s}$ .

P1:  $E_{we} = -0.2V/Ag$  wire, P2:  $E_{we} = -0.8V/Ag$  wire, P3:  $E_{we} = -1.2V/Ag$  wire.

Since we used a  $50\ \mu\text{m}$ -Pt UME for patterning, the inner centers correspond to the surface area of the substrate directly below the platinum microelectrode, where the produced aryl radicals have the highest concentration close to the gold substrate because of the short diffusion distance. The outer rings were about  $100\text{--}300\ \mu\text{m}$  in diameter and presumably result from a concentration gradient of reactional intermediates. The obtained rings resemble “Liesegang rings”,<sup>[38]</sup> which are formed in reaction-diffusion systems. It must be also noted that in these experimental conditions, a non homogeneous passivation coating is formed on the entire substrate surface as detected by SECM imaging. All these results suggest strongly that in aprotic medium, life time of radical species is increased and thus diffusion processes control the lateral growth of the coating. Moreover, if we add protic species (diluted sulfuric acid) to DMF medium, a poor localization effect appears as detected by optical microscopy and SECM images (fig. 15). It seems thus obvious that the presence of protons in the electrolytic solution is a necessary condition for driving the localization effect. As a consequence of this observed behavior, all the following experiments will be then undertaken in aqueous solution.

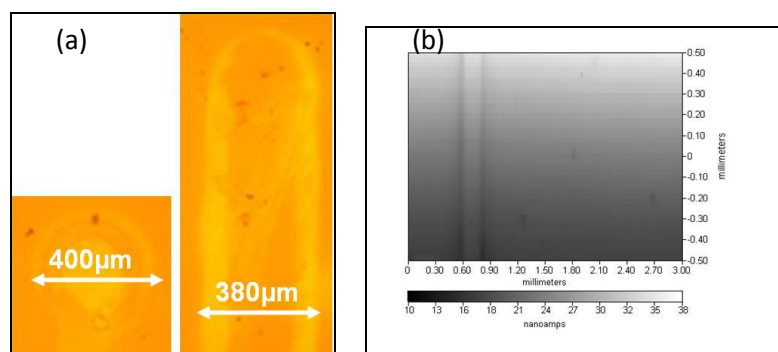


Figure 15 : (a) optical microscopy images of dot and line grafted on gold substrate with a  $100\ \mu\text{m}$ -Pt UME, (b) SECM imaging of the line pattern recorded with  $\text{Fe}^{2+}$  redox mediator (see annex for a detailed procedure).

[AA]:  $0.7\ \text{mol. dm}^{-3}$ , DNB:  $2 \cdot 10^{-3}\ \text{mol. dm}^{-3}$ ,  $\text{H}_2\text{SO}_4$ :  $0.25\ \text{mol. dm}^{-3}$ , DMF,  $d/a=0,4$ ,  $E_{we} = -0.8V/Ag$  wire; static mode:  $t=5\text{s}$ ; dynamic mode:  $v=10\ \mu\text{m/s}$ .

Since the size and the shape of the pattern formed determine the usefulness of this technique in micro-modification surface, various experiments were conducted to examine the factors that affect those parameters.

### 2.2.1: Influence of the acrylic acid concentration

First of all, we optimized the range of acrylic acid concentration in the electrolytic medium in view to obtain a well localized, defined and reproducible pattern on the substrate. We applied chronopotentiometric technique by setting the current range of the working electrode to  $-2\text{ mA}$ . As shown on figure 16, in those conditions, the potential experienced by the substrate is, whatever the acrylic acid concentration, more negative than  $-0.65\text{V}$  vs. Ag wire and thus susceptible to give localized grafting. It was found that a wide range of acrylic acid concentration ( $0.5\text{ mol.dm}^{-3} < [\text{AA}] < 7\text{ mol.dm}^{-3}$ ) can be used in view of well resolved localized electrografting (fig. 17 b, c, d, e). Outside this range, the pattern is blurred (fig. 17 a, f). Inside this range, the size of the pattern is roughly constant whatever the acid acrylic concentration (fig. 17 b, c, d, e). To ensure an easy and rapid characterization of the drawn pattern, most of the following experiments were carried out with acrylic acid concentration of  $2\text{ mol.dm}^{-3}$ .

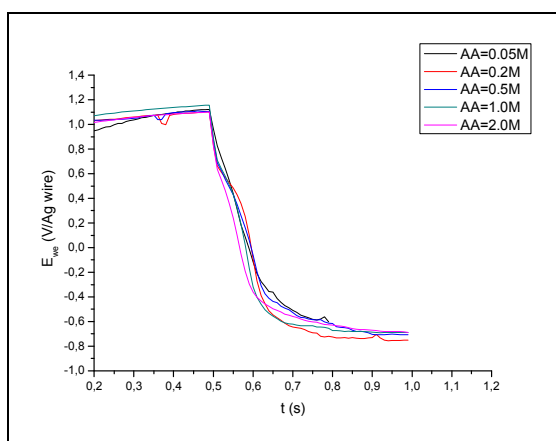


Figure 16: Chronopotentiometry recorded for different acrylic acid concentration.

$\text{NBD } 2 \cdot 10^{-3}\text{ mol.dm}^{-3}$ ,  $\text{H}_2\text{SO}_4\text{ } 0.25\text{ mol.dm}^{-3}$ ,  $[\text{AA}]$  see legend graph;  $I = -2\text{ mA}$ ,  $d/a = 0.4$ ,  $100\text{ }\mu\text{m-Pt UME}$ .

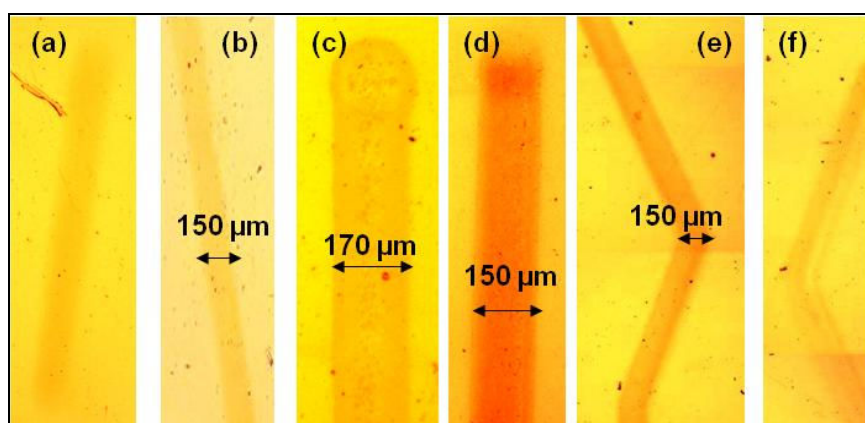


Figure 17: optical microscopy images of the localized electrografted patterns obtained with the  $100\text{ }\mu\text{m-Pt UME}$  in dynamic mode on the gold surface as a function of the acrylic acid concentration: (a)  $0.2\text{ M}$ , (b)  $0.5\text{ M}$ , (c)  $0.7\text{ M}$ , (d)  $2\text{ M}$ , (e)  $7\text{ M}$ , (f)  $8\text{ M}$ . ( $\text{NBD } 2 \cdot 10^{-3}\text{ mol.dm}^{-3}$ ,  $\text{H}_2\text{SO}_4\text{ } 0.25\text{ mol.dm}^{-3}$ ); coating obtained by chronopotentiometry ( $I = -2\text{ mA}$ ,  $d/a = 0.4$ ; scan rate =  $50\text{ }\mu\text{m/s}$ ).

### 2.2.2: Influence of electrolysis duration

An important factor in the size of the deposited feature is the time that the biased UME is held close to the surface. Chronopotentiometry technique (-2mA imposed to the substrate) was chosen to follow the growing of the polymer coating as a function of time. Experiments were carried out with the 25- $\mu\text{m}$  Pt UME in order to obtain localized grafting the size evolution of which can be easily followed by AFM analysis. A working distance equal to 10  $\mu\text{m}$  was maintained during all the experiment. After synthesis, samples were rinsed carefully before forthcoming analyses. AFM images were recorded in contact mode and gathered on figure 18.

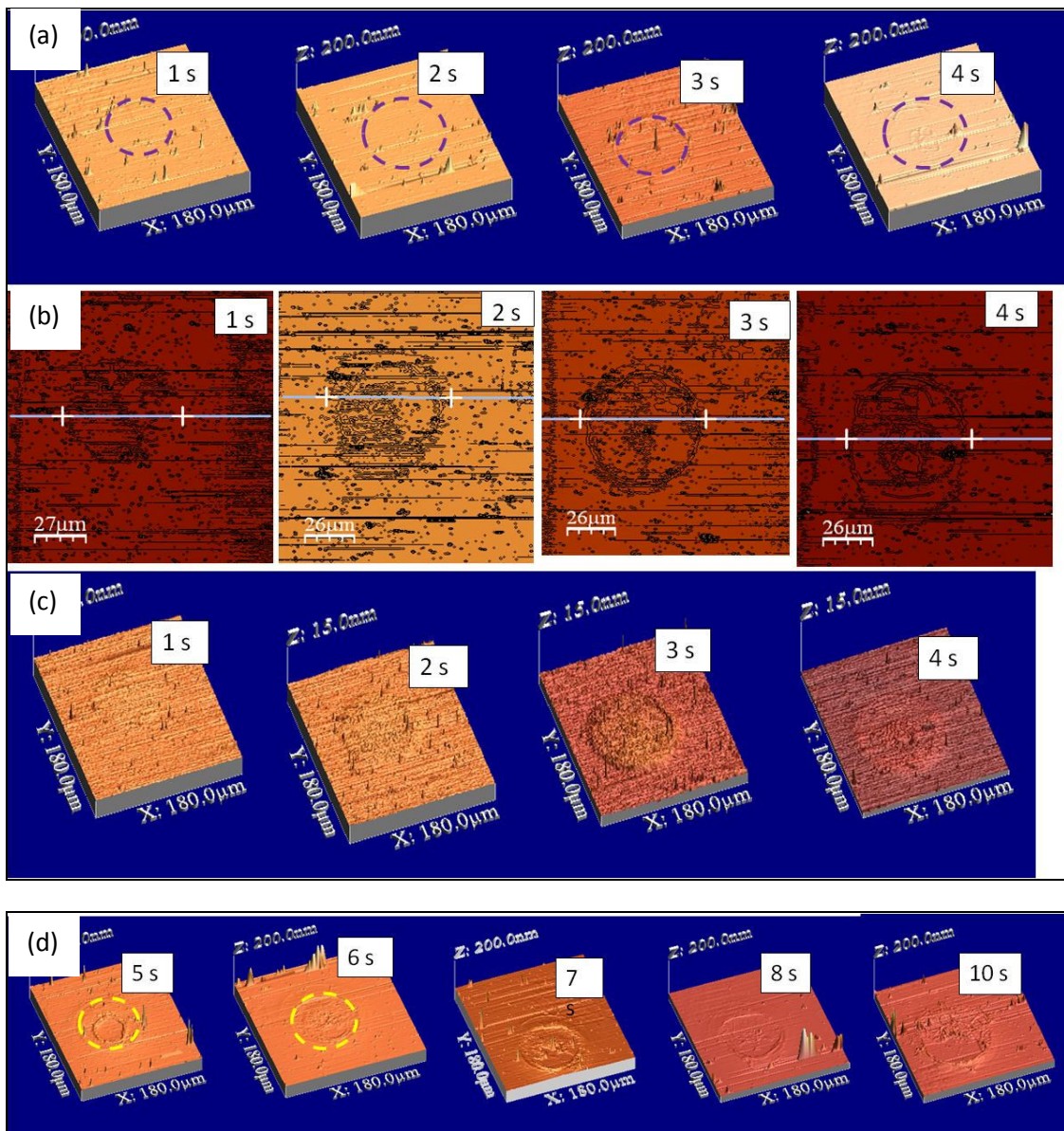


Figure 18: Evolution of the growth of the localized dot as a function of electrolysis time by AFM analysis in contact mode: (a) topographic images, (b) iso-counter plots, (c) AFM image in friction mode, (d) topographic images for  $t > 5\text{s}$ .  
[AA]:  $2.0 \text{ mol. dm}^{-3}$ , DNB:  $2 \cdot 10^{-3} \text{ mol. dm}^{-3}$ ,  $\text{H}_2\text{SO}_4$ :  $0.25 \text{ mol. dm}^{-3}$ ,  $I = -2 \text{ mA}$ , 25  $\mu\text{m}$ -Pt,  $d = 10 \mu\text{m}$ .

As we can observe on the AFM images (fig. 18), localized coating grows like disk from the center to the border. From the profile AFM images analysis (fig. 19), we can extract the thickness and the width of the coating.

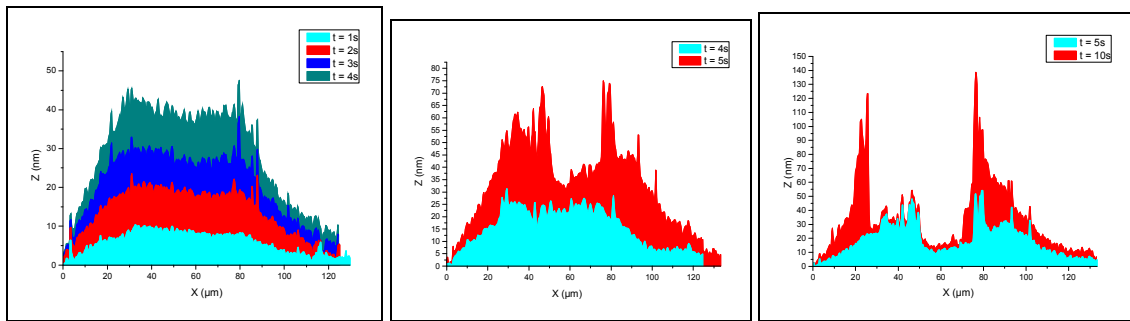


Fig. 19: AFM dots profiles as a function of time: (a) 1 - 4 s; (b) 4 -5 s, (c) 5 -10 s.  
 $[AA]: 2.0 \text{ mol. dm}^{-3}$ ,  $DNB: 2 \cdot 10^{-3} \text{ mol. dm}^{-3}$ ,  $H_2SO_4: 0.25 \text{ mol. dm}^{-3}$ ,  $I = -2 \text{ mA}$ ,  $25 \mu\text{m-Pt}$ ,  $d = 10 \mu\text{m}$ .

If we plot these data as a function of time, we observe clearly two different time regimes (fig. 20):

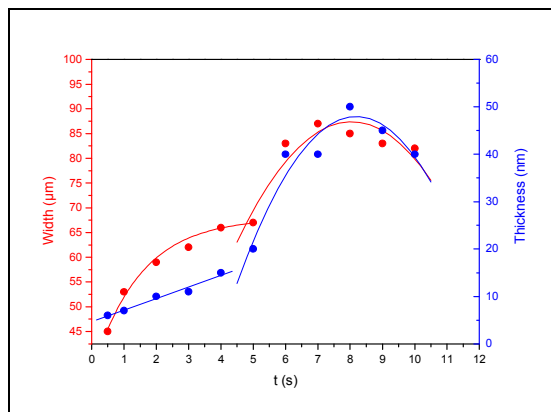


Figure 20: Evolution of the width (red) and the thickness (blue) of the dots pattern as a function of time; scatter: experimental data, line: fit data.  
 $25 \mu\text{m-Pt UME}$ ,  $d = 10 \mu\text{m}$ ,  $I = -2 \text{ mA}$ ,  
 $[AA]: 2.0 \text{ mol. dm}^{-3}$ ,  $DNB: 2 \cdot 10^{-3} \text{ mol. dm}^{-3}$ ,  
 $H_2SO_4: 0.25 \text{ mol. dm}^{-3}$ .

- (i) for  $t < 5 \text{ s}$ , the coating spreads regularly as a function of time until it reaches a certain radius value (around  $60 \mu\text{m}$ ). In the same time, its thickness increases linearly with time.
- (ii) for  $t \geq 5 \text{ s}$ , the disk pattern changes both in width and in thickness. Both parameters grow slowly following a second order polynomial fit. It must be noted that in the same time, cracks appear on the top of the coating, and crack amplitude increases with time (fig. 18d and 19b). This behavior can certainly be explained by two main reasons: (a) parasite reactions induced by the highly reactive and/or aggressive chemical environment under the UME (see chapter 4 for the mechanism description) able to ablate the growing film; (b) the high current imposed on a small area of surface, able to knock off the grafting as it happens for capacitors when their dielectric material breaks.

It must be noted that if we change the experimental conditions (for example, cathodic current or cathodic potential applied to the substrate), the general behavior of the dots pattern as a function of time is preserved but the time scale is shifted. In other words, cracks in the coating appear for shorter time for higher applied constraints (fig. 21). On the other hand, cracks occur after a longer time if the applied constraints are softer. We have also noted that applying pulsed constraints allow to reduce cracks defects. We will discuss the plausible origin of this fact in the 4<sup>th</sup> chapter devoted to the description of the mechanism.

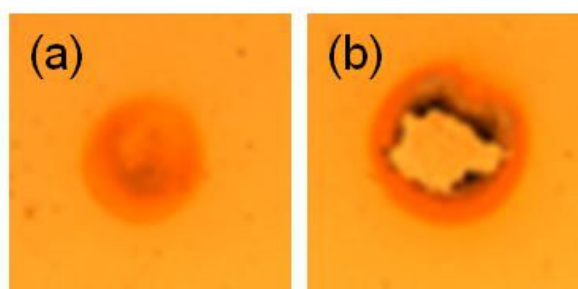


Figure 21: optical microscopy images of the localized electrografted dots obtained with the 100  $\mu\text{m}$ -Pt UME on the gold surface by chronoamperometry technique: (a)  $I_{\text{imposed}} = -2 \text{ mA}$ ,  $t = 3 \text{ s}$ ; (b)  $I_{\text{imposed}} = -5 \text{ mA}$ ,  $t = 3 \text{ s}$ .  
 $[AA]: 2.0 \text{ mol. dm}^{-3}$ ,  $DNB: 2 \cdot 10^{-3} \text{ mol. dm}^{-3}$ ,  $H_2SO_4: 0.25 \text{ mol. dm}^{-3}$ ,  $d/a = 0.4$ .

So as, in most of the following experiments, the duration of the electrolysis was chosen short enough to prevent the formation of the cracks.

### 2.2.3: Influence of the working distance and the scan rate

Let's now examine factors that affect the size and shape of the patterns. In order to study the influence of the working distance and the scan rate of the tip, we applied the chronopotentiometric method ( $I = -2 \text{ mA}$ ,  $t = 5 \text{ s}$ ) both in the static and dynamic modes. For a given UME, we carried out, on the same sample, a set of experiments including, at a fixed working distance, dots and lines drawn for different scan rates. We repeated this set of experiments for different working distances. We applied this protocol for the three studied UMEs: 25  $\mu\text{m}$ -Pt, 50  $\mu\text{m}$ -Pt, and 100  $\mu\text{m}$ -Pt. On figure 22, we report an example of experiments realized with the 25  $\mu\text{m}$ -Pt UME, for different working distances and different scan rates.

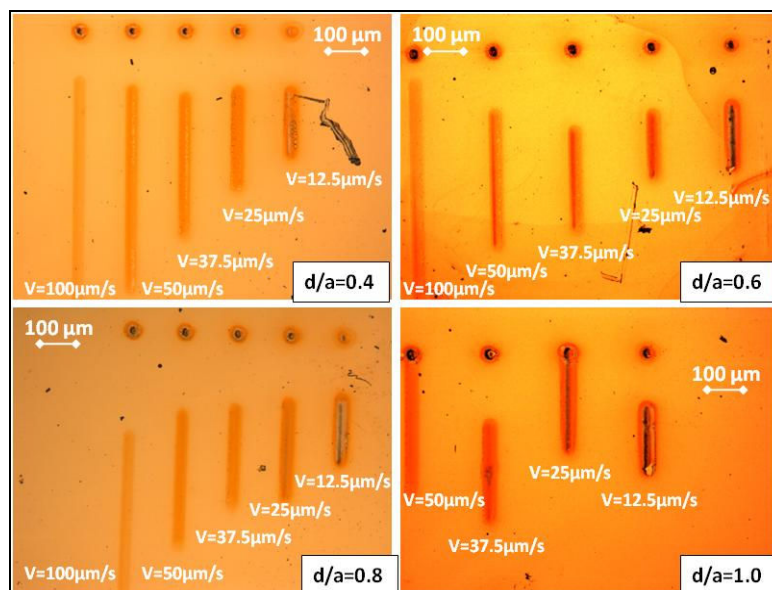


Figure 22: example of set of experiments with a 25  $\mu\text{m}$ -Pt UME on gold substrate [AA]:2.0 mol.  $\text{dm}^{-3}$ , DNB:2  $10^{-3}$  mol. $\text{dm}^{-3}$ ,  $\text{H}_2\text{SO}_4$ :0.25 mol. $\text{dm}^{-3}$ , chronopotentiometry:  $I=-2$  mA,  $t=5$  s for dots and  $t=30$ s for lines.

### 2.2.3.1: Influence of the working distance in static mode

The shape of the dots pattern is poorly dependent on the working distance. More precisely, the average width of the dots, is almost constant for a given UME whatever the working distance in the studied range ( $0.2 < d/a < 2$ ) (table 2).

Radius of the UME (a, $\mu\text{m}$ )	Width of the dot (L, $\mu\text{m}$ )	L/2a
12.5	60 $\pm$ 10	2.4 $\pm$ 0.4
25	100 $\pm$ 10	2.0 $\pm$ 0.2
50	150 $\pm$ 10	1.5 $\pm$ 0.1

Table 2: average width of the dots pattern as a function of the radius of the UME.

A linear dependence between the pattern diameter and the distance would be anticipated as originally discussed by Bard et al.<sup>[37]</sup>. Indeed, in a pure feedback mode with a redox mediator present in solution, a conical concentration profile is expected between the UME and the surface. This profile can be interpreted in terms of the shape of the UME and the diffusion field; i.e., the relatively large insulator around the electrodes provides a cylindrical volume between the UME and the surface. Inside this cylindrical volume a conical concentration profile of the electroactive species is established by diffusion. The truncated cone volume is expected to reach a steady state in which the fluxes of redox species towards and from the UME are equal. The diameter of the bigger base of the truncated cone (which is on the surface) is

proportional to the distance between the surface and the UME. In our case, it is obviously not the case meaning that our process is not mainly governed by the diffusion profile.

However, experiments performed with different electrodes, ranging from 25-100  $\mu\text{m}$  diameter, result in dots patterns which dimensions are proportional to the electrode diameter (fig. 23). Thus, smaller electrodes yield smaller dots. Or in other words, bigger dots patterns are obtained when a bigger electrode is applied for the same time and the same electrode-surface distance. If electrodes down to sub-micronic diameter could be fabricated, much smaller patterns should, in principle, be produced.

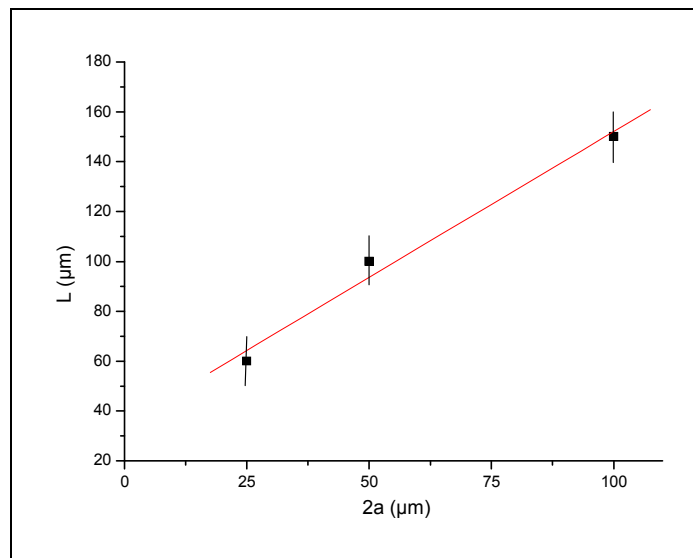
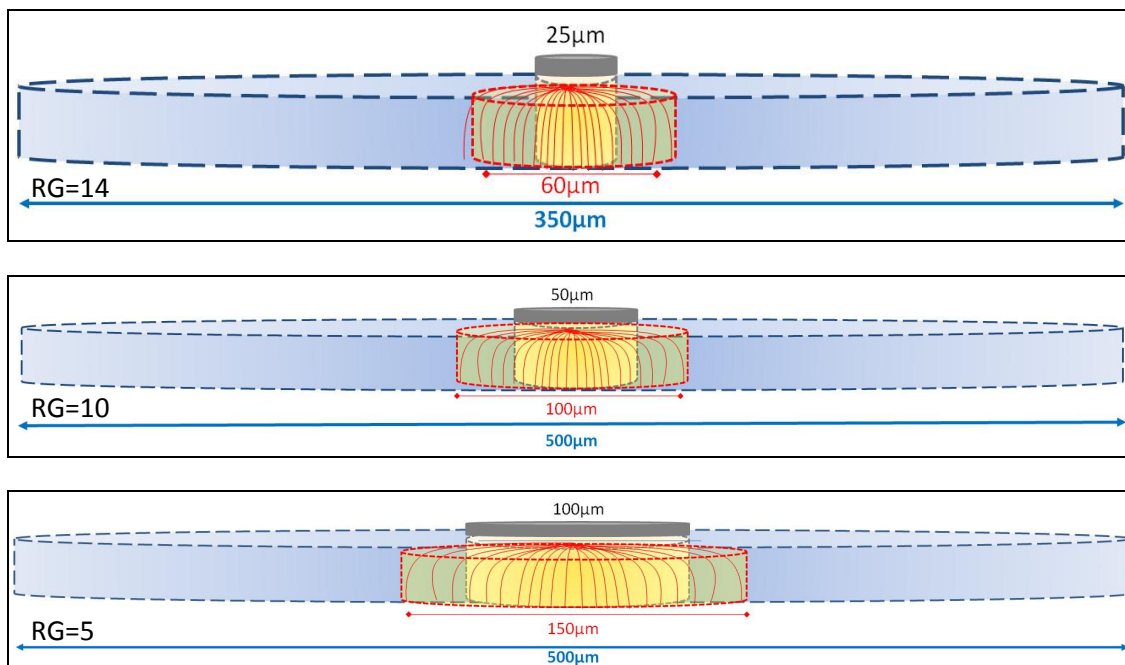


Figure 23: average normalized width of the dots as a function of the diameter of the UME.

The reactional domain seems to be delimited by two encased cylinders:

- (i) an inner one (red line on scheme 2) whose diameter is mainly controlled by the spatial extension of the current lines between the working and the counter electrodes. These current lines respect the same distribution as those of the electric field that would exist between the two electrodes in a perfect dielectric medium and through which the electroactive species are created and/or transported. A schematic view is proposed on scheme 2. The poor dependence of the width of the dots pattern as a function of the working distance may certainly be explained by the predominant influence of these current lines compared to the diffusion field. All the results suggest that the current lines "sprinkle" an activated surface on the substrate quasi equivalent whatever the considered working distance ( $0.2 < d/a < 2$ ).

- (ii) an outer one (blue dashed line on scheme 2) whose diameter depends on insulating materials and which can be view as a confined container for the species created inside or as a wall for outside species that could diffuse inside.



Scheme 2: schematic representation of the electric field map for the three considered UMEs 25- $\mu\text{m}$ , 50- $\mu\text{m}$ , 100- $\mu\text{m}$  with their own geometrical characteristics, respectively.

We propose to roughly estimate the spatial extension length of the active species from the expression:  $(L-2a)/2$ , where  $L$  is the measured width of the dot and  $a$ , the radius of the microelectrode. The obtained values are reported on table 3 and figure 24, for two different values of the AA concentration.

Radius of the UME ( $a$ , $\mu\text{m}$ )	Width of the dot ( $L$ , $\mu\text{m}$ )	Spatial extension length ( $\mu\text{m}$ )	Width of the dot ( $L$ , $\mu\text{m}$ )	Spatial extension length ( $\mu\text{m}$ )
	$[\text{AA}]=0.7$ $\text{mol}\cdot\text{dm}^{-3}$	$[L-2a]/2$	$[\text{AA}]=2$ $\text{mol}\cdot\text{dm}^{-3}$	$[L-2a]/2$
2.5	$13\pm 5$	$4\pm 2.5$		
5.0	$62\pm 10$	$26\pm 5$		
12.5	$103\pm 10$	$39\pm 5$	$60\pm 10$	$17.5\pm 5$
25			$100\pm 10$	$25\pm 5$
50	$187\pm 10$	$43\pm 5$	$150\pm 10$	$25\pm 5$

Table 3: estimated length of the spatial extension of the electroactive species for dots obtained with two acrylic acid concentration: chronopotentiometry ( $I=-2\text{mA}$ ),  $t=5\text{s}$ .

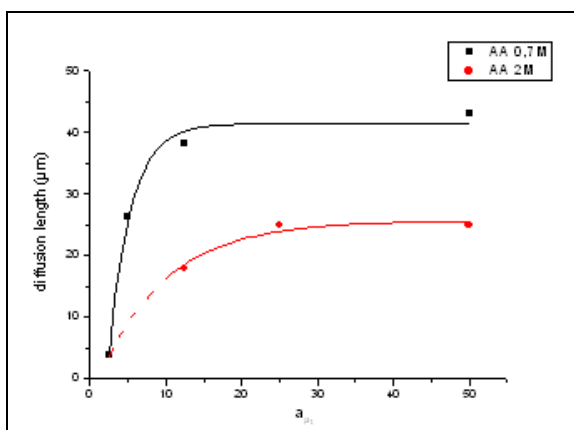


Figure 24: Spatial extension length of the electroactive species as a function of the radius of the microelectrode; scatter: experimental data, line: exponential decay fit [AA] = 0.7 mol.  $\text{dm}^{-3}$  (black), [AA] = 2 mol.  $\text{dm}^{-3}$  (red).

We observe that increasing the acrylic acid concentration allows to slightly reduce the width of the pattern. This suggests that acrylic acid monomer can be considered as a scavenger for the aryl radicals. The higher the acrylic acid concentration, the lower the lifetime of the aryl radicals. At same time, a higher concentration of monomers slightly increases the resistivity in the electrochemical solution involving most probably a tightening of the current lines under the microelectrode.

As already mentioned above, the thickness of the grafted pattern is sensitive to the working distance. This is clearly evidenced on figure 25 for 100  $\mu\text{m}$ -Pt UME. A decreasing linear relationship is observed for  $d/a < 1$ , whatever the applied current range. For higher working distances, the thickness of the coating tends to a constant value.

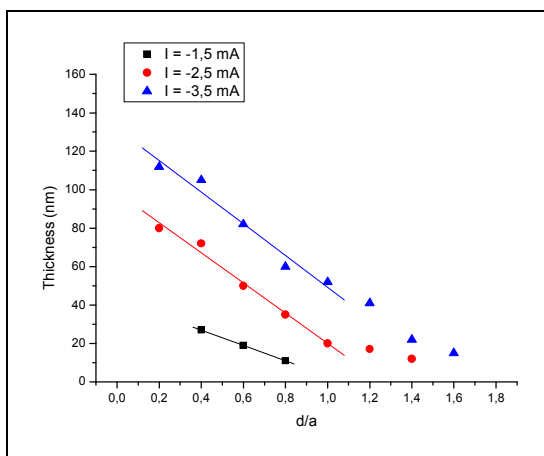


Figure 25: Thickness of the dots as a function of the normalized working distance for different current range. Scatter: experimental data, line: linear fit. [AA]: 0.7 mol.  $\text{dm}^{-3}$ , DNB:  $2 \cdot 10^{-3}$  mol. $\text{dm}^{-3}$ ,  $\text{H}_2\text{SO}_4$ : 0.25 mol. $\text{dm}^{-3}$ , 100  $\mu\text{m}$ -Pt UME, chronopotentiometry,  $t = 5$  s.

More interesting is the graph obtained by reporting the thickness of the coating as a function of the absolute value of the working distance, for all studied UMEs. We observe then that all the data follow roughly an exponential decay for  $d > 10 \mu\text{m}$  (fig. 26). For the very short working distance ( $d = 5 \mu\text{m}$ ), the low value of the coating thickness is probably due to the steric effect of the microelectrode (high RG value, see graph) which partly prevents the entering diffusion of the active species. When the working distance increases, diffusion of active molecules is favored but at the same time, as the reactional volume increases, the electrogenerated species in the gap substrate / UME are more diluted. We can thus expect that the yield of the reactions decreases. From the graph of figure 26, the best compromise seems to be found for a working distance around  $10\text{-}20 \mu\text{m}$ . For working distance higher than  $30\text{-}40 \mu\text{m}$ , the thickness of the coating is quasi stable and independent on the distance.

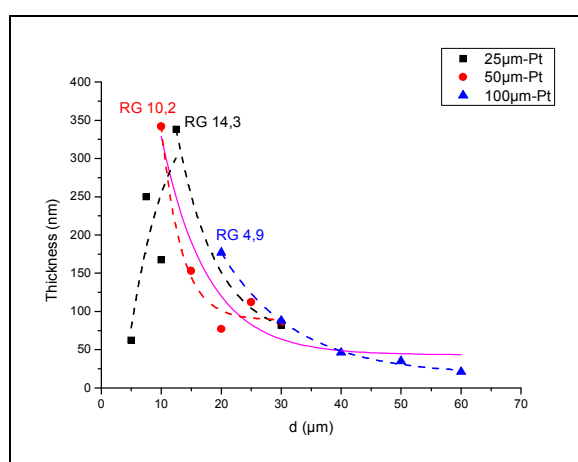


Figure 26: Thickness of the localized dots as a function of the absolute working distance. Scatter: experimental data, dash lines: exponential decay fit for each UME, solid line: exponential decay fit for all the UME for  $d > 10 \mu\text{m}$ .  
 $[AA]: 2.0 \text{ mol. dm}^{-3}$ ,  $DNB: 2 \cdot 10^{-3} \text{ mol. dm}^{-3}$ ,  $H_2SO_4: 0.25 \text{ mol. dm}^{-3}$ ,  $I = -2 \text{ mA}$ ,  $t = 5 \text{ s}$ .

### 2.2.3.2: Influence of the scan rate

Previous data concerned the static mode where the UME is used like a mold so that the electrode shape is reproduced on surface. In this configuration, the processing experimental parameters are only the intensity of the current and the time of electrolysis. However, if we want to lithograph a micro pattern on a substrate, it is necessary to work in the dynamic mode. A new factor has to be taken into account: the scan rate. Indeed, the electrode displacement introduces a convective effect which should influence the width and the thickness of the lines.

For the three tested UMEs, the width follows an exponential decay as a function of the scan rate as shown in figure 27a. The same behavior is observed whatever the working distance in the range of  $d$  where the localization is usually observed (fig. 27b). This

phenomenon is probably related to the flux convection profile of the solution in connection with the rate at which the probe is moved.<sup>[39]</sup> The dynamic mode allows thus a noticeable reduction in the dimensions of the grafted pattern. We can note that, for a given working distance, the minimal width is achieved when the ratio scan rate / tip radius is equal to 2 and does not change anymore for higher speed. On the other hand, for a given scan rate, the width decreases linearly with the working distance (fig. 27c).

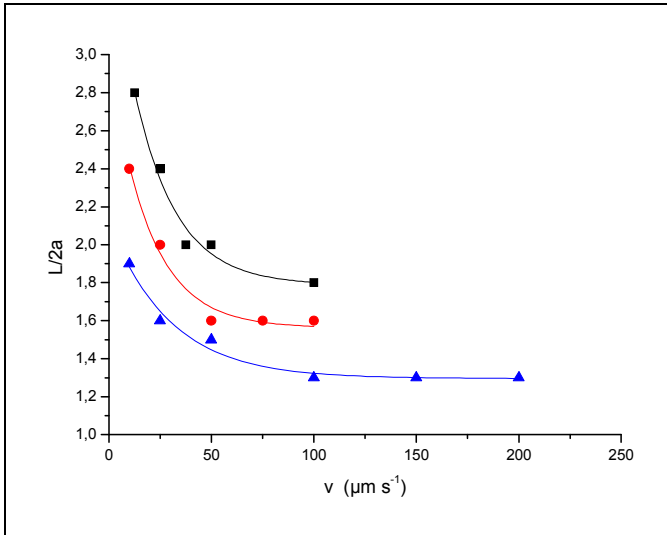
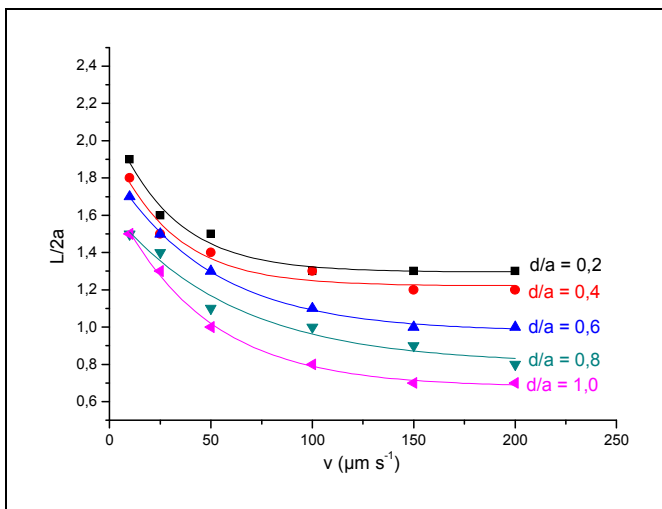


Figure 27b: Width of the line ( $L/2a$ ) as a function of the scan rate for different working distances (see graph); scatter: experimental data; line: first order exponential decay fit.  $[AA]: 2.0 \text{ mol. dm}^{-3}$ ,  $DNB: 2 \cdot 10^{-3} \text{ mol. dm}^{-3}$ ,  $H_2SO_4: 0.25 \text{ mol. dm}^{-3}$ ,  $I = -2 \text{ mA}$ ,  $100\text{-}\mu\text{m Pt UME}$ .



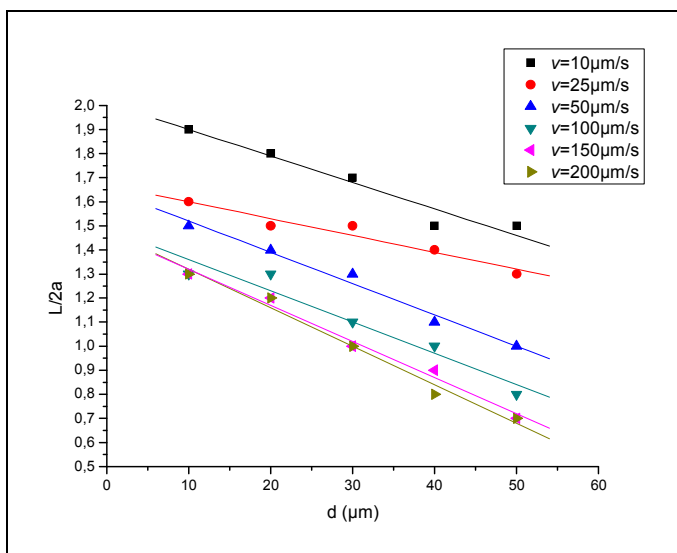


Figure 27c: Width of the line ( $L/2a$ ) as a function of the working distance for different scan rates (see graph); scatter: experimental data; line: linear fit.  $[AA]: 2.0 \text{ mol. dm}^{-3}$ ,  $DNB: 2 \cdot 10^{-3} \text{ mol. dm}^{-3}$ ,  $H_2SO_4: 0.25 \text{ mol. dm}^{-3}$ ,  $I = -2 \text{ mA}$ ,  $100\text{-}\mu\text{m Pt UME}$ .

The thickness of the coating as a function of the scan rate can be fitted with an exponential decay fit for all the considered UMEs (fig. 28) while, for a given working distance, the thickness decreases with the scan rate (fig. 29).

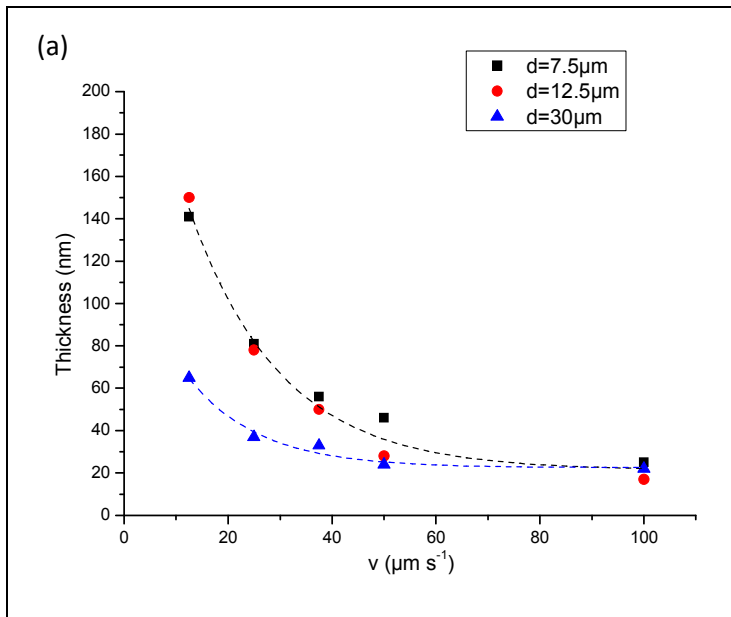
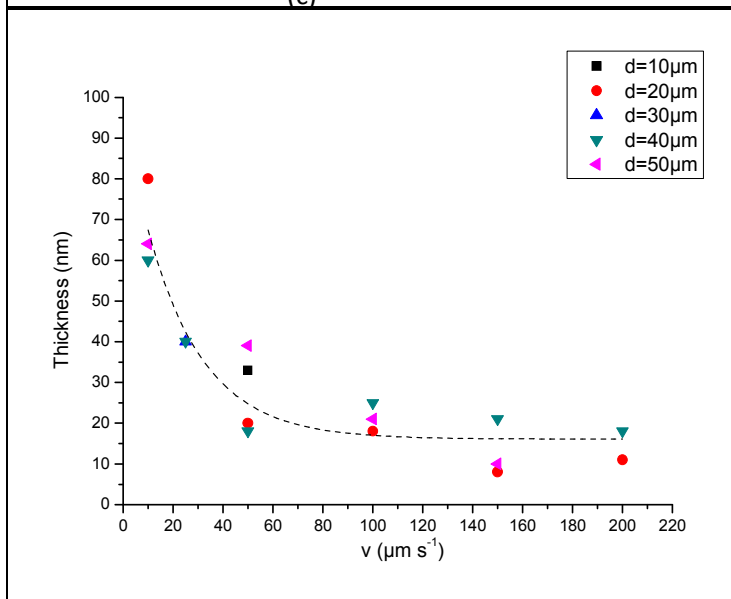
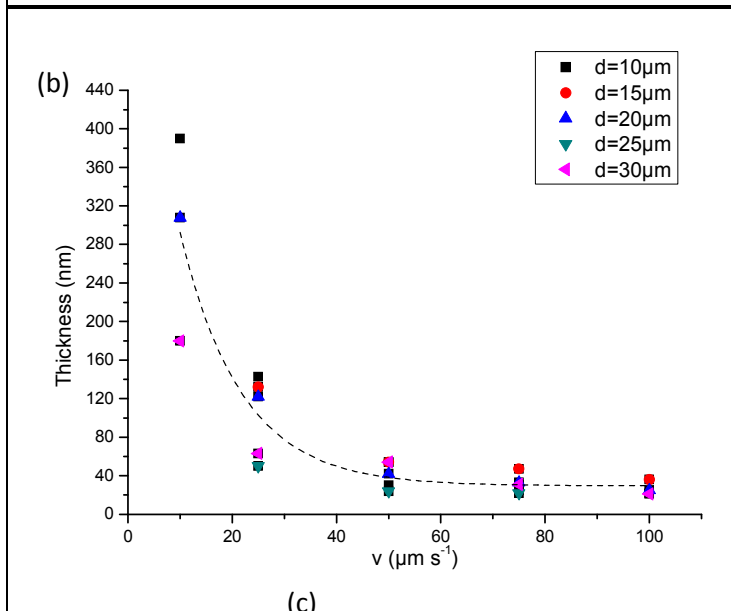


Figure 28: Thickness of the coating as a function of the scan rate for different working distance (see graph): (a) 25- $\mu\text{m}$  Pt; (b) 50- $\mu\text{m}$  Pt, (c) 100- $\mu\text{m}$  Pt. scatter: experimental data; line; first order exponential decay fit. [AA]:2.0 mol.  $\text{dm}^{-3}$ , DNB:2  $10^{-3}$  mol. $\text{dm}^{-3}$ ,  $\text{H}_2\text{SO}_4$ :0.25 mol. $\text{dm}^{-3}$ ,  $I=-2$  mA



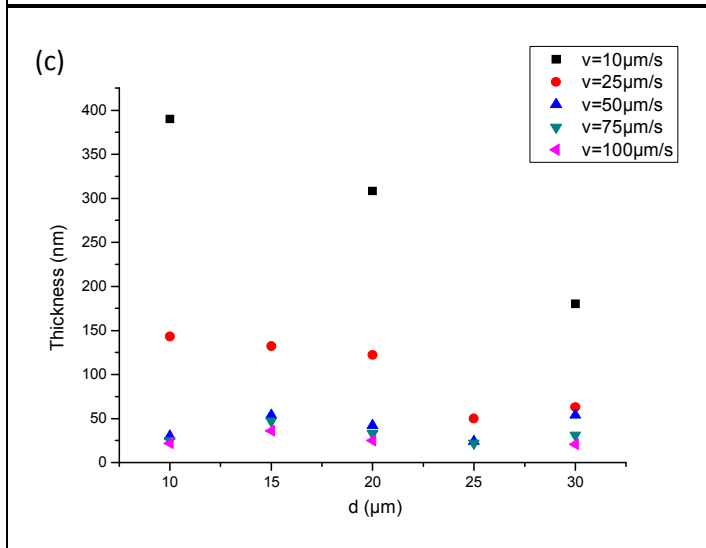
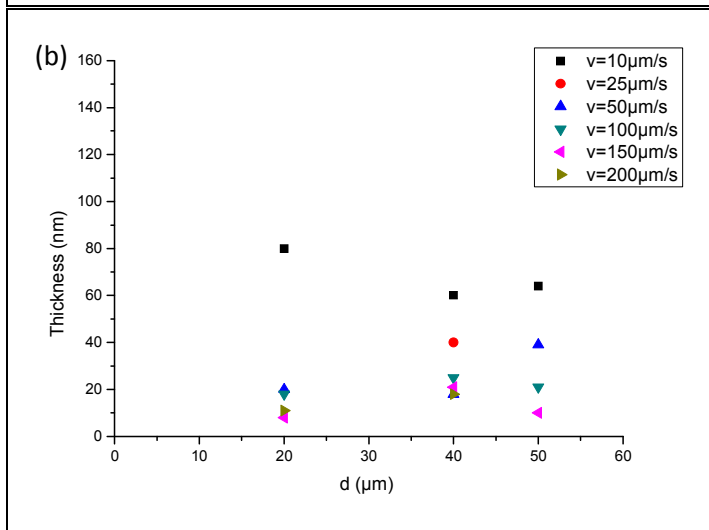
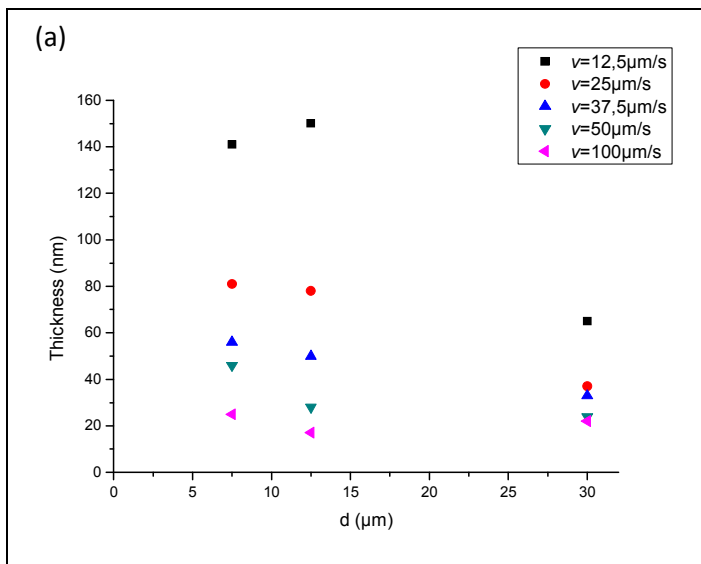


Figure 29: Thickness of the coating as a function of the working distance for different scan rate (see graph): (a) 25- $\mu\text{m}$  Pt; (b) 50- $\mu\text{m}$  Pt, (c) 100- $\mu\text{m}$  Pt. [AA]:2.0 mol.  $\text{dm}^{-3}$ , DNB:2  $10^{-3}$  mol. $\text{dm}^{-3}$ ,  $\text{H}_2\text{SO}_4$ :0.25 mol. $\text{dm}^{-3}$ ,  $I=-2$  mA

From these graphs, we observe that (see table 4):

- (i) as expected, the characteristics of the coatings tend to those of the static mode when the tip is moved very slowly.
- (ii) the width and the thickness of the coating depend on the time spent over one point. Shorter time (high speed) leads to narrower and thinner patterns.
- (iii) the influence of the working distance on the thickness of the coating is only noticeable for the slowest displacement (fig. 29). When the ratio scan rate / tip radius exceeds 2, the thickness of the coating remains more or less constant whatever the working distance and its value is around 20-30 nm whatever the tip.

<b>UME 25-<math>\mu\text{m}</math> Pt</b>				
<b><math>v</math> (<math>\mu\text{m s}^{-1}</math>)</b>	0	12.5	25	50
<b><math>d</math> (<math>\mu\text{m}</math>)</b>	10	10	10	10
<b><math>d/a</math></b>	0.8	0.8	0.8	0.8
<b><math>v/a</math></b>	-	1	2	4
<b><math>L/2a</math></b>	$2.4 \pm 0.2$	$2.4 \pm 0.2$	$2.4 \pm 0.2$	$2.0 \pm 0.2$
<b>Thickness (nm)</b>	$167 \pm 20$	$142 \pm 20$	$80 \pm 10$	$37 \pm 8$
<b>UME 50-<math>\mu\text{m}</math> Pt</b>				
<b><math>v</math> (<math>\mu\text{m s}^{-1}</math>)</b>	0	10	50	100
<b><math>d</math> (<math>\mu\text{m}</math>)</b>	10	10	10	10
<b><math>d/a</math></b>	0.4	0.4	0.4	0.4
<b><math>v/a</math></b>	-	0.4	2	4
<b><math>L/2a</math></b>	$2.0 \pm 0.2$	$2.1 \pm 0.2$	$1.8 \pm 0.2$	$1.6 \pm 0.2$
<b>Thickness (nm)</b>	$340 \pm 20$	$390 \pm 20$	$30 \pm 8$	$22 \pm 8$
<b>UME 100-<math>\mu\text{m}</math> Pt</b>				
<b><math>v</math> (<math>\mu\text{m s}^{-1}</math>)</b>	0	10	100	200
<b><math>d</math> (<math>\mu\text{m}</math>)</b>	20	20	20	20
<b><math>d/a</math></b>	0.4	0.4	0.4	0.4

<b>v/a</b>	-	0.2	2	4
<b>L/2a</b>	1.5±0.3	1.8±0.2	1.3±0.2	1.2±0.2
<b>Thickness (nm)</b>	88±10	80±10	18±8	11±8

Table 4: Characteristics of the localized coating obtained in the static mode ( $v=0$ ) compared to the dynamic mode for the three tested UMEs.

[AA]:2.0 mol. dm<sup>-3</sup>, DNB: 2 10<sup>-3</sup> mol.dm<sup>-3</sup>, H<sub>2</sub>SO<sub>4</sub>:0.25 mol.dm<sup>-3</sup>, I=-2 mA.

It must be highlighted that working in dynamic mode allows grafting a more homogeneous coating than in static mode. This phenomenon is probably to relate to the relative predominance of the different modes of transportation of the reactive species, i.e. migration diffusion, convection, into and from the reactive container, respectively. In other words, the displacement of the electrochemical reactive species is synchronized with the electrode displacement improving so the localization in term of homogeneity and selectivity.

Working in dynamic mode leads to reduce not only the width but also the thickness of the coating. So a compromise has to be found as a function of the wanted applications. If we need a thick, homogeneous localized coating, it will be preferable to work at slow scan rate while we will privilege the higher scan rate for obtaining thin homogenous grafting.

#### 2.2.4: Influence of RG parameter

The last parameter that we have not yet taken into account is the *RG* factor (glass'radius / electrode radius). In order to study its influence on the characteristics of the localized pattern, 50- $\mu$ m Pt UMEs with two very different RG values (3 and 15 respectively) were prepared and characterized as usually (fig. 30). Localized experiments were performed in static mode by chronopotentiometry.

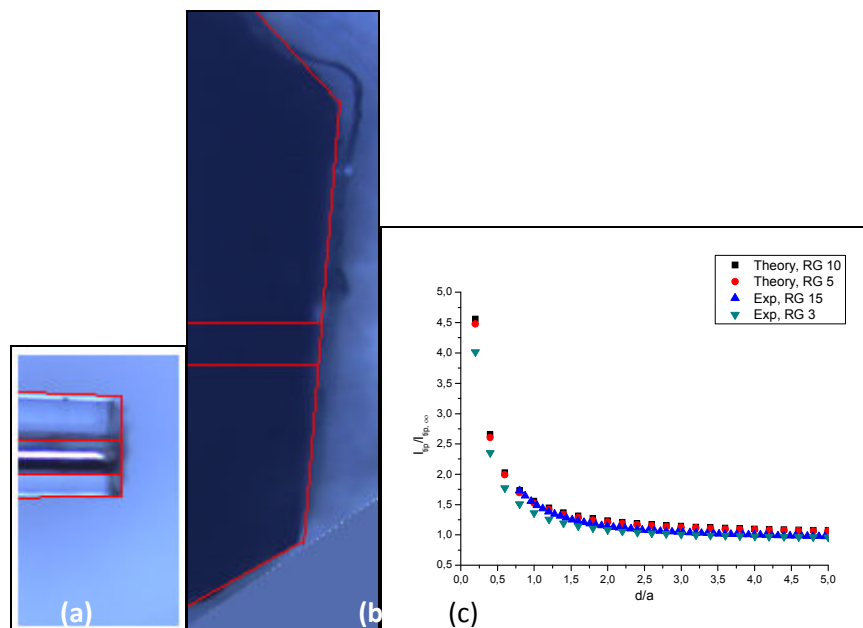


Figure 30: Optical images of the 50- $\mu\text{m}$  Pt UMES (a): RG=3.2, (b) RG=15; (c) Comparison between theoretical and experimental approach curves for different RG values in positive feedback mode.

Resulting plots were analyzed by profilometry to determine width and thickness. Results are reported in the following graphs (fig. 31). Both electrodes present a common general behavior. However, as we can see on the fig. 31a, a large RG allows to graft narrower patterns for the same working distance. A smaller insulating sheath will cause a larger diffusion range of the reactive species created at the UME. In other words, the insulator limits the spherical diffusion of the electroactive species and consequently leads to the formation of smaller patterns. In the same way, the thickness decreases with the working distance. If reducing the ratio insulator-to-electrode radius leads to the formation of bigger dots, it leads also to the grafting of a thinner coating when the working distance is very small ( $d/a \leq 0.4$ ). We can assume that the entering diffusion of the active species is partly prevented by the steric effect of the microelectrode.

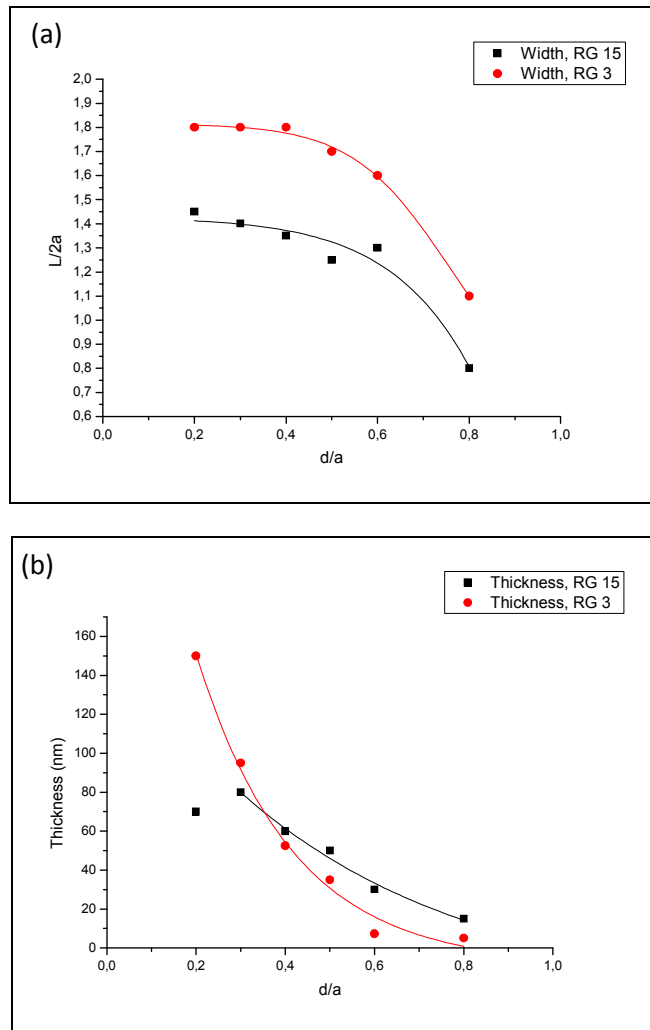


Figure 31: Width (a) and thickness (b) of the coating as a function of the working distance for two RG values: black: 50- $\mu\text{m}$  Pt RG=15, red: 50- $\mu\text{m}$  Pt RG=3. Scatter: experimental data, line: fitted data  
 $[\text{AA}]: 2.0 \text{ mol. dm}^{-3}$ ,  $\text{DNB}: 2 \cdot 10^{-3} \text{ mol. dm}^{-3}$ ,  $\text{H}_2\text{SO}_4: 0.25 \text{ mol. dm}^{-3}$ ,  $I = -0.5 \text{ mA}$ ,  $t = 5 \text{ s}$

### 3. Localized electrografting of the diazonium salts

As mentioned in the previous chapter, first attempts to localize the grafting of the polyphenylene film resulting from the reduction of the diazonium salt have failed.

Let's recall the experimental conditions used for these preliminary experiments:

- $\mu\text{m-Pt UME}$  at a fixed tip-substrate distance ( $d/a < 1$ )
- NBD  $5 \cdot 10^{-3} \text{ mol.dm}^{-3}$
- TEAP  $0,25 \text{ mol.dm}^{-3}$
- Solvent (DMF)
- cyclic voltammetry  $0\text{V} \rightarrow -0,4\text{V/Ag wire}$
- scan rate  $20 \text{ mV s}^{-1}$

Taken advantage of the conclusions that could be drawn from the experiments described in the former pages, we can point out at least three main reasons for the unsuccessful localized electrografting in that case:

- (i) The absence of water prevented its oxidation at the counter-electrode and thus the generation of protons in the electrolytic medium.
- (ii) The applied potential was not cathodic enough to induce the reduction of residual protons eventually present in the organic solution. As seen above, the reduction of the protons plays a crucial role in the localization effect.
- (iii) The ratio migration/diffusion was likely to be unsuited, which has a detrimental effect on the transportation of the reactive species. Indeed, in the presence of TEAP as supporting electrolytic in the solution, the migration effect is mainly supported by the ions of the electrolyte. However, those ions (tetraethylammonium, and perchlorate ions respectively) are not electroactive and do not play any role in the possible formation of an electrochemical loop (as collection on the substrate, and generation at the microelectrode).

New attempts of localization of the reduction of the diazonium salt were then undertaken in the following experimental conditions:

- NBD:  $2 \cdot 10^{-3} \text{ mol.dm}^{-3}$ ,
- $\text{H}_2\text{SO}_4$   $0.25 \text{ mol.dm}^{-3}$  (no supplementary supporting electrolyte)
- $I = -2\text{mA}$  (under this condition  $E_{\text{WE}}$  is more cathodic than  $-0.6\text{V}$  vs. Ag wire and  $E_{\text{CE}}$  is higher than  $10 \text{ V}$  vs. Ag wire)
- static ( $t = 5\text{s}$ ) or dynamic modes ( $v = 50 \mu\text{m.s}^{-1}$ ) were used.

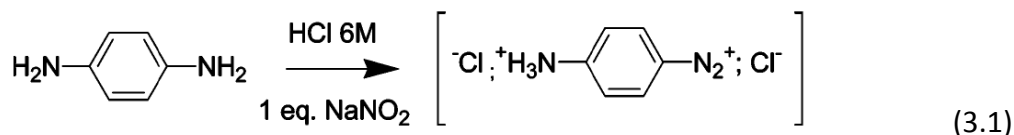
Under those experimental conditions, successful localization effect was observed (fig. 32) confirming the above assumptions.



Figure 32: Optical microscopy image of the localized electrografted PNP initiated by the electroreduction of NBD ( $2 \cdot 10^{-3} \text{ mol.dm}^{-3}$ ),  $\text{H}_2\text{SO}_4$   $0.25 \text{ mol.dm}^{-3}$ ;  $50\mu\text{m-Pt UME}$ ,  $d = 20 \mu\text{m}$ ,  $I = -2\text{mA}$ , lines obtained at a scan rate of  $50 \mu\text{m s}^{-1}$ , dots:  $t = 5 \text{ s}$ .

The characteristics of the localized electrografted coating observed in those cases are consistent to the expected ones:  $L/2a = 2.4$  for the static mode and close to 2 in dynamic mode. The thickness is of the order of 100nm. We can moreover remark that in static mode more particularly, the dot pattern exhibits a “queue” which can certainly be related to the gas evolution direction which appears at the UME electrode. This effect disappears when moving the UME and is not present when experiments were carried out in the presence of the vinylic monomer. We will describe in more details in the next chapter, the electrochemical reactions involve in the localization process.

It is noteworthy that the localized process was also successfully applied to a mixture of phenylene diamine and  $\text{NaNO}_2$ . This mixture generates the corresponding diazonium salt, following the reaction (3.1), and the diazonium salt produced this way can be then localized in a usual way (fig. 33).



Our process can thus be potentially extended to all mixtures diamine+ $\text{NaNO}_2$  even if the obtained localized pattern is a little bit less well defined. This is likely due to the presence in the solution of residual  $\text{Na}^+$  ions which competes with  $\text{H}^+$  to support the migration process. Nevertheless, if for some applications we need to use diazonium salts which are not available commercially, this procedure (whose improvement would

request many experimental tests which have not been undertaken within the time dedicated to the thesis) can be proposed.

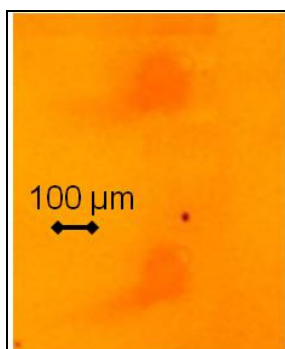


Figure 33: Optical microscopy image of the localized electrografted polyphenylene like film initiated by the electroreduction of diazonium salt generated in situ from aminobenzene ( $0.1 \text{ mol. dm}^{-3}$ ) and  $\text{NaNO}_2$  ( $0.1 \text{ mol. dm}^{-3}$ ),  $\text{HCl}$   $0.5 \text{ mol. dm}^{-3}$ ;

$50\mu\text{m-Pt UME}$ ,  $d = 10 \mu\text{m}$ ,  $I = -0.8\text{mA}$ , dots:  $t = 0.5 \text{ s}$ .

#### 4. Localized SEEP process: a “generic” process?

The results described above demonstrate unambiguously the capabilities of the SEEP process to generate a localized grafting in the SECM environment with the couple of reactants NBD/AA. It would be now interesting to check the “generic” character of this process by probing the initiation with different aryl radicals or by applying it to other vinylic monomers. However, we know now that, to obtain a well defined localized grafting, it is preferable to work in aqueous solution, limiting so, *a priori*, this process to hydrosoluble monomers.

For these reasons, hydroxylethylmethacrylate (HEMA) and bromobenzene diazonium tetrafluoroborate (BrB) were selected and tested. It must be noticed that our purpose is not to optimize the experimental conditions for all the tested systems but just to check the localized grafting concept.

A localized grafted pattern was obtained with the system BrB/AA as shown on figure 34a. The IRRAS spectrum recorded on the pattern presents the usual infrared characteristic of PAA. Tests realized with the NBD/HEMA solution (fig. 34b) are less significant. After rinsing, the organic coating tends to fall apart from the substrate, leading to a poor resolution. It is certainly possible to improve this result but that would require a more thorough parametric study which was not possible within the time frame of this thesis.

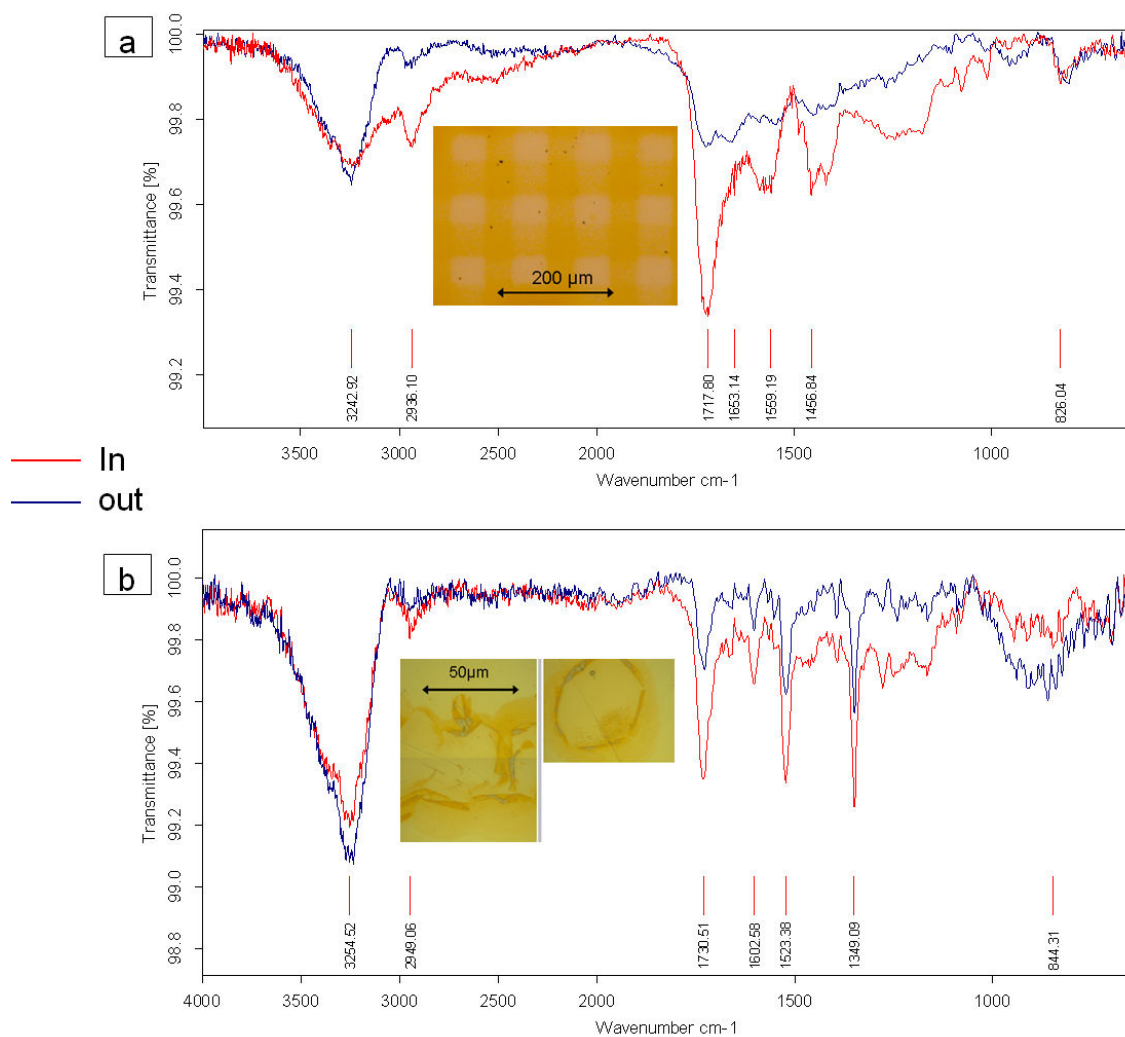


Figure 34: Optical images and infrared spectra recorded on the localized coating (red) compared to infrared spectra recorded outside the pattern (blue) of: (a) the localized electrografted PAA initiated by the electroreduction of BrB ( $2 \cdot 10^{-3} \text{ mol} \cdot \text{dm}^{-3}$ ), AA  $2 \text{ mol} \cdot \text{dm}^{-3}$ ,  $\text{H}_2\text{SO}_4$   $0.25 \text{ mol} \cdot \text{dm}^{-3}$ ;  $25 \mu\text{m}$ -Pt UME,  $d = 10 \mu\text{m}$ , lines obtained at a scan rate of  $50 \mu\text{m} \text{ s}^{-1}$ , chronopotentiometry  $I = -2 \text{ mA}$ ; (b) the localized electrografted pHEMA initiated by the electroreduction of NBD ( $2 \cdot 10^{-3} \text{ mol} \cdot \text{dm}^{-3}$ ), HEMA  $0,7 \text{ mol} \cdot \text{dm}^{-3}$ ,  $\text{H}_2\text{SO}_4$   $0.25 \text{ mol} \cdot \text{dm}^{-3}$ ;  $10 \mu\text{m}$ -Pt UME,  $d = 6 \mu\text{m}$ ,  $t = 5 \text{ s}$ .

### 5. SECM as direct lithographic tool for conducting substrates?

In collaboration with the PegasTech society, we developed a lithographic software (Elecdraw1.0) able to drive the UME of the SECM instrument in the X-Y plan above the substrate. By coupling the SECM with this software, we are thus able to "print" any complex pattern in a few minutes on the substrate. The following pictures (fig.35) give some examples of grafted patterns realized with our Elecdraw software. Behind the pleasant feature of this coupling, it will be very efficient as an actual lithographic tool with a micron-size resolution without using mask and lift-off technologies.

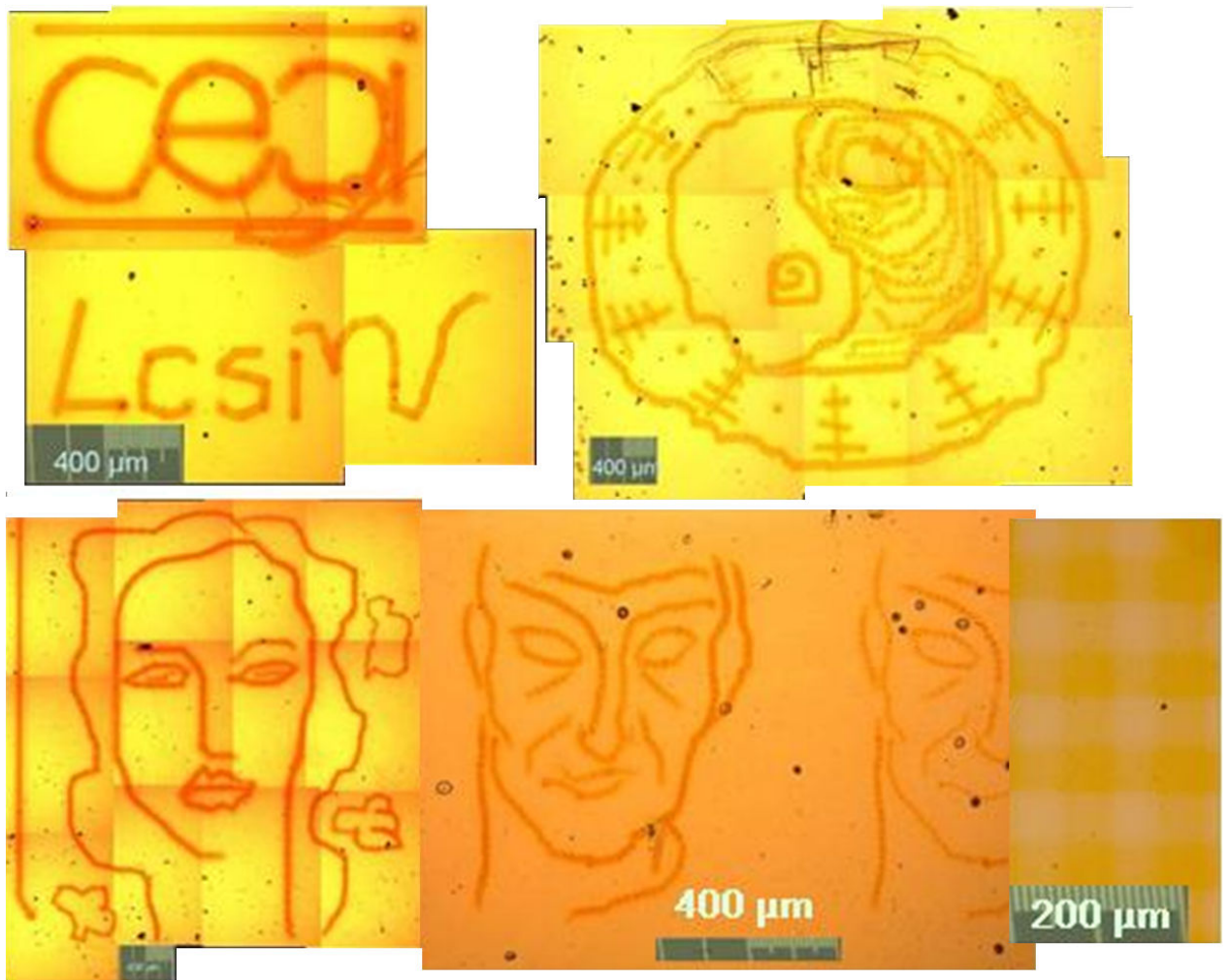


Figure 35: different patterns printed on the substrate by coupling SECM with Elecdraw software.

[AA]: $2.0 \text{ mol. dm}^{-3}$ , DNB or BrB:  $2 \cdot 10^{-3} \text{ mol. dm}^{-3}$ ,  $\text{H}_2\text{SO}_4$ : $0.25 \text{ mol. dm}^{-3}$ .

## 6. Extension of the process to sub-micronic resolution: SECM-AFM

As nanoscale effects play a more and more important role in modern science, the controlled and defined formation of nanostructures on designated substrates is of great interest. In this context, scanning probe based techniques (SPM) turned out to be not only a technique to image surfaces but also suitable tools to fabricate such nanostructures.<sup>[40-49]</sup>

The present work is related to this point. Despite many successful improvements, the spatial resolution of SECM is usually orders of magnitude worse than that of other SPM techniques, such as AFM and STM. Indeed, the achievable localization or spatial resolution for both analytical and fabrication purposes strongly depends on the shape and size of the electrochemical electrode. In our case, the best lateral resolution that we achieved in the conventional SECM environment was of the order of one micrometer (fig. 36).

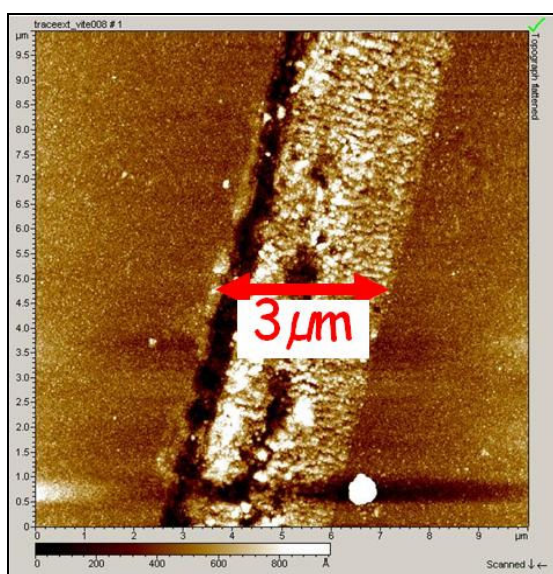


Figure 36: Topographical AFM image of the electrografted coating obtained with 5- $\mu\text{m}$  Pt UME.  $[\text{AA}]: 2.0 \text{ mol. dm}^{-3}$ ,  $\text{DNB}: 2 \cdot 10^{-3} \text{ mol. dm}^{-3}$ ,  $\text{H}_2\text{SO}_4: 0.25 \text{ mol. dm}^{-3}$ ,  $d/a=1$ ,  $I=-2 \text{ mA}$ ,  $v=100 \mu\text{m s}^{-1}$ .

So, several groups have undertaken the development of a combined AFM-SECM which represents a significant advance in SPM methodology.<sup>[50-60]</sup> Indeed, AFM gives high-resolution topographic information and is able to precisely control the distance between the sample and the probe, whereas SECM can provide detailed information of local anodic or cathodic processes. Thus, electrochemical images can be analysed with full knowledge of the corresponding surface topography.<sup>[56, 61, 62]</sup> However, up to now, works developed in that latter field are essentially devoted to cantilever tip probe development<sup>[52, 63-65]</sup> and to local electrochemical phenomena analysis, particularly for studying biological systems.<sup>[54, 61, 66, 67]</sup>

In this work, our objective is to develop an electrochemical AFM acting as an electrochemical lithographic tool. For that purpose, an integrated AFM-SECM system was first developed and then applied to induce localized grafting of organic coating on a homogeneous substrate.

### **6.1. Integrated AFM-SECM probe**

We followed the experimental set up developed by Abbou et al.<sup>[68]</sup> to fabricate an integrated AFM-SECM probe. The nanometer-sized AFM-SECM microelectrode consists of a flattened and etched gold wire, electrically insulated at all but not the apex of the tip with an electrophoretic paint<sup>[68]</sup> (see annex 1 for a detailed fabrication process). This AFM-SECM tip was first characterized by steady-state voltamperometry to get an estimate of the electro-active area of the tip from the limiting current. The well characterized rapid electron transfer ferrocenedimethanol redox species was used. The typical current-potential sigmoidal curve obtained at the Au AFM-SECM probe shows no hysteresis on the return scan, meaning a well-insulated tip (fig. 37a). Assuming that the exposed portion of the electrode fabricated above possesses a hemi-spherical shape, the diffusion-limited current is expected to follow:<sup>[69]</sup>

$$i_{lim} = 2 \pi n F D C r_0$$

where  $n$  is the number of electrons involved in the electrochemical reaction,  $F$  is Faraday's constant ( $96485 \text{ C eq}^{-1}$ ),  $D$  is the diffusion coefficient of the reacting species (for ferrocene dimethanol:  $D = 7 \times 10^{-6} \text{ (cm}^2 \text{ sec}^{-1})$ <sup>[68]</sup>,  $C$  the bulk concentration of the species ( $1 \times 10^{-6} \text{ mol.l}^{-1}$ ), and  $r_0$  the radius of the hemisphere. Using this equation, the electrode radius of our AFM-SECM tip was found close to 140 nm. This value is in relatively good agreement with the one we got from electron microscopy (150 nm, fig. 37b). The homogeneity of the coating of the electrode was assessed by measuring the diffusion limited current response as a function of the location of the meniscus when immersing the electrode into the electrolytic solution. The perfect overlapping of all cyclic voltamperograms recorded for different lengths of insertion of the coated tip into the solution suggests that there are no defects in the insulating coating along the shaft of the electrode.

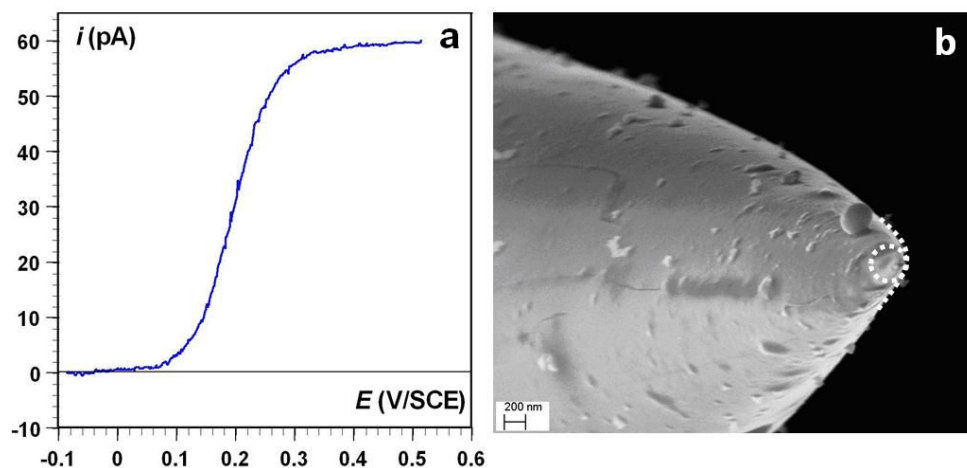
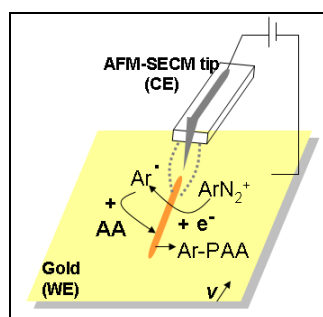


Figure 37: (a) Steady-state voltamperogram of the AFM-SECME Au tip in aqueous solution containing 1 mM ferrocenedimethanol and 0.1M  $\text{KH}_2\text{PO}_4$ . The forward and backward traces are superimposed. The potential scan rate was  $50 \text{ mV sec}^{-1}$ ; (b) SEM image of the AFM-SECME Au tip after insulation with the electrophoretic paint. Beam energy is 5 kV and working distance is 8 mm. The tip radius is around 150 nm.

## 6.2 Localized grafting at a sub-micronic scale

The capabilities of the combined AFM-SECME technique were tested with an acrylic acid - nitrobenzene diazonium tetrafluoroborate (NBD) mixture. To pattern the homogeneous substrate, the metallic substrate to coat was negatively polarized ( $-0.8\text{V}$  vs. Ag wire) with respect to the AFM-SECME tip, which acted thus as the counter-electrode (scheme 3). The tip was moved in the liquid electrolyte at a constant distance,  $d \sim 5 \mu\text{m}$ , above the surface sample and at a low rate ( $18 \mu\text{m}.\text{sec}^{-1}$ ) allowing to draw localized lines of electrografted polymer.<sup>[70]</sup> Figure 38 (a-d) shows the AFM image in acoustic mode of the line pattern drawn with the AFM-SECME tip on the gold surface. The topographical image (fig. 38e) indicates that the thickness of the coating is around 35 nm and the line width is of the order of the electro-active tip radius. This high resolution is completely comparable with that obtained with micro-contact printing methods and fully compatible with the actual requirements of many chemical and biochemical applications. Moreover, this resolution is definitely better than the one obtained with conducting polymers deposited in similar conditions using SECME.<sup>[71]</sup>



Scheme 3: Schematic of the electrografting reaction mediated by the AFM-SECME tip:  $\text{ArN}_2^+$ : aryl diazonium salt,  $\text{Ar}^\bullet$ : aryl radical, AA: acrylic acid monomer, PAA: polyacrylic acid film.

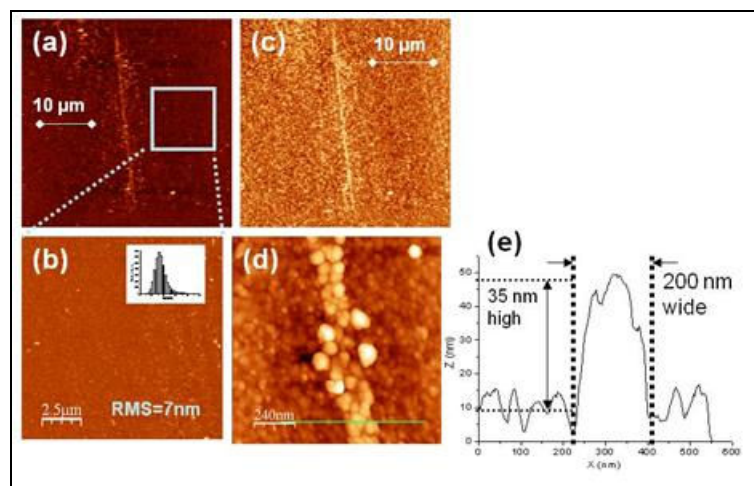


Figure 38: (a-b) topographic and phase AFM images in acoustic mode; (c) zoom on the background of the gold substrate (inlet: roughness histogram); (d-e) zoom and profile of the line pattern drawn with the AFM-SECM tip on the gold surface in the case of direct aryldiazonium salt/acrylic acid reduction. Tip-substrate distance:  $5\mu\text{m}$ ; chronoamperometry:  $-0.8\text{V}$  during 5 sec.

It must be also mentioned that if a non insulated tip was used, a localized grafting was also observed but with a poorer lateral resolution (fig. 39). The  $80\mu\text{m}$ -long line drawn with the bare gold AFM tip was around  $15\mu\text{m}$ -wide. In other words, for the same experimental setup (working distance, applied potential, duration), the width of the line was divided almost by a factor ten when the tip was insulated at all but the apex. That result clearly demonstrates that localization is mainly controlled by the spatial extension of the current lines between the working and the counter electrodes. These current lines respect the same distribution as those of the electric field that would exist between the two electrodes in a perfect dielectric medium.

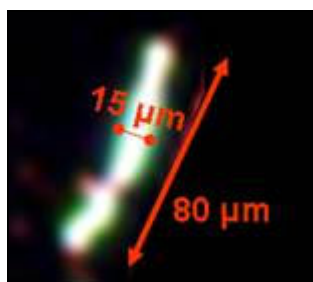
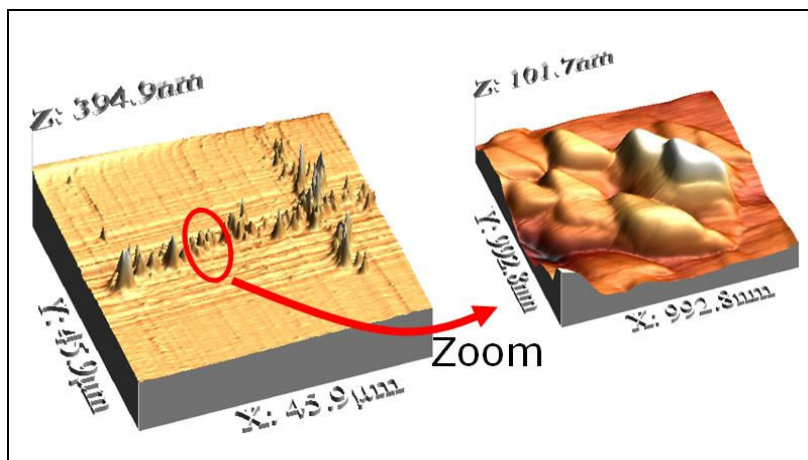


Figure 39: Optical microscope image of the line pattern drawn with the non insulated AFM-SECM tip on the gold surface in the case of direct aryldiazonium salt/acrylic acid reduction. Tip-substrate distance:  $5\mu\text{m}$ ; chronoamperometry:  $-0.8\text{V}$  during 5 sec.

However, the fabrication of an AFM-SECM insulated tip is a little bit fastidious, more particularly in view of an extension of this technology to a multi-tips cantilever. But, we have also shown that working with a non insulated tip leads to a significant enlargement of the grafted pattern when the entire tip is immersed in the solution. We can partially circumvent those drawbacks by working, in AFM-SECM tapping mode, with a non insulated tip, on a very thin layer of the electrolyte solution obtained after partial evaporation on the substrate. By a judicious choice of the tapping amplitude, we were able to graft a pattern with a sub-micronic resolution (fig. 40). This result is

just a proof of concept and may certainly be improved by technical developments which, however, are not the aim of this work.



*Figure 40: AFM image in tapping of the grafted pattern obtained by tapping AFM-SCEM on a gold substrate.*

## **Conclusions**

To sum up, we can say that the localization of the electrografting is based on the local generation of reactive species confined in the vicinity of the UME/substrate gap. Aryl radicals originated from the reduction of diazonium salts act both as surface-active reactants to form a primer PP grafted film, and as radical initiators for the final polymer coatings. The short UME/substrate working distance limits the diffusion time of the radical species generated at the electrodes surfaces and ensures a small reaction area.

The oxidation water regime, which has to be reached to observe the localization effect, induces the production of protons which are collected on the substrate. Our electrochemical system seems thus to function as a tip generator / substrate collector of reactive species. The transportation of these reactive species between both electrodes is mainly supported by the migration effect which is very sensitive to the electric field.

The vinylic monomers in the electrolyte solution may play the role of trappers which also limit the free radical diffusion. This phenomenon is very similar to the well-known "chemical lens" phenomenon<sup>[72]</sup> where the diffusion of the electrodes generated species and the scavengers are in opposite direction. If the chemical reaction between the trapper and the generated species is fast enough, the surface modification of the substrate will be spatially limited to a thin zone surrounding the tip where the two species meet.

The application of the SECM and the extended AFM-SECM to the particular case of the grafting of vinylic monomers allows to direct patterning of a homogeneous conducting substrate with a covalently grafted organic coating, which one cannot obtain with conducting polymers and SAMs on gold technology. The formation of this strong interfacial bond is a key point for the properties of the final interfaces, which can then be further processed by classical methods of organic chemistry. The polyacrylate deposit may, for example, be functionalized by almost any chemically active species by a simple amidation of the carboxylic hanging groups.

We have thus demonstrated that the UME in the environment of a SECM or the AFM-SECM tip can be used as a pencil to direct the electrografting of organic film. The process is thus similar to dip-pen coating,<sup>[39]</sup> although the final coating is here covalently grafted as in a "classical" SEEP experiment. This new extension of the SECM/SPM techniques shows great promises for directing localized modification purpose, which is of great interest for chemical, biological or technical applications.

## REFERENCES

- [1] S. P. A. Fodor, J. Leighton Read, M. C. Pirrung, L. Stryer, A. Tsai Lu and D. Solas, *Science* **1991**, *251*, 767.
- [2] C. S. Dulcey, J. H. Georger Jr., V. Krauthamer, D. A. Stenger, T. L. Fare and J. M. Calvert, *Science* **1991**, *252*, 551.
- [3] D. A. Stenger, J. H. Georger, C. S. Dulcey, J. J. Hickman, A. S. Rudolph, T. B. Nielsen, S. M. McCort and J. M. Calvert, *J. Am. Chem. Soc.* **1992**, *114*, 8435.
- [4] R. Singhvi, A. Kumar, G. P. Lopez, G. N. Stephanopoulos, D. I. C. Wang, G. M. Whitesides and D. E. Ingber, *Science* **1994**, *264*, 696.
- [5] S. Sundberg, R. W. Barrett, M. C. Pirrung, A. L. Lu, B. Kiangsoontra and C. P. Holmes, *J. Am. Chem. Soc.* **1995**, *117*, 12050.
- [6] L. M. Tender, R. L. Worley, H. Fan and G. P. Lopez, *Langmuir* **1996**, *12*, 5515.
- [7] M. Mrksich and G. M. Whitesides, *Annu. Rev. Biophys. Biomol. Struct.* **1996**, *25*, 55.
- [8] G. Buss, M. J. Schöning and J. W. Schultze, *Electrochim. Acta* **1999**, *44*, 3899.
- [9] B. A. Grzybowski, R. Haag, N. Bowden and G. M. Whitesides, *Anal. Chem.* **1998**, *70*, 4645.
- [10] G. Sreenivas, S. S. Ang, I. Fritsch, W. D. Brown, G. A. Gerhardt and D. J. Woodward, *Anal. Chem.* **1996**, *69*, 1858.
- [11] A. Kumar and G. M. Whitesides, *Appl. Phys. Lett.* **1993**, *63*, 2002.
- [12] B. Michel, A. Bernard, A. Bietsch, E. Delamarche, E. Geissler, D. Juncker, H. Kind, J.-P. Renault, H. Rothuizen and H. Schmid, *IBM J. Res. Dev.* **2001**, *45*, 697.
- [13] M. Geissler, A. Bernard, A. Bietsch, H. Schmid, B. Michel and E. Delamarche, *J. Am. Chem. Soc.* **2000**, *122*, 6303.
- [14] A. Bernard, J. P. Renault, B. Michel, H. R. Bosshard and E. Delamarche, *Adv. Mater.* **2000**, *12*, 1067.
- [15] E. Delamarche, A. Bernard, H. Schmid, A. Bietsch, B. Michel and H. Biebuyck, *J. Am. Chem. Soc.* **1998**, *120*, 500.
- [16] H. J. Levinso, *Principles of Lithography, Second Edition* SPIE Publication **2010**.
- [17] D. P. Sanders, *Chem. Rev.* **110**, 321.
- [18] S. C. H. Fred M. Dickey, David L. Shealy, *Laser beam shaping applications*, Taylor & Francis **2005** p.
- [19] K. Deguchi and T. Haga, *Comptes Rendus de l'Académie des Sciences - Series IV - Physics* **2000**, *1*, 829.
- [20] W. M. Moreau, *Semiconductor Lithography*, Plenum Publishing Co., New York, **1988**.
- [21] R. L. Gerlach and M. Utlaut, *Proc. SPIE* **4510** **2001**, pp. 96.
- [22] X. Duan, Y. Zhao, A. Perl, E. Berenschot, D. N. Reinhoudt and J. Huskens, *Adv. Funct. Mater.* **2010**, 663.
- [23] A. Bardea and R. Naaman, *Langmuir* **2009**, *25*, 5451.
- [24] M. C. McAlpine, R. S. Friedman and C. M. Lieber, *Nano Lett.* **2003**, *3*, 443.
- [25] M. A. Kramer, H. Jaganathan and A. Ivanisevic, *J. Am. Chem. Soc.* **132**, 4532.
- [26] J. Charlier, S. Ameer, J. P. Bourgoin, C. Bureau and S. Palacin, *Adv. Funct. Mater.* **2004**, *14*, 125.
- [27] J. Charlier, L. Baraton, C. Bureau and S. Palacin, *ChemPhysChem* **2005**, *6*, 70.
- [28] J. Charlier, E. Clolus, C. Bureau and S. Palacin, *J. Electroanal. Chem.* **2008**, *622*, 238.
- [29] J. Charlier, E. Clolus, C. Bureau and S. Palacin, *J. Electroanal. Chem.* **2009**, *625*, 97.
- [30] J. Charlier, S. Palacin, J. Leroy, D. Del Frari, L. Zagonel, N. Barrett, O. Renault, A. Bailly and D. Mariolle, *J. Mater. Chem.* **2008**, *18*, 3136.
- [31] L. Tessier, G. Deniau, B. Charleux and S. Palacin, *Chem. Mater.* **2009**, *21*, 4261.
- [32] C. Kranz, M. Ludwig, H. E. Gaub and W. Schumann, *Adv. Mater.* **1995**, *7*, 568.
- [33] V. Radtke, C. Hess and J. Heinze, *Z. Phys. Chem.* **2007**, *221*, 1221.

- [34] W. B. Nowall, D. O. Wipf and W. G. Khur, *Anal. Chem.* **1998**, *70*, 2601.
- [35] J. Kwak and A. J. Bard, *Anal. Chem.* **1989**, *61*, 1221.
- [36] J. Kwak and A. J. Bard, *Anal. Chem.* **1989**, *61*, 1794.
- [37] A. J. Bard, C. A. Mirkin, P. R. Unwin and D. O. Wipf, *J. Phys. Chem.* **1992**, *96*, 1861.
- [38] B. Chopard and P. Luthi, *Phys. Rev. Lett.* **1994**, *72*, 1384.
- [39] R. D. Piner, J. Zhu, F. Xu, S. Hong and C. A. Mirkin, *Science* **1999**, *283*, 661.
- [40] A. A. Gewirth and B. K. Niece, *Chem. Rev.* **1997**, *97*, 1129.
- [41] M. Kock, V. Kirchner and R. Schuster, *Electrochim. Acta* **2003**, *48*, 3213.
- [42] R. Schuster, V. Kirchner, X. H. Xia, A. M. Bittner and G. Ertl, *Phys. Rev. Lett.* **1998**, *80*, 5599.
- [43] T. H. Treutler and G. Wittstock, *Electrochim. Acta* **2003**, *48*, 2923.
- [44] S. Hou, Z. Li and Z. F. Liu, *Appl. Surf. Sci.* **2004**, *222*, 338.
- [45] P. T. Hurley, A. E. Ribbe and J. M. Buriak, *J. Am. Chem. Soc.* **2003**, *125*, 11334.
- [46] P. Kruse, E. R. Johnson, G. A. DiLabio and R. A. Wolkom, *Nano Lett.* **2002**, *2*, 807.
- [47] O. A. Semenikhin, C. Stromberg, M. R. Ehrenburg, U. König and J. W. Schultze, *Electrochim. Acta* **2001**, *47*, 171.
- [48] J. W. Schultze and A. Bressel, *Electrochim. Acta* **2001**, *47*, 3.
- [49] H. Diesinger, A. Bsiesy, R. Hérino and S. Huant, *J. Appl. Phys.* **2001**, *89*, 3328.
- [50] S. Amemiya, A. J. Bard, F.-R. F. Fan, M. V. Mirkin and P. R. Unwin, *Annu. Rev. Anal. Chem.* **2008**, *1:4*, 1.
- [51] M. N. Holder, C. E. Gardner, J. V. Macpherson and P. R. Unwin, *J. Electroanal. Chem.* **2005**, *585*, 8.
- [52] R. J. Fasching, Y. Tao and F. B. Prinz, *Sensor Actuat. B* **2005**, *108*.
- [53] Y. Hirata, S. Yabuki and F. Mizutani, *Bioelectrochemistry* **2004**, *63*, 217.
- [54] J. Abbou, A. Anne and C. Demaille, *J. Am. Chem. Soc.* **2004**, *126*, 10095.
- [55] J. V. Macpherson and P. R. Unwin, *Anal. Chem.* **2000**, *72*, 276.
- [56] C. E. Jones, J. V. Macpherson, Z. H. Barber, R. E. Somekh and P. R. Unwin, *Electrochem. Comm.* **1999**, *1*, 55.
- [57] A. L. Barker, M. Gonsalves, J. V. Macpherson, C. Slevin and P. R. Unwin, *Anal. Chim. Acta* **1999**, *385*, 223.
- [58] A. Davoodi, A. Farzadi, J. Pan, C. Leygraf and Y. Zhu, *J. Electrochem. Soc.* **2008**, *155*, C474.
- [59] A. Kueng, C. Kranz, B. Mizaikoff, A. Lugstein and E. Bertagnolli, *Appl. Phys. Lett.* **2003**, *82*, 1592.
- [60] M. R. Gullo, P. L. T. M. Frederix, T. Akiyama, A. Engel, N. F. deRooij and U. Staufer, *Anal. Chem.* **2006**, *78*, 5436.
- [61] C. Kranz, A. Kueng, A. Lugstein, E. Bertagnolli and B. Mizaikoff, *Ultramicroscopy* **2004**, *100*, 127.
- [62] J. V. Macpherson and P. R. Unwin, *Anal. Chem.* **2001**, *73*, 550.
- [63] F.-R. F. Fan and C. Demaille, in *Scanning Electrochemical Microscopy 2001*, A. J. Bard and M. V. Mirkin Ed., Marcel Dekker: New York.
- [64] D. P. Burt, P. S. Dobson, J. H. Weaver, N. R. Wilson, P. R. Unwin and J. V. Macpherson, *IEEE Sensor Conf.* **2007**, 712.
- [65] A. Lugstein, E. Bertagnolli, C. Kranz, A. Kueng and B. Mizaikoff, *Appl. Phys. Lett.* **2002**, *81*, 349.
- [66] K. Wang, C. Goyer, A. Anne and C. Demaille, *J. Phys. Chem. B* **2007**, *111*, 6051.
- [67] D. Grieshaber, R. MacKenzie, J. Vörös and E. Reimhult, *Sensors* **2008**, *8*, 1400.
- [68] J. Abbou, C. Demaille, M. Druet and J. Moiroux, *Anal. Chem.* **2002**, *74*, 6355.
- [69] A. J. Bard and M. V. Mirkin, *Scanning Electrochemical Microscopy; Marcel Dekker, Inc., New York, Basel* **2001**.
- [70] P. A. Brooksby and A. J. Downard, *J. Phys. Chem. B* **2005**, *109*, 8791.

- [71] S. A. G. Evans, K. Brakha, M. Billon, P. Mailley and G. Denuault, *Electrochem. Comm.* **2005**, *7*, 135.
- [72] K. Borgwarth and J. Heinze, *J. Electrochem. Soc.* **1999**, *146*, 3285.

## **Annex 1: Preparation and characterization of microdisk electrodes**

The Pt microdisk electrodes were prepared according to the literature. Briefly, the end of a glass capillary was sealed such that a conical shape was obtained. A straight 100, 50, 25, or 10  $\mu\text{m}$  diameter Pt wire (99.9% purity, Goodfellow, United Kingdom) was then positioned at the bottom of the sealed borosilicate glass capillary. The capillary was then slowly sealed onto the wire using a heated resistor coil. The sealed wire was then electrically connected to a larger wire by welding with tin. The microdisk electrode was then polished using sandpaper by gradually increasing grit size (600 and 1200) such that the RG value (RG = ratio of glass to metallic radii) fell if possible under 10 and a smooth surface was obtained. Before use, UMEs were washed under sonication in Milli-Q water. The quality of the microdisk electrode was checked by recording the steady-state voltamperogram of a well-characterized system exhibiting rapid heterogeneous electron transfer ( $[\text{Fe}(\text{CN})_6]^{3-}/[\text{Fe}(\text{CN})_6]^{4-}$ ). The initial potential was set from -0.25 vs. Ag wire to 0.4 V, and reversed and the current sensitivity to 100 nA. The UMEs were considered as satisfactory if the reverse scan retraced the forward scan.

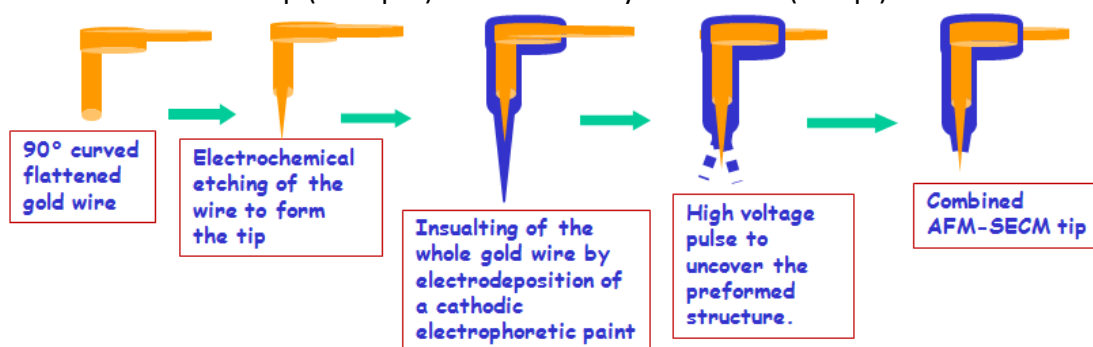
## **Annex 2: SECM imaging process**

The surface SECM images were taken in the constant-height feedback imaging mode. Constant height mode images are obtained by moving a probe laterally in the x-y plane above the substrate and monitoring the tip current,  $i_T$ , as a function of tip location. Current data are collected at each defined division of the scan; the minimum division corresponding to highest resolution is the UME diameter (2a). The output from the area scan experiment is an area graph with displacement on the X and Y axis and amplitude of current on the amplitude axis. The variation of current is plotted using a range of grey-scale intensities defined by a palette. Increasing or decreasing in the UME current obtained in line scans at homogeneously insulating or conducting surfaces can be understood as up and down in surface topography while current variations gained at flat surfaces with neighbouring conductive and insulating regions represent the local changes in electrochemical activity of the sample surface. In samples with variations in both interfacial electrochemical activity and changes in surface topography, the UME response reflects a convolution of contributions from alterations in electro-chemical activity and topography, and, in fact, additional information about the morphology of the specimen is obligatory for an interpretation of the constant-height SECM images. The first consequence is the need for a large part of the sample chemically homogeneous to flatten the surface through line scan.

In our imaging SECM experiments realized in the feedback mode, ferrocene dimethanol,  $5 \cdot 10^{-3} \text{ mol.dm}^{-3}$ , was added to the supporting electrolyte ( $\text{KCl } 10^{-2} \text{ mol.dm}^{-3}$ ), the working distance was chosen in the range of  $0.4 \leq d/a \leq 0.6$ , the step size was of the order of  $2a$ , and the sample measuring time was about  $0.4\text{s}$ . The image is composed by successive line scans and the image was carried out in a reasonable time, to guarantee the stability of the concentration of redox species in solution.

### Annex 3: Fabrication and characterization of the AFM-SECM tip

The nanometer-sized microelectrode consists of a flattened and etched gold wire, electrically insulated at all but the apex of the tip (scheme A). The experimental protocol was adapted from the procedure described by Abbou et al.<sup>[68]</sup> In brief, by generating an electric arc between an etched gold microwire and a tungsten counter electrode, the very end of the gold microwire can be melted and given a conical shape a few hundred nanometers in size. The whole wire was subsequently insulated via the cathodic deposition of electrophoretic paint. By applying a high-voltage pulse to the microwire, the film covering its very end can then be selectively removed, thus exposing a submicrometer-sized electrode surface of predefined geometry. The tip was then mounted as a combined AFM-SECM probe, and was used as the counter electrode of a standard three-electrode arrangement. The value of the conical tip radius was determined by scanning electron microscopy for several probes and was found between 70 and 150 nm depending on the probe. These fabricated AFM-SECM probes integrate tips of about 1.5mm length (fig.I). It is then possible to immerse only the final end of the tip (~200 $\mu$ m) in the electrolytic solution (300  $\mu$ l).



*Scheme A: Schematic successive steps of an AFM-SECM tip fabrication process.*

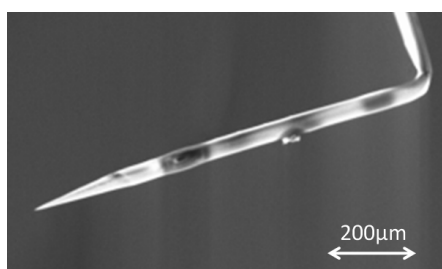


*Figure I: SEM micrographs showing the extremity of an etched microwire insulated by a film of reticulated electrophoretic cathodic paint*

#### Annex 4: Experimental setup for AFM-SECM experiments

The substrate (Pyrex glass plates coated with 2 nm of chromium and 100 nm of gold (99.99 %) by vacuum evaporation) was the working electrode and a silver wire the quasi-reference electrode. All potentials reported herein are with respect to the silver wire quasi-reference electrode unless otherwise stated. The L-AFM-SECM experiments were performed with a Molecular Imaging PicoSPMLe AFM microscope (PicoScan 2100 controller - Scientec, France) equipped with a home-modified fluid cell containing the electrolytic solution (commercial acrylic acid (Aldrich,  $0.7 \text{ mol.dm}^{-3}$ ) in acidic aqueous solution ( $\text{H}_2\text{SO}_4$   $0.25 \text{ mol.dm}^{-3}$ , analytical grade) in presence of 4-nitrobenzenediazonium tetrafluoroborate (Aldrich,  $2 \times 10^{-3} \text{ mol.dm}^{-3}$ ). Solutions for electrochemistry were not degassed prior to use, and all measurements were made at room temperature. The potentials applied to the electrodes were controlled by an external bipotentiostat (BioLogic Science Instruments). The microscope head was placed inside a Faraday cage and mounted on a floating table to achieve vibration isolation during investigations and characterizations. Reference markers made on the sample before experimental assembly allowed to locate easily the modified areas after the localized electrografting process. The working distance was set by positioning at first the tip "in contact" with the surface and then by withdrawing it from the substrate. A working distance of  $5 \mu\text{m}$  was found to be optimal. For smaller distances, the probe becomes too sensitive to the disorder of the solution caused by the dihydrogen release and for larger distances, the localization is lost. For rigorous experiments, this procedure was systematically repeated before each grafting experiment. The electro-initiated polymerization technique could be achieved using either chronoamperometric or chronopotentiometric techniques. All the samples were sonicated in ethanol and water before analyses. During AFM-SECM experiments, the tip movement was monitored via the reflection of the AFM laser onto the cantilever arm of the probe and the detection of the reflected beam on a position-sensitive detector.

The resulting localized thin films were characterized by optical microscopy (Leica DMLM with CDD camera Leica DFC 320) and by topographical AFM analysis. For imaging the localized electrografted trace by AFM in acoustic mode, the AFM-SECM tip was replaced by a commercial pyramidal Si tip (mounted on  $225 \mu\text{m}$  long single beam cantilever with a resonance frequency of approximately 75 kHz and a spring constant of about  $3 \text{ Nm}^{-1}$ ). AFM images were recorded using the retrace signal. The scan rate was in the range of 0.25 Hz with a scanning density of 512 lines/frame. The grafted polymer has characteristic spectroscopic features which can be used as a probe to trace the growth of the polymer on the surface. The samples were then analyzed by X-Ray photoelectron spectroscopy (Kratos Axis Ultra DLD, Al  $K\alpha$  monochromatic source)

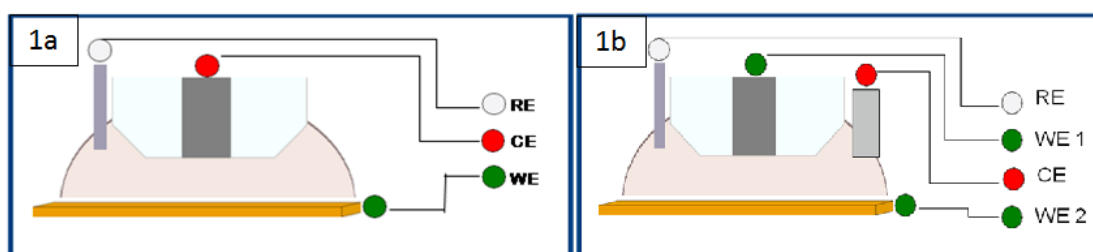
and infrared spectroscopy (Bruker VERTEX 70 spectrometer with a mono reflection ATR Pike-Miracle™ device).

## CHAPTER 4

### LOCALIZED GRAFTING IN THE FOUR-ELECTRODES CELL CONFIGURATION, REASONS INVESTIGATION FOR A LOCAL EFFECT

#### 1. Introduction

In chapter 3, we have validated the localized grafting concept in the environment of the SECM. However, the experiments undertaken in the three-electrode configuration mode (scheme 1a) may suffer from a lack of reproducibility because we do not control the applied potential to the UME. Moreover, as we have seen in chapter 3, it is necessary to reach the proton reduction regime on the substrate to observe the localization effect. In the three-configuration mode, when this regime is reached, the corresponding potential at the UME is very high and water oxidation occurs. In this configuration, it is not possible to know if this contribution is positive for the localized effect or, on the contrary, a drawback. Then, in order to put in evidence the role played by the different electrochemical species generated at the electrodes on the localized process, it would be better to control separately the potentials applied to the substrate and the UME respectively. Therefore we undertook experiments in the four-electrode configuration (scheme 1b) where the potentials applied to the UME and the substrate can be precisely controlled via the use of a bipotentiostat.



*Scheme 1 - (a) three-electrode configuration with the UME acting as the CE; (b) four-electrode configuration with two working electrodes (UME, WE1, and substrate, WE2), a common CE (Pt wire) and a common reference electrode (Ag wire).*

First of all, let's record the current flowing through the UME and the substrate respectively when both polarized electrodes approach each other. The experimental conditions are chosen close to those used for the localized electrografting process. But, in order to avoid possible disturbances due to the passivation of the surface by the electrografting of the diazonium salt, the electrolytic solution contains only sulfuric acid ( $0.25 \text{ mol.dm}^{-3}$ ) and acrylic acid ( $2 \text{ mol.dm}^{-3}$ ). It must also be noted that no supplementary redox mediator was added to the solution. Approach advancement was realized with motorized  $2 \mu\text{m}$  step corresponding to a scan rate of  $0.7 \mu\text{m.s}^{-1}$ .

On figure 1, we report the current recorded at the UME and the substrate respectively, as a function of the normalized distance between the substrate and the UME for different potentials applied to the UME while potential applied to the substrate was kept equal to -0.4V vs. Ag wire (except for experiment undertaken at  $E_{UME} = 4V$  vs. Ag wire for which  $E_s$  is equal to 0V vs. Ag wire).

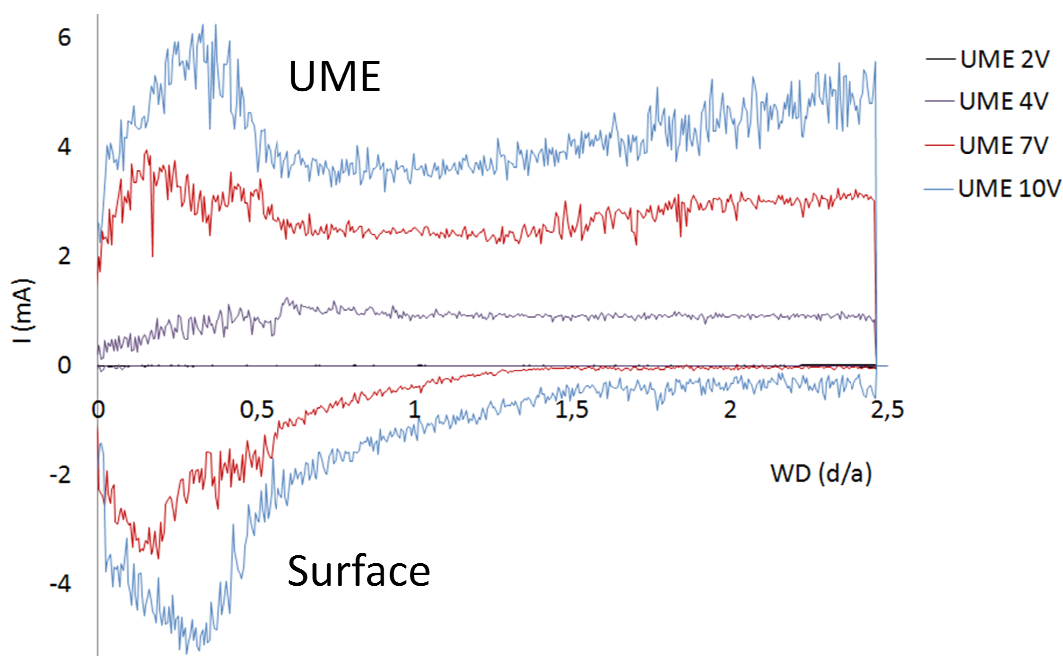


Figure 1: tip and substrate current vs. the normalized working distance for different potentials applied to the tip: 2V/Ag wire (black), 4V/Ag wire (violet), 7V/Ag wire (red), 10V/Ag wire (blue). 100  $\mu\text{m}$ -Pt, scan rate of the tip approach: 0.7  $\mu\text{m s}^{-1}$ ,  $\text{H}_2\text{SO}_4$  0.25  $\text{mol dm}^{-3}$ , acrylic acid 2  $\text{mol.dm}^{-3}$ .

(a) for  $E_{UME} \leq 2V$  vs. Ag wire, the currents flowing through the tip and through the substrate are low (2 $\mu\text{A}$  and 35 $\mu\text{A}$ , respectively) and constant whatever  $d$ . These currents correspond to the background current of the electrochemical cell.

(b) for  $E_{UME} \gg 2V$  vs. Ag wire, much higher currents are flowing through the tip since oxidation of water occurs following the relation (4.1).



However, one cannot also exclude the formation of oxygenated species like  $\text{O}_3(\text{g})$ ,  $\text{H}_2\text{O}_2$ , and  $\bullet\text{OH}$  which standard redox potentials are given in table 1. Among these species, one has to pay attention particularly to  $\bullet\text{OH}$  radicals, one of the strongest oxidizing agents, which can eventually serve as a mediator able to oxidize organic compounds by initiating radical chemical reaction.<sup>[1, 2]</sup> Even if the Pt electrode is not the best materials to produce efficiently these oxidizing species, the process may however occur as the tip is biased at very high anodic potential at which a very high current

density ( $J_{\text{UME}}$ ) is associated (for example, for 100- $\mu\text{m}$  Pt UME at  $d/a > 3$ , with  $E_{\text{UME}} = 7\text{ V}$ ,  $I_{\text{UME}} = 5\text{ mA}$ , i.e.  $J_{\text{UME}} = 64\text{ A}\cdot\text{cm}^{-2}$ !). Other labile oxygen species are also situated in the water discharge region (fig. 1).

Oxidation reaction	$E^\circ/\text{V vs. SHE}$
$\text{H}_2\text{O} \rightarrow \text{HO}^\cdot + \text{H}^+ + e^-$	2.80
$\text{O}_{2(g)} + \text{H}_2\text{O} \rightarrow \text{O}_{3(g)} + 2\text{H}^+ + 2e^-$	2.08
$2\text{H}_2\text{O} \rightarrow \text{H}_2\text{O}_2 + 2\text{H}^+ + 2e^-$	1.77
$\text{H}_2\text{O}_2 \rightarrow \text{HO}_2^\cdot + \text{H}^+ + e^-$	1.44

Table 1: standard potential of several redox couples in the water discharge region (reprinted from reference 2)

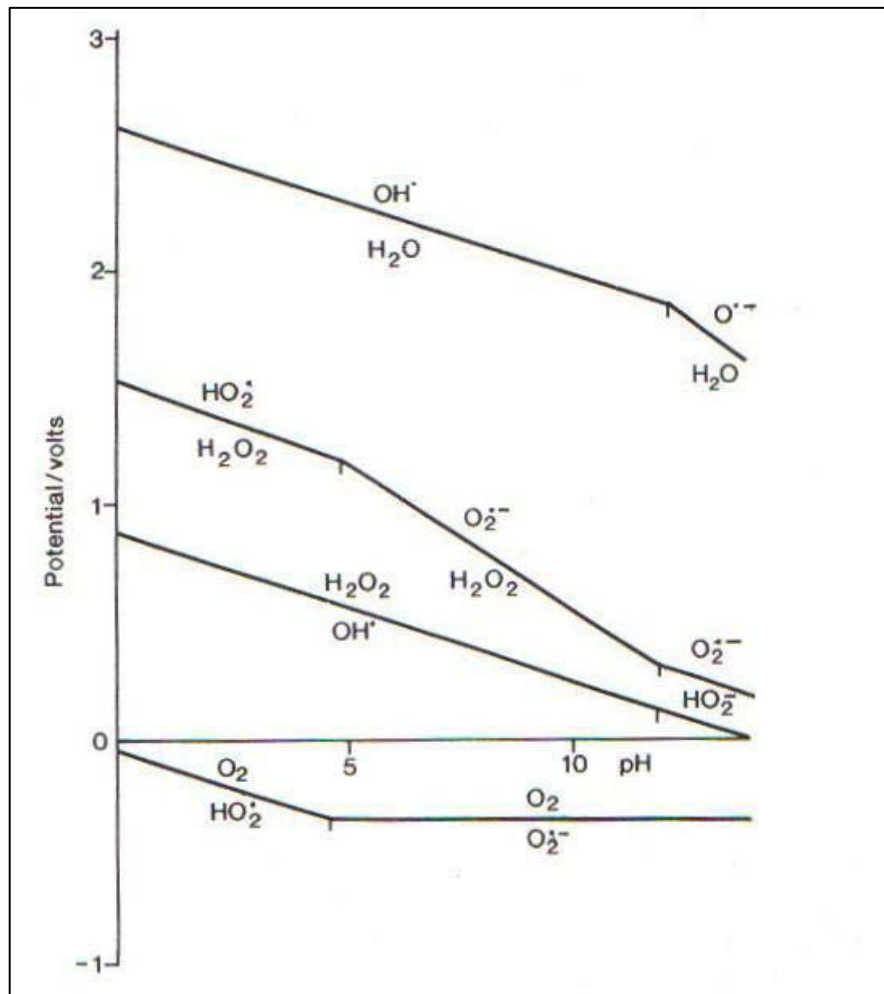


Figure 2: pH-potential diagram of oxygen reactive species.<sup>[3]</sup>

One has also to consider the plausible oxidation of disulfate anions into sulfate radical anions or/and peroxydisulfate ions (table 2) which may be not only very reactive radicals or oxidizing species,<sup>[4]</sup> but also, which are known to be able to initiate the radical polymerization of vinylic monomers.<sup>[5]</sup>

Oxidation reaction	$E^\circ/\text{V vs. SHE}$
$\text{SO}_4^{2-} \rightarrow \text{SO}_4^{\cdot-} + e^-$	2.60
$2\text{SO}_4^{2-} \rightarrow \text{S}_2\text{O}_8^{2-} + 2e^-$	2.01

Table 2: standard potential of sulfate redox couple in the water discharge region (reprinted from reference 2).

Therefore, an anodic current is recorded on the tip. Far from the substrate ( $d/a \geq 2$ ), this anodic current ( $I_{\text{UME},\infty}$ ) increases perfectly linearly with the potential applied to the tip (fig. 3). As  $d/a$  tends to zero, the correlation coefficient of the linear regression fit is not as good, suggesting that the current recorded at the tip is perturbed by the presence of the substrate at small working distance. More precisely, for  $E_{\text{UME}} \geq 7\text{V}$ , the current recorded at the tip for the smallest working distances is higher than expected, indicating probably the detection by the tip of active species coming from the substrate.

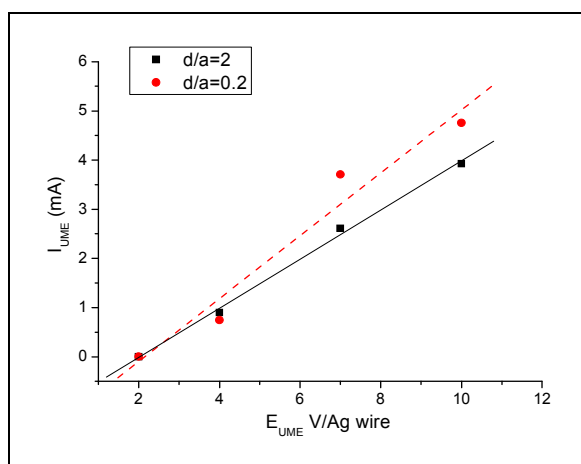


Figure 3: tip current vs. the applied tip potentials for two different normalized working distance:  $d/a=2$  (black);  $d/a=0.2$  (red). Scatter: experimental data, line: linear fit.  $100 \mu\text{m-Pt}$ ,  $\text{H}_2\text{SO}_4$   $0.25 \text{ mol dm}^{-3}$ , acrylic acid  $2 \text{ mol.dm}^{-3}$ .

It seems thus that in our system, a generation/collection like-process occurs between both electrodes. For example, on figure 4, we report the anodic ( $I_{\text{UME}}$ ) and cathodic ( $I_{\text{sub}}$ ) currents recorded simultaneously during the approach of the tip to the substrate. In this figure, the variable (abscissa) is the time, which is directly proportional to the variation of  $d/a$  since the approach rate was constant.

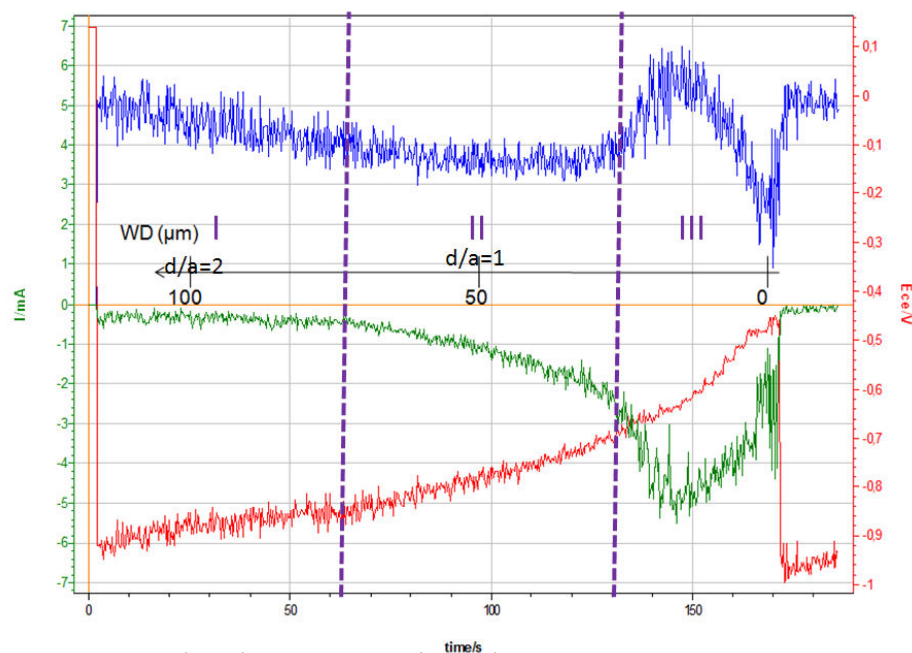


Figure 4: anodic (blue) and cathodic (green) currents recorded during the tip approach.  $E_{UME}=10$  V,  $E_{Sub}=-0.4$  V,  $E_{CE}$  (red) potential measured at counter electrode.  $100 \mu\text{m-Pt}$ , scan rate of the tip approach:  $0.7 \mu\text{m s}^{-1}$ ,  $\text{H}_2\text{SO}_4$   $0.25 \text{ mol dm}^{-3}$ , acrylic acid  $2 \text{ mol.dm}^{-3}$ .

We can observe that

(i) For  $d/a > 1.6$  (figure 4, region I), the anodic current corresponding mainly to the oxidation of water keeps constant while no significant cathodic current is recorded on the substrate.

(ii) For  $0.6 < d/a < 1.6$  (figure 4, region II),  $I_{UME}$  remains constant while, in correspondence, the cathodic current recorded on the substrate increases in absolute value. In other words, it appears thus that for  $d/a < 1.6$ , species generated at the tip begin to be detected at the substrate. Since the tip/substrate diffusion time is of the order of  $d^2/D$ , the smaller  $d/a$ , the sooner the substrate current increases.

(iii) For the smallest working distance ( $d/a < 0.6$ , figure 4 zone III), both electrodes interact with each other: species generated at the tip are collected on the substrate where they are reduced and their reduction products may, in turn, be detected at the tip, leading to an increase of the anodic current.

Another way to demonstrate the existence of the generation/collection effect between both electrodes is to plot the efficiency of the collection at the substrate ( $I_{Sub}/I_{UME}$ ) as a function of the normalized distance (fig. 5). The efficiency of the collection begins to increase for  $d/a < 1.6$  and tends to 1 (100%) for  $d/a \rightarrow 0$ . As the substrate potential is held constant at  $-0.4$  V vs. Ag wire, species able to be detected and reduced on the substrate are probably protons, according to the relation (4.2). One may also expect that dissolved  $\text{O}_2$  could be reduced on the gold substrate (relation

4.3 and/or 4.4). However, it is known that pure gold metal is poorly active for the electroreduction of oxygen and yields a significant amount of hydrogen peroxide as subproduct.<sup>[6]</sup> A large amount of these species are unstable and have a very short lifetime. Thus their detection by the tip and/or the substrate is only significant for the very short working distances. For large working distances, most of those species are lost from the electroactivity point of view.

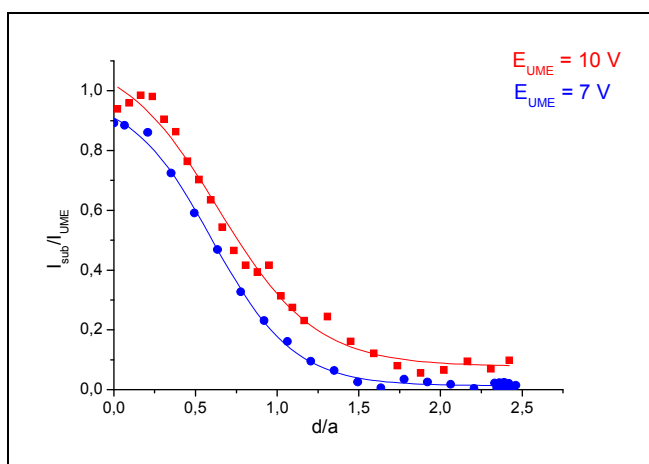
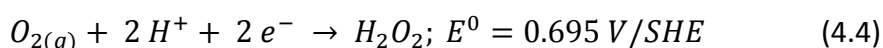
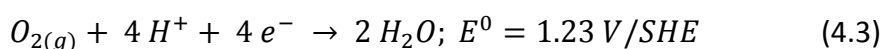


Figure 5: substrate current /tip current ratio vs. normalized working distance for two different tip potentials: 7 V/Ag wire (blue), 10 V/Ag wire (red),  $E_{sub}$  being held to -0.4 V/Ag wire. Scatter: experimental data, line: fit data. 100  $\mu\text{m}$ -Pt,  $\text{H}_2\text{SO}_4$  0.25 mol  $\text{dm}^{-3}$ , acrylic acid 2 mol. $\text{dm}^{-3}$ .



To sum up, the tip biased at high anodic potential generates constantly a flux of species which induce on the substrate a significant cathodic current when the normalized working distance is lower than 1.6. For the very short working distances, a redox loop-like phenomenon seems to take place between both electrodes, which partially compensates the hindered diffusion.

## 2. Influence of the applied potential to the microelectrode

In order to study the influence of various electrochemical parameters on the localized process, chronoamperometry experiments were undertaken where the potential applied to the UME was scanned in the range of 1V to 10V vs. Ag wire reference while the substrate was (i) held unbiased or (ii) cathodically polarized. Dots were thus realized by chronoamperometry technique ( $t=5\text{s}$ ). All these experiments were realized at  $d/a=0.4$  (i.e.,  $d=20 \mu\text{m}$  for the 100  $\mu\text{m}$ -Pt) and the electrolytic solution was the usual one: [AA] 2.0 mol.  $\text{dm}^{-3}$ , DNB  $2 \cdot 10^{-3}$  mol. $\text{dm}^{-3}$ ,  $\text{H}_2\text{SO}_4$  0.25 mol. $\text{dm}^{-3}$ .

In the first case where the substrate was unbiased whereas the UME potential was scanned to high positive values, we observed a strong degradation of the substrate as visualized on figure 6. In fact, the potential experienced by the unbiased substrate, when the UME reaches 10 V vs. Ag wire, corresponds to the open circuit potential which is sufficiently positive (around 0.8 V vs. Ag wire) to induce the local oxidation of the underlying chromium layer.



Figure 6: optical image of the degraded gold substrate.

$E_{UME} = 0.5 \text{ à } 10\text{V}$ ,  $100 \text{ mV s}^{-1}$ , 3 cycles,  $E_s^{oc} = 0.815\text{V}$  (when UME reaches 10V),  $100 \text{ }\mu\text{m-Pt}$ ,  $d = 20 \text{ }\mu\text{m}$ .  
 $[AA]: 2.0 \text{ mol. dm}^{-3}$ ,  $DNB: 2 \cdot 10^{-3} \text{ mol. dm}^{-3}$ ,  $H_2SO_4: 0.25 \text{ mol. dm}^{-3}$ ,  $100 \text{ }\mu\text{m-Pt}$ ,  $d = 20 \mu\text{m}$ .

Therefore to avoid this phenomenon, the substrate potential was held to negative values during experiments.  $-0.4 \text{ V vs. Ag wire}$  value was chosen for the substrate potential ( $E_{Sub}$ ). The average tip and substrate currents measured during the potential application were then plotted and coupled with the grafting results (fig.7).

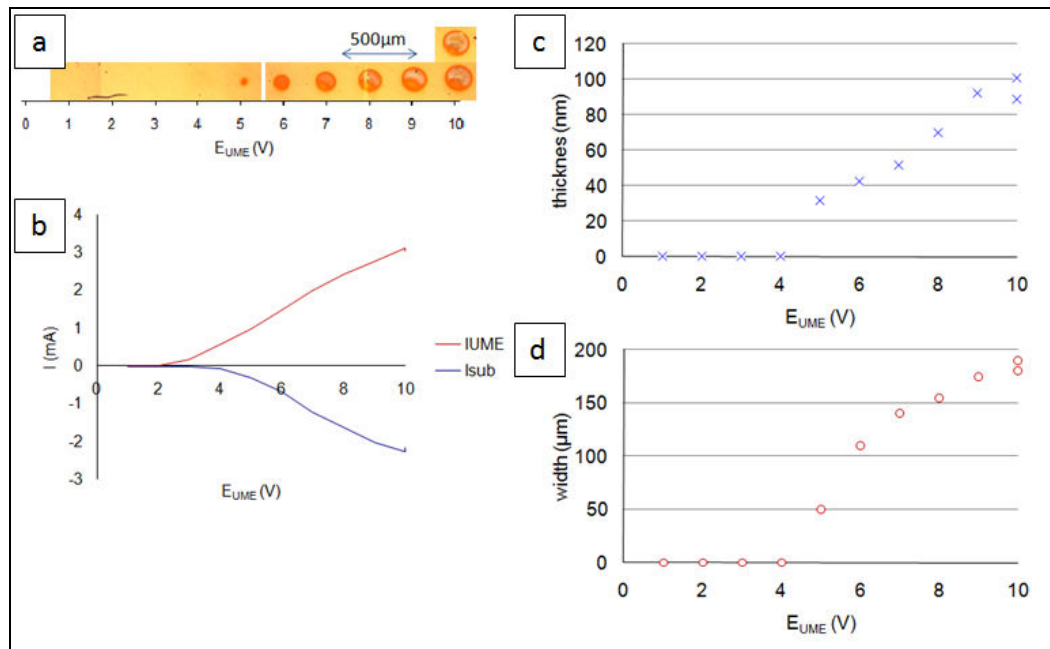


Figure 7: Optical image of grafted dots for different potential imposed to UME (a); corresponding currents recorded at both electrodes (UME in red, substrate in blue) (b); measured thickness (c) and width (d) by profilometry.  $[AA]: 2.0 \text{ mol. dm}^{-3}$ ,  $DNB: 2 \cdot 10^{-3} \text{ mol. dm}^{-3}$ ,  $H_2SO_4: 0.25 \text{ mol. dm}^{-3}$ ,  $100 \text{ }\mu\text{m-Pt}$ ,  $d = 20 \mu\text{m}$ ,  $t = 5\text{s}$ .

The localized electrografting process was detected starting from  $E_{UME} \geq 5$  V/Ag wire although oxidation of water started at  $E_{UME} > 2$  V/Ag wire ( $I_{UME} \neq 0$  for  $E_{UME} > 2$  V) (fig. 7a and 7b). In fact, the localized process starts when the substrate begins to detect a cathodic current induced by the reduction of the species electrogenerated at the tip. In other words, it seems necessary to obtain a minimal flux or concentration of the "tip-generated species" in the tip/substrate gap in order for a part of it to be detected by the substrate where they are reduced. Let's consider the collection efficiency by the substrate ( $I_{sub}/I_{UME}$ ) for the different electrolytic solutions reported in table 3: sulfuric acid alone, sulfuric acid / acrylic acid, and sulfuric acid / acrylic acid / NBD. When the tip is closed to the substrate ( $d/a=0.4$ ) and is polarized at 7 V vs. Ag wire, almost 90% of the tip generated species are detected on the substrate. However, this coefficient falls down to around 70% when acrylic acid is present in the solution. This result indicates that acrylic acid is likely to consume some "tip-generated species" which can no longer be detected by the substrate. Moreover, the collection coefficient goes down near 60% when the diazonium salt is added to the solution. In this last case,  $I_{sub}$  is affected by the passivation of the substrate due to the grafting of the polynitrophenylene-like layer.

Composition	$I_{sub}/I_{UME}$ $E_{UME} = 7V/Ag$ wire
$H_2SO_4$ 0.25 mol.dm <sup>-3</sup>	0.85
$H_2SO_4$ (0.25 mol.dm <sup>-3</sup> )/AA (2.0 mol. dm <sup>-3</sup> )	0.68
NBD ( $2 \cdot 10^{-3}$ mol.dm <sup>-3</sup> )/ $H_2SO_4$ (0.25 mol.dm <sup>-3</sup> )/AA (2.0 mol. dm <sup>-3</sup> )	0.63

Table 3: Collection efficiency ( $I_{sub}/I_{UME}$ ) as a function of the electrolytic solution for  $E_{UME} = 7V/Ag$  wire. 100- $\mu$ m Pt,  $d/a = 0.4$ ,  $E_{sub} = -0.4V/Ag$  wire.

To sum up, short working distance and high tip polarization create a channel through which the electrogenerated species are flowing. On their pathway, these species can react each other or with the components of the electrolytic solution creating active species starting the polymerization process of the vinylic monomer for the SEEP process.

The thickness of the dot pattern increases linearly with the tip potential (fig. 7c) while the width of the pattern reaches a plateau for the highest  $E_{UME}$  values (fig. 7d). This behavior can be explain by the fact that (i) the electrogenerated species are more abundant as the tip potential increases (thicker coating vs. tip potential), (ii) the area over which the generated species spread off is essentially governed by the competition between their hemispherical diffusion/migration time and their rate of consumption by coupled chemical reaction. Indeed, the tip-generated species predominantly diffuse and/or migrate toward the large substrate rather than escaping from the tip/substrate

gap, but coupled chemical reactions can occur during their journey toward the substrate.

It must be highlighted that we found the same behavior for the localization of the grafting from the diazonium salt alone, as shown on figure 8: the localization process starts from  $E_{UME} > 3V$  vs. Ag wire.



Figure 8: Localization of the grafting from the diazonium salt alone. Optical image of grafted dots for different potentials imposed to UME;  $E_{sub} = -0.4V$ /Ag wire,  $DNB: 2 \cdot 10^{-3} \text{ mol.dm}^{-3}$ ,  $H_2SO_4: 0.25 \text{ mol.dm}^{-3}$ ,  $100 \mu\text{m-Pt}$ ,  $d = 20 \mu\text{m}$ ,  $t = 5\text{s}$ .

It is also important to note that reaching the proton reduction regime on the substrate is not a necessary condition to observe the localization effect, as demonstrated by the following experiment when the potential applied to the substrate is kept at  $-0.7V$  vs. Ag wire (i.e. a potential for which the entire substrate area undergoes the reduction of the proton). At this cathodic potential corresponds, on the entire substrate, a background constant current around  $500 \mu\text{A}$  ( $I_{sub, bg}$ ). Therefore, the substrate current ( $I_{sub}$ ) recorded as a function of the tip applied potential corresponds in fact to the sum of two contributions (equation 4.5): the current coming from the reduction of the actual collected species ( $I_{sub, col}$ ) and  $I_{sub, bg}$ . Measuring  $I_{sub}$  and knowing  $I_{sub, bg}$ , we can deduce  $I_{sub, col}$ . It is this value that we use to calculate the collection efficiency reported on figure 9.

$$I_{sub} = I_{sub,col} + I_{sub,bg} \quad (4.5)$$

Even when the substrate potential is able to reduce the protons on the entire area, the localization effect only starts for  $E_{UME} \geq 5V$  vs. Ag wire, i.e. at a potential for which the collection efficiency becomes significantly different from zero (fig. 9), and in particular higher than 0.3.

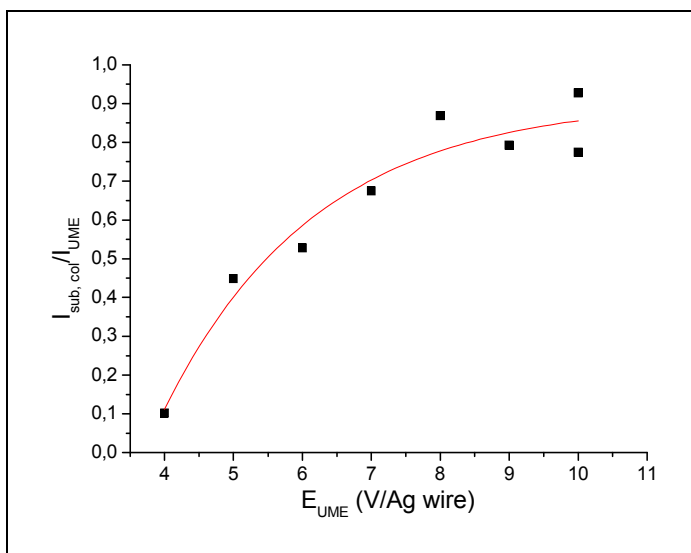
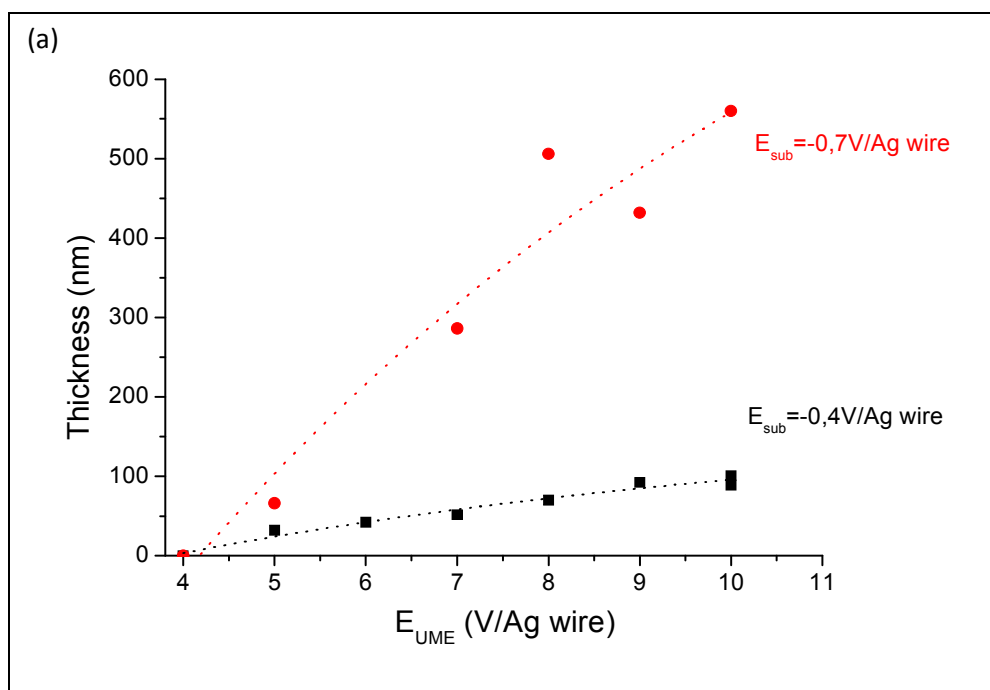


Figure 9: ratio of the current actually collected by the substrate polarized at  $-0.7V/Ag$  wire and the current measuring at UME ( $I_{sub,co}/I_{UME}$ ) as a function of the potential applied to the tip.  $100\text{-}\mu\text{m Pt}$ ,  $d/a=0.4$ ,  $t=5s$ ,  $[AA]:2.0\text{ mol. dm}^{-3}$ ,  $DNB:2\ 10^{-3}\text{ mol. dm}^{-3}$ ,  $H_2SO_4:0.25\text{ mol. dm}^{-3}$ . Scatter: experimental data, line: fit data.

On figure 10, we compare the results obtained with the two different applied substrate potentials ( $-0.4V$  and  $-0.7\text{ V vs. Ag wire}$ , respectively). We observe that the thickness of the coating increases approximately linearly with the tip potential for both applied potentials to the substrate, but with a different rate. On the other hand, the width of the pattern reaches a plateau more quickly and for a lower tip potential when the potential imposed to the substrate is more cathodic.



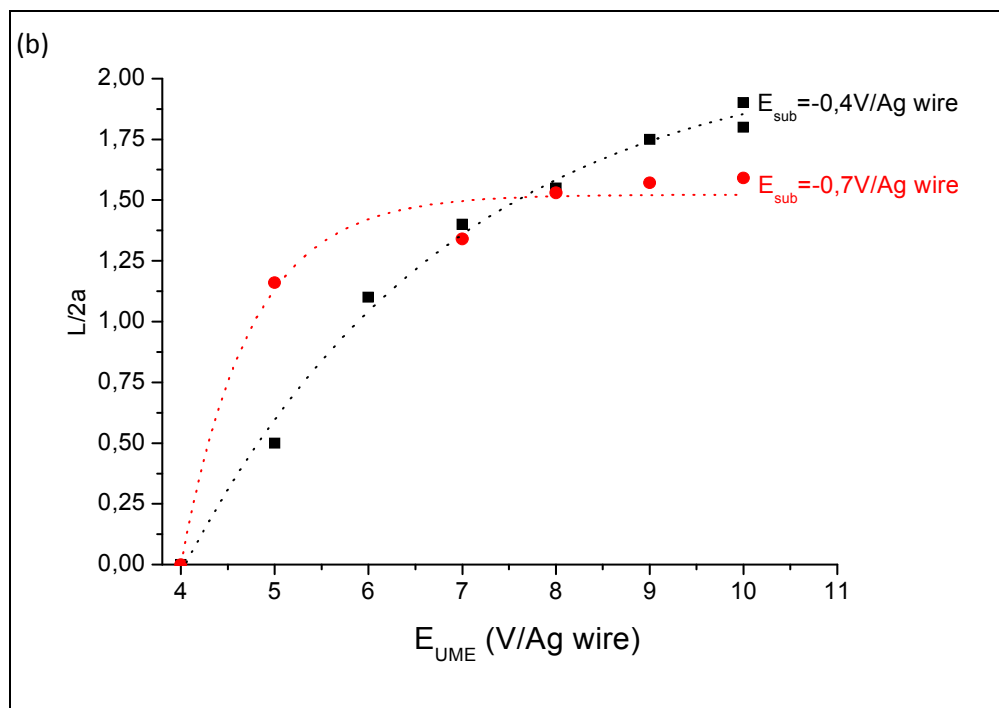


Figure 10: Thickness (a) and width (b) of the dot pattern as a function of the applied tip potential for two different imposed substrate potentials:  $-0.7V/Ag$  wire (red),  $-0.4V/Ag$  wire (black). Scatter: experimental data, dotted line: fit data.

[AA]: $2.0 \text{ mol. dm}^{-3}$ , DNB: $2 \cdot 10^{-3} \text{ mol. dm}^{-3}$ ,  $H_2SO_4$ : $0.25 \text{ mol. dm}^{-3}$ ,  $100 \mu\text{m-Pt}$ ,  $d = 20\mu\text{m}$ ,  $t=5s$ .

### 3. Influence of the potential applied to the substrate

Up to now, we have seen that the substrate potential must be more negative than the rest potential (VOC=open circuit potential) measured on surface before electrochemistry to avoid the degradation of the substrate. But, we do not know if it is a sufficient condition or if it is necessary to reach on the substrate a threshold potential beyond which the localization appears. Therefore, we performed chronoamperometry experiments where the UME potential was kept constant and equal to 7 V vs. Ag wire, while the substrate potential was scanned in the range of 0 V to  $-0.85$  V vs. Ag wire. The other experimental parameters were the same as previously, i.e. 5 s time of polarization, and  $d/a = 0.4$ . As shown on figure 11, the localized effect was observed in all the scanned range of  $E_{sub}$  potential. The beginning of the localized process seems thus to be more related to the value of the potential applied to the tip than to the value of the potential applied to the substrate. It seems that the latter only has to be kept at a potential able to reduce the tip generated species. As these species are essentially  $H^+$  and oxygen reactive species in our case, this potential has only to be more negative than zero.

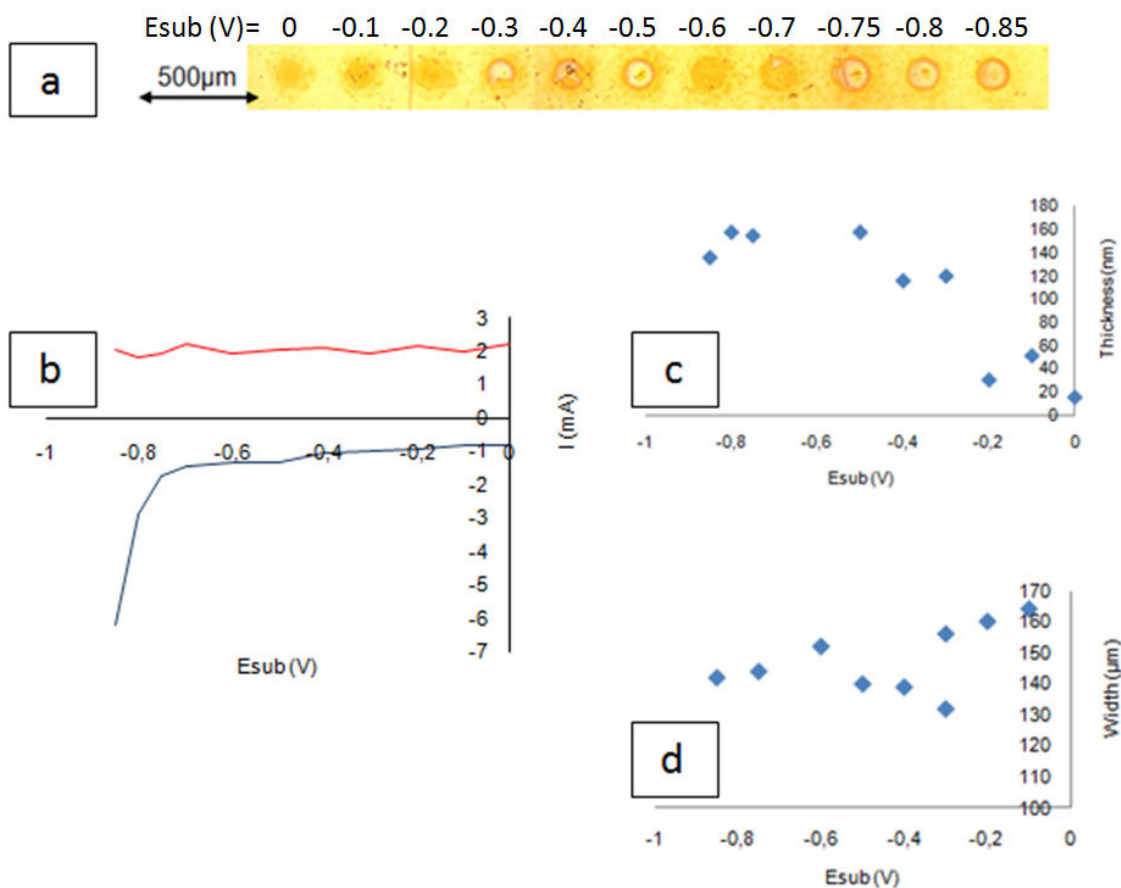


Figure 11: (a) Optical image of grafted dots for different potentials imposed to the surface; (b) corresponding currents recorded at both electrodes (UME in red, substrate in blue); measured thickness (c) and width (d) by profilometry.  $[AA]: 2.0 \text{ mol. dm}^{-3}$ ,  $DNB: 2 \cdot 10^{-3} \text{ mol. dm}^{-3}$ ,  $H_2SO_4: 0.25 \text{ mol. dm}^{-3}$ ,  $E_{UME} = -0.7 \text{ V/Ag wire}$ ,  $100 \mu\text{m-Pt}$ ,  $d = 20 \mu\text{m}$ ,  $t = 5 \text{ s}$ .

The width of the dot pattern varies very lightly with  $E_{sub}$  while the thickness first increases linearly with  $E_{sub}$  before reaching a plateau. The low dependency of the width with the substrate potential indicates that this parameter is mainly controlled by the tip potential as seen in the previous section. The thickness of the coating is related to the quantity of the tip-generated species that can be reduced on the substrate. This quantity increases with the negative potential, and most probably corresponds to the reduction of the protons generated at the tip. Indeed, following the Nernst equation (relation 7), the reduction potential of proton depends upon its concentration.

$$E = E^0 - 0.059 \text{ pH} \quad (7)$$

When  $E_{sub}$  becomes equal or more negative than -0.7 V vs. Ag wire, the recorded substrate current increases drastically since the proton reduction occurring on the entire substrate area dominates the voltamperogram.

Once again, for all the scanned substrate potential range, the collection efficiency is better than 0.30 (fig.12).

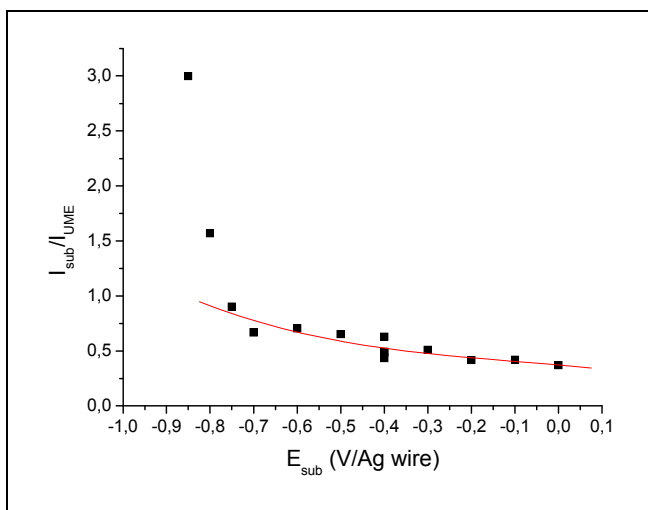


Figure 12: Collection efficiency ( $I_{\text{sub}}/I_{\text{UME}}$ ) as a function of the potential applied to the substrate.  $E_{\text{UME}}=7\text{V/Ag wire}$ ,  $100\text{-}\mu\text{m Pt}$ ,  $d/a=0.4$ ,  $t=5\text{s}$ ,  $[\text{AA}]:2.0\text{ mol. dm}^{-3}$ ,  $\text{DNB}:2\ 10^{-3}\text{ mol. dm}^{-3}$ ,  $\text{H}_2\text{SO}_4:0.25\text{ mol. dm}^{-3}$ . Scatter: experimental data, line: fit data

An analog behavior was observed for the localization of the grafting from the diazonium salt alone, i.e. a poor dependence of the shape of the localized grafting on the potential applied to the substrate (fig. 13).

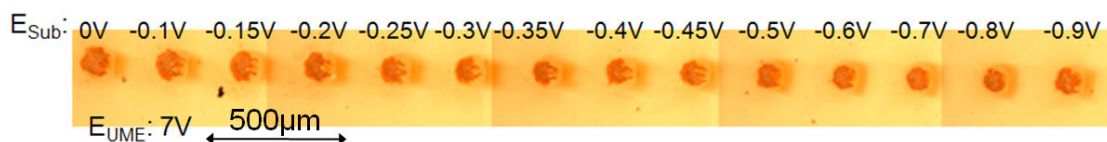


Figure 13: Localization of the grafting from diazonium salt alone. Optical image of grafted dots for different potential imposed to the substrate;  $E_{\text{UME}}=7/\text{Ag wire}$ ,  $\text{DNB}:2\ 10^{-3}\text{ mol. dm}^{-3}$ ,  $\text{H}_2\text{SO}_4:0.25\text{ mol. dm}^{-3}$ ,  $100\ \mu\text{m-Pt}$ ,  $d = 20\ \mu\text{m}$ ,  $t=5\text{s}$ .

In conclusion, this set of experiments shows clearly that the localization effect is strongly related to the potential applied to the tip rather than to the potential applied to the substrate. For the latter, the only requirement is to impose a potential that allows (i) the reduction of the diazonium salt (i.e. on gold substrate, in our electrolytic solution,  $E_{\text{sub}} \leq 0\text{ V vs. Ag wire}$  (see chapter 2)) and (ii) the reduction of the tip-generated species. Moreover, those tip-electrogenerated species have to be detected at the substrate with a minimum efficiency ( $\geq 0.35$ ) to start the localization effect. In other words, in the tip/substrate gap, a very specific reactive medium resulting from the species coming from the tip as well as from the substrate is created. In this reactive container, taken into account our very specific potential conditions, various radicals are formed which react with the components of the electrolytic solution, in particular the vinylic monomer. Moreover, in this gap, local pH variations are also produced with an acidification of the medium around the tip (resulting from the  $\text{H}^+$  production by oxidation of water) and an increase of the pH close to the substrate by consumption of  $\text{H}^+$  by the reduction process. Acrylic acid is a pH sensitive species ( $\text{pK}_a=4.2$ ) which tends to dissociation when pH increases. Hence, a potential-induced distribution of acrylic acid derivatives is likely to form in the tip-substrate gap: acrylic acid more

abundant near the tip, and its acrylate base form predominant close to the substrate; the latter species is sensitive to the electric field.

#### 4. Influence of working distance on the localized reaction

Let's now study the influence of the working distance on the localization effect for three different applied tip potentials: 4V, 7V, and 10V vs. Ag wire. The substrate potential (the less determinant parameter as we have seen above) was kept constant at -0.4V vs. Ag wire in order to avoid perturbation by the reduction of the protons on the entire substrate area. Explored working distances are included in the range of  $0.1 < d/a < 2$ . Dots were realized by chronoamperometry technique ( $t=5s$ ), with a  $100\ \mu\text{m}$ -Pt UME and using the usual electrolytic solution ( $[AA]\ 2.0\ \text{mol}\cdot\text{dm}^{-3}$ ,  $\text{DNB}\ 2\ 10^{-3}\ \text{mol}\cdot\text{dm}^{-3}$ ,  $\text{H}_2\text{SO}_4\ 0.25\ \text{mol}\cdot\text{dm}^{-3}$ ). Figure 14 shows the optical images of the localized pattern. As already observed, no localization was detected for  $E_{\text{UME}} = 4\text{V}$ , even for the shortest working distance. The localization was lost, in an abrupt way, for  $d/a > 1.2$  and  $d/a > 1.6$  when  $E_{\text{UME}}=7\text{V}$ , and  $E_{\text{UME}}=10\text{V}$  respectively. This behavior must certainly be related to the collection efficiency that goes down below 0.35, value which seems to be a threshold value for observing the localization effect (fig. 15). In other words, the localization is lost for normalized working distances higher than 1.6, which corresponds more or less to the distance above which the two electrodes stop "speaking to each other".

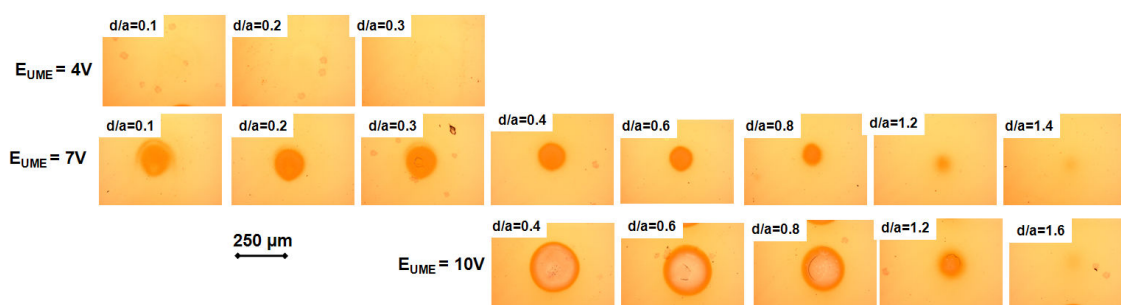


Figure 14: optical images of the dots pattern for three different tip potentials: top:  $E_{\text{UME}}=10\text{V}/\text{Ag wire}$ ; middle:  $E_{\text{UME}}=7\text{V}/\text{Ag wire}$ , bottom:  $E_{\text{UME}}=4\text{V}/\text{Ag wire}$ .  $E_{\text{sub}}=-0.4\text{V}/\text{Ag wire}$ ,  $100\text{-}\mu\text{m Pt}$ ,  $t=5\text{s}$ ,  $[AA]:2.0\ \text{mol}\cdot\text{dm}^{-3}$ ,  $\text{DNB}:2\ 10^{-3}\ \text{mol}\cdot\text{dm}^{-3}$ ,  $\text{H}_2\text{SO}_4:0.25\ \text{mol}\cdot\text{dm}^{-3}$ .

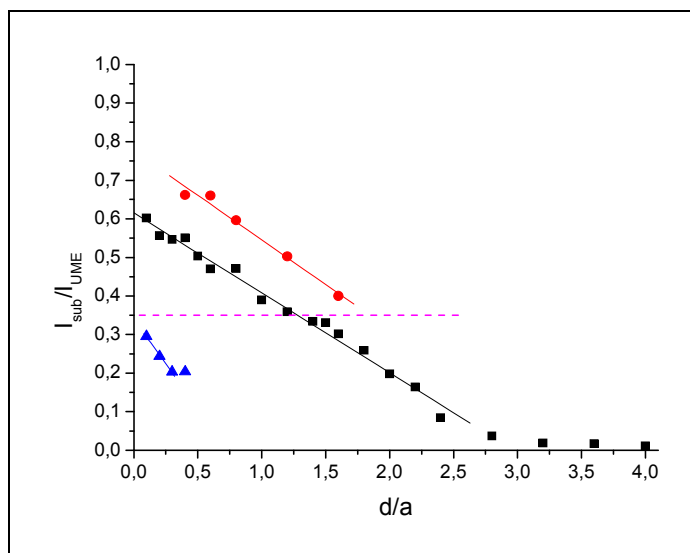


Figure 15: Collection efficiency ( $I_{sub}/I_{UME}$ ) as a function of the normalized working distance for three different potentials applied to the tip:  $E_{UME} = 10V/Ag$  wire (red),  $E_{UME} = 7V/Ag$  wire (black),  $E_{UME} = 4V/Ag$  wire (blue),  $E_{sub} = -0.4V/Ag$  wire,  $100\text{-}\mu\text{m Pt}$ ,  $t=5s$ ,  $[AA]:2.0\text{ mol. dm}^{-3}$ ,  $DNB:2 \cdot 10^{-3}\text{ mol. dm}^{-3}$ ,  $H_2SO_4:0.25\text{ mol. dm}^{-3}$ . Scatter: experimental data, line: linear fit data. Dash lines: end of the localized process.

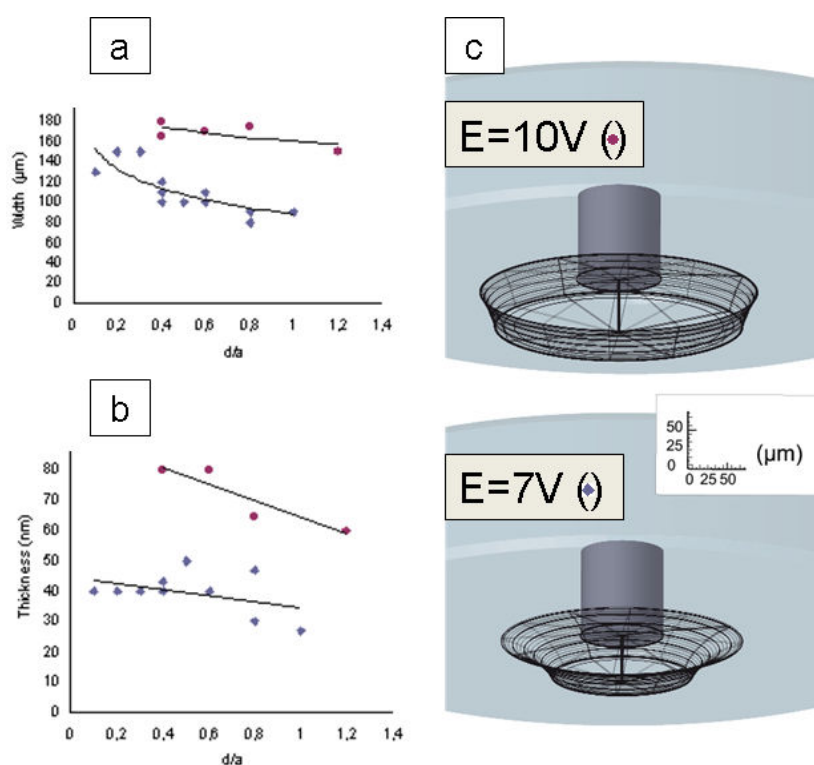


Figure 16: Width (a) and thickness (b) of the dots pattern as a function of the normalized working distance for two different tip potentials:  $E_{UME} = 7V/Ag$  wire (red),  $E_{UME} = 10V/Ag$  wire (blue), while  $E_{sub}$  is kept equal to  $-0.4V/Ag$  wire.  $[AA]:2.0\text{ mol. dm}^{-3}$ ,  $DNB:2 \cdot 10^{-3}\text{ mol. dm}^{-3}$ ,  $H_2SO_4:0.25\text{ mol. dm}^{-3}$ ,  $100\text{ }\mu\text{m-Pt}$ ,  $t=5s$ . Scatter: experimental data, lines: fit data. (c) reactive volume reconstruction under the UME for  $E_{UME} = 10V/Ag$  wire (top) and  $E_{UME} = 7V/Ag$  wire (bottom).

For a 7V bias applied to the tip, as well as for a 10V bias (vs. Ag wire), the width and the thickness of the grafting decrease slightly during the withdraw of the UME (fig. 16 a, b). The shape and the size of the dot pattern allow the reconstruction of the reactive volume under the UME in function of the working distance. Indeed, dots realized at a particular working distance represent the section of the volume where are produced the physico-chemical conditions able to localize the grafting. This volume, delimited by black lines (fig. 16c), shows the reactive domain in function of surface-UME distances; out of this volume no localization was observed. For a 100- $\mu\text{m}$  Pt UME, the "optimal" working distance to get a uniform and reproducible localized coating is around 20-40  $\mu\text{m}$ , corresponding to a normalized working distance between 0.4 and 0.8. By the way, this range is fully consistent with the results already observed in the three-electrode configuration (see chapter 3).

As also already observed for the three-electrode configuration, the range of working distance for which the localized effect is observed can be extended to larger values if harder experimental conditions are applied. For example, when the 100- $\mu\text{m}$  Pt tip is biased at 10V vs. Ag wire, the localization is lost at 80  $\mu\text{m}$  far from the substrate surface whereas this distance is only 60  $\mu\text{m}$  when 7V vs. Ag wire is applied to the tip.

## **5. Influence of the electrolysis duration**

### ***5.1. Investigation of the kinetic of reaction***

Experiments similar to those realized with the three-electrode configuration (see section 2.2.2 chapter 3) were reproduced in the four-electrode configuration. We set the tip and substrate potentials to 7V vs. Ag wire and -0.4V vs. Ag wire respectively, and we followed the growth of the polymer coating as a function of electrolysis duration by AFM analysis. 25- $\mu\text{m}$  Pt UME was used and placed at a constant normalized working distance equal to 0.8. After synthesis, samples were rinsed carefully before forthcoming analyses. AFM images were recorded in contact mode and gathered on figure 17.

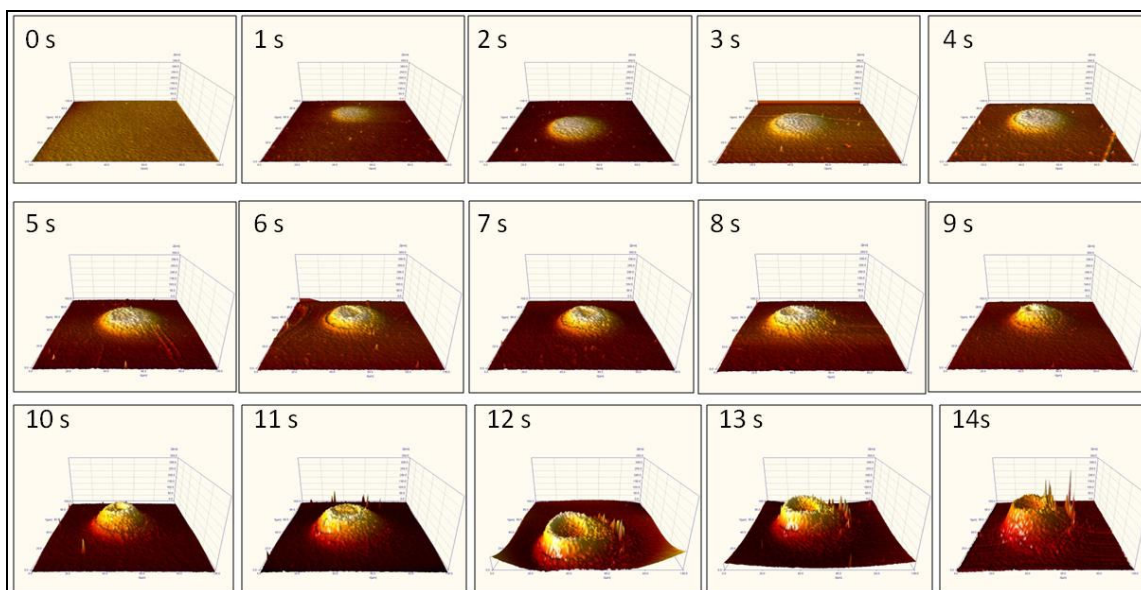


Figure 17: Evolution of the growth of the localized dot as a function of electrolysis time by AFM analysis in contact mode: 3D topographic images. The x-y-z scales are equivalent for all the images and are  $100\ \mu\text{m} \times 100\ \mu\text{m} \times 350\ \text{nm}$  respectively. [AA]:  $2.0\ \text{mol. dm}^{-3}$ , DNB:  $2 \cdot 10^{-3}\ \text{mol. dm}^{-3}$ ,  $\text{H}_2\text{SO}_4$ :  $0.25\ \text{mol. dm}^{-3}$ ,  $E_{\text{UME}} = 7\text{V}$  vs. Ag wire,  $E_{\text{sub}} = -0.4\text{V}$  vs. Ag wire,  $25\ \mu\text{m-Pt}$ ,  $d = 10\ \mu\text{m}$ .

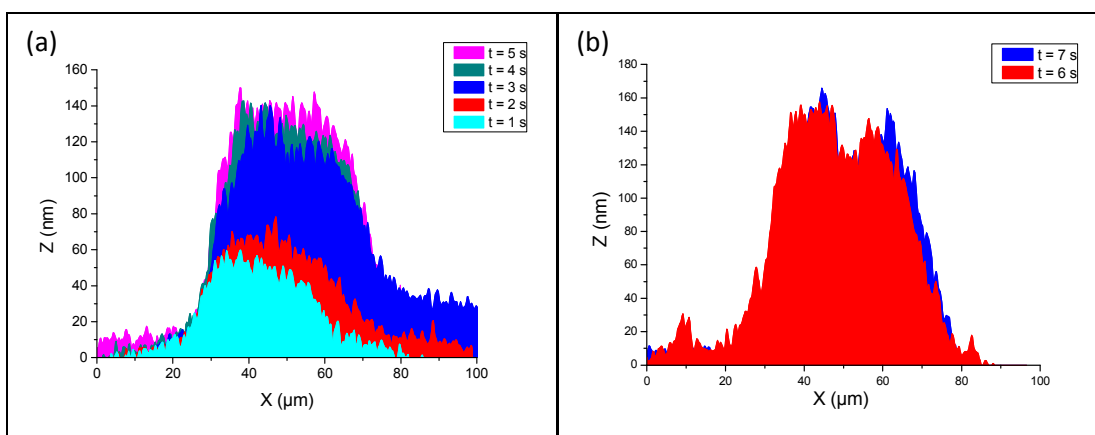


Figure 18: AFM dots profiles as a function of time: (a) 1 - 5 s; (b) 6-7 s. [AA]:  $2.0\ \text{mol. dm}^{-3}$ , DNB:  $2 \cdot 10^{-3}\ \text{mol. dm}^{-3}$ ,  $\text{H}_2\text{SO}_4$ :  $0.25\ \text{mol. dm}^{-3}$ ,  $E_{\text{UME}} = 7\text{V}$  vs. Ag wire,  $E_{\text{sub}} = -0.4\text{V}$  vs. Ag wire,  $25\ \mu\text{m-Pt}$ ,  $d = 10\ \mu\text{m}$ .

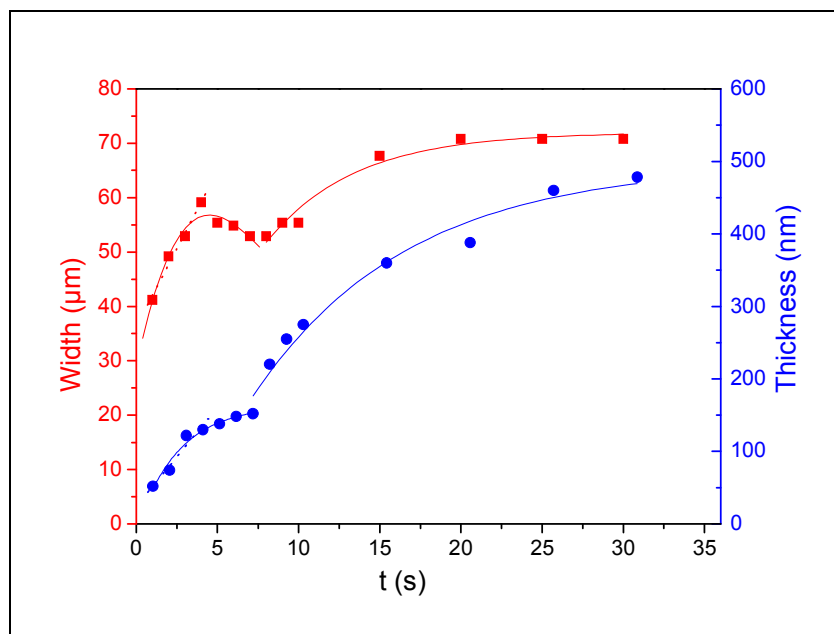


Figure 19: Evolution of the width (red) and the thickness (blue) of the dots pattern as a function of electrolysis duration; scatter: experimental data, line: fit data.  $25 \mu\text{m}$ -Pt UME,  $d = 10 \mu\text{m}$ ,  $E_{\text{UME}} = 7\text{V}$  vs. Ag wire,  $E_{\text{sub}} = -0.4\text{V}$  vs. Ag wire,  $[\text{AA}]: 2.0 \text{ mol. dm}^{-3}$ ,  $[\text{DNB}]: 2 \cdot 10^{-3} \text{ mol. dm}^{-3}$ ,  $\text{H}_2\text{SO}_4: 0.25 \text{ mol. dm}^{-3}$ .

The width and the thickness of the localized coating can be extracted from the AFM analyses (fig. 18) and the results are plotted on figure 19. We observe clearly the two different time regimes already put in evidence in the case of the three-electrode configuration (see chapter 3). It is also interesting to note that the time scale is approximately the same for both configurations; i.e. the width and the thickness of the coating first follows a polynomial fit with a linear tendency up to  $t = 5 \text{ s}$  and then, for longer time ( $8 \text{ s} < t < 30 \text{ s}$ ), follow a second order polynomial fit. The AFM images show also clearly the ablation of the top of the coating with time. Increasingly deep cracks appear with time on the top layer. Most probably, the high reactivity of the oxidative agent generated under the tip is responsible of this phenomenon. The highly polarized tip would thus act as a gun projecting very reactive agents able to etch the top surface towards the substrate. Moreover, for long time of polarization of the tip at a high anodic potential ( $t > 5\text{s}$  for  $E_{\text{UME}} = 7\text{V}/\text{Ag}$  wire), figure 20 shows that some parts of the coating break off from the substrate in the 30 s chronoamperometry. Accumulation of high electrical constraints and gaseous species formation ( $\text{H}_2$ ) at the interface are certainly responsible for that behavior.

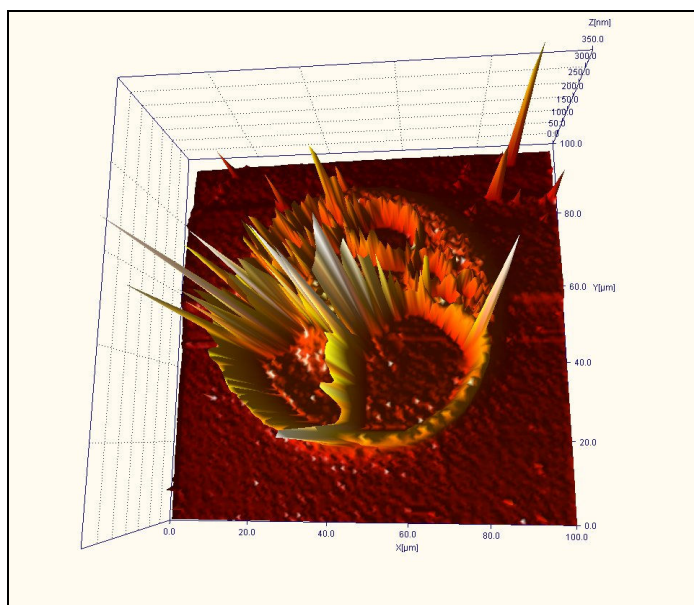


Figure 20: Inside view of the "exploded" dot pattern resulting from high tip polarization for a long time:  $25\ \mu\text{m}$ -Pt UME,  $d = 10\ \mu\text{m}$ ,  $E_{\text{UME}} = 7\text{V}$  vs. Ag wire,  $E_{\text{sub}} = -0.4\text{V}$  vs. Ag wire,  $t = 30\text{s}$ ,  $[\text{AA}]: 2.0\ \text{mol. dm}^{-3}$ ,  $\text{DNB}: 2 \cdot 10^{-3}\ \text{mol. dm}^{-3}$ ,  $\text{H}_2\text{SO}_4: 0.25\ \text{mol. dm}^{-3}$ .

## 5.2. Potential/time optimization

In paragraphs 2 and 4, we have seen that the tip potential has to be more anodic than 5 V vs. Ag wire to actually detect the localization when the duration of the electrolysis is of the order of few seconds. We have also seen that degradation of the coating appears for  $t > 5\text{s}$ . The "collateral" reactions mentioned just above could be a drawback as the chemical integrity of the coating may be threatened without actual control. For that reason, new attempts of localized grafting at lower tip potential were undertaken ( $E_{\text{UME}} = 4\text{V}$  vs. Ag wire), hoping that the weaker the applied tip potential, the weaker the rate of generation of disturbing oxidizing species, giving so time for SEEP process to proceed before aggressive attack of the generated species.

In practice, we observe that when the tip potential goes down to 4 V vs. Ag wire, the duration of the electrolysis has to be higher than 10 s to start the localization process. Between 20 s and 60 s of electrolysis, the thickness of the coating keeps around  $70 \pm 10\ \text{nm}$  thick while its width is relatively constant and close to the tip's diameter (fig. 21). Moreover, from the observation of the optical images of the grafted dots, any appreciable cracking effect appears before 60 seconds of electrolysis.

In brief, a compromise must be found between the potential applied to the tip and the duration of the electrolysis to observe localization: either we apply a high tip voltage during a short time; either a low tip voltage is privileged during a longer time.

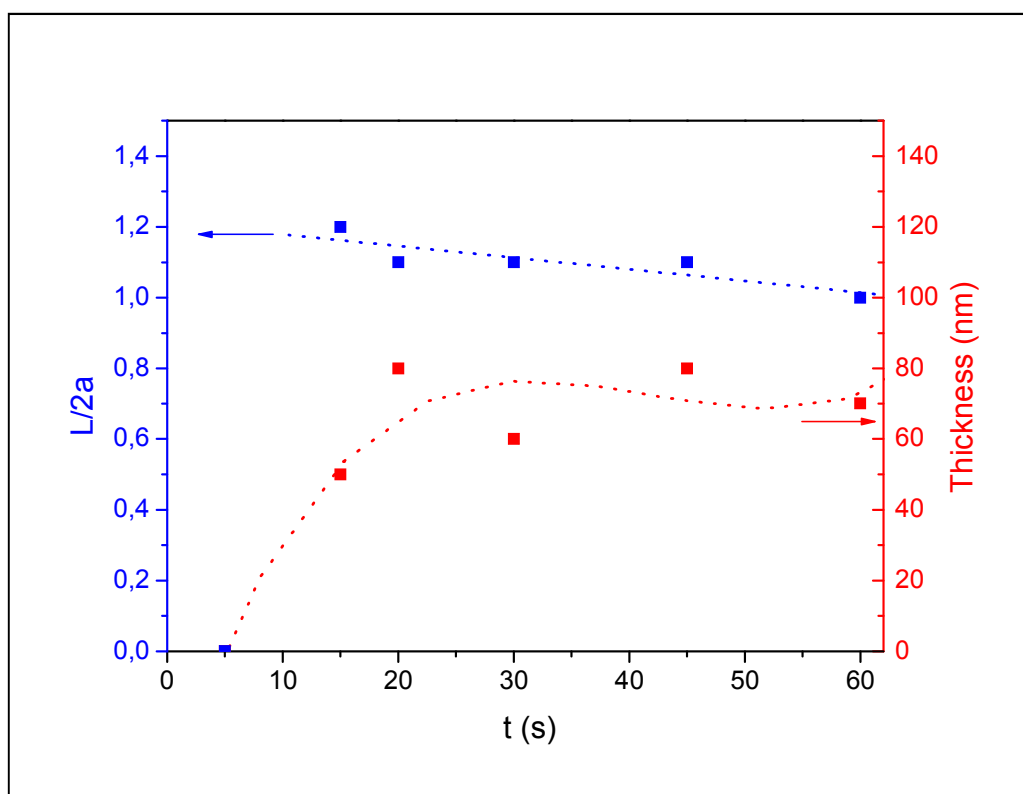


Figure 21: Width and thickness of the coating obtained as a function of electrolysis duration for  $E_{UME} = 4V$  vs. Ag wire,  $100 \mu\text{m}$ -Pt UME,  $d/a = 0.4$ ,  $E_{sub} = -0.4V$  vs. Ag wire,  $[AA]: 2.0 \text{ mol. dm}^{-3}$ ,  $DNB: 2 \cdot 10^{-3} \text{ mol. dm}^{-3}$ ,  $H_2SO_4: 0.25 \text{ mol. dm}^{-3}$ . Scatter: experimental data, line: fit data.

The same kind of experiments was undertaken in the presence of the diazonium salt alone. If we polarize the UME at the threshold potential of  $3V$  vs. Ag wire, the localization process appears for  $t \geq 10s$  and the first signs of the degradation on the top layer of the coating appear after 30 seconds (fig. 22). This observation reinforces our assumption that the biased UME acts like a gun sprinkling the substrate with highly oxidative species which “sputter” the top layer of the coating.

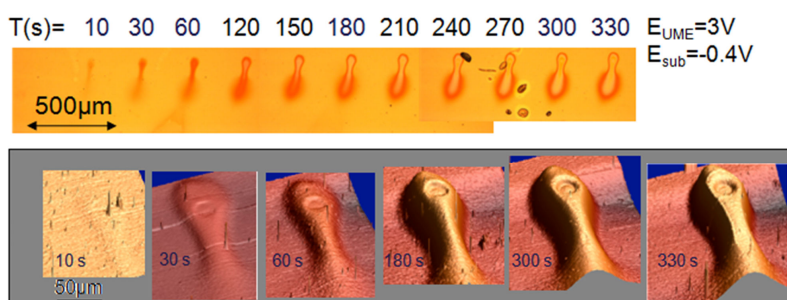


Figure 22: Evolution of the growth of the localized dot as a function of electrolysis time: (a) optical images, (b) AFM analysis in contact mode: 3D topographic images. The x-y-z scales are equivalent for all the images and  $50 \mu\text{m} \times 50 \mu\text{m} \times 200 \text{ nm}$  respectively.

$DNB: 2 \cdot 10^{-3} \text{ mol. dm}^{-3}$ ,  $H_2SO_4: 0.25 \text{ mol. dm}^{-3}$ ,  $E_{UME} = 3V$  vs. Ag wire,  $E_{sub} = -0.4V$  vs. Ag wire,  $25 \mu\text{m}$ -Pt,  $d = 10 \mu\text{m}$ .

On the above picture, we also observe clearly the presence of a “tail” on the back side of the dot, effect totally absent in the case of the mixture NBD/AA. This effect has certainly to be related to the escape of gaseous species formed at the UME which occurs preferentially in a given direction. Under the influence of this flux, the reactive species follow this direction and an image of that flux is "transferred" on the localized grafting. The addition of AA in the solution in relatively high concentration ( $2 \text{ mol. dm}^{-3}$ ) modifies the superficial tension of the liquid and likely affects the gaseous emission.

To sum up, it seems that the growth of the grafted layer and its chemical abrasion are in continuous kinetic competition with each other. Hence, decreasing the potential applied to the tip together with increasing the electrolysis duration promotes the grafting process with respect to the degradation one. The rate at which the species are created (which depends on the potential of the tip), governs the homogeneity of the coating. Lower rate gives more homogeneous coating but better localization requires longer electrolysis time.

A second strategy to minimize the degradation effects resulting from a high anodic potential applied to the tip, is to use the pulsed technique. In practice, the substrate was maintained continuously at  $-0.4\text{V}$  vs. Ag wire while short potential pulses ( $7\text{V}$  vs. Ag wire during  $0.1\text{s}$ ) were imposed to the tip. Between two pulses, the potential of the tip relaxed to  $0\text{V}$  during  $0.4\text{s}$ . On figure 23, we compare dots obtained with this pulsed technique (electrolysis during 50 pulses of  $0.1 \text{ s}$  each) with respect to the one obtained with the continuous way. In both cases, the total duration of the electrolysis was the same and equal to  $5\text{s}$ .

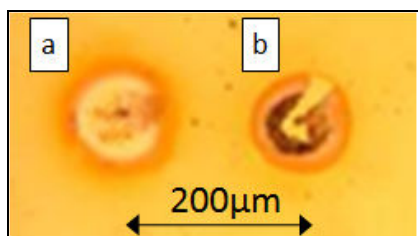


Figure 23: Dots pattern obtained by the pulsed (a) and continuous (b) technique (see text for experimental detail).  $50\text{-}\mu\text{m Pt}$ ,  $E_{\text{UME}}=7\text{V}$ ,  $E_{\text{sub}}=-0.4\text{V}$ ,  $[\text{AA}]:2.0 \text{ mol. dm}^{-3}$ ,  $\text{DNB}: 2 \cdot 10^{-3} \text{ mol. dm}^{-3}$ ,  $\text{H}_2\text{SO}_4:0.25 \text{ mol. dm}^{-3}$ ,  $d/a = 0.4$ .

The thickness of the dot pattern is of the same order in both cases (around  $100 \text{ nm}$  thick). But, the grafted coating is obviously more homogeneous and less degraded with the pulsed technique than with the continuous one. However, the width of the pattern obtained with the pulsed technique is slightly enlarged ( $\sim 10\mu\text{m}$  larger) with borders a little bit more blurred.

Rather than producing continuously a high concentrated flux of reactive agent, the pulsed technique probably generates species in lower quantity which, during the rest time, have time to diffuse rather than migrating to the substrate since the electrical constraints are released. The pulsed approach allows thus to reduce considerably the

degradation of the film and, from that point of view, represents a positive improvement for this process.

## 6. XPS analysis of the localized grafted coating

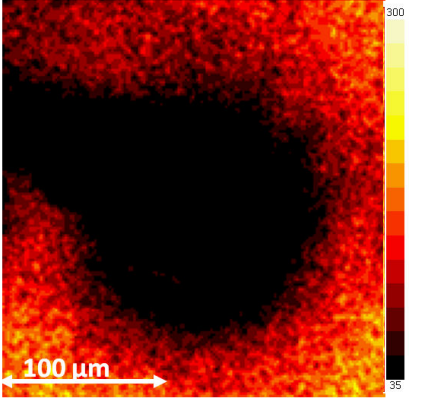
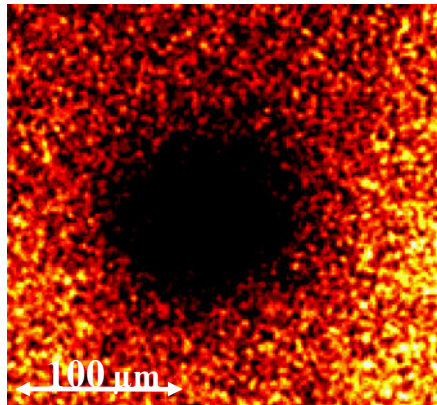
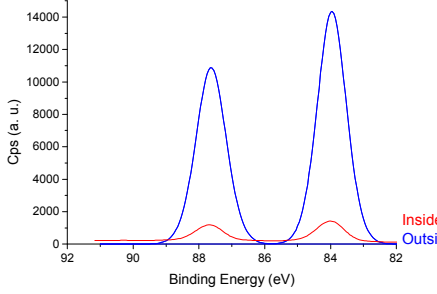
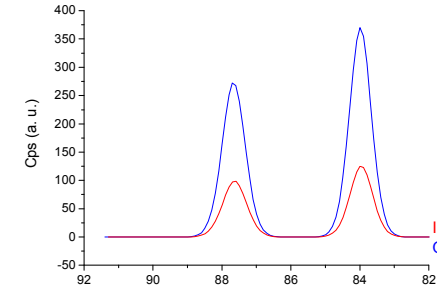
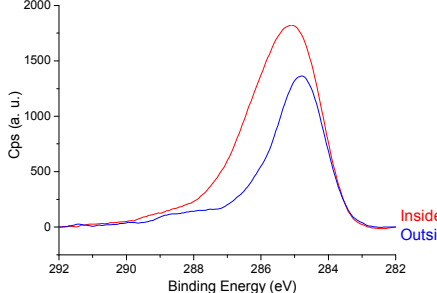
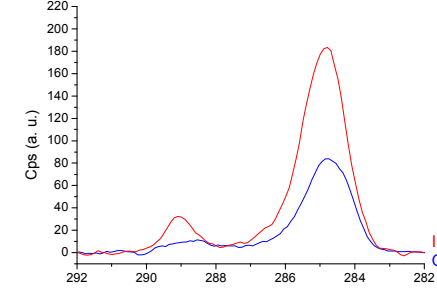
Up to now, we have explored the main experimental parameters (potentials, working distance, duration) that allow us to control satisfactorily the size and the shape of the localized coating; we however have no control on the actual chemistry under the tip. Table 1 synthesizes the XPS analyses undertaken inside and outside the localized pattern, for the NBD/AA system and for the NDB one (we will report to the annex 1 at the end of this chapter to have a complete XPS decomposition analysis of the peaks recorded inside the pattern). This table shows, in both cases, that

(i) the coating is clearly thicker in front of the UME (as shown by the higher attenuation of the Au 4f substrate signal inside the pattern than outside)

(ii) the in/out comparison shows a satisfactory selectivity in particular for the carboxylic functionalities (peak around 289 eV). The potentialities to exploit this selectivity for driving local chemical derivatization (with, for example, biomolecules) will be discussed in the perspectives of this work.

(iii) inside the pattern, the nitro group is partially preserved (peak around 406 eV) while outside the pattern the nitro functionalities disappear. This behavior means that, inside the pattern, nitro groups are partially hidden and protected by the thickness of the layer against their reduction into amino derivatives.<sup>[7]</sup> More precisely, inside the pattern the N1s signal component at high binding energy is large, revealing the presence of NO<sub>2</sub> and additional oxygenated species. We can assume that, inside the pattern, some oxidation of NO<sub>2</sub> groups into nitrate species occurs. This observation has to be related to the oxidative medium which predominates in the tip / substrate gap.

(iv) for both inside and outside analysis but much more marked for the inside one, the oxygen detected is in excess (about 25%) with respect to the carboxylic group detected on the C 1s spectra, even if the contribution of the nitro group (for the inside spectrum) is added. This excess corresponds to oxygenated species like hydroxyl, carbonates and nitrates groups, coming from reactions in our electrolytic solution with the highly oxidative species generated during electrolysis. It must be recalled that this excess of O is not observed for the electrografted coating realized in a non local way, i. e. without electrolysis of water. In this latter case the area of the O 1s peak fits at more than 95% to the sum of the contributions of the NO<sub>2</sub> and -COOH functions.

	Local electrografting in presence of diazonium salt alone in acidic aqueous solution	Local electrografting in presence of diazonium salt and acrylic acid in acidic aqueous solution
Image on Au 4f		
Au 4f		
C 1s		

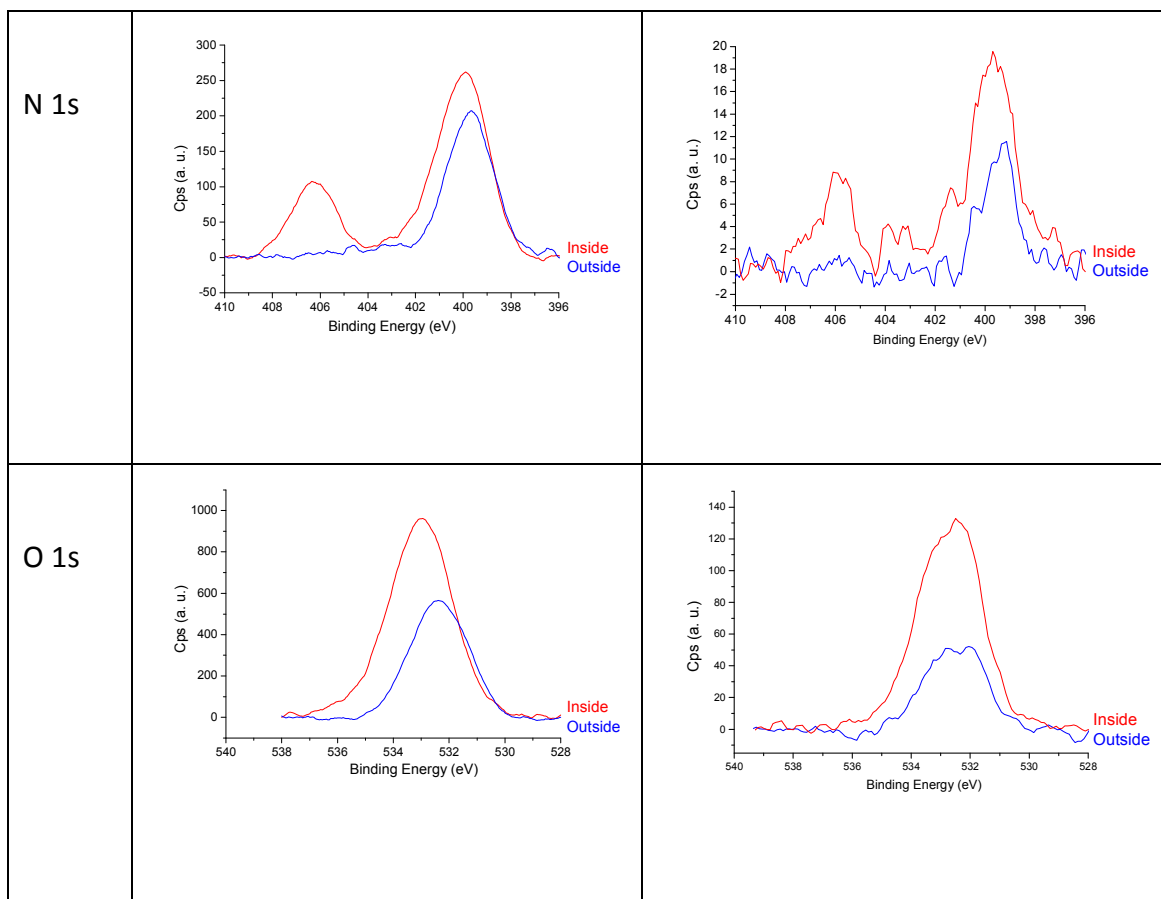


**Table 1:** Elemental map of Au obtained by XPS mapping analysis on localized grafted gold substrate. Acquisition conditions: X-ray source= 225W, high resolution FoV2 (400 x 400  $\mu\text{m}^2$ ), and pass energy= 160eV. Au 4f, C 1s, N 1s, and O 1s core level spectra of the coating recorded inside (red) and outside (blue) the grafted pattern. (top), decomposition of the inside peak (bottom). Acquisition conditions: X-ray source= 225W, high resolution FoV2 (55 x 55  $\mu\text{m}^2$ ), and pass energy= 40 eV.

Left: DNB:  $2 \cdot 10^{-3} \text{ mol} \cdot \text{dm}^{-3}$ ,  $\text{H}_2\text{SO}_4$ :  $0.25 \text{ mol} \cdot \text{dm}^{-3}$ , 100  $\mu\text{m}$ -Pt,  $d = 20 \mu\text{m}$ ,  $t = 5\text{s}$

Right : [AA]:  $2.0 \text{ mol} \cdot \text{dm}^{-3}$ , DNB:  $2 \cdot 10^{-3} \text{ mol} \cdot \text{dm}^{-3}$ ,  $\text{H}_2\text{SO}_4$ :  $0.25 \text{ mol} \cdot \text{dm}^{-3}$ , 50  $\mu\text{m}$ -Pt,  $d = 20 \mu\text{m}$ ,  $t = 5\text{s}$ .

Another aspect of the process that we have not yet discussed in detail (although it is essential for the localization) is the ionic force of the electrolytic solution. Indeed, all the above experiments were carried out in acidic solution without the addition of a supporting electrolyte. Nevertheless, UME and substrate electrodes exchange electrons through the solution thanks to ionic transport. According to the model developed by Osteryoung et al.<sup>[8]</sup> (studying the electroreduction of protons in presence or not of a supporting electrolyte in the solution), ionic transport is mainly supported by the migration of the ionic species present in the solution ( $\text{H}^+$ ,  $\text{HSO}_4^-$ ,  $^+\text{N}=\text{N}-\Phi\text{NO}_2$ ;  $\text{BF}_4^-$ ) in the absence of a supporting electrolyte. These ions migrate, with different rates (as a function of their own mobility) to the cathode (the substrate) for the cationic species and the anode (tip) for the anionic species, respectively. When the tip is biased at high anodic potential and the substrate at moderate cathodic potential, a

high electric field between both electrodes is created which is the driving force for migration of the ions. Moreover, cationic species ( $\text{H}^+$ ,  $^+\text{N}\equiv\text{N}-\Phi\text{NO}_2$ ) moving to the cathodically polarized substrate can be reduced at its surface. The reduction process is kinetically promoted under the tip because it is the place where the ohmic drop is the lowest. The migration flux of the electroactive species generates, in the confined tip / substrate gap, electro-convection movement of the solution. Indeed, near the substrate, a zone characterized by a low concentration in ionic species is created (cations are reduced and anions have migrated to the tip) whereas near the tip an area rich in ionic species is generated (anions coming from the migration and cations produced by water oxidation).<sup>[9]</sup> Therefore, electro-convective flux of the solution can take place from tip to surface and vice versa, delimiting the reactive zone<sup>[10-12]</sup>.

Let's now replace the sulfuric acid by a supporting electrolyte in the solution (e.g.  $\text{K}_2\text{SO}_4$   $0.25 \text{ mol. dm}^{-3}$ ) while maintaining a low pH in the medium. In this condition, the migration effect is mainly supported by  $\text{K}^+$  and  $\text{SO}_4^{2-}$  ions, but the flux associated to these species is null as these ions are electrochemically inert. Therefore, the ions responsible for the cathodic current are transported to the cathode by the hemispherical diffusion process. As a consequence, the localized grafting shows a ring in the presence of the supporting electrolyte instead of a dot (fig.24).

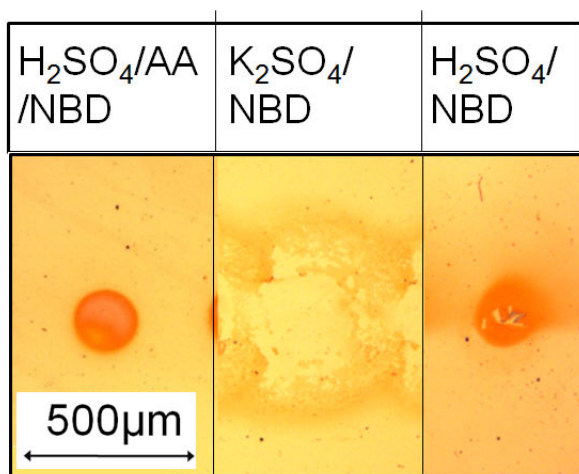


Figure 24: optical images of dot realized with and without supporting salt:  $[\text{AA}]: 2.0 \text{ mol. dm}^{-3}$ ,  $[\text{DNB}]: 2 \cdot 10^{-3} \text{ mol. dm}^{-3}$ ,  $[\text{H}_2\text{SO}_4]: 0.25 \text{ mol. dm}^{-3}$ ;  $[\text{DNB}]: 2 \cdot 10^{-3} \text{ mol. dm}^{-3}$ ,  $[\text{K}_2\text{SO}_4]: 0.25 \text{ mol. dm}^{-3}$ ;  $[\text{DNB}]: 2 \cdot 10^{-3} \text{ mol. dm}^{-3}$ ,  $[\text{H}_2\text{SO}_4]: 0.25 \text{ mol. dm}^{-3}$ .  $E_{\text{UME}} = 7\text{V}$ ,  $E_{\text{sub}} = -0.4\text{V}$ ;  $100 \mu\text{m}-\text{Pt}$ ,  $d = 20 \mu\text{m}$ ,  $t = 5\text{s}$ .

## 7. Plausible steps mechanism responsible for the localized electrografting

It is very difficult to describe the global mechanism responsible for the localized effect because we do not have experimental analysis techniques able to detect *in situ* the chemical nature of the generated species during the localized electrografting process. Moreover, it is difficult to reproduce at a macroscopic scale what is likely to occur in the specific SECM geometry. However, we know that:

- the localization process starts only when the oxidation regime of water is achieved. In this condition, a cathodic current is induced on the substrate when the tip is placed in the feedback distance, i.e.  $d/a < 1.6$ . This cathodic current corresponds to more than 90 % of the anodic current in the absence of vinylic monomer and/or diazonium salt in solution. When these components are present in solution, the collection of the current on the substrate decreases because of (i) the passivation of the substrate by the formation of the polynitrophenylene film, (ii) the consumption of the tip-generated species by the reactants in the tip/substrate gap.

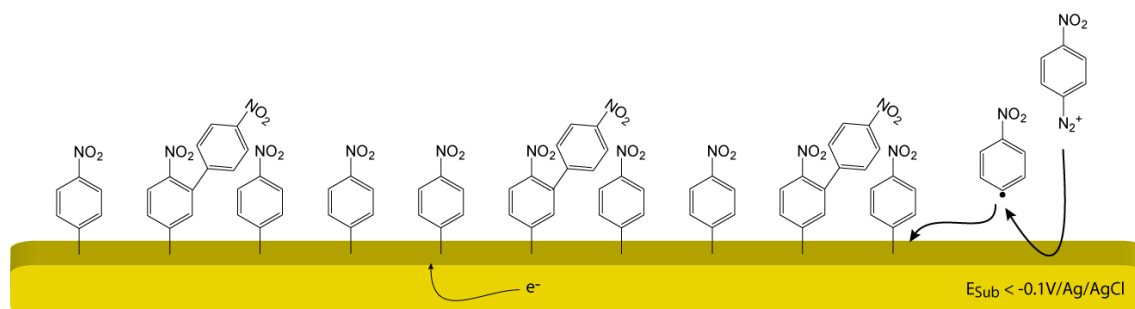
- in the absence of supporting electrolyte, the protons produced at the tip have to migrate rather than to diffuse to the substrate where they can be reduced in order to obtain a well defined localization.

- different neutral, radical and ionic species are produced or concentrated specifically in the tip / substrate gap:  $O_2$ ,  $H_2$ ,  $H_2O_2$ ,  $H_2O^\bullet$ ,  $HO^\bullet$ ,  $S_2O_8^\bullet$ ,  $H^+$ . These products react with components of the electrolytic solution ( $^{\bullet}\Phi-NO_2$ , acrylic acid (HA or A<sup>-</sup>),  $^+N\equiv N-\Phi-NO_2$ ) to induce grafting and initiate the polymerization of the vinylic monomer.

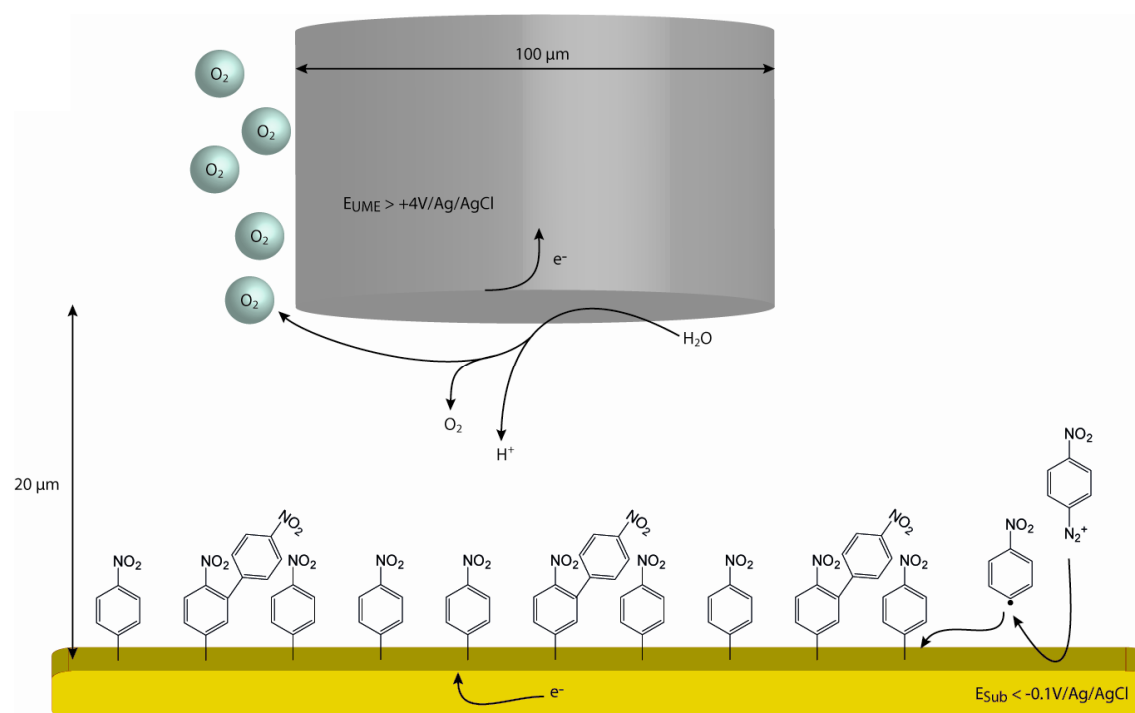
- the components of the electrolytic solution can also be partially degraded by the reactive medium generated under the tip as suggested by the oxygen derivatives detected by XPS on the coating.

This highly complex system results from the high and unusual potentials applied to UME within an aqueous media. The electrodes can be considered as two separated reactors mutually influenced when placed in a nearby position. The highly positively polarized Pt micro-disk generates radicals and cations which are collected on the negatively polarized surface of the substrate. Consequently a local induced current is detected on the substrate. Our electrochemical environment is thus very complex and it is really difficult to evaluate precisely the role played by each component of the electrolytic solution on the localized process. Moreover, most of the identified parameters are interdependent. We are thus reduced to express reasonable assumptions to explain the localized process. The following scheme mimics plausible reactions in the case of the localized grafting from the diazonium salt alone. When acrylic acid monomer is present in the solution, the main steps of the localized grafting process are not modified, the vinylic monomer acting overall as a scavenger for radicals, limiting so their spatial extension.

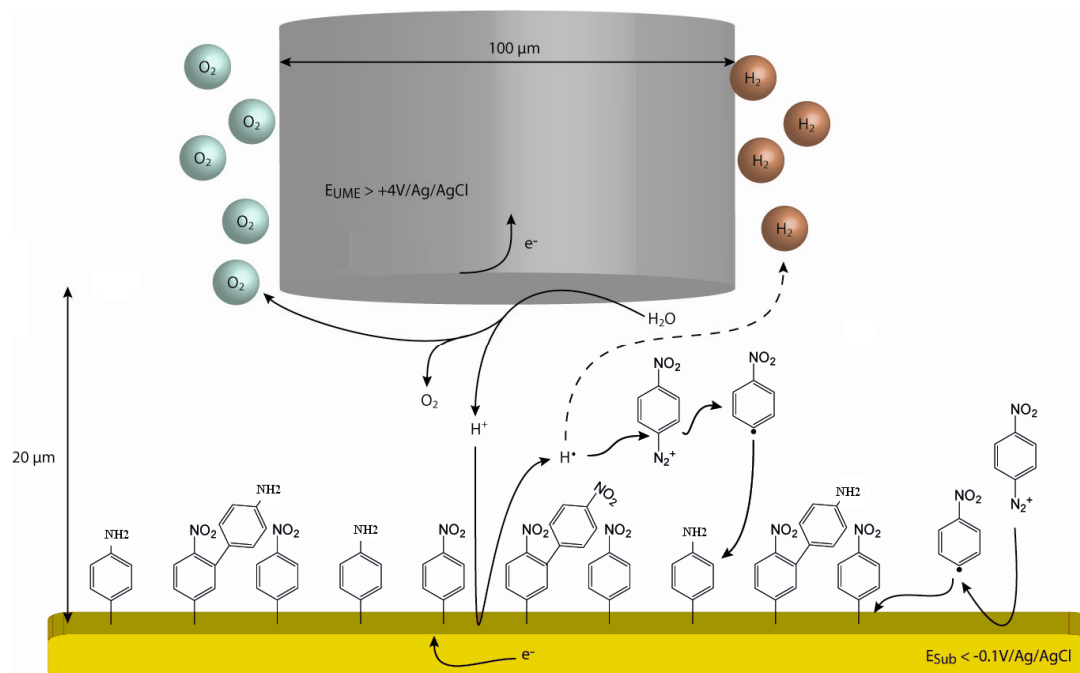
1/ reduction of the diazonium salt on the substrate to form a polynitrophenylene-like film. This film is formed on the entire surface of the substrate but remain very thin (< 10 nm) outside the tip region



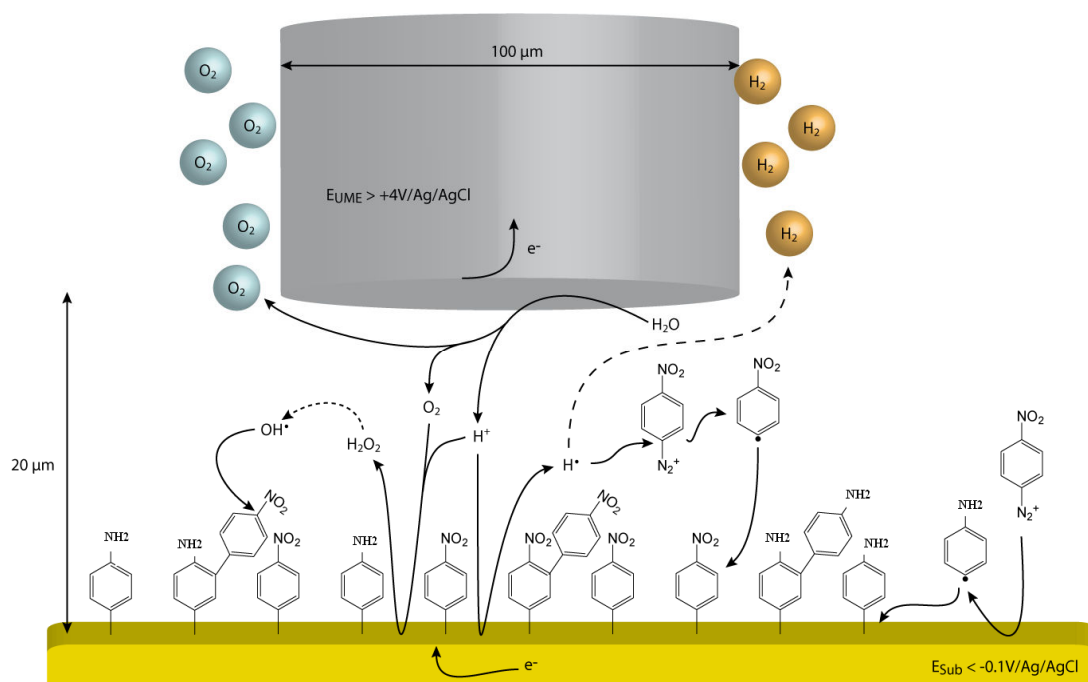
2/ water oxidation at the tip



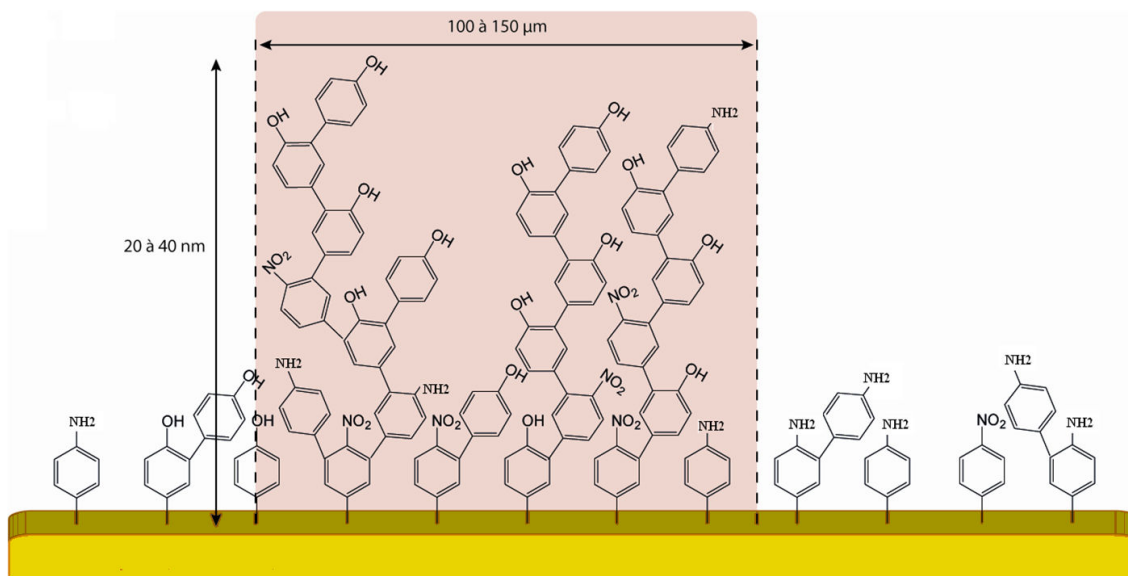
### 3/ concomitant reduction of protons on the substrate



4/ secondary reactions in the tip / substrate gap, for example: nucleophilic attack of the nitro group by OH activated species (“phenolsation effect”<sup>[13]</sup>), preferential reduction of the nitro group into amine function outside the tip region, oxidation of the phenyl group by very oxidative reagents generated under the tip, radical reaction initiating the polymerization of the vinylic monomer (when present).



5/ formation of a localized grafted coating on top of the primer polyphenylene-like one.



From the above sections, it is quite obvious that the reactions which take place under the microelectrode are complex and difficult to identify precisely. All the experimental investigations anyway show that the electrolysis of water is the key factor responsible of the localization. The resulting very reactive generated species induce chemical reactions in chain, which, most probably, occur more or less simultaneously rather than in different steps as presented above for clarity.

## 8. Extension of the process to other conducting and semi-conducting substrates (Pt, graphene, n-type Si)

In the previous sections, we described and commented the conditions for which a localized grafting can be observed on a gold surface. Let's now study the extension of the process to various conducting or semi-conducting substrates. We can, in principle, extend the process to any conducting or semi-conducting surface if this one is able to be polarized at a sufficiently cathodic potential to reduce protons and if the nature of the substrate is compatible with the acidic environment required by the process. Three substrates were then tested successfully:

- platinum
- graphene
- n-type doped silicon

### Pt surface

Platinum surfaces, well known for their catalytic properties towards the reduction of protons, were tested in local grafting process. We performed chronoamperometry experiments where the Pt substrate was kept constant and equal to  $-0.4$  V vs. Ag wire while the potential of the  $100\mu\text{m}$ -Pt UME was scanned in the range of  $1$  V to  $10$  V vs. Ag wire. The other experimental parameters were the same as previously, i.e.  $5$  s time of polarization, and  $d/a = 0.4$ .

In figure 22, we compare dots obtained for Pt and Au substrates respectively, for equivalent experimental conditions. We observe that, as for a gold substrate, the localization effect on Pt starts from  $E_{\text{UME}} \geq 5$  V vs. Ag wire for short polarization duration ( $5$  s). The size and the thickness of the localized coating are equivalent on both substrates.

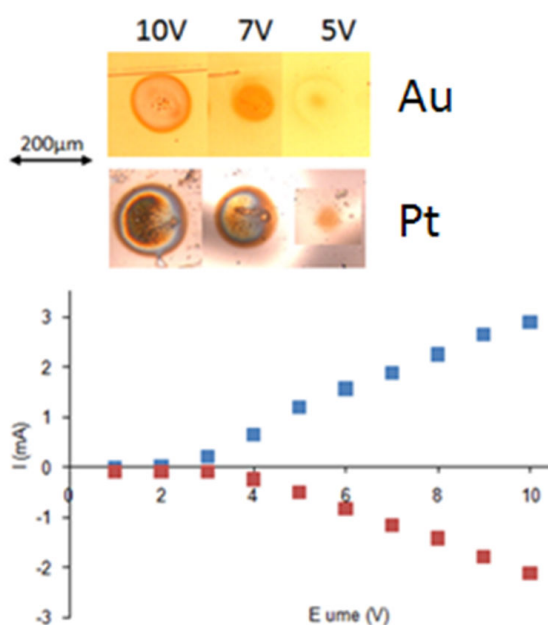


Figure 22: Optical image of grafted dots on Pt and Au substrates for different potentials applied to the UME and corresponding currents  $I_{\text{UME}}$  (■) and  $I_{\text{sub}}$  (■) for Pt substrate.

$[AA]: 2.0 \text{ mol. dm}^{-3}$ ,  $[DNB]: 2 \cdot 10^{-3} \text{ mol. dm}^{-3}$ ,  $[H_2SO_4]: 0.25 \text{ mol. dm}^{-3}$ ,  $100 \mu\text{m-Pt}$ ,  $d/a=0.4$ ,  $t=5\text{s}$ .

## Graphene

Graphene was recently taken huge interest in miniaturized electronics due to its unique properties and potential applications in capacitors,<sup>[14]</sup> cell images,<sup>[15]</sup> sensor,<sup>[16]</sup> devices,<sup>[17]</sup> drug delivery<sup>[18]</sup> and solar cell.<sup>[19]</sup> The graphitic layers are conductive and they are able to be connected as working electrodes. On figure 23, we report the voltamperogram obtained for the reduction of nitrobenzene diazonium salt in presence of acrylic acid in acidic solution in a non local way.

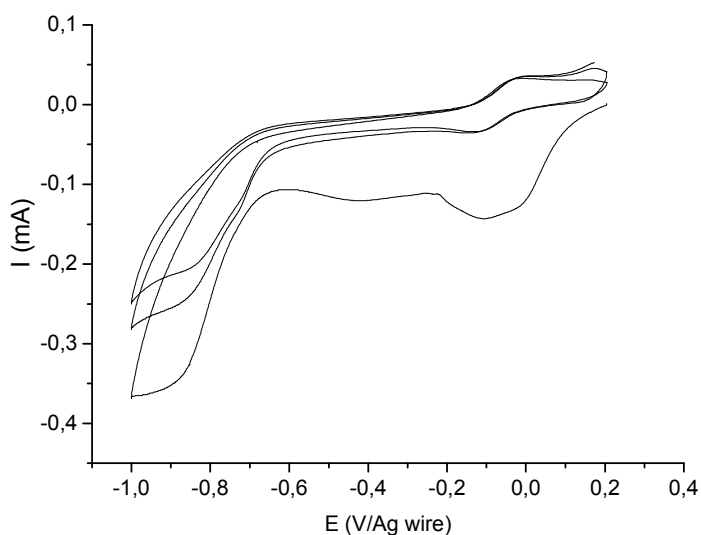


Figure 23: cyclic voltamperometry of grapheme substrate electrografted by PNP-PA; grafting solution NBD  $0.002 \text{ mol/dm}^3$ , AA  $2 \text{ mol/dm}^3$ ,  $\text{H}_2\text{SO}_4$   $0.25 \text{ mol/dm}^3$ , scan rate  $20 \text{ mV s}^{-1}$ .

As on Au and Pt substrates, the passivation of the surface occurs resulting from the formation of the grafted film. XPS spectra recorded on the grafted substrate present the characteristic features of the PNP-PAA layer: (i) carboxylic contribution detectable at  $289.0 \text{ eV}$  on the C  $1s$  spectrum (this one appears very small on the spectrum because the C  $1s$  core level spectrum is dominated by the signal of the carbon coming from the grapheme substrate) (fig. 24a); (ii) peaks corresponding the  $\text{NH}_2$ ,  $\text{N}=\text{N}$ ,  $\text{NH}_3^+$ , and  $\text{NO}_2$  functions, respectively on the N  $1s$  core level spectrum (fig. 24b).

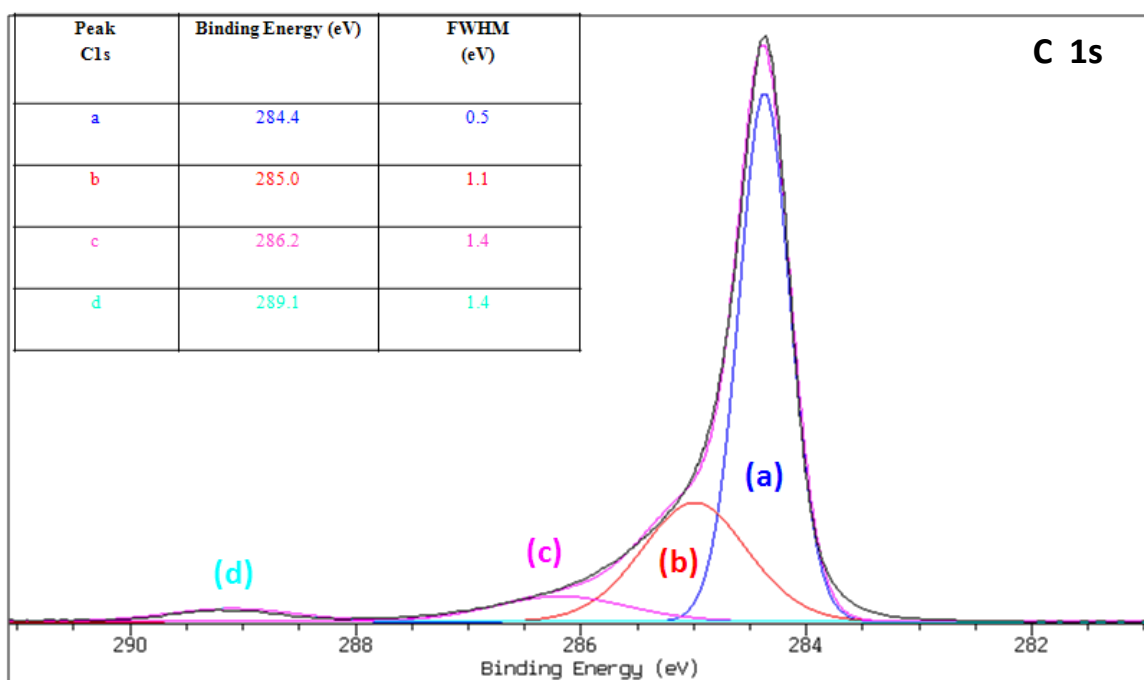


Figure 24a: XPS C 1s core level spectrum recorded on the grafted coating obtained on graphene substrate .

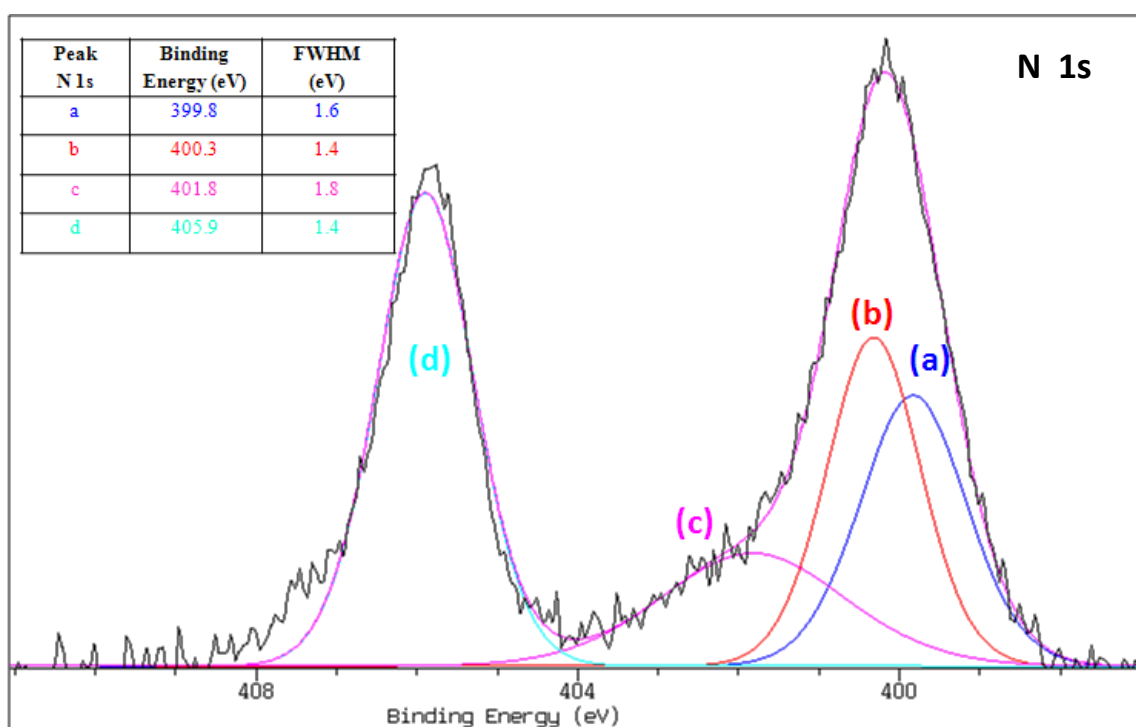


Figure 24b: XPS N 1s core level spectrum recorded on the grafted coating obtained on graphene substrate.

Figure 24 shows the localized dots obtained by applying the same experimental setup as for Au and Pt substrates, i.e. substrate potential kept constant and equal to -0.4 V vs. Ag wire, 25 $\mu$ m-Pt UME potential scanned in the range of 1 V to 10 V vs. Ag wire, 5 s time of polarization, and  $d/a = 0.4$ .

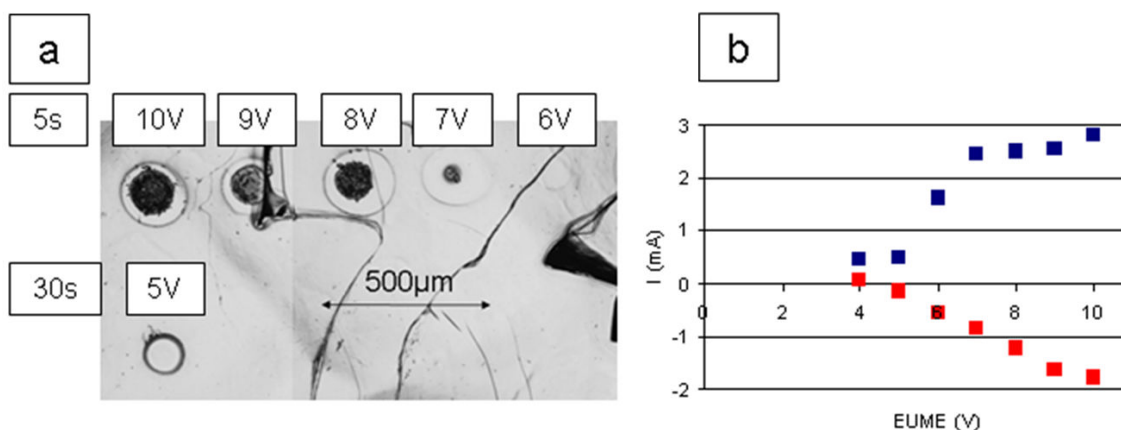


Figure 24: optical image of localized dots realized at different UME potentials and corresponding currents  $I_{UME}$  (■) and  $I_{sub}$  (■). [AA]: $2.0 \text{ mol. dm}^{-3}$ , DNB: $2 \cdot 10^{-3} \text{ mol. dm}^{-3}$ ,  $H_2SO_4$ : $0.25 \text{ mol. dm}^{-3}$ ,  $100 \mu\text{m-Pt}$ ,  $d = 20 \mu\text{m}$ .

These results show a good selectivity and a behavior similar to the one observed with the metallic surfaces.

#### Doped Silicon

Electrografting of the mixture NBD / AA takes also place on n-type silicon substrate. The XPS analysis of the grafted coating corresponds well to the PNP-PAA bi-layers-like film with the usual characteristics for the different components (C, N, O) (fig 25 a, b, c, respectively).

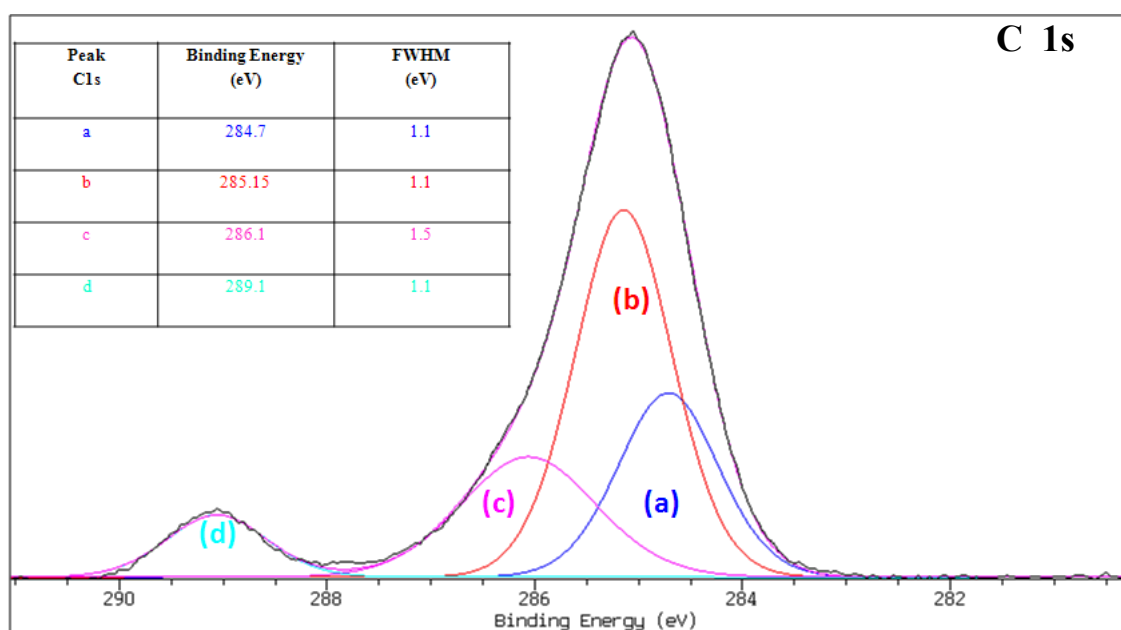


Figure 25a: XPS C 1s core level spectrum recorded on the grafted coating obtained on n-type Si substrate.

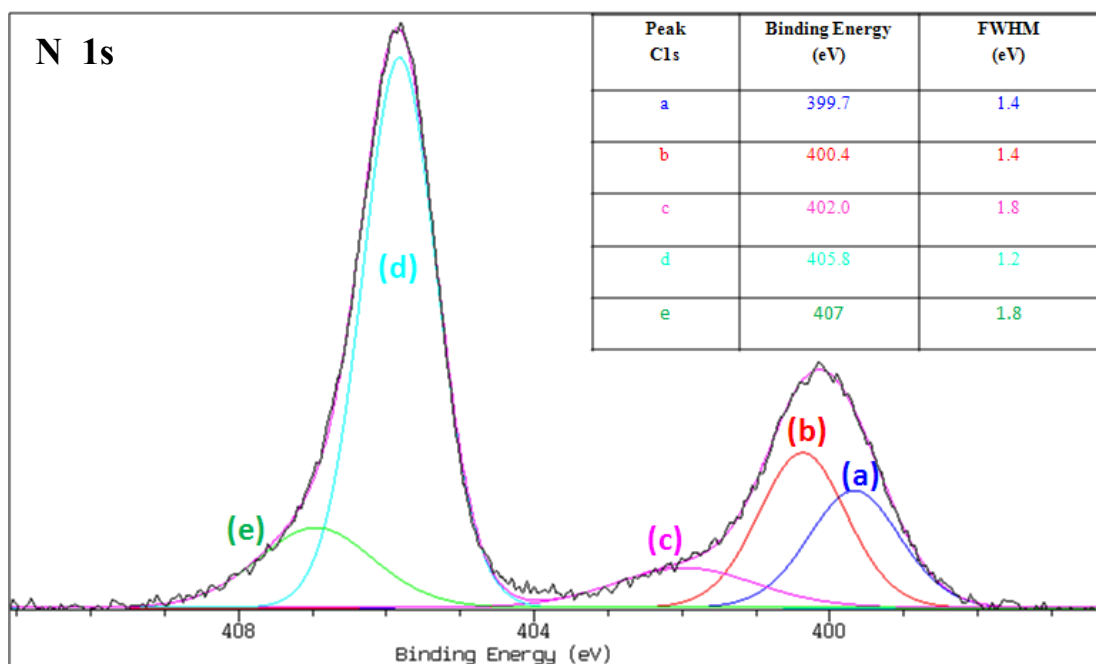


Figure 25b: XPS N 1s core level spectrum recorded on the grafted coating obtained on n-type Si substrate

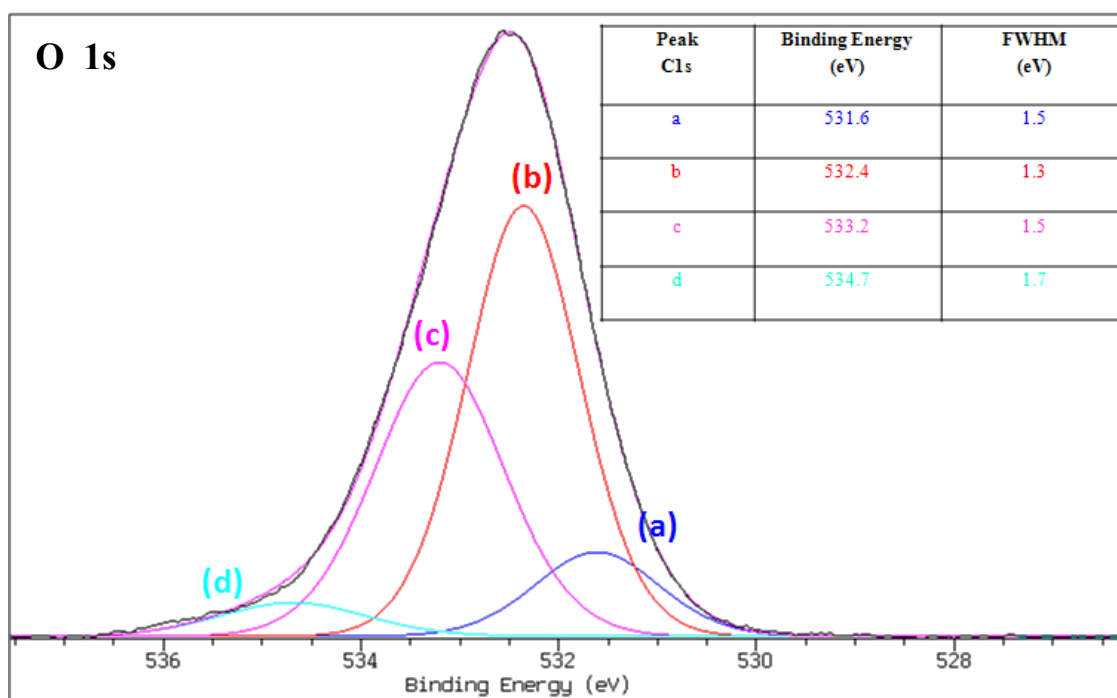


Figure 25c: XPS O 1s core level spectrum recorded on the grafted coating obtained on n-type Si substrate.

A 100 $\mu$ m-Pt UME was placed at 20 $\mu$ m ( $d/a = 0.4$ ) from the surface; its potential was scanned by chronoamperometry during 30s in the range of 1 to 10 V vs. Ag wire, while

the substrate potential was fixed at  $-0.4$  V vs. Ag wire. Under these conditions, localized dots were formed for  $E_{UME} \geq 7$  V vs. Ag wire (fig. 26). This higher starting potential for the local process compared to the one observed on metallic surfaces comes from the intrinsic higher resistivity of the Si substrate.

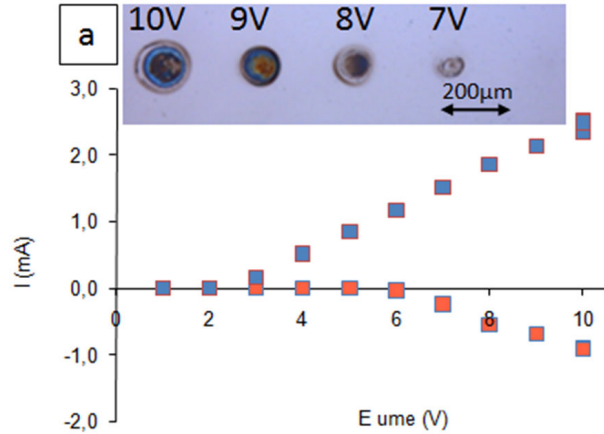
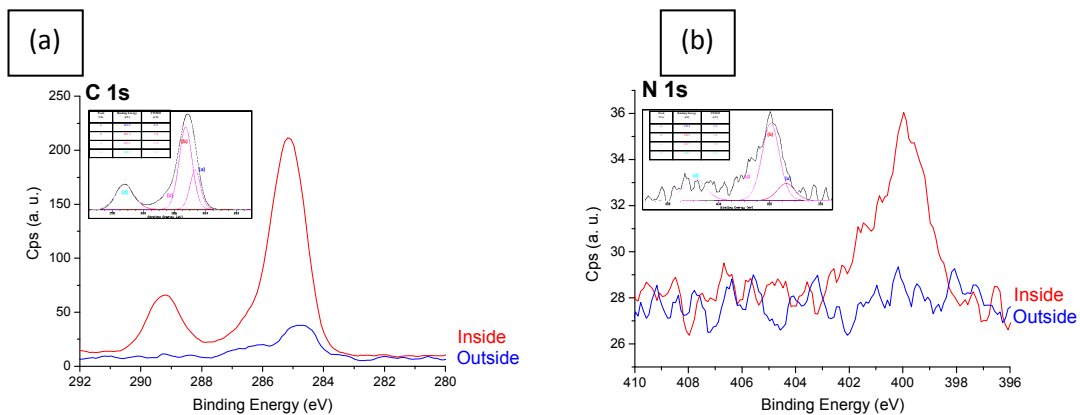


Figure 26: Optical image of grafted dots on silicon for different potential imposed to UME and corresponding currents  $I_{UME}$  (■) and  $I_{sub}$  (■).  $[AA]: 2.0 \text{ mol. dm}^{-3}$ ,  $DNB: 2 \cdot 10^{-3} \text{ mol. dm}^{-3}$ ,  $H_2SO_4: 0.25 \text{ mol. dm}^{-3}$ ,  $100 \mu\text{m-Pt}$ ,  $d/a = 4$ .

The integrity of the chemical functions of the local grafted film was checked by local XPS analysis (fig. 27) and shows a less oxidative degradation of the coating than the one observed in the same conditions on the metallic substrates.



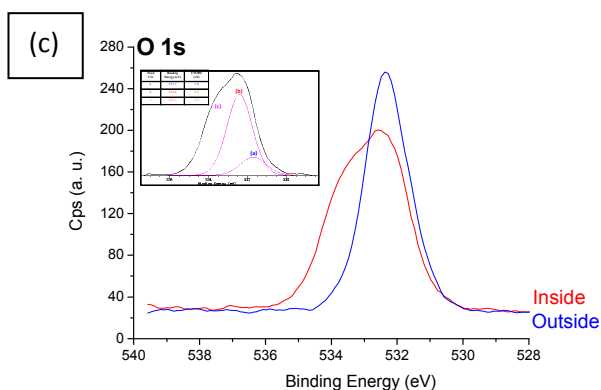


Figure 27: (a-c) C 1s, N 1s, and O 1s core level spectra of the coating recorded in (red) and out (blue) the grafted pattern. Acquisition conditions: X-ray source= 225W, high resolution FoV2 ( $55 \times 55 \mu\text{m}^2$ ), and pass energy= 40eV. Insert: decomposition of the inside peak . [AA]: $2.0 \text{ mol. dm}^{-3}$ , DNB: $2 \cdot 10^{-3} \text{ mol. dm}^{-3}$ ,  $\text{H}_2\text{SO}_4$ : $0.25 \text{ mol. dm}^{-3}$ ,  $100 \mu\text{m-Pt}$ ,  $E_{\text{UME}}=10 \text{ V/Ag wire}$ ,  $E_{\text{sub}}=-0.4\text{V/Ag wire}$ ,  $d/a=0.4$ ,  $t=30\text{s}$ .

To conclude, the localized process seems thus able to be extended to many conducting and semi conducting substrates, free from corrosion or degradation in the experimental conditions if the substrate is able to reduce the diazonium salt (to form the primer adhesive layer) and the tip-generated species with a satisfactory yield. More particularly, by computing the results obtained on the different substrates (fig. 28 and table 2), it appears that the potential conditions applied to both the substrate and the UME have to induce, on the substrate, a collection coefficient higher than 0.3 to observe the starting of the localized effect. Although very unusual potential conditions have to be reached to observe localization, the chemical integrity of the grafted coating is roughly preserved even if more oxygenated fragments are present in the localized film than expected by the theoretical stoichiometry. This effect can eventually be exploited in order to build patterned hydrophilic / hydrophobic substrates, which can find interest in the micro-fluidic domain. First attempts in that way will be presented in the perspectives of this work.

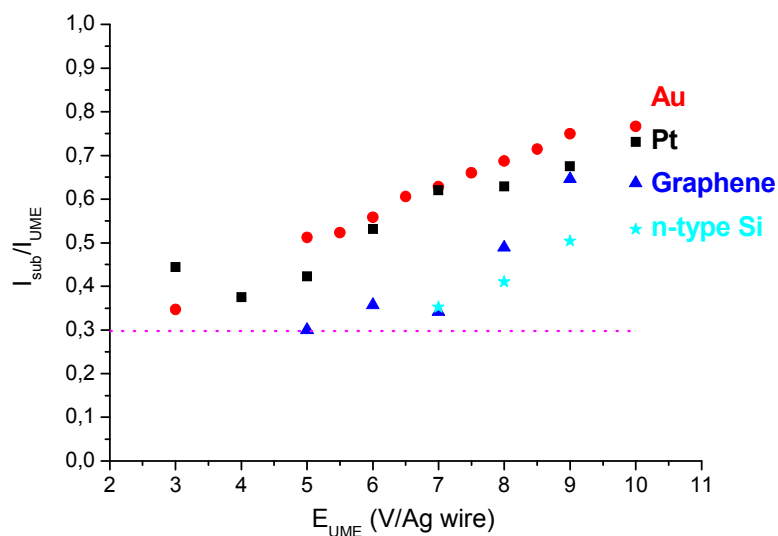


Figure 28: substrate current /tip current ratio vs. UME applied potential for different substrates: (red) gold, (black) platinum, (blue) grapheme, (cyan) n-type Si.  $E_{sub}$  is held constant at -0.4 V vs. Ag wire and -0. V vs. Ag wire for conducting and semi conducting substrates, respectively.

[AA]:2.0 mol. dm<sup>-3</sup>, DNB:2 10<sup>-3</sup> mol.dm<sup>-3</sup>, H<sub>2</sub>SO<sub>4</sub>:0.25 mol.dm<sup>-3</sup>.

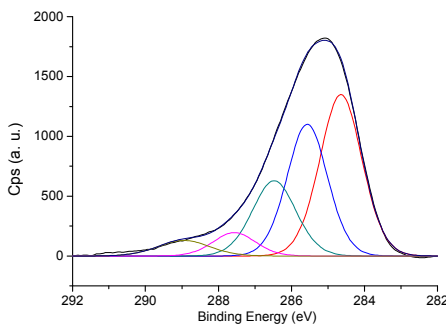
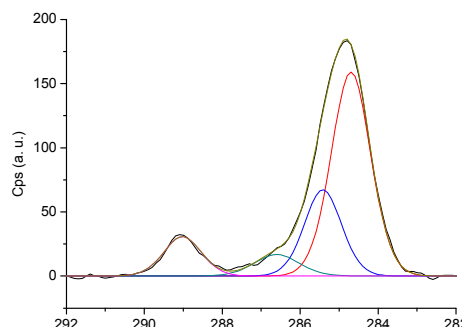
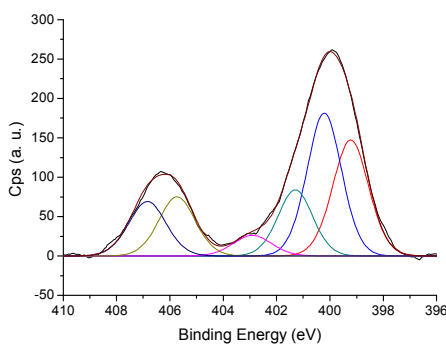
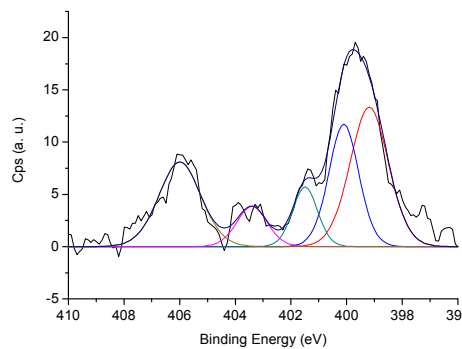
Conditions for the local process starting			
	$E_{UME}$ (V/Ag wire)	$E_{sub}$ (V/Ag wire)	Duration of electrolysis
Au	3	-0.4	10
Pt	3	-0.4	10
Grapheme	5	-0.4	30
Si	7	-0.4	30

Table 2: Experimental conditions for the starting of the localization process on different substrates by chronoamperometry. [AA]:2.0 mol. dm<sup>-3</sup>, DNB:2 10<sup>-3</sup> mol.dm<sup>-3</sup>, H<sub>2</sub>SO<sub>4</sub>:0.25 mol.dm<sup>-3</sup>, d/a=0.4.

## REFERENCES

- [1] E. Weiss, *PhD thesis, Paul Sabatier University, Toulouse III, France* **2006**.
- [2] E. Brillas, I. Sires and M. A. Oturan, *Chem. Rev.* **2009**, *109*, 6571.
- [3] M. Pourbaix, *Atlas of electrochemical equilibria in aqueous solutions. Nace International Cebelcor., 2nd ed.* **1974**.
- [4] K. Serrano, P. A. Michaud, C. Comninellis and A. Savall, *Electrochim. Acta* **2002**, *48*, 431.
- [5] D. E. Henton, C. Powell and R. E. Reim, *J. App. Polym. Sci.* **1997**, *64*, 10.
- [6] A. J. Appleby, *J. Electroanal. Chem.* **1970**, *27*, 325.
- [7] S. G. Mairanovskii, V. M. Belikov, T. B. Korchemnaya and S. S. Novikov, *Russ. Chem. Bull.* **1962**, *11*, 482.
- [8] M. Ciszowska, A. Jaworski and J. G. Osteryoung, *J. Electroanal. Chem.* **1997**, *423*, 95.
- [9] D. P. Barkey, D. Watt, Z. Liu and S. Raber, *J. Electrochem. Soc.* **1994**, *141*, 1206.
- [10] J. M. Huth, H. L. Swinney, W. D. McCormick, A. Kuhn, F. Argoul, *Phys. Rev. E* **1995**, *51*, 3444.
- [11] J. N. Chazalviel, *Phys. Rev. A* **1990**, *42*, 7355.
- [12] J. N. Chazalviel, M. Rosso, E. Chassaing and V. Fleury, *J. Electroanal. Chem.* **1996**, *407*, 61.
- [13] P. Politzer, P. R. Laurence, L. Abrahmsen, B. A. Zilles and P. Sjoberg, *Chem. Phys. Lett.* **1984**, *111*, 75.
- [14] M. D. Stoller, S. Park, Y. Zhu, J. An, R. S. Ruoff, *Nano Lett.* **2008**, *8*, 3498.
- [15] Z. L. Xiaoming Sun, Kevin Welsher, Joshua Tucker Robinson, Andrew Goodwin, Sasa Zaric, Hongjie Dai, *Nano Res.* **2008**, *1*, 10.
- [16] S. Pisana, P. M. Braganca, E. E. Marinero and B. A. Gurney, *Nano Lett.* **2009**, *10*, 341.
- [17] J. S. Bunch, A. M. van der Zande, S. S. Verbridge, I. W. Frank, D. M. Tanenbaum, J. M. Parpia, H. G. Craighead and P. L. McEuen, *Science* **2007**, *315*, 490.
- [18] K. Yang, S. Zhang, G. Zhang, X. Sun, S.-T. Lee and Z. Liu, *Nano Lett.* **2010**, *10*, 3318.
- [19] J. Wu, M. Agrawal, H. c. A. Becerril, Z. Bao, Z. Liu, Y. Chen and P. Peumans, *ACS Nano* **2009**, *4*, 43.

**Annex 1: XPS analysis of the grafted coating inside the localized pattern.**

	Local electrografting in presence of diazonium salt alone in acidic aqueous solution	Local electrografting in presence of diazonium salt and acrylic acid in acidic aqueous solution																																
C 1s																																		
	<table border="1" data-bbox="391 1075 869 1534"> <thead> <tr> <th>C 1s</th> <th>Peak BE (eV)</th> <th>FWHM (eV)</th> </tr> </thead> <tbody> <tr> <td><b>a</b></td> <td>284.6</td> <td>1.3</td> </tr> <tr> <td><b>b</b></td> <td>285.6</td> <td>1.3</td> </tr> <tr> <td><b>c</b></td> <td>286.5</td> <td>1.4</td> </tr> <tr> <td><b>d</b></td> <td>287.6</td> <td>1.3</td> </tr> <tr> <td><b>e</b></td> <td>288.9</td> <td>1.6</td> </tr> </tbody> </table>	C 1s	Peak BE (eV)	FWHM (eV)	<b>a</b>	284.6	1.3	<b>b</b>	285.6	1.3	<b>c</b>	286.5	1.4	<b>d</b>	287.6	1.3	<b>e</b>	288.9	1.6	<table border="1" data-bbox="901 1041 1380 1444"> <thead> <tr> <th>C 1s</th> <th>Peak BE (eV)</th> <th>FWHM (eV)</th> </tr> </thead> <tbody> <tr> <td><b>a</b></td> <td>284.7</td> <td>1.2</td> </tr> <tr> <td><b>b</b></td> <td>285.4</td> <td>1.1</td> </tr> <tr> <td><b>c</b></td> <td>286.6</td> <td>1.3</td> </tr> <tr> <td><b>d</b></td> <td>289.0</td> <td>1.1</td> </tr> </tbody> </table>	C 1s	Peak BE (eV)	FWHM (eV)	<b>a</b>	284.7	1.2	<b>b</b>	285.4	1.1	<b>c</b>	286.6	1.3	<b>d</b>	289.0
C 1s	Peak BE (eV)	FWHM (eV)																																
<b>a</b>	284.6	1.3																																
<b>b</b>	285.6	1.3																																
<b>c</b>	286.5	1.4																																
<b>d</b>	287.6	1.3																																
<b>e</b>	288.9	1.6																																
C 1s	Peak BE (eV)	FWHM (eV)																																
<b>a</b>	284.7	1.2																																
<b>b</b>	285.4	1.1																																
<b>c</b>	286.6	1.3																																
<b>d</b>	289.0	1.1																																
N 1s																																		

	N 1s	Peak BE (eV)	FWHM (eV)		N 1s	Peak BE (eV)	FWHM (eV)
	<b>a</b>	399.2	1.6		<b>a</b>	399.2	1.6
	<b>b</b>	400.2	1.5		<b>b</b>	400.1	1.2
	<b>c</b>	401.3	1.5		<b>c</b>	401.5	1.0
	<b>d</b>	402.9	1.7		<b>d</b>	403.4	1.3
	<b>e</b>	405.7	1.6		<b>e</b>	406.0	1.7
	<b>f</b>	406.8	1.6				

O 1s	Peak BE (eV)	FWHM (eV)	O 1s	Peak BE (eV)	FWHM (eV)
	531.7	1.6	<b>a</b>	531.3	1.4
	532.8	1.5	<b>b</b>	532.2	1.3
	533.8	1.5	<b>c</b>	533.3	1.3
	535.3	1.6	<b>d</b>	534.5	1.5

Decomposition of the C 1s, N 1s, and O 1s core level spectra of the coating recorded the grafted pattern. Left: DNB:  $2 \times 10^{-3} \text{ mol.dm}^{-3}$ ,  $\text{H}_2\text{SO}_4$ :  $0.25 \text{ mol.dm}^{-3}$ , 100  $\mu\text{m}$ -Pt,  $d = 20 \mu\text{m}$ ,  $t=5\text{s}$   
Right : [AA]:  $2.0 \text{ mol. dm}^{-3}$ , DNB:  $2 \times 10^{-3} \text{ mol.dm}^{-3}$ ,  $\text{H}_2\text{SO}_4$ :  $0.25 \text{ mol.dm}^{-3}$ , 50  $\mu\text{m}$ -Pt,  $d = 20 \mu\text{m}$ ,  $t=5\text{s}$ .

## CHAPTER 5

### SECM AS AN ETCHING TOOL FOR ITO (INDIUM TIN OXYDE) SURFACE OR A NEW TECHNIQUE TO PATTERN TRANSPARENT CIRCUITS

#### 1. Introduction

In this study, we present a new technique of micropatterning of Indium Tin Oxide (ITO) thin films deposited either on glass or on transparent flexible substrates.

ITO is a wide band gap n-type semi conductor known for its high transparency and good conductivity when deposited as a thin film (few hundred of nm) on glass or flexible substrates. With the development of new display technologies, patterned ITO films has enormous growth potential and can find applications in any devices that require transparent and conductive electrodes, such as optically transparent sensors, bioelectronics sensing, micro-nano structuration for optical devices<sup>[1]</sup>, light emitting diodes (LED) or organic light emitting diode (OLED) displays<sup>[2,3]</sup>, organic solar cells<sup>[4]</sup> ...

An important step in the ITO manufacture consists in the electrode patterning through a lithographic approach. All available techniques for ITO patterning are based on the etching realized by the removal of the negative image of the desired motif; the remaining material on the support is the desired transparent circuit.

Following the large interest of the market, many etching processes have been studied and optimized for industrial production. Available techniques can be classified in two categories: wet etching and dry etching.

Wet etching<sup>[5-7]</sup> is the traditional technology based on classical photolithography (see chapter 3), followed by a chemical ablation with an acid solution on the unprotected surface zones (fig. 1a). However this approach usually leads to many problems in the manufacturing procedure arising from chemical pollution, under-cut effect<sup>[7, 8]</sup>, damages of surface, linking of several steps (masking, etching, cleaning), high cost. Defects of this approach lead to a global degradation of the electrical and optical properties of ITO.<sup>[5]</sup>

Dry etching<sup>[1, 3, 9-13]</sup> by laser photoenergy leads to the vaporization of the ITO film and to clean patterning that can be made in any possible shape easily (fig. 1b). The laser direct writing method should replace the wet approach improving both the cost, the duration of the process and its final result; in fact it is a non-contact technique working at high speed with high-accuracy. Thermal effect and environmental pollution is minimized. However two important problems remain unresolved:

- Flexible substrates based on polymers are damaged by laser beam and lose their optical and mechanical properties
- Vaporized material condenses on the edge of the patterning and therefore, sensibly changes the thickness of the ITO film. This kind of defect can compromise the functionality of the entire device normally constituted by successive nanometer-thick layers.

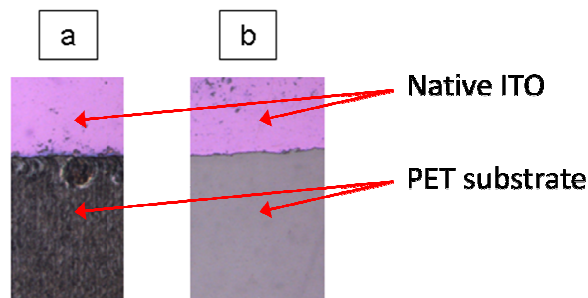


Figure 1: Two examples of ITO deposited on flexible PET® substrate etched by classical ways:  
 (a) laser ablation: damages are clearly visible on the ITO part of the substrate  
 (b) chemical etching by immersion during 120s in a (10%)<sub>v</sub> solution of HCl in water.

## 2. SECM: a new method to carry out ITO etching

SECM has proved efficient for patterning oxide films with high precision while preserving the substrate properties. Its amazing characteristics combine the best of other techniques to give a wet etching in a quick and inexpensive way:

- One step process
- Non contact lithography
- Simple aqueous solution (green chemistry)
- Not limited in surface size (mm÷m)
- Not limited in etched surface (50µm÷cm)
- Free from pre-treatment or washing
- No pollution of the surface
- Perfect shape of edge and dissolution of etched products
- It works on functionalized or coated ITO surface
- It can be adapted to a roll-to-roll or sheet-by-sheet process

### 3. Proof of concept

ITO substrates (purchased by Prazision Glas & Optik, GmbH (PGO)) have a low resistance ( $\leq 10 \Omega/\text{sq}$ ). The thin oxide film is  $120\div 200 \text{ nm}$  thick and was cleaned ethanol and deionized water before the use. The ITO substrate was then placed in the SECM cell and positioned parallel to the X-Y microscope plane. The approach and the planarization were carried by the use of a solution  $5 \times 10^{-3} \text{ mol}\cdot\text{dm}^{-3}$  of  $\text{Fe}^{3+}$  and  $0.1 \text{ mol}\cdot\text{dm}^{-3}$  KCl. The  $100 \mu\text{m}$  UME was polarized at  $-0.4 \text{ V}$  corresponding to the iron reduction potential. On the base of the approach curve, the working distance of  $20 \mu\text{m}$  ( $d/a=0.4$ ) was selected.

The etching was carried out by chronoamperometry in a four electrode configuration. The UME was placed at a feedback distance and connected as working electrode (WE1), the ITO surface played the role of the second working electrode (WE2). A platinum wire (1 mm diameter), and a silver wire (1 mm diameter), were used as counter electrode (CE) and quasi-reference electrode (RE), respectively. The selected electrochemical solution was composed by an aqueous solution of acrylic acid (AA)  $2 \text{ mol}\cdot\text{dm}^{-3}$  and sulfuric acid ( $\text{H}_2\text{SO}_4$ )  $0.25 \text{ mol}\cdot\text{dm}^{-3}$ . This electrochemical system was used in static and in dynamic mode to realize either dots or lines. The applied potential was similar to that chosen for localized electrografting (10 V vs. Ag wire at WE1 and  $-0.4 \text{ V}$  vs. Ag wire at WE2). In the following graphs (fig. 2) are reported the applied potentials (a) and corresponding measured currents (b).

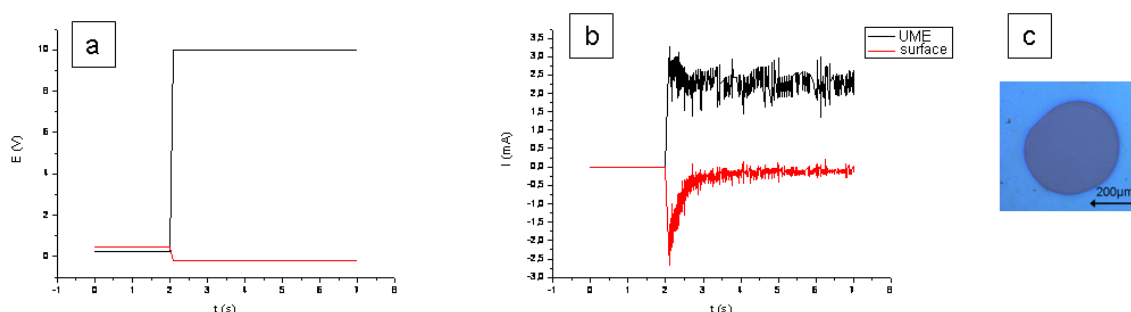


Figure 2: Electrochemical dot etching; (a) applied potential at the UME (black) and the surface (red) during 5s; (b) measured currents; (c) optical image of the resulting dot. UME  $100 \mu\text{m}$ -Pt,  $d/a=0.4$ ,  $E_{\text{UME}}=10\text{V}$ ,  $E_{\text{sub}}=-0.4\text{V}$ ;  $[\text{AA}]=2 \text{ mol}\cdot\text{dm}^{-3}$ ,  $[\text{H}_2\text{SO}_4]=0.25 \text{ mol}\cdot\text{dm}^{-3}$ .

At the UME, a constant current was measured. This current was only perturbed by bubbling that modifies instantly the electrode surface generating a noise on the measured current. At the surface, we observed, a rapid decrease of the past current in the first second of the potential application; its value then stabilized on a low negative value, around  $-100 \mu\text{A}$ .

X-ray photoelectron spectroscopy analysis carried out with the  $110 \mu\text{m}$  XPS microprobe, inside the etched cavity (yellow circle on fig. 3) compared to the non

etched outside area confirms the complete removal of the conductive oxide layer in the treated zone (table 1).

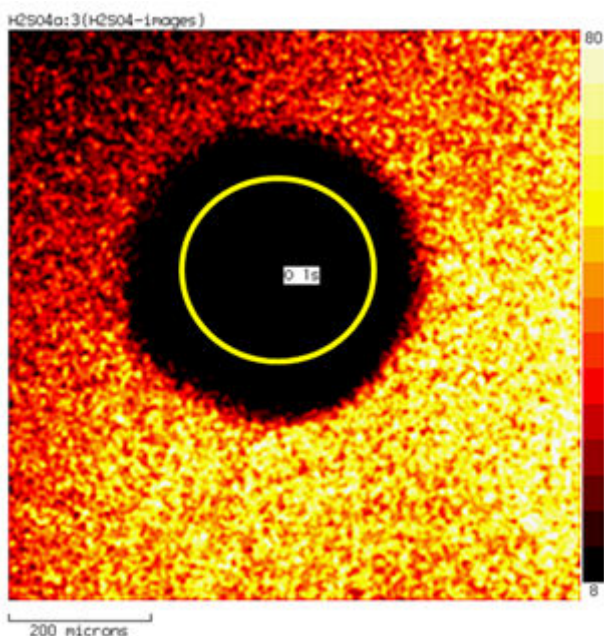


Figure 3: Elemental map of In obtained by XPS mapping analysis on localized etched ITO substrate. Acquisition conditions: X-ray source= 225W, high resolution FoV 1 ( $800 \times 800 \mu\text{m}^2$ ), and pass energy= 160eV. Yellow circle: area for the recorded XPS core levels spectra. Etching conditions:  $E_{UME} = 10 \text{ V}$  vs. Ag wire,  $E_{ITO} = -0.4\text{V}$  vs. Ag wire,  $[AA]: 2.0 \text{ mol. dm}^{-3}$ ,  $\text{H}_2\text{SO}_4: 0.25 \text{ mol. dm}^{-3}$ ,  $100 \mu\text{m-Pt}$ ,  $d = 20\mu\text{m}$ ,  $t=5\text{s}$ .

Element	Atomic% Inside the etched zone	Atomic% Outside the etched zone
O	52.8	33.6
Sn	0.1	2.2
In	0.4	20.4
N	2.4	0.6
C	13.2	41.9
Si	31.1	1.2

Table 1: Sn, In, and Si atomic percentage extracted from the respective core levels XPS spectra recorded inside and outside the etched area. Acquisition conditions: X-ray source= 225W, high resolution FoV2 ( $55 \times 55 \mu\text{m}^2$ ), and pass energy= 40 eV. Etching conditions:  $E_{UME} = 10 \text{ V}$  vs. Ag wire,  $E_{ITO} = -0.4\text{V}$  vs. Ag wire,  $[AA]: 2.0 \text{ mol. dm}^{-3}$ ,  $\text{H}_2\text{SO}_4: 0.25 \text{ mol. dm}^{-3}$ ,  $100 \mu\text{m-Pt}$ ,  $d = 20\mu\text{m}$ ,  $t=5\text{s}$ .

In the created cavity, the Sn and In components are thus reduced by more than 95% and 99% percent respectively. The etching process is thus able to ablate the conductive layer up to the glass support as proven by the emergence of the Si signal.

The clear-cut of the shape of the etched pattern is evidenced by AFM analysis. Figure 4a reports the 3D topographical image of a line cavity realized on an ITO thin film deposited on glass and obtained with a 25- $\mu\text{m}$  Pt tip. The width of the line is 40  $\mu\text{m}$  and the edges of the cavity appear as abrupt walls as shown on the recorded profile (fig. 4b). The small walls deviation from the perpendicular was evaluated at 7° and corresponds to lateral overetching of 20nm for ITO on glass.

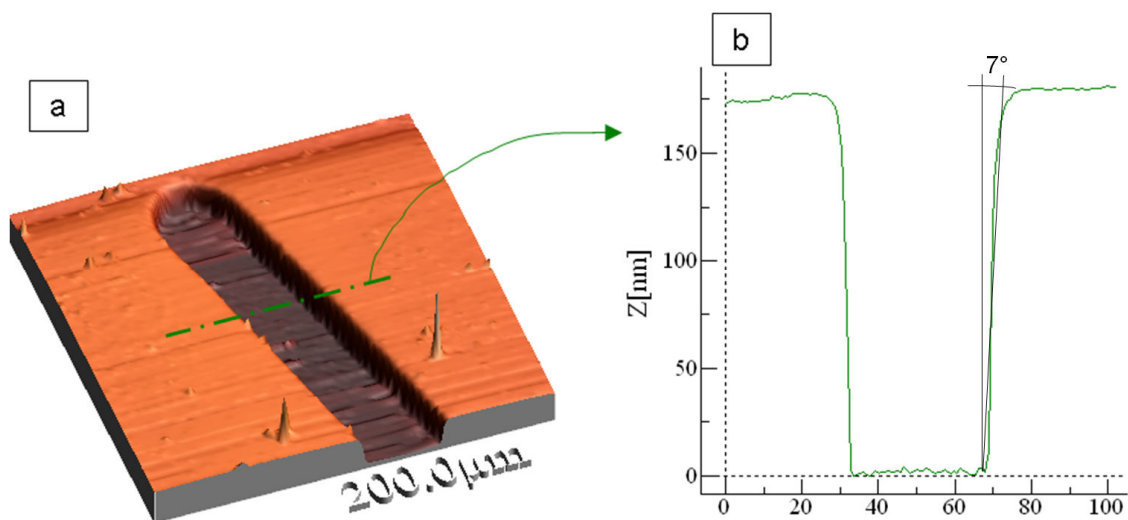


Figure 4: (a) 3D topographical AFM image of the terminal portion of an etched line on ITO substrate. (b) Profile of the etched line. Etching conditions:  $E_{UME}=7\text{V}$  vs. Ag wire,  $E_{ITO} = -0.4\text{V}$  vs. Ag wire,  $[AA]:2.0 \text{ mol. dm}^{-3}$ ,  $\text{H}_2\text{SO}_4:0.25 \text{ mol.dm}^{-3}$ , 25 $\mu\text{m}$ -Pt,  $d = 10\mu\text{m}$ ,  $v=100\mu\text{m/s}$ .

The homogeneity of the etched area, the clear-cut of the edge and the absence of redeposited material on the side of the line should all be highlighted; all are remarkable properties but are seldom joined together in the same process with the usual dry or wet techniques.

The lateral resolution of the technique was evaluated on the base of a sharp angle designed with a couple of lines inclined of 3° and realized with a 25 $\mu\text{m}$ -Pt UME (fig. 5). The intrinsic properties of the ITO (15 ohm resistivity and 200 nm thick) are well preserved until the track reaches 10  $\mu\text{m}$  width. Below this value, the track is partially etched and its thickness goes down regularly until the electrical conductivity is lost (width < 3  $\mu\text{m}$ ). However, the etching minimal size can certainly be reduced more through the use of smaller electrodes (<25 $\mu\text{m}$ ) by analogy with localized functionalization with AFM-SECM.

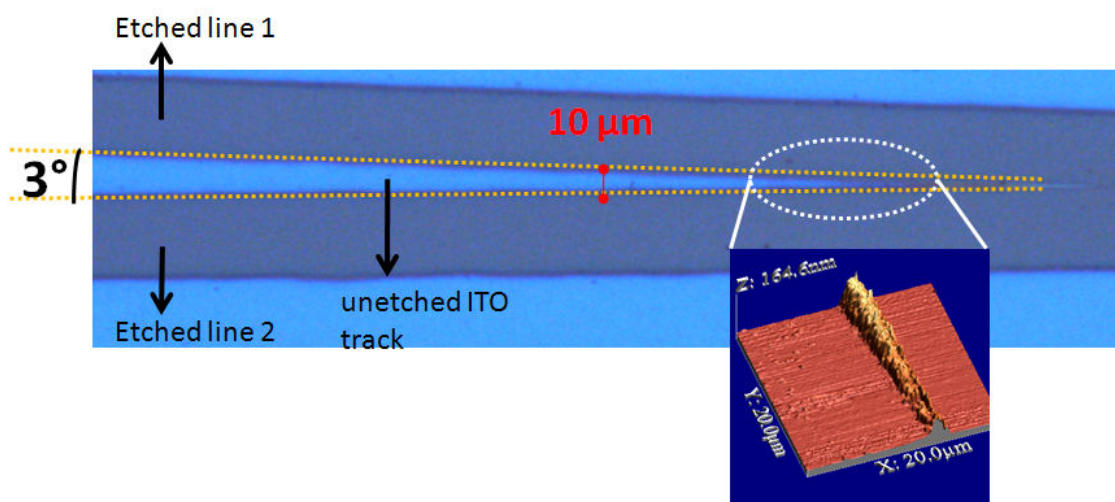


Figure 5: optical image of the unetched ITO microtrack obtained with two etched lines in dynamic mode, and 3-D AFM topographic image of the end of the sharp angle. Etching conditions:  $E_{UME} = 7 \text{ V vs. Ag wire}$ ,  $E_{ITO} = -0.4 \text{ V vs. Ag wire}$ ,  $[AA]: 2.0 \text{ mol. dm}^{-3}$ ,  $\text{H}_2\text{SO}_4: 0.25 \text{ mol. dm}^{-3}$ ,  $25 \mu\text{m-Pt}$ ,  $d = 10 \mu\text{m}$ ,  $v = 100 \mu\text{m/s}$ .

## 4. Parametrical study

### 4.1 Influence of the applied potentials

The potential applied to both working electrodes was varied in the interval between 1 and 10V at the UME, with the surface polarized at -0.2V, and between 0 and -0.5V at surface with the UME polarized at 7V. For both configurations (Scan of  $E_{UME}$  at constant  $E_{Sub}$  and scan of  $E_{Sub}$  at constant  $E_{UME}$ ), currents passed through the two electrodes were recorded simultaneously and reported on figure 5a1 and 5a2, respectively. On this figure, we also plot the width of the etched pattern as a function of the applied potential to the UME (fig. 5b1) and to the ITO substrate (fig. 5b2). Finally we show the optical images of the etched zones as a function of the experimental conditions (fig. 5c).

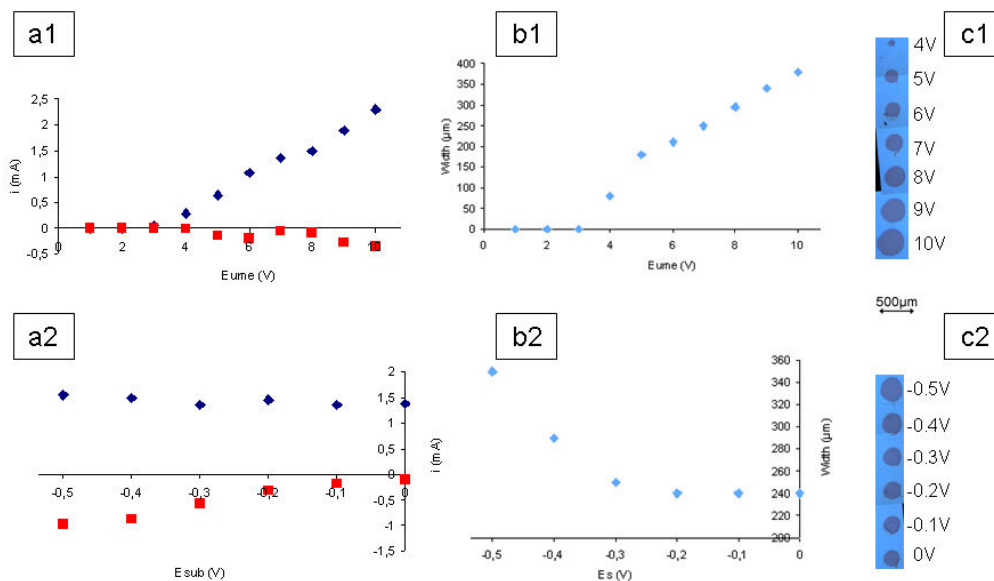


Figure 5: Electrodes potential scan in static mode. (1) UME potential scan,  $E_{sub} = -0.1V$ ; (2) surface potential scan,  $E_{UME} = 7V$ . (a) Measured currents; (b) measured width; (c) optical image of etched dots. UME  $100\mu m$ -Pt,  $d/a = 0.4$ ;  $[AA] = 2\text{mol}\cdot\text{dm}^{-3}$ ,  $[H_2SO_4] = 0.25\text{mol}\cdot\text{dm}^{-3}$ ,  $t = 5\text{ s}$

When we scan the  $E_{UME}$  from 1V to 10V while the  $E_{sub}$  is maintained constant, we observe that, as for the local electrografting process on conductive substrates, the etching process starts from 4V vs. Ag wire applied to UME. In these conditions, by using a  $100\text{-}\mu m$  Pt UME, the width of the etched dot pattern is about  $80\text{ }\mu m$ . As shown on figure 5b1, the width of the pattern increases linearly with the UME potential.

The surface scan shows a different behavior (fig. 5b2): the width remains relatively constant until  $E_{sub}$  is less negative than  $-0.3V$  vs. Ag wire. Beyond this threshold value, the size of the etching starts to grow. We can also note that the increase of the width of the etched cavity corresponds simultaneously to the increase of the cathodic current on the substrate.

In conclusion, as for the electrografting process, the size of the etched pattern is essentially governed by the potential applied to the UME: by varying the UME potential from 4V to 10V, the value of the current measured on the tip is multiplied by five just as the width of the etched zone.

#### 4.2 Influence of the working distance

The influence of the working distance on the size and the shape of the etched area was studied in the range of  $0.1 < d/a < 2$ . For this set of experiments, the ITO substrate was polarized at  $-0.2V$  vs. Ag wire and the microelectrode was biased at  $7V$  vs. Ag wire. As shown on figure 6, we observe an increase of the width of the etched pattern with the

working distance until  $d/a=1.4$ ; beyond this value, the width decreases slightly and the localization effect is lost for  $d/a > 2$ .

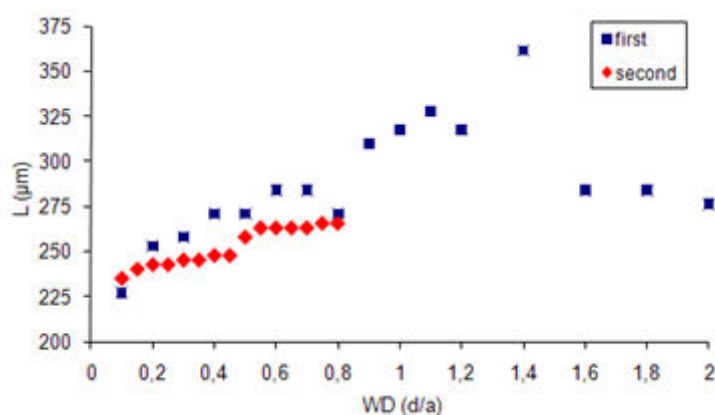


Figure 6: Width of the etched dots as a function of the normalized working distance. chronoamperometry, 100 $\mu\text{m}$ -Pt UME,  $E_{UME} = 7\text{V}$  vs. Ag wire,  $E_{sub} = -0.2\text{V}$  vs. Ag wire,  $t = 5\text{ s}$ ,  $[AA] = 2\text{ mol}\cdot\text{dm}^{-3}$ ,  $[\text{H}_2\text{SO}_4] = 0.25\text{ mol}\cdot\text{dm}^{-3}$ .

It must be noted that when the working distance is higher than 70  $\mu\text{m}$  (for a 100- $\mu\text{m}$  UME), the etching process becomes incomplete with less defined edges. At  $d/a=2$ , for example, it remains ITO film about 50nm thick in the cavity.

#### 4.3. Nature of the electrolytic solution optimization

Different electrolytic solutions were tested and compared with respect to their efficiency towards the etching process in terms of homogeneity of the etched area, clear-cut of the edge and absence of redeposited material on the side of the etched area. The results are summarized in table 2. For all these experiments, the 100- $\mu\text{m}$  Pt UME was placed at 20  $\mu\text{m}$  from the surface ( $d/a=0.4$ ), biased at 10 V vs. Ag wire during 5 s while the ITO substrate was polarized simultaneously at -0.4V vs. Ag wire.

Electrolytic solution	Optical image of the etched zone	Comments
$\text{H}_2\text{O}$ $E_{ume} = 10\text{ V}$ , $E_{sub} = -0.4\text{ V}$ , 100 $\mu\text{m}$ -Pt, $d/a=0.4$ , $t=5\text{ s}$		Local water electrolysis is able to etch the ITO substrate but leads to an undefined etched area.

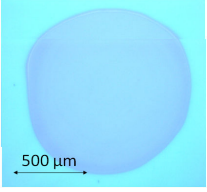
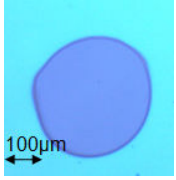
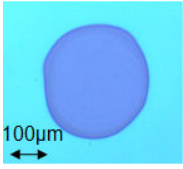
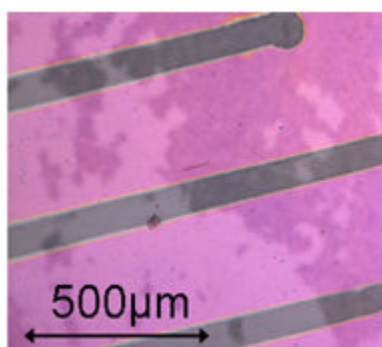
$\text{H}_2\text{SO}_4$ 0.25 mol.dm <sup>-3</sup> $E_{\text{ume}} = 10$ V, $E_{\text{sub}} = -0.4$ V, 100 $\mu\text{m}$ -Pt, $d/a = 0.4$ , $t = 5$ s		Enlarged etched zone with non abrupt edge
AA 2 mol.dm <sup>-3</sup> ; $\text{H}_2\text{SO}_4$ 0.25 mol.dm <sup>-3</sup> $E_{\text{ume}} = 10$ V, $E_{\text{sub}} = -0.4$ V, 100 $\mu\text{m}$ -Pt, $d/a = 0.4$ , $t = 5$ s		well defined etched area
Acetic acid (AcA) 2 mol.dm <sup>-3</sup> , $\text{H}_2\text{SO}_4$ 0.25 mol.dm <sup>-3</sup> $E_{\text{ume}} = 10$ V, $E_{\text{sub}} = -0.4$ V, 100 $\mu\text{m}$ -Pt, $d/a = 0.4$ , $t = 5$ s		some residual material in the etched zone

Table 2: optical images of the etched zone as a function of the composition of the electrolytic solution

From these results it is clear that electrolysis of water at high anodic potential creates species able to dissolve the thin oxide film. Indeed the local oxidation of water generates, in the small volume gap between both electrodes, a continuous and chemical aggressive flow of protons and radical oxygenated intermediates which give rise to the etching. The species coming from the electrolysis of water in our given electrochemical conditions is thus able to attack the ITO thin film. The “star” shape of the etched zone disappears in the dynamic mode and a homogeneous line can be obtained. The introduction of sulfuric acid improves the regularity of the pattern, but only acrylic acid and acetic acid give a regular shape to the etched area. This behavior has probably to be related to the capability of these acids to bring and maintain in the solution by complexation the removed ions from the ITO substrate.

However, a possible drawback of the etching process described above is the presence of sulfuric acid in the electrolytic solution. Indeed, this acidic medium can damage soft flexible substrates such as PET film on which ITO thin film can be deposited. This kind of flexible conductive surface is more fragile than glass, as the polymeric substrate

limits the compatible post treatments. In particular, the annealing treatment used to homogenize the ITO structure is then prohibited. Consequently, the oxide thin layer presents some defects and is less resistant to chemical attacks. In response to this problem, a solution of acrylic acid in the absence of sulfuric acid was tested as etching agent in the SECM environment. By biasing the UME at high anodic potential in a solution containing only concentrated acrylic acid ( $2 \text{ mol.dm}^{-3}$ ), it was possible to etch the ITO layer deposited on a polyethyleneterephthalate (PET) substrate without damage to this flexible substrate (fig. 7). The performances of the etching process are preserved: clear-cut and no redeposition of the layer on the borders.



*Figure 7: Optical image of etched ITO deposited on PET. Dynamic mode at  $100 \mu\text{m/s}$ . UME  $25 \mu\text{m-Pt}$ ;  $d/a=0.8$ ;  $[\text{AA}]=2 \text{ mol.dm}^{-3}$ .*

#### **4.4. Application of the process to different substrates**

In this section, our objective is to study the potentialities of extending our etching process to different coated or modified ITO surfaces. These substrates may have applications in several fields. For example, the oxide functionalization of ITO is widely studied for the energy photo-production field<sup>[14, 15]</sup>.

To explore this domain, we synthesized a multi-layered film based on  $\text{TiO}_2$  (n-type semiconductor) and  $\text{NiO}$  (p-type semiconductor) deposited on cleaned ITO substrates. These multi-layered films were prepared as follows: a titanium oxide ( $\text{TiO}_2$ ) nanoparticles dispersion, purchased from Solaronix (Ti-nanoxide HT-L/SC), was deposited by spin coating (3000 rpm, 60s), and then annealed in a furnace at  $140^\circ\text{C}$  for 1 hour. The average thickness of the samples was 150 nm. A similar treatment was used for nickel oxide ( $\text{NiO}$ ) deposition to obtain a 50 nm thick coating. For comparison, the same deposition process of  $\text{TiO}_2$  and  $\text{NiO}$  was applied directly on a pure glass sheet.

When  $\text{TiO}_2$  and  $\text{NiO}$  are directly deposited on glass and submitted to the etching protocol ( $E_{\text{UME}}=10\text{V/Ag wire}$ ,  $E_{\text{sub}}=-0.4\text{V/Ag wire}$ ), any appreciable effect or modification of the surface can be detected as observed by optical microscopy. However, the presence of the ITO conductive film under the oxide allows the localized etching to occur as shown on figure 8.

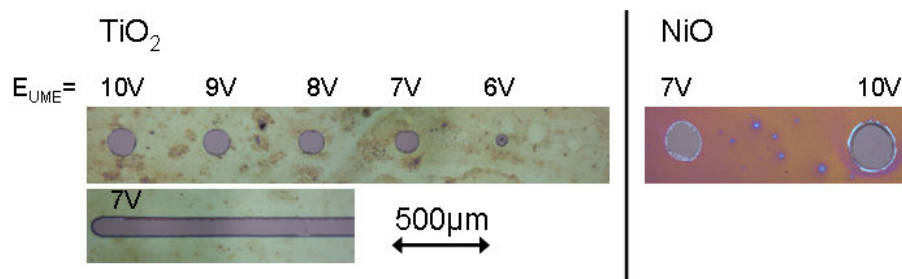


Figure 8: Optical images of etched dot on ITO surface modified by  $TiO_2$  and  $NiO$  deposition for different  $E_{UME}$ .  $E_{sub} = -0.4$ ,  $50\mu m$ -Pt UME,  $d/a=0.4$ ,  $t=5s$ ,  $[AA]=2mol.dm^{-3}$

This last result highly suggests that ITO removal starts from the surface, catalyzed by the local chemical conditions produced under the UME. But those local chemical conditions alone are not able to etch the  $TiO_2$  or  $NiO$  oxide layer itself.

## 5. Fields of applications

Using the home made Elecdraw2.0 software combined with the SECM instrument, it is possible to lithograph any complex electrical circuit on ITO substrate. The etching lithography process consists in biasing the microelectrode and the substrate to 7V vs. Ag wire and -0.2V vs. Ag wire, respectively. The UME positioned at a fixed working distance ( $d/a=0.8$  for  $25\mu m$ -Pt UME) was then moved in the  $x$ - $y$  plane above the substrate at  $300\mu m/s$ . The use of Elecdraw2.0 software enables automatic drawing of the pattern. Figure 9 shows an example of such a circuit.

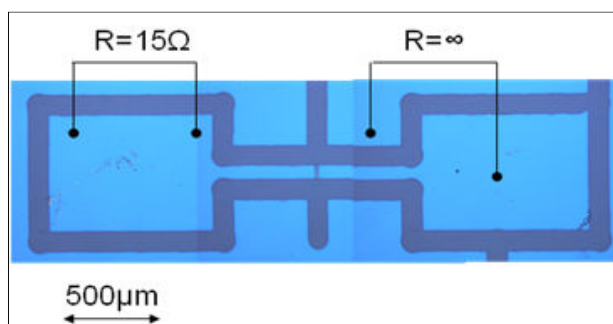


Figure 9: Example of electrical circuit designed by etching lithography on ITO substrate.  $E_{UME} = 7V$ ,  $E_{sub} = -0.4V$ ,  $25\mu m$ -Pt UME,  $d/a=0.8$ ,  $v=100\mu m/s$ ,  $[AA]=2mol.dm^{-3}$ .

The tracks (clear zones on the optical image) separated by an etched area (dark zones on the optical image) are perfectly electrically insulated as checked by the electrical resistivity measurement which tends to infinite. On the other hand, the resistivity of the conductive tracks itself is not affected by the etching treatment.

This experiment demonstrates thus that it is possible to electrically isolate a portion of the ITO substrate. As a consequence, if we submit a patterned ITO surface to the electrografting process, only the connected tracks undergo the reduction process and electrografting develops only in these areas. This behavior was checked experimentally as show in figure 10. We have isolated an ITO square by SECM etching and the sample was then submitted to electrografting of a Ru-containing photosensitizer (red colour). We can clearly see that the isolated ITO square is not grafted with Ru-photosensitizer thus confirming the electric isolation of the square from the substrate. The photosensibilizer ( $[\text{Ru}(\text{bipy})_2(\text{bipy-ph-N}_2^+)](\text{PF}_6)_3$  (abbreviated as  $\text{Ru}(\text{bipy})_3^{2+}$ ) was synthesized as described by Jusselme et al.<sup>[16]</sup>

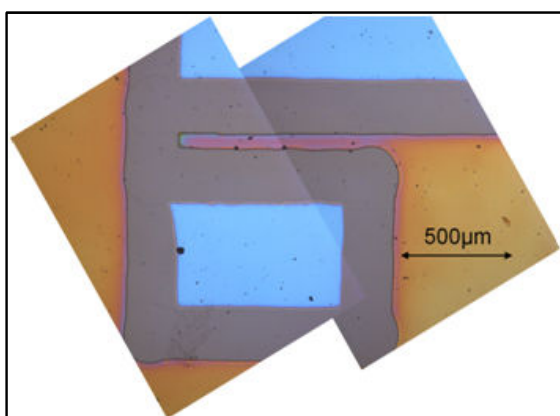


Figure 10: patterned ITO substrate by local etching.  $100\mu\text{m}$  Pt UME;  $d/a=0.4$ ; scan speed  $50\mu\text{m}\cdot\text{s}^{-1}$ .  $[\text{AA}]=2\text{mol}\cdot\text{dm}^{-3}$ ,  $[\text{H}_2\text{SO}_4]=0.25\text{mol}\cdot\text{dm}^{-3}$ . Electrografting of diazonium salt only on the electrically connected tracks. Modified  $\text{Ru}(\text{bipy})_3^{2+}$  ( $0.002\text{mol}\cdot\text{dm}^{-3}$ ) in acetonitrile/TEAP ( $0.1\text{mol}\cdot\text{dm}^{-3}$ ); cyclic voltamperometry from  $0\text{V}$  to  $-2\text{V}$  at  $100\text{mV}\cdot\text{s}^{-1}$  vs.  $\text{Ag}/\text{AgNO}_3$  ( $0.1\text{mol}\cdot\text{dm}^{-3}$ ) in acetonitrile.

To resume, we are able to generate thin conductive tracks that can be useful in several domains, (for example cell culture<sup>[17]</sup> or microfluidics<sup>[18]</sup>) and conductive micro tracks can be modified by electrochemistry to introduce chemical functionalities.

Another field of applications for which the ITO patterning can be attractive is the OLED manufacturing domain. The OLED process is complex and very sensitive to any perturbation such as the contamination of the ITO substrate. In that case, the OLED transmission fails. So as, to realize an OLED on a patterned ITO thin film on a flexible substrate is not a trivial challenge. In collaboration with the group, we took up the challenge. The Charlie Chaplin's portrait was printed by local SECM etching on the ITO flexible substrate, which was then coated with the organic multi layers necessary to the good performance of the OLED. The result shown in figure 11 speaks for itself. The dark areas represent the disconnected ITO.

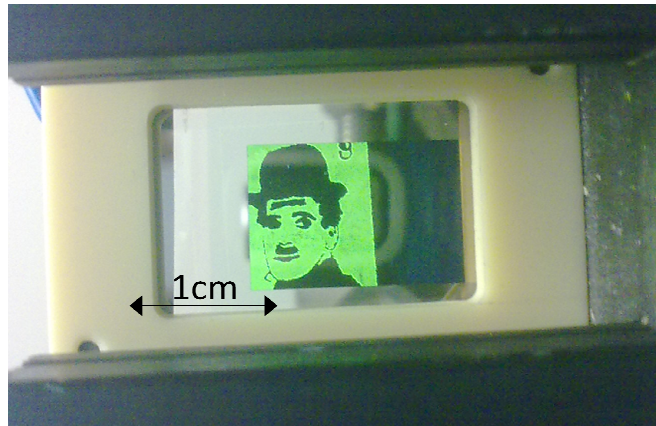


Figure 11: Charlie Chaplin's portrait imprinted on ITO flexible substrate by local SEM etching to realize an OLED.

## 6. Conclusions

Several advantages can be found in SECM etching of ITO films:

- (i) similar to laser ablation no mask is needed and any pattern can be obtained in a quick time when the SECM is coupled to a drawing software. The etching of the ITO film can also be made by a preformed microelectrode to obtain directly the desired shape.
- (ii) this technique is suitable for a roll to roll or sheet by sheet process.
- (iii) it leads to clean etching with straight walls and no redeposition of the ablated part.
- (iv) the substrate (glass or plastic) is not damaged by this technique.
- (v) the minimal cropped line of ITO is 10  $\mu\text{m}$  width. For the transfer to larger surfaces there are no limitation for the (micro) electrode size and shape.
- (vi) the isolation-delimitation of ITO domain gives important supplementary facilities. Electro grafted polymers can be localized on different tracks of the same sample creating a pattern of functional surface.

## References

- [1] C. Ji-Yen and et al., *J. Micromech. Microeng.* **2007**, *17*, 2316.
- [2] J. Chae, S. Appasamy and K. Jain, *App. Phys. Lett.* **2007**, *90*, 261102.
- [3] U. Geyer, J. Hauss, B. Riedel, S. Gleiss, U. Lemmer and M. Gerken, *J. App. Phys.* **2008**, *104*, 093111.
- [4] F. C. Krebs, H. Spanggard, T. Kjaer, M. Biancardo and J. Alstrup, *Mat. Sci. Eng. B-Solid* **2007**, *138*, 106.
- [5] C. J. Huang, Y. K. Su and S. L. Wu, *Mater. Chem. Phys.* **2004**, *84*, 146.
- [6] M. Scholten and J. E. A. M. van den Meerakker, *J. Electrochem. Soc.* **1993**, *140*, 471.
- [7] J. E. A. M. van den Meerakker, P. C. Baarslag and M. Scholten, *J. Electrochem. Soc.* **1995**, *142*, 2321.
- [8] J. E. A. M. van den Meerakker, P. C. Baarslag, W. Walrave, T. J. Vink and J. L. C. Daams, *Thin Solid Films* **1995**, *266*, 152.
- [9] M. Takai, D. Bollmann and K. Habberger, *App. Phys. Lett.* **1994**, *64*, 2560.
- [10] O. Yavas and M. Takai, *App. Phys. Lett.* **1998**, *73*, 2558.
- [11] Z. H. Li, E. S. Cho and S. J. Kwon, *App. Surf. Sci.* **2009**, *255*, 9843.
- [12] G. Raciukaitis, M. Brikas, M. Gedvilas and T. Rakickas, *App. Surf. Sci.* **2007**, *253*, 6570.
- [13] Q. Wei, H. Zheng and Y. Huang, *Sol. Energ. Mat. Sol. Cells* **2001**, *68*, 383.
- [14] C. J. L. F. X. Xie, Z. Q. He, and Y. L. Tao, *Int. J. Photoenergy* **2008**, *vol. 2008*, 6.
- [15] D. B. B. Michael D. Irwin, Alexander W. Hains, Robert P. H. Chang, and Tobin J. Marks, *PNAS* **2008**, *105*, 5.
- [16] B. Joussetme, G. Bidan, M. Billon, C. Goyer, Y. Kervella, S. Guillerez, E. Abou Hamad, C. Goze-Bac, J. Y. Mevellec and S. Lefrant, *J. Electroanal. Chem.* **2008**, *621*, 277.
- [17] J. W. Lee, K. S. Lee, N. Cho, B. K. Ju, K. B. Lee and S. H. Lee, *Sensor Actuat. B Chem.* **2007**, *128*, 252.
- [18] A. Tourovskaia, T. F. Kosar and A. Folch, *Biophys. J.* **2006**, *90*, 2192.

## CONCLUSIONS AND PERSPECTIVES

At the crossroads of multiple disciplines (physics, chemistry, biology, mechanics, etc), nanotechnologies and nanosciences appear today among the major fields of research for the coming years. Nanotechnology aims at working out new materials and components increasingly smaller, more powerful, lighter and less expensive. In parallel, nanosciences tend to understand and explore new phenomena, which appear only at the nanometre scale. Our work falls under both fundamental and applied themes, since it concerns localized modification of surfaces. It is only relatively recently that electrochemistry joined the field of nanotechnology thanks, among others, to the development of the SECM as this technique enables both surface analysis and surface modification.

Our group has historically been developing the electrografting of vinylic polymers via an electro-induced anionic polymerization that starts from a precursor chemically bound to the electrode. A second family of precursors, aryl diazonium derivatives, has also been investigated. Diazonium salts in acidic solution, alone or in presence of vinylic monomer reveal to be suited precursors for the local electrografting process. Indeed, as the grafting is electro-induced and originates from the surface, it is strongly dependent on the local efficiency of the electron transfer to the electro-active species in solution. We have clearly demonstrated that this efficiency of the local electron transfer may be driven by field-induced means. The localization of the electrografting process is controlled by adjusting the tip-substrate distance, the current density, and the reaction time. The local electrochemical grafting of different polymers onto conductive surfaces as well as the localized process on different conductive and semi-conductive substrates have been studied. The resulting thin films were characterized by X-ray photoelectron spectroscopy, infrared spectroscopy, atomic force microscopy, and optical microscopy.

In this work, we have also clearly demonstrated that SECM can be used as an actual lithographic tool to locally graft a non conductive organic coating on conductive and semi-conductive homogeneous substrates. Species suitable for modifying the surfaces of the samples by chemical or electrochemical reactions are electrogenerated by the tip. The small distance between the tip and the substrate reduces the diffusion time of the electrogenerated species and ensures a small reaction area. No preformed stamp or mask is needed prior to patterning the substrate, since the pattern is formed by scanning the UME. The lateral resolution depends on the size and the shape of the tip and is about two times the size of the microelectrode. With the AFM-SECM tool, a nanometric resolution has been reached.

One of the most common reproaches towards the local probes techniques for the potential lithography applications is their relative slow writing speed. A way to circumvent this drawback is to use a structured microelectrode, acting thus as a

"electrified stamp". Like demonstrated by Amatore et al.,<sup>[1]</sup> the microelectrode stationary state is indeed realizable where one of the planar electrode dimensions is micrometric. In a preliminary trial experiment, a linear micro-band electrode was realized and used as the SECM tip in the local electrografting process. As shown on figure 1a, this band electrode can be easily imprinted on an homogeneous substrate with lateral dimensions accorded with the band electrodes dimensions. Preliminary results obtained with a more complex structured microelectrode are also encouraging. For this experiment, we used a patterned gold/silicon electrode as the microelectrode in the SECM environment (fig. 1b, left). Even if the experimental parameters were not optimized in this peculiar application, we clearly obtained on the homogeneous Si substrate the duplication of the gold pattern of the structured microelectrode (fig. 1b, right). Those results open thus the way for a competitive 2D microfabrication. The local graft method could then be integrated into a microelectronic fabrication process to get micron or sub-micron local selective coatings on conducting and semiconducting substrates.

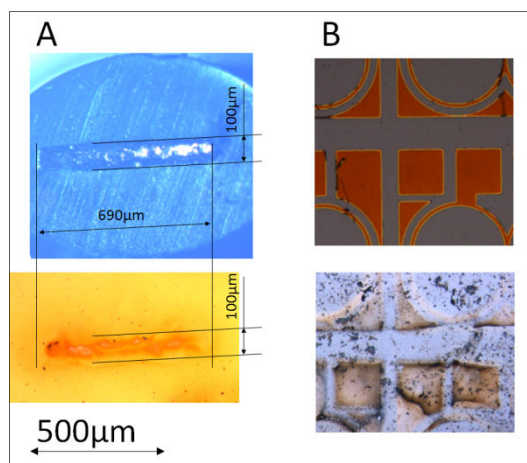


*Figure 1: electrografting carried out with structured UME electrodes. (a, top) gold band microelectrode sealed in the glass; (a, down) local grafting with the gold band microelectrode. [AA]:2.0 mol. dm<sup>-3</sup>, DNB:2 10<sup>-3</sup> mol.dm<sup>-3</sup>, H<sub>2</sub>SO<sub>4</sub>:0.25 mol.dm<sup>-3</sup>; E<sub>UME</sub>=3V, E<sub>sub</sub>=-0.5V; d ≈50μm, t=30s.*

*(b, top) structured gold/Si microelectrode; (b, down) local grafting on n-type Si, duplicating the structured microelectrode pattern. [AA]:2.0 mol. dm<sup>-3</sup>, DNB:2 10<sup>-3</sup> mol.dm<sup>-3</sup>, H<sub>2</sub>SO<sub>4</sub>:0.25 mol.dm<sup>-3</sup>; E<sub>UME</sub>=10V, E<sub>sub</sub>=-0.4V; d ≈20μm, t=10s.*

The development of microsystems, using or transporting fluids or submitted to flows accelerated during the ten past years. New applications regularly come to enrich an already abundant panel, in particular in the fields of health, biochemistry and fine chemistry. The micro-/nano-fluidic appears today among the most dynamic emergent fields. This rise was made possible by the development of techniques able to structure materials on a micro- /nanometric scale thanks, in particular, to the emergence of new methods of nanofabrication, such as nanoimpression, nanocompression or soft

lithography. The work developed during this thesis may bring some contribution in this field of “*micro-channel design*”. For example, micrografted lines of polyacrylic acid (PAA) were realized following the local grafting process and served as a mask towards a second forthcoming electrografting process realized, in a non local way in a classical electrochemical cell, with a fluorinated diazonium salt (figure 2). XPS analysis was carried out to highline this contrast on the bidimensional pattern. This procedure is synthesized on scheme 1.

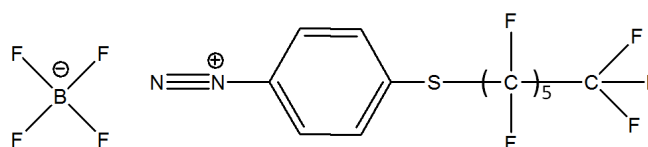
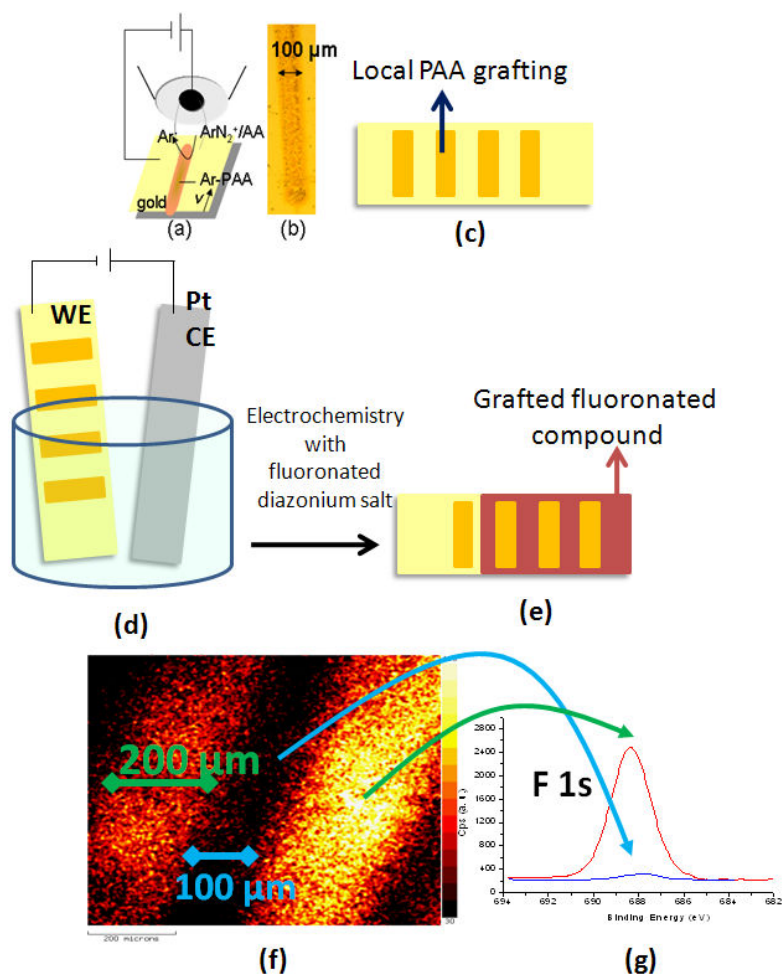


Figure 2: fluorinated diazonium salt used for the hydrophobic surface functionalization of a patterned gold substrate by cyclic voltamperometry from 0V vs.VOC to -1.5V vs. Ag wire; FBD  $2 \cdot 10^{-3} \text{ mol.dm}^{-3}$ ,  $\text{H}_2\text{SO}_4$   $0.25 \text{ mol.dm}^{-3}$ .



Scheme 1: sequences for bipatterning of a homogeneous gold substrate. (a) Local grafting process, (b) optical image of the grafted line of PAA; (c) schematic view of the patterned PAA/Au substrate; (d) classical electrochemistry in a three-electrode configuration with the PAA/Au substrate as working electrode and a Pt sheet as counter-electrode ; (e) schematic view

*of the fluoro-compound/PAA bipatterned Au substrate; (f) Elemental map of Au obtained by XPS mapping analysis on the grafted gold substrate. Acquisition conditions: X-ray source= 225W, high resolution FoV1 (800 x 800  $\mu\text{m}^2$ ), and pass energy= 160eV; (g) F 1s core level spectra of the coating recorded on two different locations on the grafted substrate. Acquisition conditions: X-ray source= 225W, high resolution FoV2 (55 x 55  $\mu\text{m}^2$ ), and pass energy= 40 eV.*

This approach allows thus to define regions on the surface with different hydrophilicity which can constitute microchannels for driving, for example, liquids in function of the liquid/surface interactions. The PAA channel will indeed present a more hydrophilic behavior than the fluorinated regions.

Modified surfaces containing spatially defined functionalities are a desirable goal for numerous applications. Recent years have seen considerable progress in the development of microfabricated systems for use in the chemical and biological sciences. The need to analyze complex biological samples and to measure multiple analytes simultaneously has led to the development of new analytical strategies, which are mainly based on array technologies. Generally, the fabrication of such high-density arrays containing different features in different locations is a challenging problem, despite constant advances in micro/nano-technology. In this context, we are convinced that the localized organic grafting at a micronic or sub-micronic scale obtained with our local process may play an interesting role for the localized immobilization of micro to nanometer sized biological recognition elements.

In collaboration with the laboratory of Chemistry for Research and Engineering of Architectures for Biology (CREAB, joint research unit of CNRS, CEA and University Joseph Fourier), we have evaluated the potentialities of our local graft process for the identification of analytes in biological samples through their nucleic acid sequences. For that purpose, a PAA patterned gold substrate was realized by applying different potential conditions with a pulsed approach in order to improve the selectivity. In practice, a 50  $\mu\text{m}$ -Pt UME was placed at 15 $\mu\text{m}$  from the gold surface and then polarized at the working potential during 0.1s with 0.4s of rest on 60 times; the surface was biased continuously at -0.25 V vs. Ag wire during all the duration (30 s) of the experiment. For every tested potential (6, 8, and 10 V respectively), four dots were realized. To determine the chemical contrast on the surface, IRRAS localized spectra were recorded on the chip (fig. 3). As expected, the thickness of the localized coating increases with the applied tip potential from 80 nm thick ( $E_{\text{UME}}=6\text{V}$ ) to 130 nm thick ( $E_{\text{UME}}=10\text{V}$ ) while the width varies from 80  $\mu\text{m}$  width to 110  $\mu\text{m}$  width, respectively.

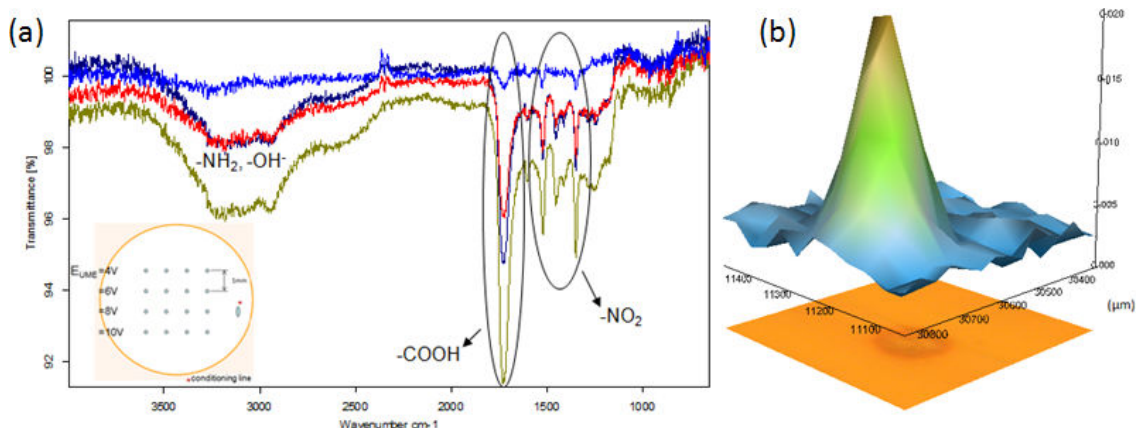
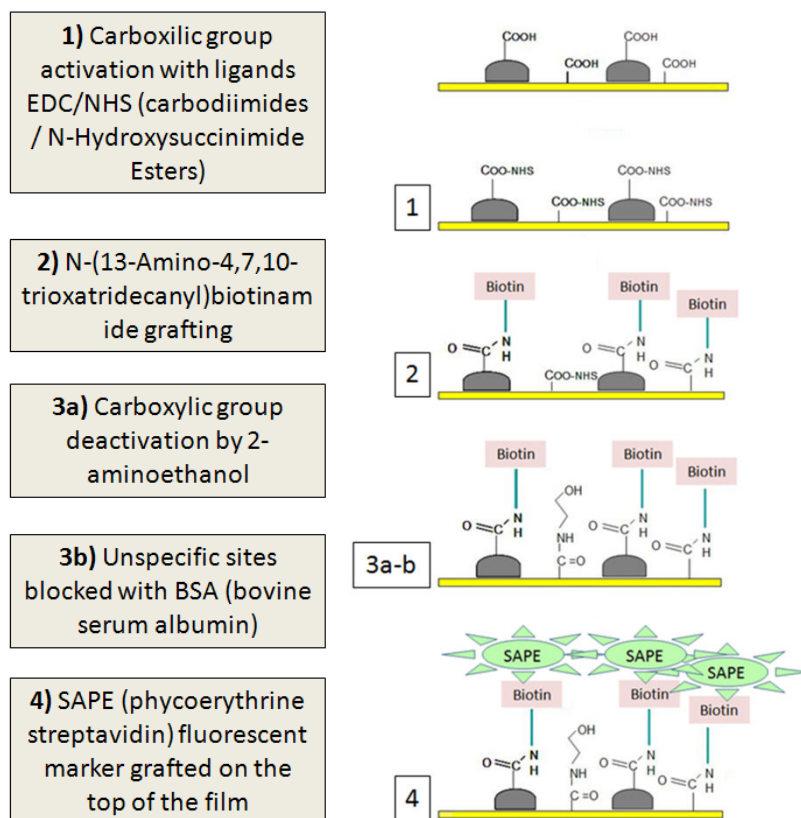


Figure 3: IRRAS localized spectra of: (a) electrografted dot at different UME potential by pulsed technique: passivation film (—);  $E_{UME}=6V$  (—);  $E_{UME}=8V$  (—);  $E_{UME}=10V$  (—); insert: design of the patterned gold chip; (b) absorbance 3D scan image recorded at  $1730\text{ cm}^{-1}$  for dot realized at  $E_{UME}=8V$ .  $E_{sub}=-0.25V$ . AA: $2.0\text{ mol. dm}^{-3}$ , DNB: $2\cdot 10^{-3}\text{ mol. dm}^{-3}$ ,  $H_2SO_4$ : $0.25\text{ mol. dm}^{-3}$ ,  $50\text{ }\mu\text{m-Pt}$ ,  $d = 15\mu\text{m}$

The patterned chips were then sent to CREAB's lab to carry out the biofunctionalization. For this first trial experiment, it was chosen an usual method based on fluorescent molecules grafted on biotin. The procedure is briefly described in the scheme 2:



Scheme 2: Biotin-streptavidin fluorescent complex functionalization steps.

Figure 4 shows the fluorescent image of the patterned gold substrate after biological functionalization. The fluorescent signal was measured on the dots pattern (numbered 1 to 3 on figure 4) and outside the patterned region (numbered 4 on figure 4) at each time of the functionalization process. The comparison between these different measures allows to evaluate the intensity of the contrast between localized grafting zones and the background surface. From those measurements, one can deduce that the specific recognition on a dot is about 51% higher than that observed for the zone 4. According to the specialists of the technique, this result is very significant and encouraging, suggesting that this work deserves to be continued.

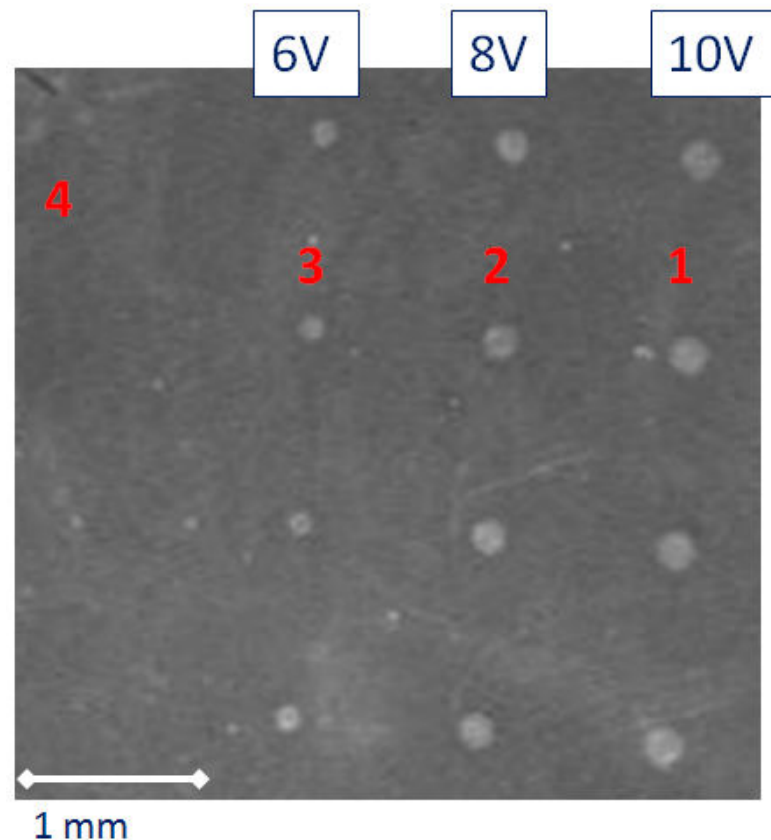


*Figure 3: Fluorescence image of the patterned gold substrate realized at different tip potential after biological functionalization.*

To sum up, electronic, biology and chemical biology have pushed the scientists to develop new techniques to graft locally organic molecules on surfaces. The objective of the thesis was to develop a cheap and lithography-free technique by combining local probes techniques and electrografting processes in view of tuning locally chemical and physical surface properties on initially homogeneous substrates. The potentialities of a micro or submicro-electrode to create organic patterns on surfaces electrically connected have been validated. Dots, lines or more complex 2D-patterns have been

“imprinted” on conducting (Au, Pt, graphene), and semiconducting (n-type Si) substrates with a lateral resolution equal to one or two times the probe size. By combining AFM and SECM, the technique has been transposed to a submicronic scale with the size resolution preserved.

The big advantage of grafted organic layers is that they are covalently bonded to the substrate and then chemically stable so that they can be further processed by classical chemistry. The polyacrylate deposit can, for example, be functionalized by a simple amidation of the carboxylic hanging groups and thus can serve as primer coatings for the attachment of various molecules, biomolecules or particles. The local graft developed process thus has all qualities necessary for a large field of applications.

[1] C. Amatore, C. Combellas, F. Kanoufi, C. Sella, A. Thiébault and L. Thouin, *Chemistry – A European Journal* **2000**, *6*, 820.



**Publications** "Direct SECM Localized Electrografting of Vinylic Monomers on a Conducting Substrate"  
*F. Grisotto, A. Ghorbal, C. Goyer, J. Charlier, S. Palacin, Chem. Mater, 2011, doi: 10.1021/cm101563n*

"Localized Electrografting of Vinylic Monomers on a Conducting Substrate by Means of an Integrated Electrochemical AFM Probe"  
*A. Ghorbal, F. Grisotto, J. Charlier, S. Palacin, C. Goyer, C. Demaille, ChemPhysChem, 2009, 10, 1053 - 1057*

"Surface Homogeneity of Anion Exchange Membranes: A Chronopotentiometric Study in the Overlimiting Current Range"  
*J. Phys. Chem. B, 2009, 113, 5829-5836*

"Main Strategies to Direct Localized Organic Grafting on Conducting and Semiconducting Substrate"  
*J. Charlier, A. Ghorbal, F. Grisotto, E. Clolus and Serge Palacin, New Nanotechniques, 2009, Editors: A. Malik and R.J. Rawat, chapter 9, 319-350*

"The in situ characterization and structuring of electrografted polyphenylene films on silicon surfaces. An AFM and XPS study"  
*A. Ghorbal, F. Grisotto, M. Laudé, J. Charlier, S. Palacin, J. Coll. Interf. Sc., 2008, 328, 308-313*

**Conferences** *XIII International Cyclodextrin Symposium, Torino (IT)* May 14-17, 2006  
"Preparation and characterisation of  $\gamma$ -cyclodextrin based nanosponges "

*Congresso Nazionale di Chimica e Tecnologia delle Ciclodestrine, Asti (IT)* May 6-8, 2007  
Secretary

*Colloque Electrochimie dans les Nanosciences 2, Grenoble (FR)* February 5- 6, 2008  
"Organic thin films grafted onto silicium substrate: from micro-grafting by SECM to nano-grafting by AFM"

*4th ECHEMS Meeting* June 25 - 28, 2008  
Camaret-sur-mer, Finistère (FR)  
"Scanning electrochemical microscopy (SECM) in direct grafting of conductive surfaces."

*The 5th Workshop on Scanning Electrochemical Microscopy, Blue Mountain Lake, New York (USA)* August 24-28, 2008  
"Direct SECM localized electrografting of vinylic monomers onto conducting substrates"

*4th ELECMOL International Conference on Molecular and Organic Electronics, Grenoble (Fr)* December 8-12, 2008

"Localized electrografting of vinylic monomers on conducting substrate using an integrated electrochemical AFM probe"

*ElecNano3 Electrochemistry in Nanoscience*, Paris (Fr)

April 21-21, 2009

"Direct localized electrografting of vinylic monomers onto conducting substrates: from micro- to nano- electrografting"

*2nd Journée POL-IdF*, Paris (Fr)

September 4, 2009

« Micro et nano-lithographie par voie électrochimique. Un outil simple et robuste de localisation des couches polymers »

*24th, Journées Surfaces et Interfaces*, Nantes (Fr)

January 27-29 2010

" Scanning electrochemical microscopy (SECM) in localized grafting of conductive and semi-conductive surfaces"

6th ECHEMS  
Sandbjerg (Denmark)

June 20 – 23, 2010

"SECM localized electrografting onto conducting and semi-conducting substrates. A new covalent lithography"

*61th ISE, International Society of electrochemistry*, Nice (Fr)

September 26th  
October 1st, 2010

"SECM localized electrografting onto conducting and semi-conducting substrates. A new covalent lithography"

